Optimizing Magnetotelluric Studies for Geothermal Exploration in Western Saudi Arabia: A Comprehensive Study of 3D Forward and Inverse Modeling Approaches

Inaugural-Dissertation

zur Erlangung des Doktorgrades
der Mathematisch-Naturwissenschaftlichen Fakultät
der Universität zu Köln

vorgelegt von

Abdul Latif Ashadi

aus Demak, Indonesien

Köln, 2025

1. Gutachter: Prof. Dr. B. Tezkan
2. Gutachter: Prof. Dr. M. Becken

Tag der mündlichen Prüfung: 28.04.2025

Abstract

With its ambitious vision of 2030, Saudi Arabia has recognized the need to reduce its dependence on fossil-based energy and has taken concrete steps to diversify its energy sources. Among the priorities is the development of renewable energy, including geothermal resources. This thesis focuses on the application of Electromagnetic (EM) methods, specifically Magnetotellurics (MT) and Transient Electromagnetics (TEM), for the exploration of geothermal resources in the Al-Lith's area, western Saudi Arabia, one of the most promising sites for geothermal development in Saudi Arabia.

To comprehensively investigate and explore the prospect of geothermal resources in the area, broadband MT data covering a period range of 0.001–512 seconds were acquired at 50 locations, along with 13 TEM soundings. The phase tensor and its skew calculations revealed a complex subsurface conductivity structure, characterized by predominantly 1D/2D geoelectric behavior for short periods ($<$ 2 sec) and a more complex 3D structure for longer periods. Prior to the inversion of the MT data, 3D MT synthetic modeling and inversion studies were carried out to assess the detectability of geothermal anomalies, optimize survey parameters, and evaluate the sensitivity of various parameter inputs applied in the 3D inversion. In order to ensure the robustness of the inversion results, extensive 3D MT inversion tests were performed. The resistivity model derived from TEM data was incorporated to optimize the 3D MT inversion.

The final 3D resistivity model, with an RMS of 1.96, provides a high-resolution image of the geothermal system, delineating the heat source, convection pattern, and groundwater system. The geothermal reservoir is represented by deep elongated conductive bodies ($<$ 20 Ωm) extending from 2.5 to over 8 km in depth. The individual protrusions above the reservoir indicate the pathways for geothermal fluids, forming convection cells from the reservoir to the surface or near the surface, potentially leading to an active geothermal surface manifestation (hot spring). The outcome of this study serves as the key input to understanding the complexity and characterization of the geothermal system of the Al-Lith region, confirming its potential for geothermal exploration and development efforts in Saudi Arabia.

Zusammenfassung

Mit seiner ehrgeizigen Vision für 2030 hat Saudi-Arabien die Notwendigkeit erkannt, seine Abhängigkeit von fossilen Energieträgern zu verringern, und hat konkrete Schritte zur Diversifizierung seiner Energiequellen unternommen. Eine der Prioritäten gehört die Entwicklung erneuerbarer Energien, einschließlich geothermischer Ressourcen. Diese Arbeit befasst sich mit deri Anwendung elektromagnetischer (EM) Methoden, insbesondere der Magnetotellurik (MT) und der Transienten Elektromagnetik (TEM), zur Exploration geothermischer Ressourcen im Gebiet von Al-Lith, das im westlichen Saudi-Arabien liegt. Die Region Al-Lith ist bekannt für geothermische Oberflächenerscheinungen wie heiße Quellen was sie zu einem der vielversprechendsten Standorte für die geothermische Entwicklung in Saudi-Arabien macht.

Um das Potenzial geothermischer Ressourcen in diesem Gebiet umfassend zu untersuchen, wurden breitbandige MT-Daten mit einer Periodendauer von 0,001–512 Sekunden an 50 Messpunkten erfasst, ergänzt durch 13 TEM-Sondierungen. Dimensionalitätsanalysen mittels Phasentensor und seiner Schiefe zeigten eine komplexe Leitfähigkeitsstruktur des Untergrunds, die sich durch ein überwiegend 1D/2D-geoelektrisches Verhalten bei kurzen Perioden (< 2 Sek.) und eine komplexere 3D-Struktur bei längeren Perioden auszeichnet. Vor der Inversion der MT-Daten wurden synthetische 3D-MT Modellierungen und Inversionsstudien durchgeführt, um die Erkennbarkeit geothermischer Anomalien zu bewerten, die Messparameter zu optimieren und die Empfindlichkeit verschiedener Parameter in der 3D-Inversion zu untersuchen. Um die Robustheit der Inversionsergebnisse zu gewährleisten, wurden umfangreiche 3D-MT-Inversionstests durchgeführt, bei denen verschiedene Startresistivitätsmodelle, Glättungsfaktoren, statische Verschiebungskorrekturen, Einfluss der Topographie und unterschiedliche Tensor-Datenarten variiert wurden. Das aus den TEM-Daten abgeleitete Resistivitätsmodell wurde als A-Priori-Information in das Startmodell integriert, um die 3D-MT-Inversion zu optimieren.

Das endgültige 3D-Resistivitätsmodell, mit einem RMS von 1,96, liefert ein hochauflösendes Bild des geothermischen Systems, das die Wärmequelle, das Konvektionsmuster und das Grundwassersystem abbildet. Das geothermische Reservoir wird durch tiefreichende, langgestreckte leitfähige Strukturen (< 20 Ωm) dargestellt, die sich von 2,5 bis über 8 km Tiefe erstrecken. Einzelne aufsteigende Strukturen über dem Reservoir deuten auf Aufstiegswege für geothermische Flüssigkeiten hin, die

Konvektionszellen vom Reservoir bis zur Oberfläche oder in oberflächennahe Bereiche bilden und möglicherweise zu aktiven geothermischen Manifestationen (heiße Quellen) führen. Die Ergebnisse dieser Studie stellen einen entscheidenden Beitrag zum Verständnis der Komplexität und Charakterisierung des geothermischen Systems der Al-Lith-Region dar und bestätigen dessen Potenzial für die geothermische Exploration und Entwicklung in Saudi-Arabien.

Contents

List of Figures

List of Tables

Chapter 1

Introduction

1.1 Motivation

Geothermal energy has emerged as a promising renewable energy source with the potential to play a significant role in the global energy landscape. Geothermal resources, which harness the Earth's internal heat, offer a continuous and low-carbon power source that can supplement and diversify the energy mix in many regions. This type of energy is required to replace the carbon dioxide spewed by oil, coal, and other fossil fuels, which are the main source of global warming emissions, one of humanity's most pressing existential issues today. To control these global warming phenomena, it is imperative to enhance energy efficiency and to transition from fossil fuels and other environmentally harmful energy sources to renewable and sustainable energy alternatives. Unlike fossil fuels, geothermal power generation does not produce harmful greenhouse gas emissions, making it a sustainable option for energy production. Therefore, geothermal energy is one of the geo-resources that serve as a critical foundation for facilitating reductions in gas emissions (Herrington, 2021; Younger, 2014).

In addition to its environmental benefits, geothermal energy also offers practical advantages in terms of its accessibility and versatility. Geothermal resources are widely distributed across the globe, with significant potential in regions with high volcanic and tectonic activity. Furthermore, geothermal energy can be used not only for electricity generation but also for direct heating and cooling applications, making it a versatile energy solution for a variety of residential, commercial, and industrial needs (Lund & Toth, 2021). As the global demand for renewable and sustainable energy sources continues to rise, the development of geothermal energy resources will become increasingly important. With its clean, continuous, and versatile nature, geothermal energy has the potential to play a vital role in the transition towards a more sustainable energy future (Adams et al., 2015; Zhang et al., 2019).

The Kingdom of Saudi Arabia has long been recognized as a global leader in the oil and gas industry, but as the world transitions towards renewable energy, the country has also set its sights on tapping into the vast potential of geothermal resources (Melouah et al., 2023). This shift is a key component of Saudi Arabia's Vision 2030, a strategic plan aimed at diversifying the nation's economy, reducing its reliance on fossil

fuels, and achieving Net Zero carbon emission by 2060 (Ali et al., 2021; Hassan, 2020). Saudi Arabia possesses significant geothermal energy resources, particularly in its western region along the Red Sea coast, where numerous tectonic activities, volcanic fields, and hot springs are located, as shown in Figure 1.1 (Aboud et al., 2021; Demirbas et al., 2016; Lashin, Al Arifi, et al., 2015; Rehman & Shash, 2005). By harnessing these geothermal assets, Saudi Arabia can not only contribute to global efforts to combat climate change but also bolster its economic diversification efforts. By diversifying its energy mix and reducing its reliance on fossil fuels, the Kingdom can enhance its energy security, create new economic opportunities, and contribute to a more sustainable future for the region and the world (Aldabesh et al., 2021; Melouah et al., 2023).

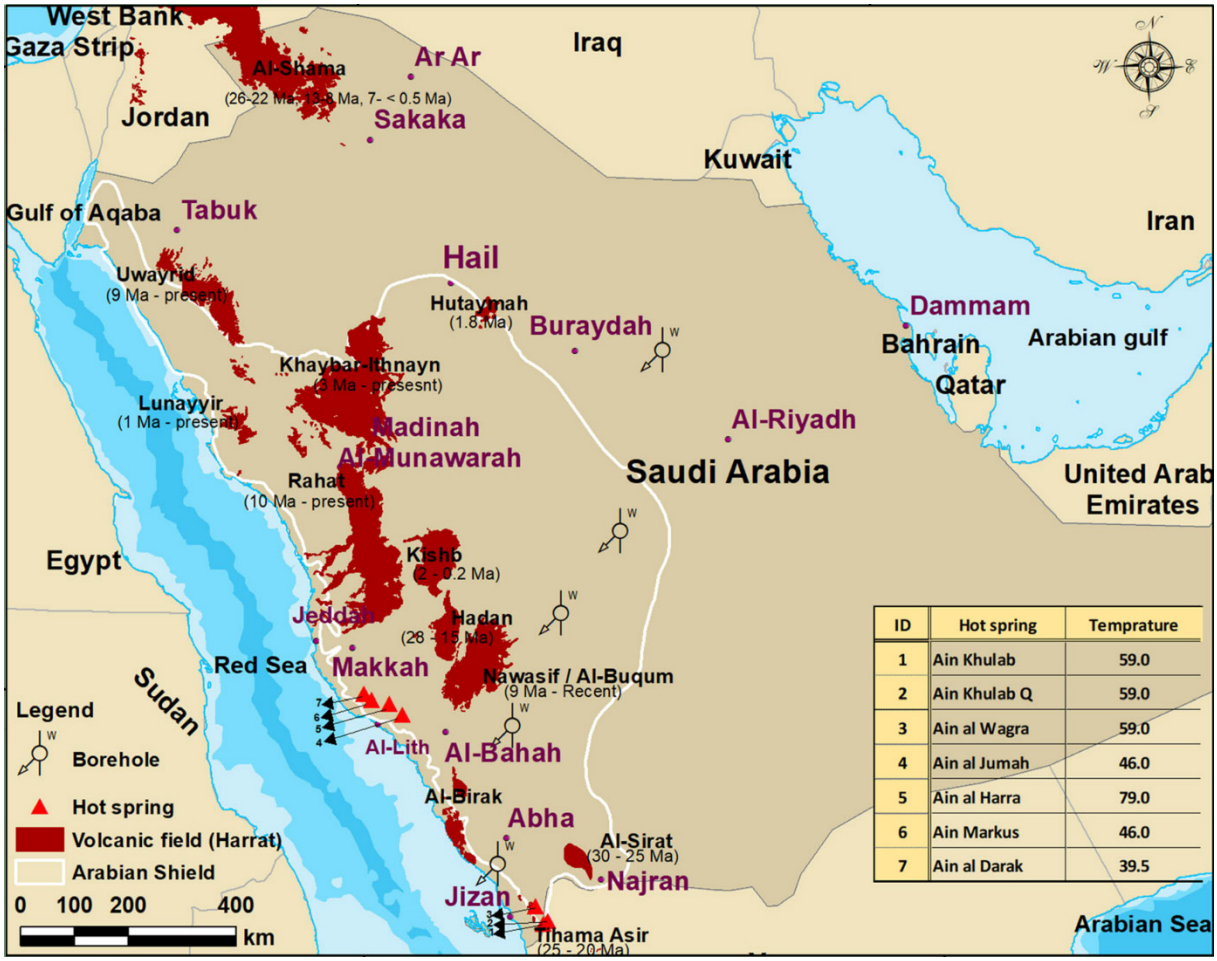

Figure 1.1: Saudi Arabia's map showing the main geothermal features, including volcanic fields (red polygons), hot springs (red triangles), and measurements of heat flow. Figure taken from Aboud et al. (2021).

Several exploration campaigns and research studies have been carried out to investigate the potential of the geothermal resources of Saudi Arabia (Al-Dayel, 1988; Chandrasekharam et al., 2014, 2015; Demirbas et al., 2016; Hussein et al., 2013; Lashin et al., 2014; Lashin & Al Arifi, 2014; Ouda et al., 2022; Ashadi et al., 2024). The aforementioned geothermal studies suggested that Al-Lith area, located south of Jeddah, is known for its geothermal activity and is considered one of the most

prominent sites for geothermal resources in the Kingdom of Saudi Arabia (Aboud et al., 2021; Hussein et al., 2013; Lashin et al., 2014; Lashin, Pipan, et al., 2015). Its geothermal reserve holds a significant promise for providing clean power energy on a long-term basis. Although geothermal energy utilization for power generation is not yet economically viable, some direct-use applications of low-grade geothermal resources have already been implemented. In 2023, the construction of the Hot Spring Park near the Ain Al-Harrah hot spring was completed, featuring amenities such as steam baths, swimming pools, and children's playgrounds (Figure 1.2). Despite this, geothermal energy studies in Al-Lith require more detailed and comprehensive investigations to fully characterize the geothermal system. A critical missing component in these studies is a deep subsurface geoelectrical/electromagnetic survey, which is essential for understanding the geothermal reservoir's structure and potential.

Figure 1.2: Photo showing the Hot Spring Park near the Ain Al-Harrah hot spring, featuring amenities such as steam baths, swimming pools, and children's playgrounds.

Among the geophysical methods employed in geothermal exploration, electromagnetic (EM) methods have proven to be particularly effective due to their ability to effectively map the subsurface electrical properties and identify key features, such as heat sources, faults, fractures, and fluid pathways. The EM methods can also be used to assess the depth and extent of geothermal resources, which is essential for the development and exploitation of geothermal energy (Adams et al., 2015). During the last decades, the applied EM method has become an industry standard for geothermal exploration due to its ability to detect conductive zones commonly present in a geothermal system (Muñoz, 2014; Wright et al., 1985). Enhanced hardware, interpretation methodologies, data processing tools, and modeling software have further increased the popularity of EM over other geophysical methods (Spichak & Manzella, 2009). Among several EM techniques, Magnetotelluric (MT) has become the most widely used for exploration in the geothermal field due to its relatively low cost, highly effective, and deep subsurface

penetration (Pellerin et al., 1996). In addition to MT, the Transient Electromagnetic (TEM) method is also used in geothermal exploration, albeit less frequently. TEM is particularly effective for investigating shallow subsurface features and for providing higher-resolution data in the near-surface region. Integrating MT and TEM data allows for static shift corrections and improves the accuracy of subsurface models (Cumming & Mackie, 2010; Pellerin & Hohmann, 1990). Advanced 3D inversion techniques should be applied to the acquired geophysical data to develop robust resistivity models, which can delineate the geothermal reservoir's depth, extent, and fluid pathways—crucial for resource assessment and development (Árnason et al., 2010).

The key motivations for this thesis are:

1. Bridging knowledge gaps in the geothermal exploration in Saudi Arabia. While previous studies in the Al-Lith region have primarily focused on surface manifestations, such as hot springs and geochemical analyses of thermal waters, there remains a significant need to investigate the subsurface characteristics, depth, and fluid circulation within the geothermal reservoir.

2. Demonstrating the integration of MT and TEM methods. This research highlights the value of integrating MT and TEM methods to develop a more reliable subsurface resistivity model. Such an approach is crucial for delineating fluid pathways, assessing geothermal potential, and characterizing reservoir structures.

3. Identifying key geothermal features and assessing energy potential. By characterizing geothermal reservoirs, this research directly supports Saudi Arabia's Vision 2030 by contributing to sustainable energy development and resource management.

1.2 Thesis Outline

This thesis is structured to provide a logical progression from foundational concepts to detailed analysis and interpretation of results. Chapter 1 serves as the introduction, outlining the motivation behind this research, highlighting the significance and objectives that drive the study. Chapter 2 explores the theoretical aspects of electromagnetic methods in applied geophysics, laying the groundwork for the methodologies employed in the thesis. In Chapter 3, the focus shifts to the inversion theory of electromagnetic data, specifically addressing the inversion methods utilized in this study. Chapter 4 offers an overview of various geothermal energy resources, including a discussion on geothermal resources and exploration activities in Saudi Arabia. Chapter 5 describes the field survey conducted at Al-Lith region, detailing how

the data was collected and outlining the primary geological features of the study area. A comprehensive description of the processing applied to the datasets from both MT and TEM measurements, along with an analysis of the processed data, is provided in Chapter 6. Moving on to Chapter 7, a comprehensive exploration of 3-D synthetic modeling and inversion studies is presented. This section elaborates on the principles of 3-D MT forward modeling and the subsequent inversion studies conducted, showcasing how these techniques contribute to a deeper understanding of the subsurface structures.

Chapter 8 offers an in-depth look at the 3D inversion scheme that was utilized to analyze the MT data collected from the Al-Lith area. It begins with a thorough overview of the selected inversion parameters, discussing their significance in achieving accurate models. This chapter also highlights the innovative approach of optimizing 3D MT inversion by incorporating TEM data as prior information to enhance the robustness of the inversion results. Finally, Chapter 9 wraps up the thesis with the presentation of a preferred model for the resistivity distribution of the subsurface, along with an interpretation of these results. This chapter synthesizes the main findings, highlighting their implications and providing recommendations for future research directions in geothermal exploration and geophysical methodologies.

Chapter 2

EM Methods in Applied Geophysics

The subsequent chapter delineates the theoretical foundations of applied electromagnetic (EM) methods, which are widely used in geophysics to investigate the subsurface's electrical properties. Two common EM techniques employed in this thesis are Magnetotellurics (MT) and Transient Electromagnetics (TEM). Each technique has unique advantages and applications depending on the survey objectives and geological context. These applied EM methods are based on Maxwell's equations, which govern the propagation and diffusion of electromagnetic waves. The chapter begins with a brief overview of the electrical properties of Earth materials, followed by the derivation of the diffusion equation. Next, an overview of the MT method is provided, detailing its transfer functions and main characteristics. Finally, the fundamental aspects of the TEM technique are discussed.

2.1 Electrical Properties of Earth Materials

The electrical properties of earth materials are fundamental to many geophysical methods, especially EM methods used to explore the subsurface. These properties, primarily electrical conductivity and resistivity, influence how materials respond to electromagnetic fields. Understanding these properties helps geophysicists interpret the underlying geological structure from electromagnetic surveys and other geophysical techniques.

2.1.1 Electrical Resistivities of Rocks and Minerals

Electrical resistivity (ρ) is a measure of how strongly a material opposes the flow of electric current. Since the 1940s (e.g. Archie, 1942), numerous studies have investigated the electrical conductivity of rocks, driven by the need to understand subsurface properties for resource exploration, including geothermal energy, oil and gas, and minerals. Figure 2.1 shows the typical values of resistivity and conductivity of various rock materials.

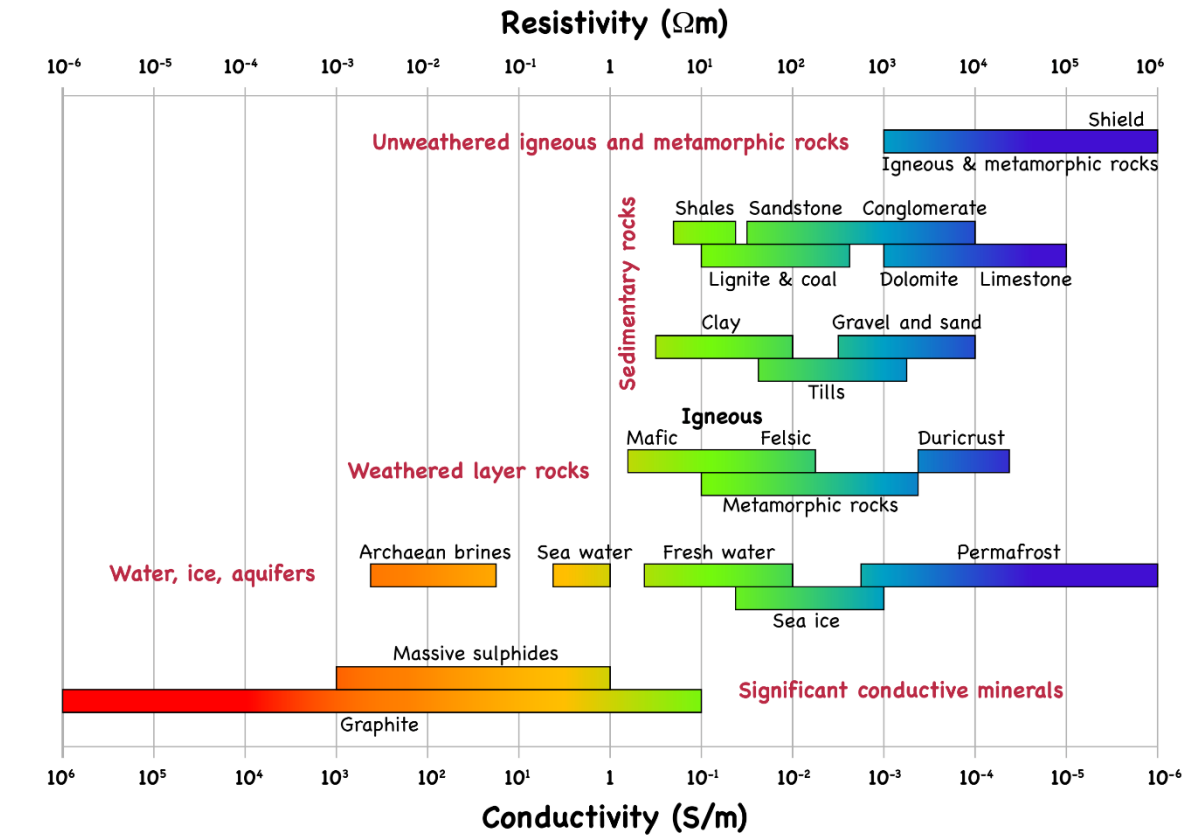

Figure 2.1: Electrical resistivity and conductivity values of rocks and other common Earth materials (Miensopust, 2010). The values were taken from (Palacky, 1988), and references therein.

The property of electrical resistivity is influenced by the mobility and density of charge carriers within the material, which refers to the so-called conduction mechanism. The conduction mechanisms in the Earth can be categorized into three main types (Caldwell et al., 1986): Electronic, ionic, and metallic conduction. Electronic conduction involves the movement of free electrons within the material. It is commonly observed in metallic minerals and rocks, such as sulfide ores (e.g., pyrite, chalcopyrite) and graphite. In ionic (electrolytic) conduction, the movement of charged ions, such as sodium (Na+), potassium (K+), or chloride (Cl-) ions, is the primary mechanism of electrical charge transport. This type of conduction is typically found in rocks and minerals that contain dissolved salts or ionic compounds, such as saline groundwater or evaporite deposits. Metallic conduction is a type of electronic conduction that occurs due to the mobility of free electrons in pure metals, which are very rare in the crust. This metallic conduction mechanism is in contrast with other conduction mechanisms, which involve the movement of different charge carriers (ions or electron-hole pairs).

2.1.2 Electrical Resistivity of Rocks in Geothermal System

Geothermal systems are complex environments where the interaction between hot fluids and the surrounding rock matrix can lead to significant changes in the physical and

chemical characteristics of the rock. One of the key parameters that is affected by these hydrothermal alteration processes is the electrical resistivity of the rock (Wyering et al., 2014). The high temperatures, the presence of hot (often saline) fluids, and alteration minerals (when present) can greatly influence the electrical properties of rocks (Caldwell et al., 1986; Ussher et al., 2000). Elevated temperatures in geothermal regions generally decrease rock resistivity because increased thermal energy enhances ion mobility in fluids. In more detail, at temperatures of 200 °C or lower for example, fluid resistivity decreases as temperature increases (Llera et al., 1990). Conversely, at temperatures of 300 °C or higher, the increased temperature of water leads to the dissociation of ions, resulting in higher fluid resistivity (Quist & Marshall, 1968).

Regarding the alteration minerals, Caldwell et al. (1986) discovered that the presence of alteration minerals, often referred to as clay minerals, has a significant impact on bulk conductivity. Specifically, an increase of 10% in clay content within the rock samples decreases conductivity by one order of magnitude. They also noted that in geothermal rocks, temperature is a lesser factor compared to clay content, fluid conductivity, and porosity (Caldwell et al., 1986).

Following the clay content, Caldwell et al. (1986) suggested that the next key factor influencing conductivity in geothermal rocks is a combination of the conductivity and porosity of the fluid. Laboratory measurements indicate that increasing porosity by one order of magnitude, for instance, from 0.01 to 0.1, results in an approximate increase of one order of magnitude in bulk conductivity (Caldwell et al., 1986; Hersir & Árnason, 2013; Ussher et al., 2000). High salinity fluids lead to increased electrical conductivity due to enhanced ion mobility (Caldwell et al., 1986; Ucok et al., 1980). When salinity is raised by one order of magnitude (such as from 10^3 to 10^4 ppm NaCl), fluid conductivity increases by a similar magnitude, which subsequently results in nearly one order of magnitude increase in bulk conductivity (Hersir & Árnason, 2013).

Therefore, the mixture of hot and saline fluids in permeable host rocks in geothermal environments leads to high conductivity. This low resistivity signature is an attractive target for Electromagnetic (EM) methods, including Magnetotellurics (MT). Enhanced hardware, methodologies, data processing, and modeling software have further increased the popularity of EM over other geophysical methods (Muñoz, 2014; Spichak & Manzella, 2009).

2.2 Maxwell's Equations

Maxwell's equations are the foundation of classical electromagnetism, describing how electric and magnetic fields propagate and interact with matter (Ward & Hohmann, 1988). Here are Maxwell's equations in their differential forms:

$$\nabla \cdot \boldsymbol{B} = 0 \tag{2.1}$$

$$\nabla \cdot \boldsymbol{D} = q \tag{2.2}$$

$$\nabla \times \boldsymbol{E} = -\frac{\partial \boldsymbol{B}}{\partial t} \tag{2.3}$$

$$\nabla \times \boldsymbol{H} = \boldsymbol{j} + \frac{\partial \boldsymbol{D}}{\partial t} \tag{2.4}$$

Table 2.1: Basic physical parameters and their symbols used in EM fields.

Symbol	Property	SI Units
$\boldsymbol{E}$	electric field intensity	V/m
$\boldsymbol{D}$	electric flux density	As/m^2
$\boldsymbol{B}$	magnetic flux density	T = Vs/ m^2
$\boldsymbol{H}$	magnetic field intensity	A/m
$\boldsymbol{j}$	current density	A/m^2
$\boldsymbol{q}$	electric charge	As/m^3
$\boldsymbol{\varepsilon = \varepsilon_0 \varepsilon_r}$	electrical permittivity	As/Vm
$\boldsymbol{\varepsilon_0 = 8.854 \cdot 10^{-12}}$	permittivity of free space	As/Vm
$\boldsymbol{\varepsilon_r}$	relative dielectric permittivity	non-dimensional
$\boldsymbol{\mu = \mu_0 \mu_r}$	magnetic permeability	Vs/Am
$\boldsymbol{\mu_0 = 4\pi \cdot 10^{-7}}$	permeability of free space	Vs/Am
$\boldsymbol{\mu_r}$	relative permeability	non-dimensional
$\boldsymbol{\sigma}$	electric conductivity	S/m = A/Vm
$\boldsymbol{\rho}$	electrical resistivity	Ωm = Vm/A
$\boldsymbol{f}$	frequency	Hz = 1/s
$\boldsymbol{\omega = 2\pi f}$	angular frequency	Rad/s

The quantities of Maxwell's equations are listed in Table 2.2. Equation 2.1 represents Gauss's law for magnetism and states that Magnetic flux through a closed surface is zero (no magnetic monopoles). Gauss's law for electricity is expressed in equation 2.2 and shows that the electric field is the result of the distribution of electric charges.

Equation 2.3 represents Faraday's law which indicates that the induced electric field is equal to the time rate of change of the magnetic field. Ampère's law is given in equation 2.4 and it relates the magnetic field with the electric current density and the electric displacement field.

In order to apply Maxwell's equations to Earth models and understand how the Earth responds to electric and magnetic fields, it is necessary to define the relationships between the displacement field ($\boldsymbol{D}$) and the electric field ($\boldsymbol{E}$), as well as the magnetizing field ($\boldsymbol{H}$) and the magnetic field ($\boldsymbol{B}$). These relationships are described by constitutive equations. To simplify these equations, two basic assumptions are made: (i) all media are linear, isotropic, and homogeneous, and their electrical properties are independent of time, temperature, and pressure; and (ii) the magnetic permeability has the same value as in free space ($\mu = \mu_0$).

The constitutive relations can be written as:

$$\boldsymbol{B} = \mu\, \boldsymbol{H} \tag{2.5}$$

$$\boldsymbol{D} = \varepsilon\, \boldsymbol{E} \tag{2.6}$$

$$\boldsymbol{j} = \sigma\, \boldsymbol{E} \tag{2.7}$$

Equation 2.7 is known as Ohm's law. In general, μ, ε and σ are tensors, but in isotropic media they are reduced to scalar quantities.

2.2.1 Telegraph and Helmholtz Equations

Telegraph or wave equations are derived following the assumptions that no free charges exist outside of external sources and in regions of homogeneous conductivity ($\nabla \cdot \boldsymbol{E} = 0$), and the current density is source-free in homogeneous regions ($\nabla \cdot \boldsymbol{j} = 0$). Using these assumptions, we can perform a transformation of the Maxwell equations by taking the curl of Faraday's law (2.3) and $\boldsymbol{B}$ is eliminated using constitutive relation (2.5) and subsequently 2.4, resulting in a second order differential equation for the electric field ($\boldsymbol{E}$). An identical equation is derived for the magnetic field ($\boldsymbol{H}$) in a similar way (Ward & Hohmann, 1988). Finally, considering the vector identity $\nabla \times \nabla \times \boldsymbol{\mathcal{F}} = \nabla(\nabla \cdot \boldsymbol{\mathcal{F}}) - \Delta\boldsymbol{\mathcal{F}}$ and $\nabla \cdot \boldsymbol{\mathcal{F}} = 0$, the telegraph equation can be stated as

$$\Delta\boldsymbol{\mathcal{F}} - \mu\sigma\frac{\partial \boldsymbol{\mathcal{F}}}{\partial t} - \mu\varepsilon\frac{\partial^2 \boldsymbol{\mathcal{F}}}{\partial t} = 0 \qquad\qquad \boldsymbol{\mathcal{F}} \in \{\boldsymbol{E}, \boldsymbol{H}\} \tag{2.8}$$

The telegraph equation can be transformed into a frequency domain by applying a Fourier transformation, rewriting the time derivative as $\frac{\partial \boldsymbol{\mathcal{F}}}{\partial t} = i\omega\boldsymbol{\mathcal{F}}$. This leads to the Helmholtz equation:

$$\Delta\boldsymbol{\mathcal{F}} - \underbrace{i\omega\mu\sigma\boldsymbol{\mathcal{F}}}_{\text{conduction}} + \underbrace{\mu\varepsilon\omega^2\boldsymbol{\mathcal{F}}}_{\text{displacement}} = 0 \qquad \mathcal{F} \in \{\boldsymbol{E}, \boldsymbol{H}\} \tag{2.9}$$

with the wavenumber k, which implies the physical properties of the media: $\mathrm{k}^2 = \mu\varepsilon\omega^2 - \mathrm{i}\omega\mu\sigma$.

2.2.2 Quasi-Static Approximation

In most earth material conductivities and the period range used in MT applications, the conduction currents ($\sigma\boldsymbol{E}$) are much larger than the displacement currents ($\partial t\boldsymbol{D}$). Therefore, we have the quasi-static approximation:

$$\frac{\omega\mu\sigma}{\mu\varepsilon\omega^2} = \frac{\sigma}{\varepsilon\omega} \gg 1 \tag{2.10}$$

In this case, the Telegraph equation (2.8) and Helmholtz equation (2.9) are reduced to:

$$\Delta\boldsymbol{\mathcal{F}} - \mu\sigma\frac{\partial\boldsymbol{\mathcal{F}}}{\partial t} = 0 \qquad \boldsymbol{\mathcal{F}} \in \{\boldsymbol{E}, \boldsymbol{H}\} \tag{2.11}$$

$$\Delta\boldsymbol{\mathcal{F}} - i\omega\mu\sigma\boldsymbol{\mathcal{F}} = 0 \qquad \boldsymbol{\mathcal{F}} \in \{\boldsymbol{E}, \boldsymbol{H}\} \tag{2.12}$$

which is known as the diffusion equation in time and frequency domain. In the quasi-static approximation, the wavenumber is:

$$k = \sqrt{-i\omega\mu\sigma} = (1-i)\sqrt{\frac{\mu\sigma\omega}{2}} \tag{2.13}$$

We can solve the telegraph equations (2.11) by assuming a plane wave solution. This assumes that voltage and current vary sinusoidally with position and time, which is common in EM field applications. The solution is a positive downward decaying EM field with a harmonic time dependence $e^{i\omega\mathrm{t}}$ in a uniform conductor with conductivity σ (Ward & Hohmann, 1988):

$$\begin{aligned}\boldsymbol{\mathcal{F}}(\mathrm{z},\mathrm{t}) &= \boldsymbol{\mathcal{F}}_0^+ e^{i\omega t} e^{-ikz} \\ &= \boldsymbol{\mathcal{F}}_0^+ e^{i\omega t} e^{-i\sqrt{\frac{\mu\sigma\omega}{2}}z} e^{-\sqrt{\frac{\mu\sigma\omega}{2}}z} \quad \boldsymbol{\mathcal{F}} \in \{\boldsymbol{E}, \boldsymbol{H}\}\end{aligned} \tag{2.14}$$

$\boldsymbol{\mathcal{F}}_0^+$ is the initial amplitude of the EM field and the wavenumber k is given in equation (2.13).

With equations (2.13) and (2.14), we can define the **skin depth** (denoted as δ) that refers to the distance into a conductor at which an electromagnetic wave's amplitude decays to $\frac{1}{e}$ (about 37%) of its value at the surface. It measures how far an electromagnetic wave can penetrate into a conductor before significant attenuation occurs.

$$\delta_{FD} = \sqrt{\frac{2}{\mu_0\sigma\omega}} \quad or \quad \delta_{FD}(\text{in km}) \approx 0.5 \cdot \sqrt{\rho\ (\Omega\mathrm{m}) \cdot T\ (\mathrm{s})} \tag{2.15}$$

This is referred to as the frequency domain skin depth.

2.3 Magnetotelluric (MT) Method

Electromagnetic (EM) methods are widely used in geophysics to investigate the subsurface's electrical properties. Two common EM techniques are Magnetotellurics (MT) and Transient Electromagnetics (TEM). Each technique has unique advantages and applications depending on the survey objectives and geological context. MT is a passive EM technique that measures natural variations in the Earth's magnetic and electric fields to determine the electrical conductivity structure of the subsurface. The principle of the MT method was first described independently by Tikhonov (1950) and Cagniard (1953). Over the decades, continuous advancements in technology and methodology have enhanced the MT method's accuracy and broadened its applications, making it a crucial tool in modern geophysical exploration. It is typically measured in the frequency range of 10^{-4} to 10^{5} s. It can be particularly useful for deep investigations, ranging from a few hundred meters to several hundred kilometers depending on the resistivity of the structure and frequency contents of the EM field (Chave & Jones, 2012; Simpson & Bahr, 2005; Vozoff, 1990). The ability of MT to penetrate deep into the Earth's crust makes it a powerful tool for exploring geothermal systems, as it can reveal the distribution of conductive and resistive zones associated with geothermal fluids/heat source and host rocks, respectively.

Natural Source Fields of MT Signals

Natural electromagnetic (EM) signals originate from various sources, spanning from the Earth's core to distant galaxies, and are the result of diverse processes (Vozoff, 1990). The spectrum of EM field variations used in MT is very wide, covering frequencies from 10^{4} to 10^{-5} Hz. Within this frequency range, two significant source regions are observed:

- Global lighting activity at frequencies higher than 1 Hz, including the so-called Schumann resonances.
- Interactions between the solar wind and the Earth's magnetosphere which generate current systems in the auroral ionosphere, which in its turn produce major EM signals globally at frequencies lower than 1 Hz.

A frequency range spanning approximately 0.5–5 Hz lies the so-called *dead-band* at which natural electromagnetic fluctuations are of low intensity, and it leads to significantly lower signal-to-noise ratios (Simpson & Bahr, 2005).

In the MT method, the sources of the EM fields are assumed to be laterally uniform across the region of interest, which allows the signals to be described as vertically propagating plane waves. However, it can be violated in auroral areas where the MT signal may be distorted by polar electro-jet currents, which can introduce significant anomalies in the data (Hill, 2020).

2.3.1 The MT Transfer Functions

The primary objective of the MT field campaign is to obtain the MT transfer function, which provides critical information about the subsurface electrical conductivity over a hemispherical volume centered at the MT site. MT transfer functions describe the relationship between naturally occurring variations in the Earth's electromagnetic fields and the electrical conductivity structure of the Earth's subsurface. These transfer functions are derived from the ratio of electric and magnetic field components recorded at the surface and are used to infer information about subsurface conductivity.

Impedance Tensor ($\boldsymbol{Z}$)

The primary transfer functions in MT are composed of the impedance tensor ($\boldsymbol{Z}$) and the vertical magnetic transfer function (also known as the tipper, $\boldsymbol{T}$). The basic MT response, $\boldsymbol{Z}$, is a complex matrix that relates the horizontal electric field ($\boldsymbol{E}$) to the horizontal magnetic field ($\boldsymbol{H}$) (Cagniard, 1953; Tikhonov, 1950). Thus, it can be formulated as

$$\begin{pmatrix} \boldsymbol{E}_x \\ \boldsymbol{E}_y \end{pmatrix} = \begin{pmatrix} \boldsymbol{Z}_{xx} & \boldsymbol{Z}_{xy} \\ \boldsymbol{Z}_{yx} & \boldsymbol{Z}_{yy} \end{pmatrix} \begin{pmatrix} \boldsymbol{H}_x \\ \boldsymbol{H}_y \end{pmatrix} \tag{2.16}$$

Each element of the tensor ($\boldsymbol{Z}_{xx}, \boldsymbol{Z}_{xy}, \boldsymbol{Z}_{yx}, \boldsymbol{Z}_{yy}$) is frequency-dependent and complex, meaning it has both a real and an imaginary part. The $\boldsymbol{Z}_{xx}$ and $\boldsymbol{Z}_{yy}$ called diagonal elements represent the direct coupling of the electric and magnetic fields in the same direction. On the other hand, the $\boldsymbol{Z}_{xy}$ and $\boldsymbol{Z}_{yx}$ called off-diagonal elements represent the cross-coupling of the electric and magnetic fields and typically the primary focus in MT interpretation because they contain the most information about the subsurface resistivity.

The tensor $\boldsymbol{Z}$ can be more effectively interpreted by examining derived quantities such as the apparent resistivity (ρ_a) derived from the magnitude of the off-diagonal elements and the phase (ϕ), which is the argument of the off-diagonal elements. The ρ_a and ϕ can be expressed as (Berdichevsky & Dmitriev, 2008; Chave & Jones, 2012; Simpson & Bahr, 2005):

$$\rho_{a,\mathrm{ij}} = \frac{1}{\omega\mu_0}\left|\frac{\boldsymbol{E}_\mathrm{i}}{\boldsymbol{H}_j}\right|^2 = \frac{\left|\boldsymbol{Z}_\mathrm{ij}(\omega)\right|^2}{\omega\mu_0}, \qquad i,j \in [x,y] \tag{2.17}$$

$$\phi_{ij} = tan^{-1}\left(\frac{Im\left(\boldsymbol{Z}_{ij}(\omega)\right)}{Re\left(\boldsymbol{Z}_{ij}(\omega)\right)}\right), \qquad i,j \in [x,y] \tag{2.18}$$

where x and y are directed northwards and eastwards respectively.

Vertical Magnetic Transfer Function (Tipper)

In addition to the impedance, further information about lateral changes in subsurface conductivity structure can be obtained from the vertical magnetic transfer function or tipper ($\boldsymbol{T}$). It is particularly useful for identifying 3D structures and detecting anomalies that might not be evident from the impedance tensor alone (Berdichevsky & Dmitriev, 2008). The concept of tipper ($\boldsymbol{T}$) was independently discovered by Parkinson (1959, 1962) and Wiese (1962) and can be formulated as:

$$\boldsymbol{H}_z = \left(\boldsymbol{T}_{zx}\, \boldsymbol{T}_{zy}\right) \cdot \begin{pmatrix} \boldsymbol{H}_x \\ \boldsymbol{H}_y \end{pmatrix} \tag{2.19}$$

Where $\boldsymbol{H}_x$, $\boldsymbol{H}_y$ and $\boldsymbol{H}_z$ are the magnetic field components and $\boldsymbol{T}_{zx}$ and $\boldsymbol{T}_{zy}$ represent the components of the tipper.

A widely used method to visualize tippers is through the use of induction arrows. A complex tipper, also known as an induction arrow, comprises both real and imaginary tippers (or real and imaginary induction arrows). There are two conventions regarding the direction of the real tipper: the Wiese convention, where the real tipper points away from areas of higher conductivity, and the Parkinson convention, in which it points toward regions of higher conductivity. This thesis adopts the Parkinson convention. The magnitude of the arrows reflects the intensity of the current concentrations associated with the anomaly, providing a visual indication of the strength of these anomalies (Jones & Price, 1970). The arrows' direction is particularly important, as they are oriented perpendicular to the regional geoelectric strike. This characteristic can be used to verify and delineate the strike direction of subsurface geological features, enhancing the accuracy of resistivity models (Berdichevsky & Dmitriev, 2008).

The length of the induction arrows is utilized from the tipper components, such as

$$Re(\boldsymbol{T}) = \sqrt{Re(\boldsymbol{T}_x)^2 + Re\left(\boldsymbol{T}_y\right)^2}, \tag{2.20}$$

and their direction is given by

$$\alpha = tan^{-1}\left(\frac{Re\left(\boldsymbol{T}_y\right)}{Re(\boldsymbol{T}_x)}\right) \tag{2.21}$$

where α is measured clockwise from geomagnetic north. It is important to note that the geomagnetic transfer functions, or tippers ($\boldsymbol{T}$) are less susceptible to galvanic

distortion compared to the impedance tensor ($\boldsymbol{Z}$). Galvanic distortion arising from near surface inhomogeneities can significantly alter the impedance tensor, leading to inaccuracies in the derived resistivity models. In contrast, tippers are more robust against such distortions. As a result, incorporating tippers into a joint inversion scheme, which simultaneously inverts both impedance tensor and tipper data, can mitigate the effects of static shifts. This approach enhances the reliability of geo-electrical conductivity models by providing a more accurate representation of the subsurface conductivity structure (Berdichevsky et al., 2003; Siripunvaraporn & Egbert, 2009).

Phase tensor

Understanding the MT transfer function, specifically the impedance tensor, poses a significant challenge due to the distortion of the electric field caused by near-surface heterogeneities. The introduction of the phase tensor by Caldwell et al. (2004) and Bibby et al. (2005) marked a significant development in distortion analysis. The phase-tensor analysis is valuable in identifying and displaying the unaffected portions of the response function, such as regional strike in the presence of local 3D effects. Assessing the dimensionality and regional strike is crucial as an initial step in the MT data modeling process. The phase tensor ($\boldsymbol{\Phi}$) is defined as the ratio of the real and imaginary parts of the complex impedance tensor:

$$\boldsymbol{\Phi} = \boldsymbol{X}^{-1}\boldsymbol{Y} \tag{2.22}$$

where $\boldsymbol{X}$ and $\boldsymbol{Y}$ are the real and imaginary parts of the $\boldsymbol{Z}$. This operation essentially removes distortion effects associated with galvanic distortions that can affect the real part of the impedance tensor.

The MT phase tensor is characterized by a direction and three scalar coordinate invariants, which are intrinsic properties of the tensor and remain unchanged by the coordinate system or the presence of galvanic distortion. The direction of the phase tensor refers to the geoelectric strike, which is the orientation of the major axis of the phase tensor ellipse. The geoelectric strike angle (θ) is determined by the principal directions of the phase tensor. It provides crucial information about the alignment of subsurface structures, such as faults, lithological boundaries, or other conductive anomalies. The three invariants are typically defined as maximum ($\boldsymbol{\Phi}_{\max}$) and minimum ($\boldsymbol{\Phi}_{\max}$) tensor values and the skew angle (β), and they can be used to infer properties about subsurface dimensionality and the complexity of resistivity structures. The phase tensor can be written as a product of its invariants, $\boldsymbol{\Phi}_{\max}$, $\boldsymbol{\Phi}_{\min}$, and β:

$$\boldsymbol{\Phi} = \boldsymbol{R}^{T}(\alpha - \beta)\begin{pmatrix}\boldsymbol{\Phi}_{\max} & 0 \\ \boldsymbol{0} & \boldsymbol{\Phi}_{\min}\end{pmatrix}\boldsymbol{R}(\alpha + \beta) \tag{2.23}$$

where $\boldsymbol{R}(\alpha + \beta)$ is the rotation matrix:

$$\boldsymbol{R}(\alpha+\beta)=\begin{pmatrix}\cos(\alpha+\beta) & \sin(\alpha+\beta)\\ -\sin(\alpha+\beta) & \cos(\alpha+\beta)\end{pmatrix} \tag{2.24}$$

Both angles α and β can be expressed as:

$$\alpha=\frac{1}{2}\arctan\left(\frac{\boldsymbol{\Phi}_{xy}+\boldsymbol{\Phi}_{yx}}{\boldsymbol{\Phi}_{xx}-\boldsymbol{\Phi}_{yy}}\right) \tag{2.25}$$

$$\beta=\frac{1}{2}\arctan\left(\frac{\boldsymbol{\Phi}_{xy}-\boldsymbol{\Phi}_{yx}}{\boldsymbol{\Phi}_{xx}+\boldsymbol{\Phi}_{yy}}\right) \tag{2.26}$$

The phase tensor can be graphically represented as an ellipse, as shown in Fig. 2.2. The major and minor axes of the ellipse represent the principal values of the tensor with the orientation of the major axis specified by the angle $\alpha-\beta$. In the case of 1-D subsurface structure, the phase tensor ellipse is nearly circular and $\boldsymbol{\Phi}_{max}=\boldsymbol{\Phi}_{min}$. In a 2-D environment, the ellipse becomes elongated, with a clear major axis indicating the dominant direction of resistivity contrast (the geoelectric strike). For a 3-D resistivity structure, the ellipse may become skewed, meaning it is tilted or asymmetric, and the skewness increases ($\beta \neq 0$) as the structure becomes more complex and involves lateral changes in conductivity in multiple directions (Caldwell et al., 2004).

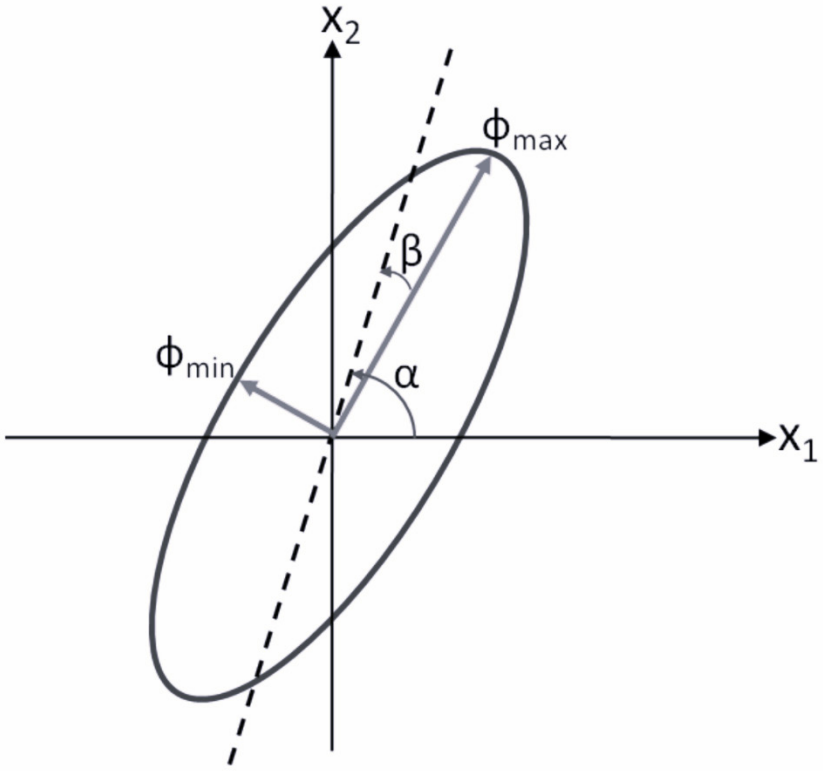

Figure 2.2: Graphical representation of the phase tensor. The three invariants ($\boldsymbol{\Phi}_{max}$, $\boldsymbol{\Phi}_{min}$, and β) are used to infer properties about subsurface dimensionality and the complexity of resistivity structures. Figure redrawn from Caldwell et al. (2004).

2.3.2 Dimensionality

In a 1-D subsurface structure, isotropic layered Earth (i.e., the conductivity changes only with depth), the diagonal components of the impedance tensor, which correspond to the horizontal electric and magnetic fields, are both zero ($\boldsymbol{Z_{xx}} = \boldsymbol{Z_{yy}} = 0$). Due to the absence of lateral conductivity variations, the off-diagonal components are equal in magnitude but have opposite signs in order to maintain the right-hand rule ($\boldsymbol{Z_{xy}} = -\boldsymbol{Z_{yx}}$). The phase tensor is graphically represented with a circle ($\boldsymbol{\Phi}_{\max} = \boldsymbol{\Phi}_{\min}$) and the tipper components equal to zero ($\boldsymbol{T_{zx}} = \boldsymbol{T_{zy}} = 0$).

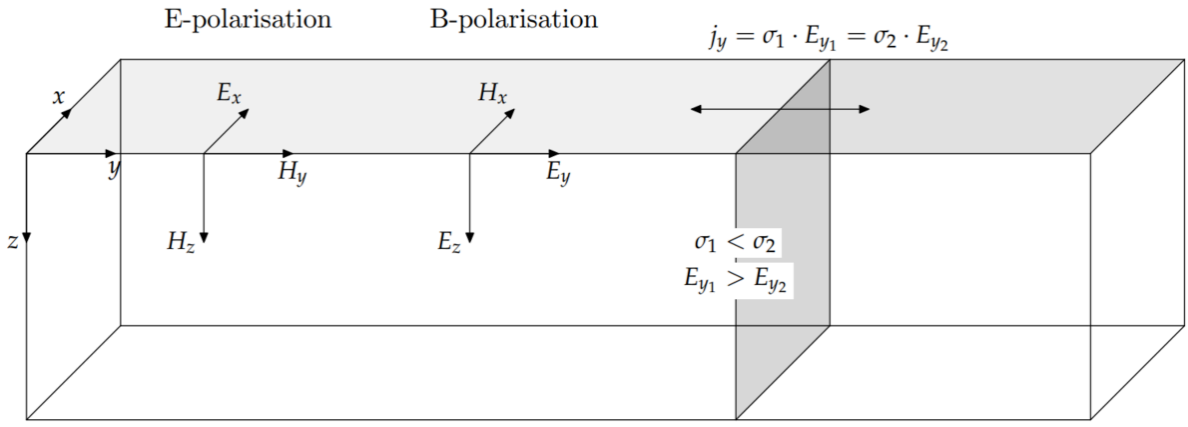

Figure 2.3: Simple 2-D model to illustrate the EM fields decoupled into two modes, known as E-polarization and B-polarization. Figure taken from Thiel (2008).

In a 2-D Earth, in which resistivity varies with depth and along one horizontal direction (i.e., in the strike direction), the diagonal components of the impedance tensor are equal in magnitude but with different sign ($\boldsymbol{Z_{xx}} = -\boldsymbol{Z_{yy}}$) and the off-diagonal elements do not have the same value ($\boldsymbol{Z_{xy}} \neq \boldsymbol{Z_{yx}}$). For the ideal 2-D case, as shown in Figure 2.3, electric and magnetic fields are perpendicular to each other. When electric fields ($\boldsymbol{E_x}$) parallel to the strike direction, they induce magnetic fields perpendicular to the strike ($\boldsymbol{H_y}$, $\boldsymbol{H_z}$ or $\boldsymbol{B_y}$, $\boldsymbol{B_z}$). Conversely, when magnetic fields ($\boldsymbol{H_x}$ or $\boldsymbol{B_x}$) are parallel to the strike direction, they only induce electrical fields in the vertical plane perpendicular to the strike ($\boldsymbol{E_y}$, $\boldsymbol{E_z}$) (Chave & Weidelt, 2012). Under these conditions, Maxwell's equations can be decoupled into two modes. One mode, which describes electric currents flowing parallel to the strike direction (i.e., in the x-direction), is known as the Transverse Electric (TE) Mode or E-Polarization and can be represented as follows:

$$\left.\begin{aligned} \frac{\partial B_z}{\partial y} - \frac{\partial B_y}{\partial z} &= \mu_0 \sigma E_x \\ \frac{\partial E_x}{\partial z} &= -i\omega B_y \\ \frac{\partial E_x}{\partial y} &= i\omega B_z \end{aligned}\right\} E - polarization\ (TE\ mode) \tag{2.27}$$

The other mode, which describes currents flowing perpendicular to the strike direction, is called the Transverse Magnetic (TM) Mode or B-Polarization:

$$\left.\begin{aligned} \frac{\partial E_y}{\partial z} - \frac{\partial E_z}{\partial y} &= i\omega B_x \\ \frac{\partial B_x}{\partial z} &= \mu_0 \sigma E_y \\ -\frac{\partial B_x}{\partial y} &= \mu_0 \sigma E_z \end{aligned}\right\} B - polarization\ (TM\ mode) \tag{2.28}$$

If the impedance tensor is not aligned with the electrical strike coordinates, which is typically the case for most recorded MT data, the TE and TM modes will be mixed in the tensor. In this case, the 2-D impedance tensor needs to be rotated into the strike direction through:

$$\boldsymbol{Z}_{2\mathrm{D}} = \boldsymbol{R}_\theta \boldsymbol{Z}_{obs} \boldsymbol{R}_\theta^T \tag{2.29}$$

where $\boldsymbol{Z}_{obs}$ is the recorded impedance tensor in the observational reference frame, and $\boldsymbol{R}_\theta$ is the rotation matrix:

$$\boldsymbol{R}_\theta = \begin{pmatrix} \cos\theta & \sin\theta \\ -\sin\theta & \cos\theta \end{pmatrix} \tag{2.30}$$

The rotation angle θ can be estimated as follows (Swift, 1967):

$$\theta_{\mathrm{Swift}} = \frac{1}{4}\tan^{-1}\left(\frac{2 \cdot Re\left(\left(Z_{xx} - Z_{yy}\right)^*\left(Z_{xy} + Z_{yx}\right)\right)}{\left|Z_{xx} - Z_{yy}\right|^2 - \left|Z_{xy} + Z_{yx}\right|^2}\right) \tag{2.31}$$

It helps rotate the impedance tensor to a new coordinate system where the off-diagonal components of the tensor are maximized, providing a more unambiguous indication of the subsurface resistivity structure.

Finally, if the conductivity distribution varies in all three directions ($\sigma(x, y, z)$), the problem becomes three-dimensional (3-D). In this case, decoupling into two separate modes is no longer applicable, and the determination of four elements of the full impedance tensor is required. Moreover, all components of the impedance tensor are different, and nonzero values (i.e., $\boldsymbol{Z}_{xx} \neq \boldsymbol{Z}_{yy}$, and $\boldsymbol{Z}_{xy} \neq \boldsymbol{Z}_{yx}$). The ellipse of the MT phase tensor is asymmetrical, and the skew angle increases ($\beta \neq 0$).

2.3.3 Distortions and Static Shift

Distortions of the Magnetotelluric (MT) signal can occur due to a variety of factors, both natural and anthropogenic, leading to inaccurate interpretations of the Earth's subsurface resistivity structure. These distortions in the measured EM fields can generally be classified into galvanic and inductive effects. Inductive effects alter both the electric and magnetic fields, typically at lower frequencies, and are often associated with large-scale geological inhomogeneities (e.g., ore bodies and salt domes) or extensive conductive materials like seawater. Induced currents primarily cause the distortion effects due to the time-varying magnetic fields interacting with conductive bodies, which in turn generate secondary EM fields (Chave & Jones, 2012; Jiracek, 1990).

The galvanic distortions result from local charge accumulation at small-scale, near-surface inhomogeneities features, which directly distort the electric field but typically leave the magnetic field unaffected (Jiracek, 1990; Sternberg et al., 1988). These distortions are often frequency-independent, meaning they affect all frequencies in a similar way. When near-surface heterogeneities are more conductive than the geological background, the measured electric field decreases, while it increases when the heterogeneities are more resistive.

Considering a small anomaly below an MT station, the measured electric field $\boldsymbol{E}$ is given by:

$$\boldsymbol{E} = \boldsymbol{D}\boldsymbol{E}_R = \boldsymbol{D}(\boldsymbol{Z}_R\boldsymbol{B}_R) = (\boldsymbol{D}\boldsymbol{Z}_R)\boldsymbol{B} \tag{2.32}$$

Where $\boldsymbol{D}$ is a distortion tensor, $\boldsymbol{E}_R$, $\boldsymbol{Z}_R$, and $\boldsymbol{B}_R$ are the regional electric field, impedance tensor, and magnetic field in the absence of the anomaly, respectively. Because the horizontal magnetic field components are not severely affected, the distortion in the magnetic field can be neglected ($\boldsymbol{B} = \boldsymbol{B}_R$). Thus, the observed impedance is also distorted:

$$\boldsymbol{Z} = \boldsymbol{D}\boldsymbol{Z}_R \tag{2.33}$$

The galvanic effects are also produced by topography, which can cause the so-called galvanic topographic effect. This effect occurs when the primary electric field is perpendicular to the trend of the topography. The topographic distortions can produce both galvanic and inductive effects, influenced by the terrain's roughness and measurement periods. In mountainous regions like in the Al-Lith area, the apparent resistivity values may appear higher on the slopes and lower in the valleys (Jiracek, 1990). While topographic effects predominantly impact the electric field, they can also influence the magnetic field, especially when significant elevation changes exist between measurement points.

The most common manifestation of galvanic distortions is static shift, where the apparent resistivity curves are shifted vertically without changing their shape. This shift is frequency-independent, meaning it does not affect the phase curve of the impedance tensor, resulting in either an underestimation or an overestimation of subsurface resistivity. This property highlights the need for careful correction of static shifts to ensure the accurate representation of the subsurface conductivity structure (Árnason et al., 2010; Jiracek, 1990; Jones, 1988; Sternberg et al., 1988).

There are several approaches available for correcting the static shift in MT data. Sternberg et al. (1988) and Pellerin and Hohmann (1990) for example, proposed the use of TEM soundings to address static shift effects. TEM data are relatively unaffected by galvanic distortions, making them a useful tool for this purpose. The approach involves using 1D TEM data to iteratively adjust the invariant of the MT data towards the TEM response. This is based on the assumption that the TEM response accurately reflects the actual 1D conductivity of the subsurface (Árnason et al., 2010). The method of using TEM data for static shift corrections works by aligning the apparent resistivity curves from MT data with those derived from TEM surveys. Since TEM measurements are less susceptible to near-surface inhomogeneities, they provide a reliable reference. This iterative process continues until the MT data invariant matches the TEM response, ensuring the static shift is mitigated effectively. However, the effectiveness of this method can vary depending on the geological context.

Cumming & Mackie (2010) pointed out that TEM might be ineffective for correcting MT static shift in areas where the surface is predominantly covered by thick and resistive rocks. These conditions can impede the TEM method's ability to provide an accurate shallow subsurface resistivity profile, leading to suboptimal corrections. Later, Watts et al. (2013) highlighted the limitations of correcting MT static shifts using TEM data, as it can produce misleading results. They emphasized that, with modern broad-band MT instrumentation, comprehensive modeling of the topography is more likely to yield an accurate image of the subsurface. Static shift corrections and the inclusion of topography in inversion cannot be applied simultaneously. Correcting static shifts using TEM data, while also incorporating topography would account twice for shifts due to topography (Árnason, 2015).

2.4 Transient Electromagnetic (TEM) Method

The Transient Electromagnetic (TEM), also known as the Time-Domain Electromagnetic (TDEM), is an active EM method used to investigate the electrical

conductivity of the subsurface by measuring the earth's response to time-varying electromagnetic fields. Unlike MT, which uses natural EM variations, TEM employs a controlled source to generate primary EM fields, making it a highly versatile tool for near-surface to mid-depth investigations. TEM technique has been developed and refined most intensively since the mid-1980s (Christiansen et al., 2009). There are various configurations utilized for conducting time domain electromagnetic (TDEM) measurements. For shallow investigations, a loop source is commonly used instead of a grounded wire. Receivers such as a magnetometer, an induction coil, or a wire loop can be used to record the vertical component of the magnetic field (or its time derivative). When the receiver is positioned in the center of the transmitter loop, it is referred to as a central loop or in-loop; when placed outside, it is called a separate loop. Soundings conducted with a loop source are known as SHOTEM (short offset transient electromagnetic method) or simply TEM.

The TEM technique has several key advantages, such as achieving relatively large investigation depths using relatively small transmitter loop sizes. In addition, no galvanic ground coupling is required, allowing for a fast deployment and setup of a TEM sounding station. The response is measured without the primary field, meaning that the investigation depth depends on the transmitter moment (transmitter size and current) and acquisition time. TEM is also highly sensitive to conductive targets (Dentith & Mudge, 2014; Goldman & Neubauer, 1994).

2.4.1 Basic Principle and Measuring Technique

The fundamental principle behind the TEM method is electromagnetic induction, governed by Faraday's Law of Induction. When an alternating or time-varying current flows through a conductor, it generates a changing magnetic field. If the current is turned off suddenly, the collapse of the magnetic field induces eddy currents in nearby conductive materials. These eddy currents generate their own magnetic fields, which decay over time. These currents form closed loops, which resemble the shape of a "smoke ring" when visualized in cross-section. Figure 2.4a depicts the outcome of the current flow beneath the transmitter loop, referred to as a “smoke ring”. In a uniform half-space, as depicted in Figure 2.4b, the induced current quickly diffuses downward at an angle of around 30 degrees (Dentith & Mudge, 2014; Nabighian, 1979; Nabighian & Macnae, 1991).

After turning off the current in the transmitting loop, the current in the ground will initially be concentrated near the surface, and the recorded signal will mainly reflect the conductivity of the upper layers. At later times, the current will penetrate deeper into the ground, and the recorded signal will provide insights into the conductivity of

the underlying layers. Measuring the current in the receiving coil allows for the information of conductivity at different depths, which is often referred to as a sounding. It is important to note that a single transient in a TEM sounding is typically impacted by noise. Conducting multiple measurements can improve the signal-to-noise (S/N) ratio. When employing a log-gating technique, the S/N ratio is directly proportional to the square root of the number of measurements in the stack. Since it's assumed that the noise conforms to a Gaussian distribution, doubling the number of measurements in the stack enhances the S/N ratio by a factor of 1.41 (Christiansen et al., 2009).

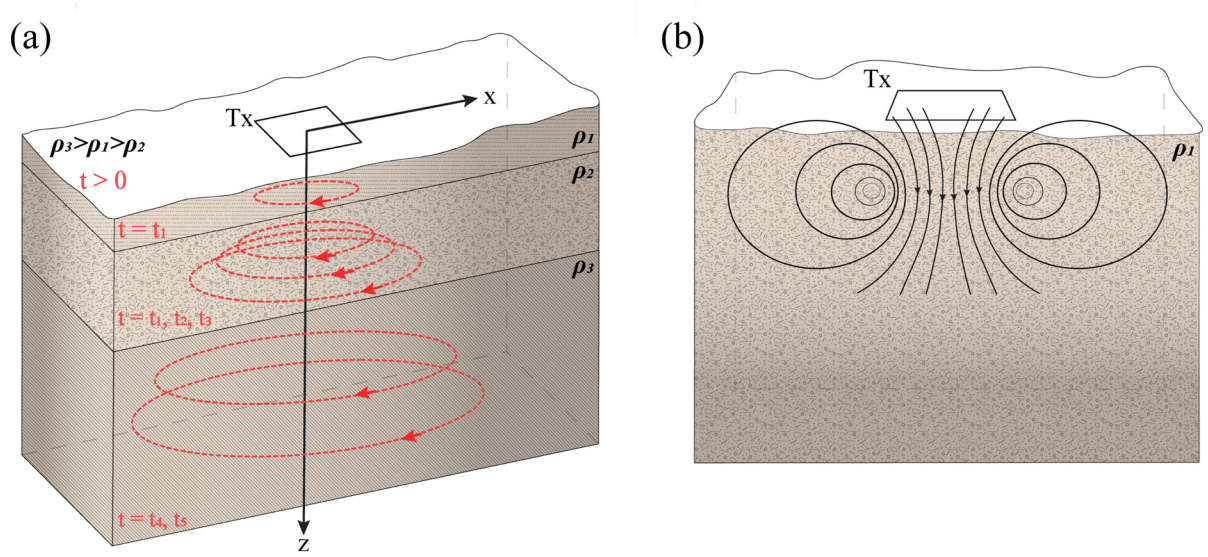

Figure 2.4: (a) System of equivalent current filaments over conductive layers at various times after current switch-off in the transmitter loop. (b) Magnetic field lines and equivalent current filament for one particular time over a conducting half-space after current switch-off. Both figures taken from Blanco-Arrué (2024).

2.4.2 Solution for a Uniform Half-Space

The TEM method in uniform conducting half-space scenario provides a simplified model to understand the subsurface conductivity response. The model assumes that the earth is made of a homogeneous, isotropic, and conductive medium. In this case, when an electromagnetic field is applied to the half-space, the field propagates in a predictable manner, allowing the formulation of an analytical solution for the transient response. According to Ward and Hohmann (1988), with an assumption of a horizontal loop with radius a and current I located at $z = 0$, the vertical component of the magnetic field $\dot{H}_z$ at the center of the loop is given by:

$$\dot{H}_z = \frac{-I}{\sigma\mu_0 a^3}\left[3\,\mathrm{erf}(\Theta a) - \frac{2}{\sqrt{\pi}}\Theta a(3 + 2\Theta^2 a^2)e^{(\Theta^2 a^2)}\right] \tag{2.34}$$

where Θ is

$$\Theta = \frac{1}{\sqrt{2}\delta_{TD}} = \sqrt{\frac{\sigma\mu_0}{4t}} \tag{2.35}$$

The Gauss' error function is defined as:

$$erf(x) = \frac{2}{\sqrt{\pi}}\int_0^x e^{-\tau^2}\, d\tau \tag{2.36}$$

In TEM method, the electromagnetic response is divided into two-time regimes: early-time and late-time approximations. These approximations relate the decay of the EM field to the subsurface conductivity structure at different depths and also reduce equation (2.34) to simple relations between $\dot{H}_z$ and the subsurface resistivity ρ.

The **early-time approximation** corresponds to the initial moments after the transmitter current is switched off ($t \to 0, \Theta \to \infty$). In this regime, the decay of the electromagnetic signal is dominated by the near-surface layers, and the eddy currents are concentrated near the surface. In other words, the Gauss' error function approaches unity and $e^{(\Theta^2 a^2)}$ vanishes. Thus, the equation 2.34 is reduced to:

$$\dot{H}_{z,et} = -\frac{3I}{\sigma a^3} \tag{2.37}$$

Equation 2.37 is then rearranged to define the early time apparent resistivity ($\rho_{a,et}$):

$$\rho_{a,et} = -\frac{a^3}{3I}\,\dot{H}_{z,et} \tag{2.38}$$

The second approximation, the so-called **late-time approximation**, corresponds to the later moments after the transmitter current is switched off. In this regime, the eddy currents have diffused to greater depths, and the response reflects the conductivity of deeper subsurface layers. For $t \to 0$ and $\Theta \to \infty$, the error-function vanishes and $e^{(\Theta^2 a^2)}$ approaches unity. Thus,

$$\dot{H}_{z,lt} = -\frac{Ia^2}{20\sqrt{\pi}}(\sigma\mu)^{\frac{3}{2}} t^{-\frac{5}{2}} \tag{2.39}$$

And the late time apparent resistivity ($\rho_{a,lt}$) is obtained by rearranging equation 2.39:

$$\rho_{a,et} = -\left[\frac{Ia^3}{20\sqrt{\pi}}\right]^{\frac{2}{3}} t^{-\frac{2}{3}}\,\mu_0 \dot{H}_{z,lt}^{-\frac{2}{3}} \tag{2.40}$$

Beyond the near and far zone ranges, the apparent resistivity no longer accurately represents the true earth resistivity (Spies & Frischknecht, 1991). Nonetheless, both transformations are valuable as they allow for a preliminary understanding of the

resistivity structure and serve as an initial estimate for the inversion process (Raiche, 1983).

2.4.3 Depth of Investigation

When using diffusive methods such as ground-based electromagnetic techniques, it is important to determine the depth at which the resistivity structure of the ground can be reliably characterized. This necessitates establishing a specific depth of investigation (DOI) that represents the desired level of information for the model. A common DOI for central loop transient electromagnetic (TEM) soundings using the late time approximation (near zone) was proposed by Spies (1989):

$$\delta_{doi} \approx 0.55 \left(\frac{I A_{Tx} \bar{\rho}}{\eta_v}\right)^{\frac{1}{5}} \tag{2.41}$$

where I is the transmitter current in A unit, A_{Tx} is the size of the transmitter loop in m^2, and η_v is the voltage noise level and its value is typically 0.5 $\frac{nV}{m^2}$. The δ_{doi} depends directly on the average resistivity $\bar{\rho}$ with $z \leq \delta_{doi}$:

$$\bar{\rho} = \frac{1}{\delta_{doi}} \int_{z=0}^{\delta_{doi}} \rho(z) d \tag{2.42}$$

Before a field campaign, equation (2.39) can be utilized to estimate appropriate configuration parameters, such as transmitter size and current. The δ_{doi}-value may also be used to estimate the lower depth bound of the 1-D inversion models. Then, the noise level η_v was measured at each sounding and corresponded to the induced voltage value of the last recorded time point. However, there is a limitation on the δ_{doi}, that is easily overestimated. For instance, if a poorly resolved deep layer shows large resistivities, the average resistivity ($\bar{\rho}$) also becomes large. Therefore, the δ_{doi}-value is considered a rough and additional estimate. Following an example discussed by Spies (1989) and to prevent overestimation, only 70% of δ_{doi} is considered as the depth of exploration (Blanco-Arrué, 2024; Yogeshwar, 2014). Specifically, for frequency domain soundings, Spies (1989) suggested that $1.5 \cdot \delta_{FD}$ is a reasonable estimate of the doi, where δ_{FD} is the skin depth in Equation 2.15.

Chapter 3

Inversion Theory of EM Data

In applied electromagnetic (EM) geophysics, an inversion scheme is used to infer the subsurface electrical properties, such as electrical conductivity or resistivity, from surface or airborne electromagnetic data. The goal is to translate the electromagnetic responses measured at the surface into a model of the Earth's subsurface, describing how these properties vary with depth and sometimes laterally. This chapter explains the inversion theory of the different algorithms used for the inversion of MT and TEM field data measured in Al-Lith, western Saudi Arabia. The two common inversion techniques, the Levenberg-Marquardt and the Occam inversion schemes, are presented, which are used to invert TEM field data. Both methods are implemented in the utilized 1D inversion algorithm EMUPLUS (Scholl, 2005). The first method employs a minimal number of model parameters to interpret the data, while the second method seeks to identify a subsurface model with a smooth structure. The Non-Linear Conjugate Gradient (NLCG) is also described, which is used in the ModEM algorithm for the 3D inversion of MT data. Many of the described inversion theoretical principles are found in Meju (1994), Menke (2012), and Rodi & Mackie (2012).

3.1 Formulation of the Inverse Problem

The inverse problem of EM data seeks to estimate the subsurface conductivity distribution (or its reciprocal resistivity) from observed data, such as electric and magnetic field measurements (Meju, 1994). In the acquired dataset, i.e. the induced voltages at a specific location and time (or frequency) can be stored as components of an N-dimensional data vector $\boldsymbol{d}$, with the corresponding data errors represented in an error vector $\boldsymbol{e}$ (Rodi & Mackie, 2012).

$$\boldsymbol{d} = (d_1, d_2, \dots, d_N)^T \tag{3.1}$$

$$\delta\boldsymbol{d} = (\delta d_1, \delta d_2, \dots, \delta d_N)^T \tag{3.2}$$

The model parameters $\boldsymbol{m}$ can be stored in the same way as components in an M-dimensional model parameter:

$$\boldsymbol{m} = (m_1, m_2, \dots, m_M)^T \tag{3.3}$$

The inversion process aims to find a model $\boldsymbol{m}$ that explains the observed data $\boldsymbol{d}$ within their errors $\delta\boldsymbol{d}$. According to this notation, the inverse problem can be written as:

$$\boldsymbol{d} = \boldsymbol{F}(\boldsymbol{m}) + \delta\boldsymbol{d} \tag{3.4}$$

where $\boldsymbol{F}$ is the forward operator which denotes the transformation from model space to data space with the model vector as its argument. In cases where the inverse of $\boldsymbol{F}$ exists and $\delta\boldsymbol{d} = 0$, the solution of the forward problem is simply expressed as $\boldsymbol{m} = \boldsymbol{F}^{-1}(\boldsymbol{d})$, and the model parameters can be derived by finding the inverse of $\boldsymbol{F}$. However, in most scenarios, this solution does not exist, necessitating the need to make an estimation for $\boldsymbol{m}$.

3.1.1 Well and Ill-Posed Problems

In the context of a simple linear relationship $\boldsymbol{d} = \boldsymbol{F}\,\boldsymbol{m}$ between the forward operator and the model parameters, the solution $\boldsymbol{m} = \boldsymbol{F}^{-1}\boldsymbol{d}$ is feasible only if the problem is **well-determined** with $N = M$ and there exists a unique solution. In this scenario, a model can be obtained through direct inversion. When there is more data or information available than unknown model parameters, resulting in an **over-determined** problem ($N > M$), a unique solution is typically not achievable. In such cases, the goal is to find a model that best explains the available data. Conversely, an **under-determined** problem with $N < M$ results in an infinite number of models that can explain the data. If the inverse problem is to a certain degree overdetermined and to another degree underdetermined, i.e. some parameters are better resolved than others, the problem becomes **mixed-determined**, which is commonly encountered in geophysical data sets. These problems are called *ill-posed* and require some type of constraint to stabilize the solution.

Essentially, the inversion aims to minimize the misfit between measured data $\boldsymbol{d}$ and the calculation of the model response $\boldsymbol{F}(\boldsymbol{m})$. In a least-square sense, the function to minimize is described as a minimization of a data misfit functional or cost-function:

$$\boldsymbol{\Phi}_d(\boldsymbol{m}) = \big(\boldsymbol{d} - \boldsymbol{F}(\boldsymbol{m})\big)^T \boldsymbol{W}_d^2 \big(\boldsymbol{d} - \boldsymbol{F}(\boldsymbol{m})\big) = \boldsymbol{\epsilon}^T \boldsymbol{W}_d^2 \boldsymbol{\epsilon} \tag{3.5}$$

where $\big(\boldsymbol{d} - \boldsymbol{F}(\boldsymbol{m})\big)$ is called the residual vector ($\boldsymbol{\epsilon}$) and $\boldsymbol{W}_d$ denotes the diagonal error weighting matrix:

$$\boldsymbol{W}_d = \begin{pmatrix} \frac{1}{\delta d_1} & & 0 \\ & \ddots & \\ 0 & & \frac{1}{\delta d_N} \end{pmatrix} \tag{3.6}$$

For a Gaussian process, the least square estimator is known to be optimal. Hence a measure of data fit is estimated through:

$$\chi = \sqrt{\frac{\boldsymbol{\Phi}_d}{N}} = \sqrt{\frac{1}{N}\sum_{i=1}^{N}\left(\frac{\left(\boldsymbol{d}_i - \boldsymbol{F}_i(\boldsymbol{m})\right)}{\delta d_i}\right)^2} \tag{3.7}$$

In this thesis, note that the root mean square (RMS) is also termed as χ. An RMS or χ value of 1 indicates an optimal fit, meaning that the model fits the data within the level of data error. Values < 1 correspond to overfitted data, where the mean deviation between observed and calculated data is smaller than the data error. If the RMS is significantly > 1, it suggests a poor fit, where the model is not capturing the data well, and there are large discrepancies between the observed and predicted values. A high RMS value can also indicate underfitting, where the model is too simple to capture the complexity of the data (Menke, 2012).

3.1.2 The Unconstrained Linearized Least Square Problem

The theory of linear inverse problems is a well-established area with a wide range of analytical and numerical methods. However, EM problems – like most applied geophysical problems – are associated with a forward operator that depends on nonlinear system equations (Meju, 1994). This nonlinearity arises from the product of electric conductivity and the electric field in the Maxwell equations. Nonlinear inverse problems pose greater theoretical and numerical challenges compared to linear ones. The most common approach for dealing with nonlinear problems involves leveraging linear methods through the consideration of a *linearized* version of the inverse problem. Linearization is accomplished by expanding the functional $\boldsymbol{F(m)}$ using Taylor approximation of first order for small model perturbations $\boldsymbol{\Delta m_k = m - m_k}$ with a given model $\boldsymbol{m_k}$:

$$\boldsymbol{F(m)}\Big|_{m_k} \approx \boldsymbol{F(m_k)} + \frac{\partial \boldsymbol{F}}{\partial \boldsymbol{m}}\Big|_{m_k}(\boldsymbol{m - m_k}) = \boldsymbol{F(m_k)} + \boldsymbol{J}\Big|_{m_k}\boldsymbol{\Delta m_k} \tag{3.8}$$

where $\boldsymbol{J} = \frac{\partial \boldsymbol{F}_i(\boldsymbol{m_k})}{\partial \boldsymbol{m}_j}$ is the $N \times M$ matrix of partial derivatives of the forward functionals with respect to a small perturbation in the model parameters, known as the Jacobian or sensitivity matrix, and the higher-order terms in Taylor approximation are neglected.

By replacing $\boldsymbol{F(m)}$ in equation (3.5) with the linearized forward operator yields:

$$\boldsymbol{\Phi}_d(\boldsymbol{\Delta m_k}) = (\boldsymbol{d - F(m_k) - J\Delta m_k})^T \boldsymbol{W}_d^2(\boldsymbol{d - F(m) - J\Delta m_k}) \tag{3.9}$$

To find the minimum of the cost-function, the derivative of equation 3.9 with respect to the model update $\Delta \boldsymbol{m_k}$ is computed and set to zero. Therefore, the least-square solution for the model update is:

$$\Delta \boldsymbol{m}_k = (\boldsymbol{J}^T \boldsymbol{W}_d^2 \boldsymbol{J})^{-1} \boldsymbol{J}^T \boldsymbol{W}_d^2 \big(\boldsymbol{d} - \boldsymbol{F}(\boldsymbol{m}_k)\big) \tag{3.10}$$

In order to achieve the updated model $\boldsymbol{m}_{k+1}$, the model perturbation is added to the model from the previous step k, e.g. the starting model $k = 0$. Then, on each iteration k, the model update $\Delta \boldsymbol{m_k}$ is determined and the current iteration model is updated:

$$\boldsymbol{m}_{k+1} = \boldsymbol{m}_k + \Delta \boldsymbol{m}_k \tag{3.11}$$

The iterative inversion process is repeated until a model adequately fits the data or a desired number of iterations is reached. This method is commonly known as the unconstrained iterative least squares fitting or the Gauss-Newton method. It is important to note that the convergence of this technique may be slow due to the strong dependence on a suitable initial model, and if the eigenvalues of the Jacobian are close to zero, the matrix $\boldsymbol{J}^T \boldsymbol{W}_d^2 \boldsymbol{J}$ may become singular or close to singular, resulting in an ill-conditioned matrix where Equation 3.10 would not have a solution. To avoid potential solution instability or ill-posed problems, the Gauss-Newton method is modified by imposing additional constraints to minimize the cost function in Equation 3.10.

3.2 Occam Inversion

Occam inversion introduced by Constable et al. (1987) is designed to solve the geophysical inverse problem, which is often ill-posed and non-unique. This inversion technique imposes a smoothness constraint on the model and balances data misfit with model simplicity through regularization, ensuring stable, interpretable solutions while avoiding overfitting. Therefore, the objective function $\boldsymbol{\Phi(m)}$ to minimize has the following form:

$$\boldsymbol{\Phi(m)} = \boldsymbol{\Phi}_d(\boldsymbol{m}) + \lambda \boldsymbol{\Phi}_m(\boldsymbol{m}) \tag{3.12}$$

where $\boldsymbol{\Phi}_d(\boldsymbol{m})$ and $\boldsymbol{\Phi}_m(\boldsymbol{m})$ are the data misfit and the model regulation term, respectively, and λ is the Tikhonov regularization parameter.

The regularization parameter (λ) serves as a trade-off between data fit and the smoothness of the resulting model. For large λ values, the model tends to be smoother, albeit with a greater data misfit. In contrast, a small λ value ($\lambda \to 0$) prioritizes data fit during the inversion process. At each iteration, a λ that minimizes data misfit is sought (Constable et al., 1987). In practice, a higher initial λ value is chosen, which is

then gradually decreased throughout the inversion iterations. However, this reduction should be limited between iterations to prevent introducing additional structure into the model (Farquharson & Oldenburg, 2004). In this context, Scholl (2005) incorporated a restriction on A within the EMUPLUS software. This constraint makes the results highly sensitive to the initial value of λ (Scholl, 2005).

Occam scheme imposes a stabilization term as a measure of the model roughness $\boldsymbol{R}$ of the model $\boldsymbol{m}$. Considering a linearized inverse problem, Equation (3.12) can be rewritten as:

$$\boldsymbol{\Phi}(\boldsymbol{m}_k) = (\boldsymbol{d} - \boldsymbol{F}(\boldsymbol{m}_k) - \boldsymbol{J}\Delta\boldsymbol{m}_k)^T \boldsymbol{W}_d^2 (\boldsymbol{d} - (\boldsymbol{F}(\boldsymbol{m}) + \boldsymbol{J}\Delta\boldsymbol{m}_k)) + \lambda \boldsymbol{m}^T \boldsymbol{R}_{1,2}^T \boldsymbol{R}_{1,2} \boldsymbol{m} \quad (3.13)$$

Constraints in the form of roughness are defined as the derivative of the first ($\boldsymbol{R}_1$) and second ($\boldsymbol{R}_2$) order of $\rho(z)$ with respect to depth. However, in the 1D case, $\rho(z)$ is not continuous, and therefore the discrete form is given:

$$\boldsymbol{R}_1 = \sum_{i=2}^{M} (\rho_i - \rho_{i-1})^2 \quad (3.14)$$

$$\boldsymbol{R}_2 = \sum_{i=2}^{M-1} (\rho_{i+1} - 2\rho_i + \rho_{i-1})^2 \quad (3.15)$$

Considering the forward operator presented in Equation 3.8, the model update ($\Delta\boldsymbol{m}_k$) derived from Equation 3.13 concerning the model parameters leads to the linearized problem:

$$\Delta\boldsymbol{m}_k = \left(\boldsymbol{J}^T \boldsymbol{W}_d^2 \boldsymbol{J} + \lambda \boldsymbol{R}_{1,2}^T \boldsymbol{R}_{1,2}\right)^{-1} \left[\boldsymbol{J}^T \boldsymbol{W}_d^2 \left(\boldsymbol{d} - \boldsymbol{F}(\boldsymbol{m}_k)\right) - \lambda \boldsymbol{R}_{1,2}^T \boldsymbol{R}_{1,2} \boldsymbol{m}_k\right] \quad (3.16)$$

Occam $\boldsymbol{R}_1$, representing first-order roughness, corresponds to the first derivative of ρ with respect to depth z, capturing the differences between neighboring model parameters. Occam $\boldsymbol{R}_2$, on the other hand, reflects the second-order derivative and penalizes changes in the gradient among model parameters. In simpler terms, when applying roughness $\boldsymbol{R}_1$, the inverse model typically exhibits a very smooth profile. In contrast, the application of $\boldsymbol{R}_2$ results in a slight curvature of the model parameters, indicating a uniform resistivity contrast.

3.3 Levenberg-Marquardt Algorithm

Levenberg (1944) introduced a damped least squares method to address the instability and non-convergence associated with the solution to the normal equation 3.10. Marquardt (1963) later adopted this approach to develop nonlinear least squares

algorithms, which are widely used in geophysical data inversion (Meju, 1994). To stabilize the cost function, a tradeoff parameter—also known as the damping parameter—is incorporated into the length of the model update $\Delta \boldsymbol{m}_k$. The total cost function is expressed in the following form:

$$\boldsymbol{\Phi}(\boldsymbol{m}_k) = (\boldsymbol{d} - \boldsymbol{F}(\boldsymbol{m}_k) - \boldsymbol{J}\Delta \boldsymbol{m}_k)^T \boldsymbol{W}_d^2 \big(\boldsymbol{d} - (\boldsymbol{F}(\boldsymbol{m}_k) + \boldsymbol{J}\Delta \boldsymbol{m}_k)\big) + \beta^2 (\Delta \boldsymbol{m}_k^T \Delta \boldsymbol{m}_k) \quad (3.17)$$

For minimization, the extended cost function is derived with respect to $\Delta \boldsymbol{m}_k$, equated to zero and subsequently solved for the model update:

$$\Delta \boldsymbol{m}_k = (\boldsymbol{J}^T \boldsymbol{W}_d^2 \boldsymbol{J} + \beta^2 \boldsymbol{I})^{-1} \boldsymbol{J}^T \boldsymbol{W}_d^T \boldsymbol{W}_d \big(\boldsymbol{d} - \boldsymbol{F}(\boldsymbol{m}_k)\big) \quad (3.18)$$

Here, $\boldsymbol{I}$ is the identity matrix and the β is a Lagrange multiplier and weights between the data misfit term and the model update term.

This approach is known as Levenberg-Marquardt inversion or damped least squares inversion. This method implemented in the EMUPLUS algorithm is typically conducted with a minimal number of layers, particularly when $N > M$. However, a drawback of the Levenberg-Marquardt inversion scheme is that the results are highly sensitive to the chosen starting model.

3.3.1 Singular Value Decomposition (SVD)

In order to calculate the inverse of equation 3.18, a singular value decomposition (SVD) is often utilized. Any $N \times M$ matrix with N data entries and M model parameters can be decomposed using SVD as (Menke, 2012):

$$\boldsymbol{G} = \boldsymbol{U}\boldsymbol{\Lambda}\boldsymbol{V}^T \quad (3.19)$$

With the following matrices:

- The matrix $\boldsymbol{U} \in \mathbb{R}^{N \times N}$ is an orthogonal matrix that spans the data space, providing insights into how changes in a data point will affect the model. The columns of $\boldsymbol{U}$ consist of the individual eigenvectors of $\boldsymbol{G}\boldsymbol{G}^T$.
- The orthogonal matrix $\boldsymbol{V} \in \mathbb{R}^{M \times M}$ spans the model space and contains the eigenvectors of $\boldsymbol{G}^T\boldsymbol{G}$. These eigenvectors represent linear combinations of independently resolved model parameters.
- $\boldsymbol{\Lambda} \in \mathbb{R}^{N \times M}$ is a diagonal eigenvalue matrix containing the non-zero eigenvalues $(\lambda_1, \ldots, \lambda_N)$, which is called singular values of $\boldsymbol{G}$. They are typically sorted in decreasing order, emphasizing the influence of the linear combinations on the model outcome.

The SVD is applied to the weighted Jacobian $\boldsymbol{J_w = W_d J}$ and equation 3.18 can be expressed as (Lines & Treitel, 1984):

$$\Delta \boldsymbol{m}_k = \boldsymbol{V} \underbrace{(\boldsymbol{\Lambda}^2 + \beta^2 \boldsymbol{I})^{-1} \boldsymbol{\Lambda}^T \boldsymbol{\Lambda}}_{\hat{\boldsymbol{Q}}} \boldsymbol{\Lambda}^{-1} \boldsymbol{U}^T \boldsymbol{W}_d \big(\boldsymbol{d} - \boldsymbol{F}(\boldsymbol{m}_k)\big) \tag{3.20}$$

where the damping matrix $\boldsymbol{Q}$ is a diagonal matrix and has the following values:

$$\boldsymbol{Q}_{ii} = \frac{\lambda_i^2}{\lambda_i^2 + \beta^2} \tag{3.21}$$

If λ_i is nearly zero, a positive β will prevent the singularity problem. A singular value with $\lambda_i = \beta$ will be damped by a factor of $\boldsymbol{Q}_{ii} = 0.5$. In this thesis, the 1D inversion algorithm EMUPLUS employs a default normalized singular value threshold of 1%. This means that singular values that are less than 1% of $\boldsymbol{Q}_{ii}$ will be damped by a factor of 0.5.

3.3.2 Equivalent Models

Equivalent models refer to different models that all fit the observed data to a similar response within a certain error-bound (Spies & Frischknecht, 1991). This concept highlights one of the fundamental challenges of inversion theory: many different distributions of model parameters can yield very similar (or identical) predictions for the measured data, making it difficult to identify a single unique solution. Considering data errors, several models may fit the data similarly within the error bars. Additionally, poorly resolved parameters are not supported by the data and typically result in significant equivalence. The equivalence principle can theoretically be derived from the thin sheet solution for an inductive source, as discussed in Nabighian & Macnae (1991).

In the 1D inversion scheme EMUPLUS, a Hybrid Marquardt Monte Carlo scheme is implemented to generate equivalent models (Scholl, 2005). Typically, model parameters are randomly perturbed within a specified percentage range, and the equivalent results are compared against one another. This process yields several Marquardt inversion models, all of which demonstrate a sufficiently low data misfit. Consequently, these equivalent models serve to assess the resolution of the model parameters. If the equivalent models exhibit significant variability within a model parameter, it indicates that the model parameter is not well resolved. Conversely, when the equivalent models show minimal variability, it suggests that the corresponding parameter is well resolved.

3.4 Nonlinear Conjugate Gradient (NLCG) Inversion

The Non-linear Conjugate Gradient (NLCG) method is an iterative optimization technique that minimizes a non-linear objective function commonly encountered in large-scale geophysical problems like EM. NLCG was first proposed by Fletcher & Reeves (1964) and later improved by Polak & Ribiere (1969). It extends the linear conjugate gradient (CG) method to non-linear problems, finding solutions without explicitly forming the Hessian (second derivative) matrix, which is advantageous for high-dimensional, computationally intensive problems. It has been implemented to solve the inversion problem in both 2D (Rodi & Mackie, 2001) and 3D (Kelbert et al., 2014; Newman & Alumbaugh, 2000) MT data.

Numerical tests have demonstrated that NLCG is more efficient than Gauss-Newton methods in terms of computational requirements (Rodi & Mackie, 2012). The NLCG approach is nearly twice as fast as evaluating the full Jacobian matrix $\boldsymbol{J}$ required by Newton-type methods (Avdeev, 2005). Despite this significant improvement in speed, implementing the NLCG method still necessitates either a massively parallel computing architecture (Newman et al., 2002; Newman & Alumbaugh, 2000) or the use of a message passing interface (MPI) running on PC clusters (Mackie et al., 2001). Since the NLCG method is closely related to the linear conjugate gradient (CG) method, CG will be explained before the NLCG scheme is described.

The conjugate gradient (CG) method

The normal equations (e.g., equation 3.18) can be rewritten in matrix vector notation as:

$$\boldsymbol{Ax} = \boldsymbol{b} \tag{3.22}$$

where $A = (\boldsymbol{J}^T\boldsymbol{W}_d^2\boldsymbol{J} + \beta^2\boldsymbol{I})$, $\boldsymbol{x} = \Delta\boldsymbol{m}_k$, and $\boldsymbol{b} = \boldsymbol{J}^T\boldsymbol{W}_d^2\boldsymbol{W}_d\big(\boldsymbol{d} - \boldsymbol{F}(\boldsymbol{m}_k)\big)$. The system of equations presented in equation 3.22, which is real, symmetric, and positive definite, can be solved using a standard equation system solver. Equation system solvers can be broadly categorized into two main types: direct and iterative solvers. Direct solvers include methods such as Cholesky and LU decompositions. An example of an iterative solver for the inversion problem is the conjugate gradient method (CG). To solve the system of equations in equation 3.22, CG generates a sequence of approximated solutions by iteratively minimizing the quadratic form:

$$\boldsymbol{\Phi}(\boldsymbol{x}) = \frac{1}{2}\boldsymbol{x}^T\boldsymbol{Ax} - \boldsymbol{b}^T\boldsymbol{x} \tag{3.23}$$

along a sequence of conjugate search directions $\boldsymbol{p}$, starting from $\boldsymbol{p}_0 = 0$ as the initial guess, the next search direction is obtained using:

$$\boldsymbol{p}_{k+1} = \boldsymbol{g}_{k+1} - \gamma_k \boldsymbol{p}_k \tag{3.24}$$

where $\boldsymbol{g}_{k+1}$ is the gradient of equation 3.23 and given by:

$$\boldsymbol{g}_{k+1} = \frac{\partial}{\partial \boldsymbol{x}_k}\left(\frac{1}{2}\boldsymbol{x}_k^T \boldsymbol{A}\boldsymbol{x}_k\right) = \boldsymbol{A}\boldsymbol{x}_k - \boldsymbol{b} \tag{3.25}$$

Increment k and repeat until the residual $\boldsymbol{g}_k$ is below a pre-defined tolerance, or the maximum number of iterations is reached.

The scalar γ_k is calculated as:

$$\gamma_k = \frac{\boldsymbol{g}_{k+1}\boldsymbol{A}\boldsymbol{p}_k}{\boldsymbol{p}_k^T \boldsymbol{A}\boldsymbol{p}_k} \tag{3.26}$$

This scalar (γ_k) ensures that the search direction $\boldsymbol{p}_k$ is conjugated to all other previous search directions. The solution $\boldsymbol{x}_{k+1}$ which ensures that $\boldsymbol{\Phi}(\boldsymbol{x})$ in its minimum is:

$$\boldsymbol{x}_{k+1} = \boldsymbol{x}_k - \boldsymbol{\beta}_{k+1}\boldsymbol{p}_{k+1} \tag{3.27}$$

where $\boldsymbol{\beta}_{k+1}$ is the scalar step size and given by:

$$\boldsymbol{\beta}_{k+1} = \frac{\boldsymbol{p}_{k+1}^T \boldsymbol{g}_{k+1}}{\boldsymbol{p}_{k+1}^T \boldsymbol{A}\boldsymbol{p}_{k+1}} \tag{3.28}$$

In the CG scheme, the primary computational tasks involve the matrix-vector multiplications $\boldsymbol{Ap}$ as outlined in equations 3.26 and 3.28. Rodi & Mackie (2001) demonstrated that this multiplication can be achieved at the expense of two pseudo-forward modeling computations. Furthermore, there is no need to compute and store the sensitivity matrix. The CG scheme is typically implemented within an outer iterative loop that minimizes the objective function $\boldsymbol{\Phi}$ as specified in equation 3.12. The flowchart for the algorithm to solve the normal equations using CG could be represented in Figure 3.1:

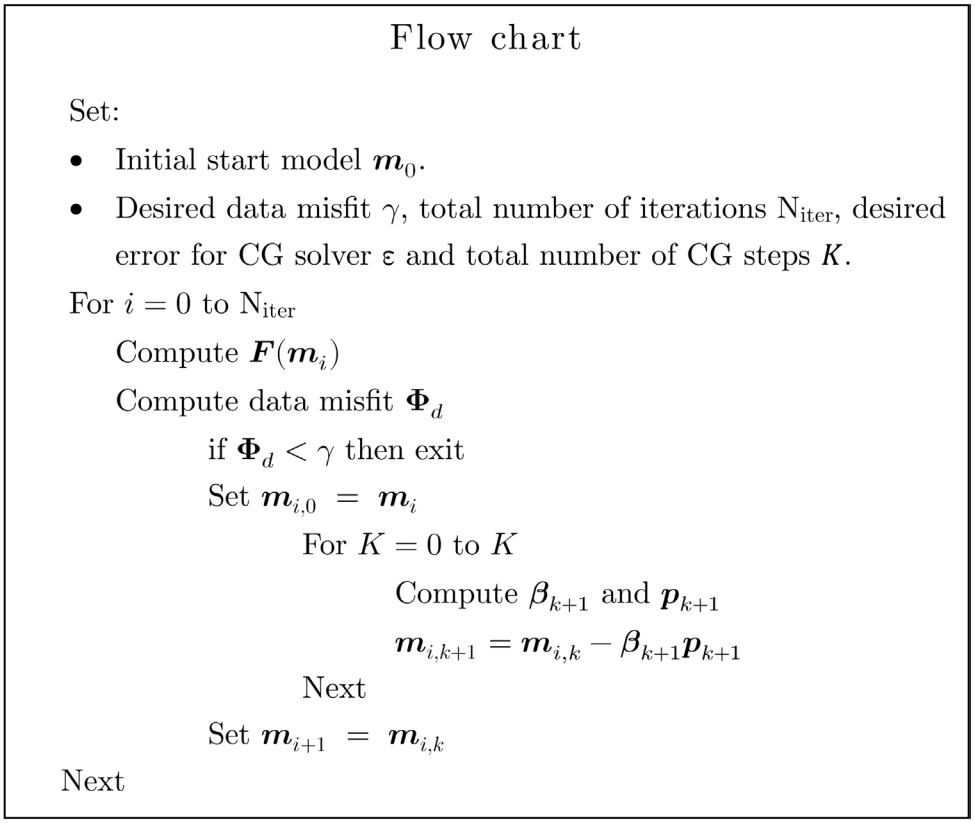

Figure 3.1: The flow chart for the CG algorithm scheme to solve the linearized normal equation. Modified from Meqbel (2009).

Nonlinear conjugate gradients (NLCG) method

NLCG are closely related to the linear conjugate gradient method previously discussed, particularly in the context of solving the linearized inverse problems. Unlike the linear CG method, however, the NLCG technique directly tackles minimization problems that are not quadratic and avoids the iterative linearized inversion procedure commonly used in Gauss-Newton style inversion (Rodi & Mackie, 2001). The NLCG method essentially employs the same fundamental computational steps as those used to solve the linearized problem through a CG approach. In implementing the NLCG, it is essential to evaluate the gradient of equation 3.12 with respect to the model parameters ($\boldsymbol{m}$). Additionally, one must consider the nonlinear form of $\boldsymbol{\Phi}_d$ in equation 3.5. In this context, we can express:

$$\boldsymbol{\nabla\Phi} = \boldsymbol{\nabla\Phi}_d + \lambda\boldsymbol{\Phi}_m \tag{3.29}$$

Considering the function $\boldsymbol{\Phi}_m = \|\boldsymbol{Lm}^2\|$, it leads to:

$$\boldsymbol{\nabla\Phi}_m = 2\boldsymbol{L}^T\boldsymbol{L}_m \tag{3.30}$$

And the gradient of equation 3.5 is calculated as:

$$\nabla \Phi_d = -2\boldsymbol{J}^T \boldsymbol{W}_d^2 (\boldsymbol{d} - \boldsymbol{F}(\boldsymbol{m})) \tag{3.31}$$

In a uniform grid, the term $\boldsymbol{L}_m$ refers to the Laplacian of the model parameters, which describes the variations between adjacent model parameters (Rodi and Mackie, 2001). Consequently, the NLCG scheme aims to minimize the cost function $\boldsymbol{\Phi}$ but with respect to the step size $\boldsymbol{\beta}$.

The minimization problem is given by:

$$\boldsymbol{\Phi}_d(\boldsymbol{m}_k + \boldsymbol{\beta}_k \boldsymbol{p}_k) = \underbrace{min}_{\boldsymbol{\beta}} \boldsymbol{\Phi}\,(\boldsymbol{m}_k - \boldsymbol{\beta} \boldsymbol{p}_k) \tag{3.32}$$

The NLCG scheme generates a sequence of models that are determined:

$$\boldsymbol{m}_{k,j} = \boldsymbol{m}_k + \boldsymbol{\beta}_{k,j} \boldsymbol{p}_k \tag{3.33}$$

where the step size $\boldsymbol{\beta}$ is defined as:

$$\boldsymbol{\beta}_{k,0} = 0, and\ \boldsymbol{\beta}_{k,j+1} = \boldsymbol{\beta}_{k,j+1} - \frac{\boldsymbol{g}_{k,j}^T \boldsymbol{p}_k}{\boldsymbol{p}_k^T \widetilde{\boldsymbol{H}}_{k,j} \boldsymbol{p}_k} \tag{3.34}$$

The approximate Hessian matrix is calculated as $\widetilde{\boldsymbol{H}} = 2\boldsymbol{J}^T \boldsymbol{W}_d^2 + 2\lambda \boldsymbol{L}^T \boldsymbol{L}$ and the vector gradient is given by $\boldsymbol{g} = -2\boldsymbol{J}^T \boldsymbol{W}_d^2 \big(\boldsymbol{d} - \boldsymbol{F}(\boldsymbol{m})\big) + 2\lambda \boldsymbol{L}^T \boldsymbol{L}_{\boldsymbol{m}}$. The conjugate gradient direction $\boldsymbol{p}_k$ is determined by the steepest descent direction:

$$\begin{aligned} \boldsymbol{p}_0 &= -\boldsymbol{C}_0 \boldsymbol{g}_0 \\ \boldsymbol{p}_k &= -\boldsymbol{C}_k \boldsymbol{g}_k + \gamma_k \boldsymbol{p}_{k-1} \end{aligned} \tag{3.35}$$

The scalar γ_k is calculated using the Polak-Ribiere technique (Polak, 1971):

$$\gamma_k = \frac{\boldsymbol{g}_k^T \boldsymbol{C}_k (\boldsymbol{g}_k - \boldsymbol{g}_{k-1})}{\boldsymbol{g}_{k-1}^T \boldsymbol{C}_{k-1} \boldsymbol{g}_{k-1}} \tag{3.36}$$

where $\boldsymbol{C}_k$ is the preconditioner, and it's defined as:

$$\boldsymbol{C}_k = (\eta_k \boldsymbol{I} + \lambda \boldsymbol{L}^T \boldsymbol{L})^{-1} \tag{3.37}$$

with term η_k is a specified scalar. The use of the preconditioner effectively guides the gradient vector towards a more productive search direction (Rodi & Mackie, 2001). The NLCG algorithm keeps track of the best model found during the line search:

$$\boldsymbol{m}_{k,best} = \boldsymbol{m}_k + \boldsymbol{\beta}_{k,best} \boldsymbol{p}_k \tag{3.38}$$

And the final result of the k-th line search is taken as the best model $\boldsymbol{m}_{k+1} = \boldsymbol{m}_{k,best}$.

Therefore, a starting model $\boldsymbol{m}_0$ is provided, and the subsequent model $\boldsymbol{m}_{k+1}$ is determined using the step size $\boldsymbol{\beta}_{k,j}$ in the search direction $\boldsymbol{p}_k$. Because of the non-linearity of the problem, a line search process is implemented, as opposed to merely identifying the step length parameter, as is done in the Conjugate Gradient (CG)

method. This line search process helps to circumvent the need to compute a large Hessian matrix ($\widetilde{\boldsymbol{H}}$ in equation 3.34). However, a noted drawback of the NLCG scheme is that it tends to require more iterations for convergence. As previously mentioned, the NLCG and CG methods are closely related; their primary distinction lies in the fact that the CG method is designed for minimizing quadratic cases (e.g., equation 3.23), while the NLCG method addresses non-quadratic scenarios. Both algorithms avoid the explicit computation of the Jacobian matrix, instead only requiring a product of $\boldsymbol{J}$ or $\boldsymbol{J}^T$ with an arbitrary vector. Similar to the NLCG, a preconditioner can also be utilized in the CG method to enhance the performance of the algorithm.

Chapter 4

Overview of Geothermal Energy Resources

Geothermal energy is a renewable and sustainable energy source with significant potential to contribute to the global energy transition. It is derived from the Earth's internal heat, which has an immense reserve. This vast and largely untapped resource is concentrated in specific regions, primarily at the boundaries of tectonic plates, where volcanic and seismic activities are prevalent. These high-temperature geothermal reservoirs make it possible to efficiently harness geothermal energy for power generation and direct heating applications. This energy form is essential in mitigating the carbon dioxide emissions produced by oil, coal, and other fossil fuels, which are principal contributors to global warming—one of the most pressing existential threats facing humanity today. There is an increasing agreement among experts that a swift decrease in greenhouse gas emissions is essential to avert the severe consequences associated with climate change. To achieve climate objectives, it is imperative to enhance energy efficiency and to transition from fossil fuels, coal, and other environmentally harmful energy sources to renewable and sustainable energy alternatives. Therefore, geothermal energy is one of the geo-resources that serve as a critical foundation for facilitating reductions in greenhouse gas emissions (Herrington, 2021; Younger, 2014). In addition to electricity generation, geothermal energy has diverse applications, including district heating, greenhouse agriculture, industrial processes, and thermal energy storage.

Geothermal energy has several advantages over other renewable energy sources. Unlike solar, wind, or hydropower, it is a stable and reliable resource that is generally unaffected by geography, climate, or season. Additionally, geothermal energy can be utilized continuously, as long as the upper limit of geothermal utilization is properly controlled, ensuring the long-term sustainability of the resource (Zhang et al., 2019). Globally, geothermal activity is concentrated in areas exhibiting relatively high heat flow, which is a consequence of extensive magmatism and/or crustal thinning (Elders & Moore, 2016; Jolie et al., 2021). At present, there are several hundred geothermal power plants of various types and capacities generating electricity in the world, and the vast majority of them are located in areas of high seismic activity near the boundaries of the tectonic plates (Figure 4.1). This is because the geothermal gradients are higher in tectonically and volcanically active regions where heat transfer is controlled by

convection. This happens because the Earth's crust is thinner and more heat flows to the surface (Elders & Moore, 2016; Stimac et al., 2015). However, despite its advantages, geothermal energy development faces several challenges, such as high upfront costs, resource exploration risks, and limited accessibility in some regions. Addressing these barriers through advancements in exploration technologies, enhanced geothermal systems (EGS), and improved drilling techniques is essential to unlocking the full potential of geothermal energy as a cornerstone of a sustainable energy future.

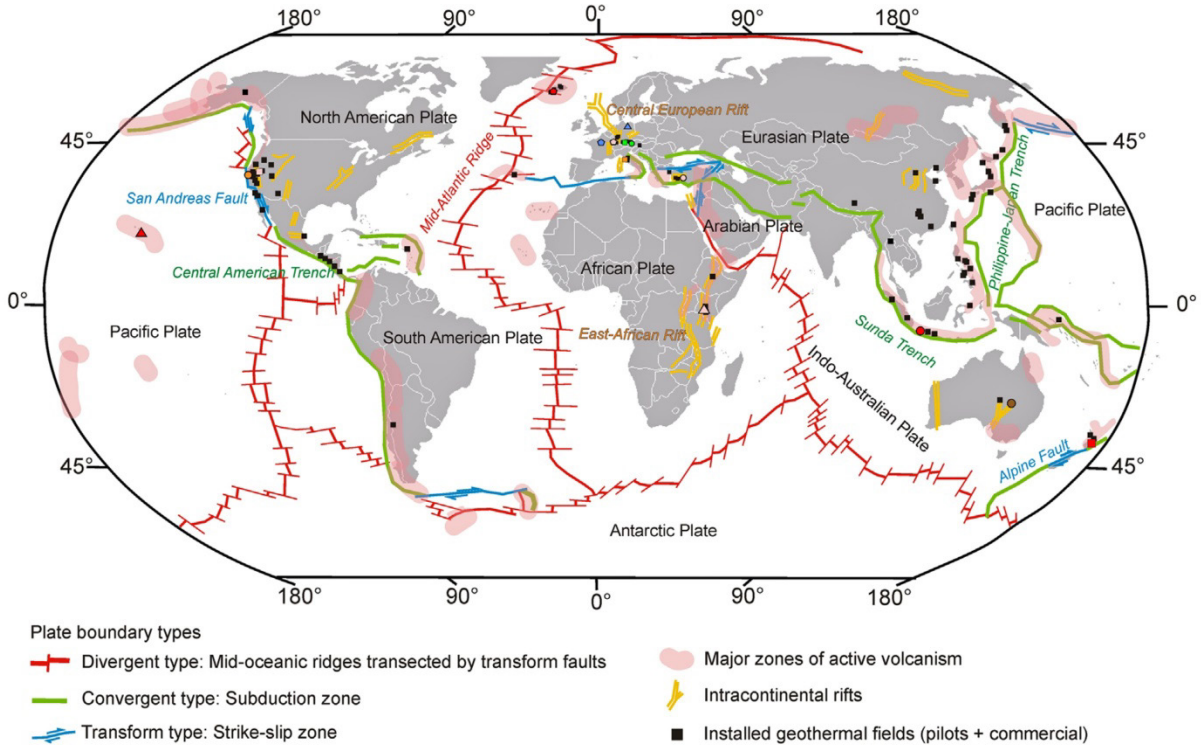

Figure 4.1: Geothermal fields established globally within a plate tectonic framework. Overview of key geothermal power plants, focusing on their relation to major fault zones and tectonic boundaries. Figure taken from Moeck (2014).

In recent years, the installed geothermal capacity worldwide has grown significantly, driven by advancements in production engineering and a multi-disciplinary effort to make geothermal energy a more competitive renewable energy resource. Geothermal energy holds significant potential, with recent estimates suggesting that around 43 × 10^15 GJ of energy is stored at a depth of 3 km from the Earth's surface (DiPippo, 2012). The commercial application of geothermal energy resources has been recorded for more than 100 years, and it is expected that geothermal energy will play an increasingly important role in global power generation, with a forecast contribution of more than 8.3% of the world's power generation by 2050. Total geothermal power generation reached 116,000 GWh in 2018 and can be extended to 282,000 GWh by 2030 (Ghoddousi et al., 2021). This growth is further reflected in the direct use of geothermal energy for thermal applications, which reached approximately 141 TWh in 2021,

including around 128 TWh attributed to direct geothermal heat utilization (Lund & Toth, 2021). As the global community strives to achieve net-zero emissions by mid-century, the strategic development of geothermal energy resources will be crucial for decarbonizing power generation, district heating, and industrial processes.

4.1 Geothermal System Overview

The geothermal system, a complex and dynamic phenomenon, can be understood through a conceptual model that represents its components and their intricate interactions. Such a model provides insights into the processes of heat formation, storage, and heat-mass transport, essential for sustainable geothermal resource development. Regardless of the type of geothermal resources, which is explained in the next sub-chapter, a general geothermal system conceptually involves the presence of a heat source, a permeable reservoir, a recharge mechanism, and an impermeable rock known as a clay cap (Berktold, 1983; Cumming, 2009; Muñoz, 2014).

A typical geothermal system includes four main elements: a heat source, a permeable reservoir, a recharge mechanism, and an impermeable caprock. The heat source is typically a magmatic intrusion or deep-seated geothermal gradient from radioactive decay, particularly prevalent in tectonically active or volcanic regions. The heat source provides the necessary thermal energy to heat the surrounding rock and any groundwater present. The next critical component is the permeable reservoir where the hot groundwater or other fluids circulate through permeable rock formations. Depending on the composition, reservoirs can be liquid-dominated ($\geq$60% water), vapor-dominated ($\geq$60% vapor, typically at $\geq$200°C), or mixed-phase (Williams et al., 2011). These reservoirs are key for energy extraction due to their heat transport properties.

The recharge mechanism is the process by which the geothermal reservoir is replenished with new heated fluid, either from the surrounding groundwater system or from the deep circulation of fluids. The clay cap, also known as the caprock, is a layer of impermeable clay or shale that overlies the geothermal reservoir and prevents the escape of the geothermal fluid, ensuring the sustainability of the resource. The clay cap forms through prolonged reactions between thermal fluids and surrounding rocks, creating a clay alteration layer. This alteration can occur over a wide temperature range, typically from under 100 °C to over 200 °C (Essene & Peacor, 1995). The presence of a clay cap typically results in a low resistivity signature, which is indicative of geothermal systems. This signature allows for the identification of high-temperature areas beneath the

surface. However, in some high-temperature geothermal systems, especially those associated with volcanic activity, a clay cap may be absent due to their unique geological conditions (Muñoz, 2014; Patro, 2017).

4.2 Classification of Geothermal Resources

Geothermal resources can be classified based on several criteria such as temperature, geological setting, and assessment confidence, reflecting the evolving understanding of their characteristics and applications. These classifications aid exploration, development, and decision-making for stakeholders like investors and developers (Furqan et al., 2016; Rybach, 2015; Williams et al., 2011). Although no universal classification system exists, several widely used methods provide insights tailored to specific objectives and contexts (Jalilinasrabady, 2022). Among these, three key classification approaches have gained prominence and been widely used.

4.2.1 Temperature Classification

Temperature plays a critical role in determining the quality of geothermal resources and is the primary factor in most classification systems. Temperature-based classification is widely used due to its simplicity and the consensus among scientists regarding its significance. The most commonly recognized categories are low-temperature, intermediate-temperature, and high-temperature geothermal resources. However, there is no universally accepted standard for the specific temperature boundaries of each category (Jalilinasrabady, 2022; Moeck, 2014; Williams et al., 2011). Various researchers have proposed different classification systems, leading to some variations in the defined temperature ranges. For instance, some classifications may set the threshold for high-temperature resources at 150°C, while others may consider it to begin at 200°C. Table 4.1 summarizes the temperature classification of geothermal resources according to different researchers.

Table 4.1: Classifications of geothermal resources by temperature.

Enthalpy	**Muffler and Cataldi** (1978)	**Haenel et al.** (1988)	**Hochstein** (1990)	**Benderitter and Cormy** (1990)
Low	$<$ 90 °C	$<$ 150 °C	$<$ 125 °C	$<$ 100 °C
Intermediate	90 – 150 °C	-	125 – 225 °C	100 – 200 °C
High	$>$ 150 °C	$>$ 150 °C	$>$ 225 °C	$>$ 200 °C

Later, Sanyal (2005) also proposed a new temperature classification method for geothermal resources into seven distinct classes:

- Class 1 (non-electrical grade): Below 100 °C
- Class 2 (very low temperature): 100 °C to <150 °C
- Class 3 (low temperature): 150 °C to 190 °C
- Class 4 (moderate temperature): 190 °C to <230 °C
- Class 5 (high temperature): 230 °C to <300 °C
- Class 6 (ultra-high temperature): Above 300 °C
- Class 7 (steam fields): Approximately 240 °C with steam as the only mobile phase

While temperature classification is a straightforward method for understanding geothermal resources, it does not consider other critical parameters, such as pressure and geological environment, which are essential for a more accurate assessment of geothermal resource potential. As a result, additional classifications may be necessary to fully evaluate geothermal resources (Jalilinasrabady, 2022).

4.2.2 Exergy Classification

The classification of geothermal resources has traditionally been based on temperature or enthalpy, as previously explained. However, temperature or enthalpy alone may not provide a comprehensive understanding of the resource's potential. To address this limitation, researchers have proposed using the concept of exergy, which refers to the maximum amount of work that can be extracted from a system as it approaches equilibrium with the environment, offering a more comprehensive understanding of resource quality and potential (Jalilinasrabady & Itoi, 2013; Lee, 2001). The first application of exergy analysis to a geothermal power plant was reported in the late 1970s, as researchers sought to develop more efficient methods of harnessing this renewable energy source (Bodvarsson & Eggers, 1972). In the modern days, the exergy method has been applied to classify the geothermal resources in many countries, such as Japan (e.g. Jalilinasrabady & Itoi, 2013), Turkey (e.g. Etemoglu & Can, 2007), and Indonesia (e.g. Mohammadzadeh Bina et al., 2018).

In practice, geothermal resources can be classified as low, medium, and high-quality resources with reference to their specific exergy indices (SExI), which can be calculated by dividing the total exergy of the geothermal resource by its mass flow rate, providing a measure of the exergy content per unit of mass flow rate. SExI of 0.5 is the lower limit for the high-quality geothermal resources, while low-quality resources would have an SExI below 0.05, and medium-quality resources would fall in between (Lee, 2001).

A study conducted in Japan examined the exergy-based classification of 18 operational geothermal power plants (Jalilinasrabady & Itoi, 2013). The results showed that six geothermal fields had high-exergy resources, with specific exergy indices exceeding 0.5, while the remaining fields were classified as medium-quality resources (Figure 4.2).

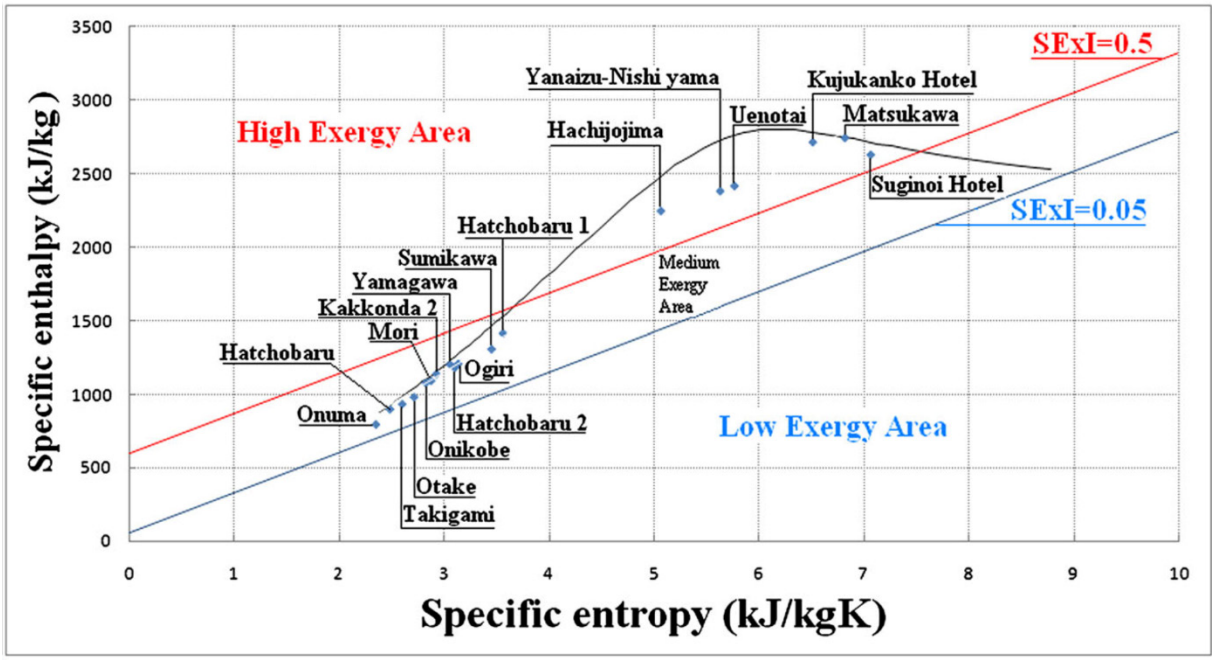

Figure 4.2: Distribution of an exergy-based classification of geothermal fields in Japan according to calculated SExI values: SExI ≥ 0.5 (high exergy), 0.5 < SExI ≥ 0.05 (medium exergy), and SExI < 0,05 (low exergy). Figure taken from Jalilinasrabady & Itoi (2013).

Exergy-based geothermal classification has some advantages, as it offers a more nuanced measurement of geothermal potential compared to temperature and enthalpy alone and allows for evaluating how effectively geothermal fluids can be utilized for energy production. However, it does not incorporate geological and hydrogeological elements such as geological settings, fluid flow controls, fluid chemistry, and mineral precipitation impacts, which are crucial for energy production and economic viability. The exergy method also relies on temperature and pressure estimates from the wellhead, meaning it can only be implemented post-drilling, limiting its applicability for pre-drilling assessments. These limitations highlight the necessity for a more integrated approach that includes geological factors, ensuring the catalog is helpful for both pre-drilling assessments and sustainable resource management (Moeck, 2014).

4.2.3 Geologic Classification

The geological setting of a geothermal system fundamentally determines the resource's characteristics and potential. Regions with active tectonic processes, such as subduction zones, rift valleys, and volcanic arcs, often host high-temperature geothermal resources

due to the proximity of magma bodies. These systems benefit from enhanced heat flow and greater resource availability. In contrast, areas without active tectonics may host low-temperature geothermal resources. These are often found in sedimentary basins or regions with substantial insulation from underlying heat sources, limiting their utilization for energy production or direct-use applications. The geological, structural, and tectonic characteristics of a geothermal resource heavily influence its efficiency and economic viability, making a thorough understanding of these factors essential for effective exploration and utilization (Hoteit et al., 2023; Jalilinasrabady, 2022; Moeck, 2014).

Geothermal resources can be broadly classified into two major categories based on their heat transfer mechanisms and geological settings: convection-dominated systems and conduction-dominated systems. Convection-dominated geothermal systems typically occur in areas with active volcanism and tectonic activity, where the Earth's internal heat is efficiently transported to the surface by circulating groundwater (Moeck, 2014). These systems are typically shallow ($<$ 3 km depth) with high temperature or enthalpy and characterized by surface manifestations such as hot springs, geysers, fumaroles, and boiling mud pots, all fed by the heated groundwater (Moeck, 2013). The formation of a viable convection-dominated geothermal system requires three essential conditions: an underground heat source, a heat transfer medium (often in the form of circulating groundwater), and a heat conducting channel that allows the heated fluids to reach the surface.

In contrast, conduction-dominated geothermal plays are found in regions with low to moderate levels of tectonic activity, where the heat from the Earth's interior is primarily transported through the surrounding rock by thermal conduction (Moeck, 2014). These systems are typically devoid of surface manifestations, and the geothermal energy is often stored as high-temperature, high-pressure fluids deep underground, such as in large sedimentary basins. Harnessing the energy from conduction-dominated plays often requires deeper drilling ($>$ 2 km depth) to reach the geothermal reservoirs, which can be technologically and economically challenging.

Both convection-dominated and conduction-dominated types of geothermal systems can be subdivided into three sub-types based on the specific characteristics of the geological settings, as summarized in Table 4.2. The classification of the convection-dominated geothermal system can be subdivided into three geologic settings: magmatic-volcanic, magmatic-plutonic and non-magmatic or extensional type. While the conduction-dominated geothermal systems contain three settings: the intracratonic basin type, the orogenic belt type, and the basement/crystalline rock type.

Table 4.2: Summary of the geologic-based classification of geothermal resources, modified from Moeck (2014).

Convection-dominated geothermal systems (CV)			
Resources type	***Geological settings***	***Temperature***	***Host rock***
Magmatic – Volcanic	Mid-oceanic ridges, volcanic arc regions, and mantle plumes (hot spots)	70 – 320 °C	Rhyolites, andesites, and basalt
Magmatic – Plutonic	Decrescent volcanism at young orogenic	100 – 350 °C	Sediments Granite and Gabbro
Non-magmatic	Metamorphic core complexes, back-arc basins, pull-apart basins and intracontinental rifts	150 – 240 °C	Volcanic sedimentary rock
Conduction-dominated geothermal systems (CD)			
Resources type	***Geological settings***	***Temperature***	***Host rock***
Intracratonic basin	Rift basins and passive margin basins	$<$ 150 °C	High–low permeability fluvial sediments
Orogenic belt	Fold-and-thrust belts and foreland basins	$<$ 160 °C	High–low permeability marine sediments
Basement/crystalline (hot dry rock)	Intercontinental intrusion in flat terrain	150 – 320 °C	Granite rock with high radiogenic heat

Magmatic – Volcanic Type

Volcanic geothermal plays are among the most productive and well-known types of geothermal systems, largely due to their association with active volcanic regions. These systems are characterized by shallow heat sources in the form of magma chambers, which provide intense thermal energy to the surrounding rock and fluids, as illustrated in Figure 4.3a. Volcanic geothermal systems are often found near volcanic features such

as calderas, craters, and lava flows. The proximity of magma to the Earth's surface in these regions ensures that circulating water or steam reaches very high temperatures, making volcanic geothermal plays particularly suited for electricity generation. The high heat flow and availability of steam in these systems allow for the efficient operation of geothermal power plants. For example, Iceland's geothermal power industry thrives on volcanic systems, with locations such as the Reykjanes Peninsula and Krafla providing abundant geothermal resources (Pope et al., 2016; Wang et al., 2022). The Kamojang power plant in Wests Java, Indonesia, is another example of volcanic geothermal fields that produce substantial amounts of electricity (Dwikorianto & Zuhro, 2010; Suryadarma et al., 2010).

Magmatic – Plutonic Type

Plutonic geothermal plays are closely related to volcanic systems but differ in terms of their heat sources (see Figure 4.3b). These systems are associated with large intrusive bodies of igneous rock, known as plutons, that were emplaced deep within the Earth's crust. While these plutonic bodies may have been associated with volcanic activity in the past, they are no longer linked to active volcanism. Instead, the heat within plutonic geothermal plays is derived from the residual thermal energy retained by the slowly cooling plutonic rock. Plutonic geothermal systems are typically found at greater depths than volcanic systems. They are characterized by high-temperature rocks that can still provide significant geothermal energy, despite the absence of active magma. These systems are often located in tectonically active regions, where the cooling of large igneous intrusions has created long-lasting reservoirs of heat. Plutonic geothermal systems can be used for both electricity generation and direct heat applications. However, because they tend to be located deeper within the Earth's crust, tapping into these resources often requires more advanced drilling techniques and higher initial investment costs. Nevertheless, the potential for long-term energy production makes plutonic geothermal systems an attractive option for sustainable energy development. The geysers in California, USA, are famous examples of plutonic geothermal fields that produce substantial amounts of electricity from recent magmatism (Peacock et al., 2020).

Non-Magmatic Type

Non-magmatic or extensional geothermal plays represent a distinct category of convection-dominated geothermal systems that are not directly associated with magmatic activity. Instead, these systems rely on the Earth's natural geothermal gradient, which causes heat to rise from the Earth's interior toward the surface. Non-magmatic geothermal systems are often found in regions of extensional tectonics, where the Earth's crust is being stretched and thinned, allowing heat to rise more easily

through fractures and faults, as illustrated in Figure 4.3c. These systems are widespread and can be found in various geological settings, including sedimentary basins and rift zones. For example, the Basin and Range Province in the western United States and the Rhine Graben in Europe are both regions with significant non-magmatic geothermal potential (Faulds & Coolbaugh, 2010; Frey et al., 2022; McKenna & Blackwell, 2004). Unlike volcanic and plutonic systems, non-magmatic geothermal plays generally produce lower-temperature fluids, making them more suitable for direct heat applications rather than electricity generation. However, in some cases, low-temperature geothermal electricity generation is possible, especially when enhanced geothermal systems (EGS) are employed.

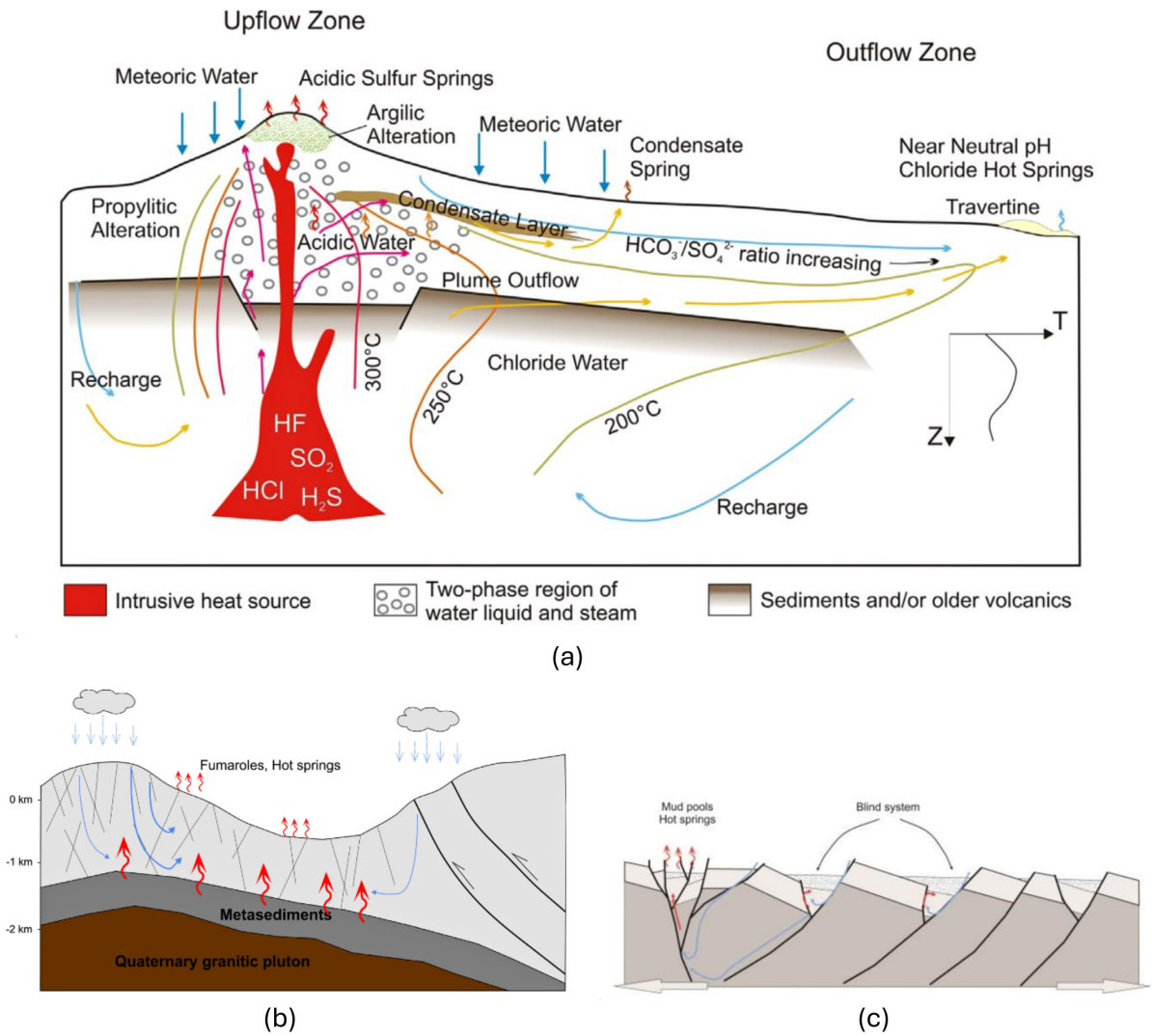

Figure 4.3: Conceptual model of (a) a magmatic – volcanic type, (b) a magmatic – plutonic type, and (c) a non-magmatic type of geothermal systems. Figures from Moeck (2013, 2014).

Intracratonic Basin Type

Intracratonic basins are large, stable sedimentary basins that form within continental interiors, often far from tectonic plate boundaries. These basins are characterized by thick sequences of sedimentary rocks that have accumulated over millions of years with minimal tectonic disturbance. Intracratonic basins are often found in regions with ancient cratonic shields, where the Earth's crust is thick and stable. Examples of these basins include the North Dakota Basin in the United States, the Williston Basin in Canada, and the Nort German Basin (Hartig, 2018; I. Moeck et al., 2009). The primary heat source in intracratonic basins is the natural geothermal gradient, which results from the slow conduction of heat from the Earth's interior through the sedimentary rock layers. While these basins generally exhibit lower geothermal gradients compared to volcanic regions, the thick sedimentary sequences can act as insulators, allowing heat to accumulate over time. Furthermore, the high porosity and permeability of some sedimentary rock layers can enhance the ability to store and transfer geothermal heat.

Orogenic Belt Type

Orogenic belts, also known as mountain belts, are regions of the Earth's crust that have been significantly deformed by tectonic processes such as the collision of continental plates. These regions are characterized by complex geological structures, including folded and faulted rock layers, as well as the presence of metamorphic and igneous rocks. Orogenic belts often contain large quantities of stored thermal energy due to the thickened crust and the thermal insulation provided by the overlying rock layers. The heat in orogenic belt geothermal systems is conducted through the thickened crust, which results from tectonic compression and uplift during mountain-building processes. These regions may contain significant geothermal potential, particularly in areas where deep crustal rocks are exposed to elevated temperatures. However, due to the complexity of the geological structures in orogenic belts, the development of geothermal resources can be challenging. Drilling and exploration require a detailed understanding of the subsurface geology to identify areas with sufficient heat and permeability. One example of geothermal potential in an orogenic belt is the Molasse Basin in Germany (Cacace et al., 2013).

Basement/Crystalline Rock Type

Basement or crystalline rock geothermal systems are found in areas where the Earth's crust is composed primarily of ancient, stable crystalline rocks, such as granite or gneiss. These rocks are typically found in the lower crust and are exposed at the surface in many stable continental regions, such as shield areas or regions with deeply eroded terrain. The heat in basement geothermal systems is derived from the natural

geothermal gradient, as well as from the decay of radioactive isotopes within the crystalline rock. These rocks, particularly granite, often contain significant amounts of uranium, thorium, and potassium, which generate heat through radioactive decay. This makes crystalline rock geothermal systems a potential source of long-term, sustainable heat. However, one of the main challenges with basement geothermal systems is the low permeability of crystalline rocks. Unlike sedimentary rocks, which often have natural porosity and permeability, crystalline rocks are typically impermeable and lack natural fluid pathways. To exploit these systems, enhanced geothermal systems (EGS) are often employed.

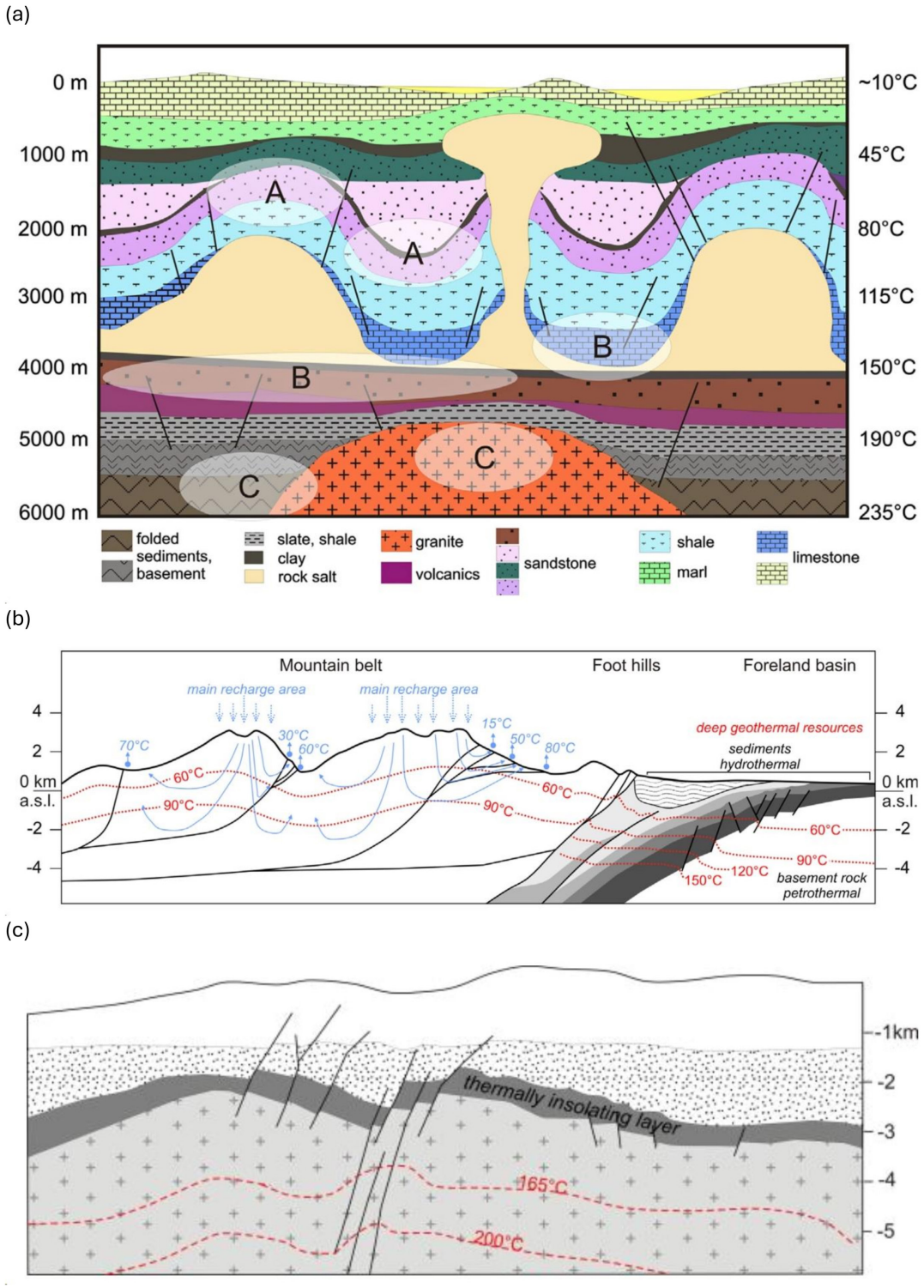

Figure 4.4: Conceptual model of (a) intracratonic basin type with different temperature ranges depending on the geothermal gradient, (b) orogenic belt type, and (c) basement/crystalline rock type of the conduction-dominated geothermal systems. Figures taken from Moeck (2013, 2014).

4.3 Geothermal Resources and Explorations in Saudi Arabia

The Kingdom of Saudi Arabia is located on the Arabian Plate, bordered to the west by the tectonically active Red Sea Rift. This rift marks a divergent boundary where the Arabian Plate is moving away from the African Plate, resulting in crustal thinning, elevated heat flow, and volcanic activity—favorable conditions for geothermal energy development. The western region of Saudi Arabia, particularly the volcanic fields of Harrat Rahat, Harrat Khaybar, and Harrat Lunayyir, has experienced recent volcanic activity, indicating the presence of potential heat sources from magmatic intrusions. In addition to volcanic features, several hot springs, such as those in Al-Lith and Jizan, provide surface evidence of geothermal activity, further supporting the potential for subsurface heat reservoirs. Figure 4.5 shows a geothermal favorability map developed as part of a geothermal resources database for Saudi Arabia (Aboud et al., 2021). This map highlights the western region as a particularly promising area for geothermal exploration. This area is characterized by shallow Curie depths, high heat flow, the presence of volcanic vents, and notable seismic activity. These factors underscore the necessity for further studies to facilitate geothermal exploration in these regions.

According to several research studies, e.g. Hussein et al. (2013), Lashin & Al Arifi (2014), Lashin et al. (2014), and Ashadi et al. (2024), among several regions in western Saudi Arabia, the Al-Lith area is considered as one of the most prominent sites of Saudi Arabia's geothermal resources, with the occurrence of four hot springs (see Table 4.3). The Ain Al-Harrah hot spring, one of the hot springs, was observed to have the highest temperature exceeding 96 °C, indicating the presence of well-seated geothermal reservoirs. It has become the main geothermal target in the region and may be used to provide clean power energy on a long-term basis. Although geothermal energy utilization for power generation is not yet economically viable, some direct-use applications of low-grade geothermal resources have already been implemented, such as the Hot Spring Park near the Ain Al-Harrah hot spring, featuring amenities such as steam baths and swimming pools, and recreational facilities like children's playgrounds, demonstrating the potential for geothermal resources to support local tourism and community services. Further exploration and feasibility studies are necessary to assess the full potential of the Al-Lith geothermal systems for power generation and to develop technologies that can make geothermal energy a more viable component of Saudi Arabia's renewable energy mix.

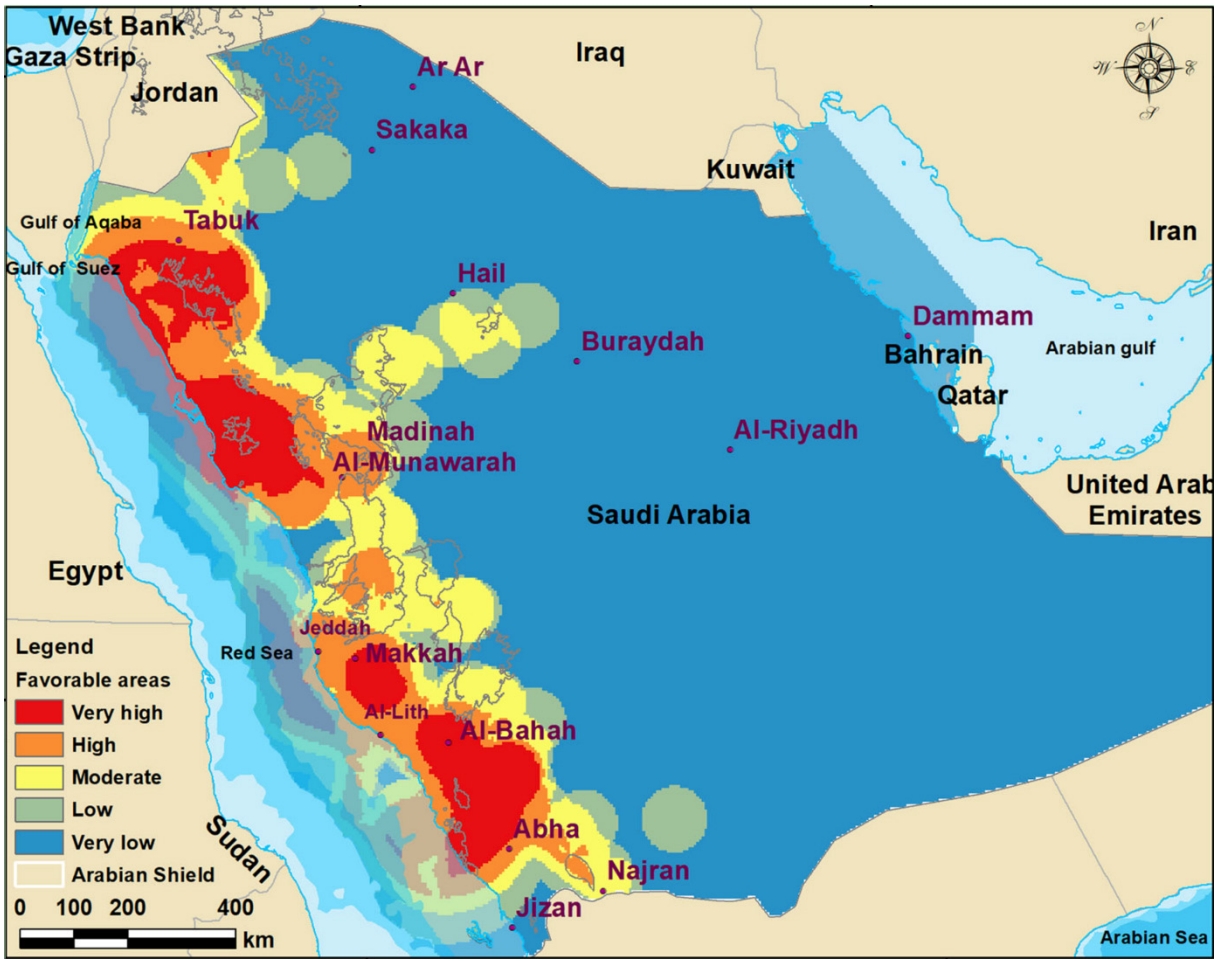

Figure 4.5: The map of geothermal potential favorability in Saudi Arabia. Figure taken from Aboud et al. (2021).

Table 4.3: Four hot springs in the Al-Lith area and their respective reported information.

Hot Spring	**Latitude**	**Longitude**	Lashin et al. (2020)		Al-Douri et al. (2019)		Lashin et al. (2012)	
			Reservoir Temp. (°C)	Surface Temp. (°C)	Surface Temp. (°C)	Flow rate (kg/s)	Discharge Enthalpy (Kj/Kg)	Heat Flow (nW/M^2)
Ain Al-Harrah	40.471 N	20.461 E	185	96	79	0.064–0.08	218.96	182.79
Bani Hilal	40.705 N	20.303 E	120	45	46	0.0048	193.74	159.63
Wadi Markub	40.156 N	20.528 E	120	56	46	0.0048	193.30	159.23
Al-Darakah	40.039 N	20.671 E	105	41	40	0.0016	169.21	136.93

Geothermal studies in the Al-Lith region began five decades ago. Stieltjes (1974) was the pioneer, conducting geochemical analysis on water samples from several hot springs

in Al-Lith and Jizan. The author found that the Al-Lith area has promising geothermal resources. Later, Al-Dayel (1988) reviewed the geothermal prospects not only in the hot springs of Al-Lith and Jizan, but also in the volcanic fields of Khaybar and Rahat, through geochemical analysis of water samples from the hot spring. Al-Dayel (1988) concluded that Al-Lith has a high temperature of circulated aquifer, exemplified by the 90 °C temperature at the Ain Al-Harrah hot spring. Khiyami et al. (2012) conducted a biodiversity analysis of the geothermal springs in Al-Lith and Jizan to study the water samples' physical and chemical analysis. Their findings suggested that all Al-Lith water samples exhibited low bacteria counts. Furthermore, the prominent bacteria identified in this area were similar to those found in other geothermal habitats worldwide.

Lashin et al. (2012) and later followed by Hussein et al. (2013) were the first to conduct limited shallow 2-D electrical resistivity tomography (ERT) surveys in Al-Lith, along with remote sensing and geochemical analysis. Their studies concluded that Al-Lith region, particularly the Ain Al-Harrah hot spring, is the most promising geothermal resources in Saudi Arabia. The region exhibits high surface temperatures of up to 96°C, reservoir temperature of more than 135 °C, good discharge enthalpy of more than 215 kJ/kg, and a high heat flow of 183 mW/m^2. The geothermal power potential was estimated to be 26.99 MWt which could support a medium scale power plant for the Al-Lith region.

Lashin et al. (2014) conducted more comprehensive geological and geochemical investigations on the hot springs in the same region. They estimated that the temperature of the geothermal reservoir exceeded 200 °C, circulating within granitic formations. These granites were estimated to produce 120 × 10^6 TWh electricity, with the power plant's operational lifespan exceeding 30 years. Subsequently, Lashin et al. (2015) presented preliminary results of the subsurface's structure, conducting MT and seismic reflection imaging studies at Ain Al-Harrah. Their findings suggested that the geothermal reservoir is categorized as shallow at a depth of 2.5 km, with complex fractures observed in the shallow layers. Further studies by Lashin et al. (2015), Al-Douri et al. (2019), Lashin et al. (2020), and Aboud et al. (2021) focused on consolidating and reviewing previous research findings, which collectively advanced the understanding of the geothermal potential in the Al-Lith region.

The most recent geothermal exploration in Al-Lith was conducted by Ashadi et al. (2024). They performed a high-quality MT survey along a 7.8 km profile crossing the main hot spring of Ain Al-Harrah in Al-Lith. This survey's 2D MT inversion results provided critical insights into the geothermal system (see Appendix A). They imaged the geothermal reservoir at depths below 800 m and identified heat sources below 3.5 km. Ashadi et al. (2024) suggested that Al-Lith's geothermal source can be classified

as a high-temperature volcanic-associated geothermal system. This classification is supported by the absence of a highly conductive clay cap in the 2D resistivity model, a feature typically associated with volcanic geothermal systems. However, the study acknowledged limitations in the 2D inversion results. The MT soundings were conducted along with the major geological strike, and dimensionality analysis indicated the presence of a 3D conductivity structure at longer periods. This suggests that a 3D inversion approach would be more appropriate for accurately characterizing the subsurface conductivity and provide a more detailed understanding of the geothermal system. Despite these limitations, the results were geologically significant, contributing valuable information for future geothermal exploration and guiding further investigations in the Al-Lith region.

Chapter 5

Field Survey and Geological Background

5.1 Geological Settings

Saudi Arabia's geological setting is complex due to its location at the intersection of the Arabian, African, and Eurasian tectonic plates, significantly influencing the region's geological features and geothermal potential. The western region is dominated by the Arabian Shield, a vast plateau primarily composed of metamorphic and igneous rocks. This shield is part of the Precambrian basement complex, which has been subjected to multiple tectonic events, leading to a rich and varied geological history. Wadi (valley) Al-Lith, located in the western part of Saudi Arabia, is a significant catchment area that exemplifies complexity. The region, situated along the western coast of the Red Sea, encompasses a diverse and dynamic landscape that spans from the coastal plains to the high mountains in the east (Hussein et al., 2013; Monged et al., 2018). The survey area is located in steep mountains with an altitude difference of approximately 600 m.

The geological history of Wadi Al-Lith spans from the Precambrian to the Quaternary periods, showcasing a diverse range of rock types and formations. The Precambrian rocks of the Arabian Shield in Wadi Al-Lith include granites, gneisses, and schists, which have been intruded by younger igneous bodies and significantly metamorphosed. Overlying these are sedimentary rocks from various ages, disrupted by faults and folds, reflecting the region's dynamic tectonic history. The Quaternary period saw the deposition of alluvial sediments, shaping the varied landscape of valleys, plateaus, and coastal plains.

The major rock units covering the Al-Lith catchment area are summarized from oldest to youngest as follows:

(a) Baish and Baha groups: The Baish group, classified as Ablah intrusive, is exposed in the southern part of the basin (Figure 5.1) and includes gabbro, tonalite, quartz diorite, granodiorite and monzodiorite. These rocks are characterized by hornblende-rich basic varieties and felsic members enrich with biotite, potash feldspars, and large pyrite crystals (Fleck et al., 1976). It has been suggested by Hussein et al. (2013) that rocks from the undivided Baish

and Bahah groups, such as basalt, amphibolite, and dacite, crop out in the eastern part of the Al-Lith basin, covering approximately 23% of the area.

(b) Lith Suite and Equivalents: This suite, a prominent rock unit in the Al-Lith catchment including the Khasrah complex, diorite, and gabbro, is composed primarily of mafic and metavolcanic rocks, intruded by various plutonic rocks. It forms an extensive NE-trending belt across the western part of the basin, covering more than 35% of the area.

(c) Tectonic Granitic Rocks: The less prominent Proterozoic intrusive rocks, including plutons, dikes, and ring dikes, are prevalent throughout of the basin and extend along the entire western margin of the Arabian Shield from Midyan to Jizan (Lashin et al., 2014). It has been estimated by Hussein et al. (2013) that these intrusive rocks cover about 13% of the basin area.

(d) Quaternary Formation: Sand, gravel, silt, and sabkhah deposits (Figure 5.1) represent 18% of the Al-Lith area (Hussein et al., 2013; Lashin et al., 2014). These deposits are characterized by horizontal bedding and are poorly consolidated, typically averaging around 2 km in thickness, though they rarely exceed 10 m (Pallister, 1986).

(e) Other Rock Units: These units constitute about 9% of the basin in the study area and include various rock types, such as metagabbro, gabbro dikes, granodiorite, syntectonic granitic rock, and some granite (Hussein et al., 2013). Numerous gabbro dikes are present in the northwest Al-Lith, aligning parallel to the Red Sea axis and associated with Red Sea tectonism. These younger dikes have K–Ar ages of approximately 19–27 Ma (Bosworth et al., 2005).

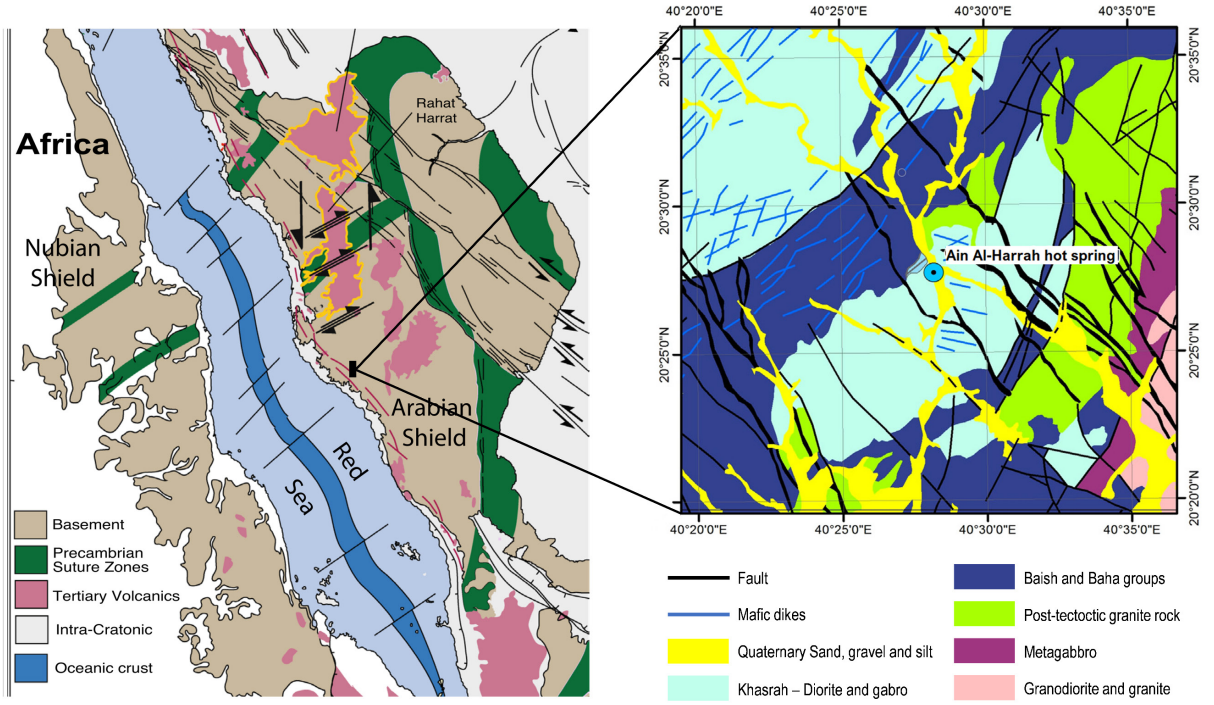

Figure 5.1: Geological map of the Al-Lith area showing the different rock units and geological features present in the region (modified from Hussein et al. (2013) and Aldaajani & Furlong (2022)).

5.2 Data Acquisition

The geothermal exploration in Al-Lith, western Saudi Arabia, was performed in two stages of field campaigns: the first stage was carried out in May 2022 and the second stage was from December 2022 to January 2023. During the first stage, a couple of MT measurement tests and 15 real MT soundings were measured, with 13 sounding of them are oriented along a North–South transect inside a valley filled with quaternary fluvial deposits and partly water flooded crossing the hot springs. Toward both sides of the valley, steep mountains are present with an altitude difference of approximately 600 m. A 2-D resistivity section was produced from the first stage of MT measurement and successfully imaged the main geothermal features, such as the heat source, the fracture zone and its role in the convection pattern, and the groundwater system as part of the Ain Al-Harrah geothermal system (Ashadi et al., 2024). The 2D geo-electrical model can be seen in Appendix A (Appendix Figure A-2).

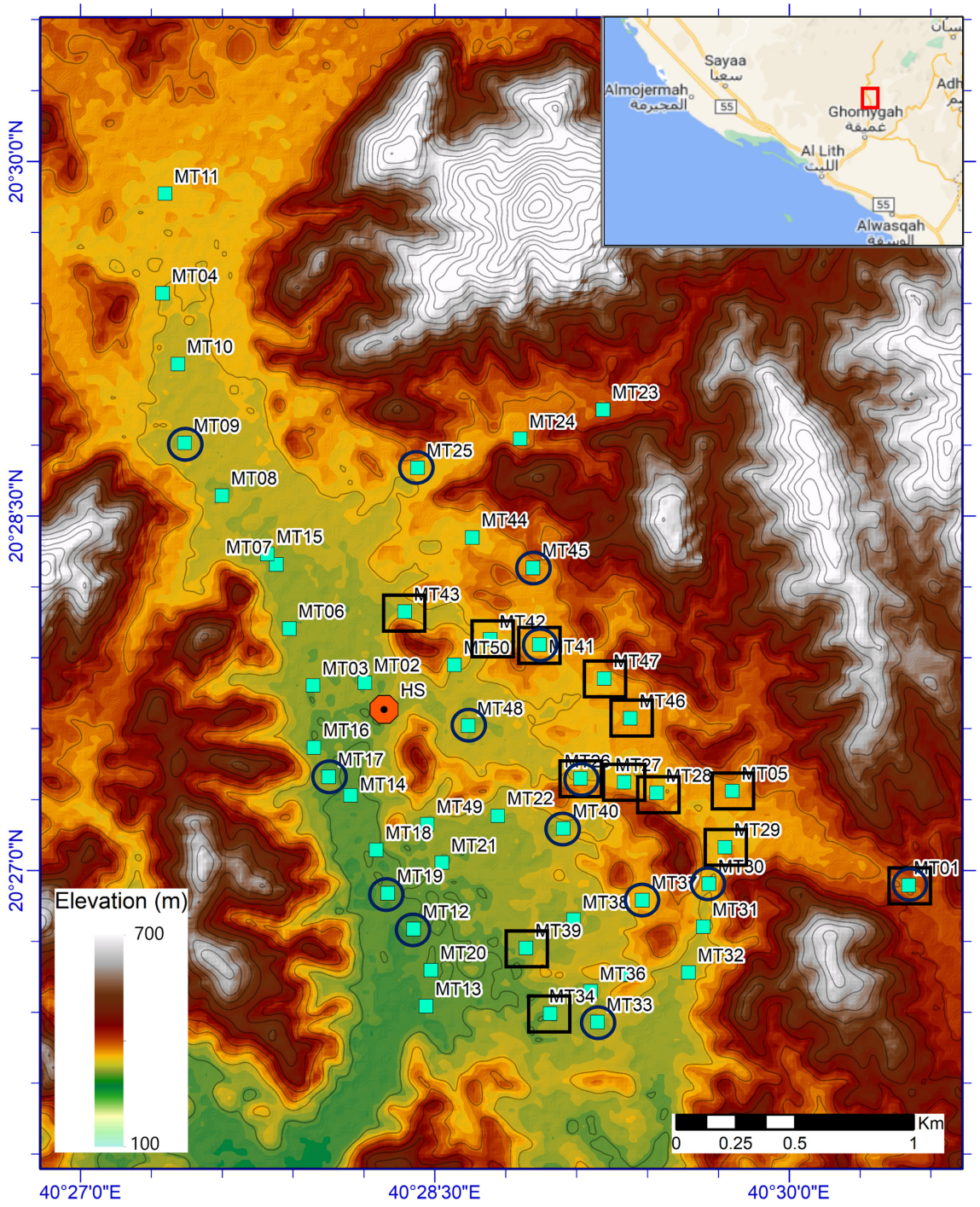

Figure 5.2: Topographic map of the study area showing the locations of all 50 MT soundings (green squares). The blue circle indicates the 14 MT sites where the vertical magnetic field component was measured. The black squares represent the location of the TEM soundings. The red octagon marks the location of the Ain Al-Harrah hot spring.

Following the 2-D result, the second stage of the field survey was carried out, with 35 MT stations and 13 TEM soundings measured in order to generate a 3-D resistivity model that would be more appropriate for accurately characterizing the subsurface conductivity. In total, there are 50 MT, and 13 TEM soundings measured in the study

area. The coordinates of the soundings are listed in Appendix B (Table B-1). The average spacing between neighboring MT stations was approximately 400 m, ensuring adequate spatial resolution for the survey. Due to logistical constraints and the challenging terrain of the study area, the magnetic field vertical component was only measured at 14 sites. The distribution of MT stations was strategically planned considering the proximity to the Ain Al-Harrah hot spring and the conductive anomaly identified by Ashadi et al. (2024). Figure 5.2 shows the topographic map depicting the distribution of all measured MT and TEM sites.

5.2.1. MT Measurements

The 50 broad-band MT soundings were conducted over the period range of 0.001-512 s around the main hot spring in Al-Lith. The MT data were collected using KMS-820 acquisition system (kmstechnologies.com) along with two or three low frequency induction coils (LEMI-120) and four non-polarizable electrodes (LEMI-701) with horizontal dipoles lengths varied from 40 to 100 m, depending on site-specific conditions/obstacles (Fig. 5.3). The recording duration at each MT station ranged from 6 to 8 hours, with data sampled at three different frequencies (4 kHz, 1 kHz, and 40 Hz). The detailed duration for each sampling frequency is listed in Table 5.1. To ensure high-quality data, we measured the ground resistances before and after each MT measurement to maintain good electrode contact and improve the signal-to-noise ratio in the electric field recordings (Ashadi et al., 2022, 2024). All induction coils were carefully oriented, leveled, and buried to minimize environmental noise and ensure accurate measurements. The cables used to connect the sensors to the acquisition system were also buried to minimize the recorded noise during the acquisition. In addition, wet bentonite was used in each electrode to lower the ground resistance, as advocated by some MT practitioners. The distribution of MT stations was strategically planned considering the proximity to the Ain Al-Harrah hot spring and the conductive anomaly identified by Ashadi et al. (2024).

Table 5.1: Sequence task index used during MT acquisitions. The duration of each sampling frequency is determined.

Task Index	Sampling Frequency	Duration
0	4 kHz	00:26:15
1	1 kHz	01:44:55
2	40 Hz	08:00:00 (max)

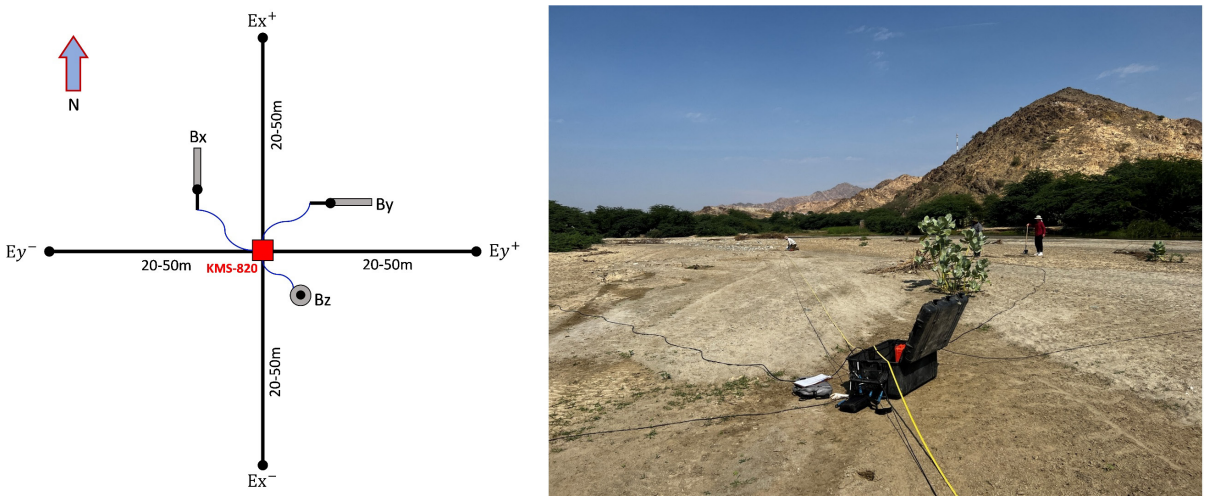

Figure 5.3: MT scheme layout used in this study, with three induction coils and two pairs of electrodes (left), and a picture of the MT deployment and installation on the field (right).

5.2.2. TEM measurements

The TEM data acquired using the ABEM WalkTEM time-domain ground EM system took place in January 2023 during the winter season. A total of 13 TEM soundings were conducted using a central-loop configuration. Each sounding employed a 40x40 m2 transmitter loop with an inner RC-5 receiver antenna. The soundings were placed in various geological settings to ensure reasonable wide spatial coverage, despite logistical constraints that prevented a more extensive survey. Each measurement utilizes a dual-moment script with a maximum time (t_{max}) of 10 ms and 32 gates to capture a broad range of subsurface responses. In addition to the noise measurement, the WalkTEM system operated in dual acquisition modes to enhance data quality and depth penetration:

- Low Moment (LM): Used for acquiring early-time data, this mode captures signals from shallow subsurface layers.
- High Moment (HM): Used for recording late-time data, this mode is capable of imaging deeper subsurface structures.

To further improve data quality, a 200 Ω damping resistor was connected in parallel with the transmitter loop during each measurement. This configuration helped to prevent rapid signal decay caused by less resistivity near the surface. The dual-moment acquisition allowed for a comprehensive analysis of the subsurface, with early-time data providing detailed information about shallow layers and late-time data offering insights into deeper geological formations.

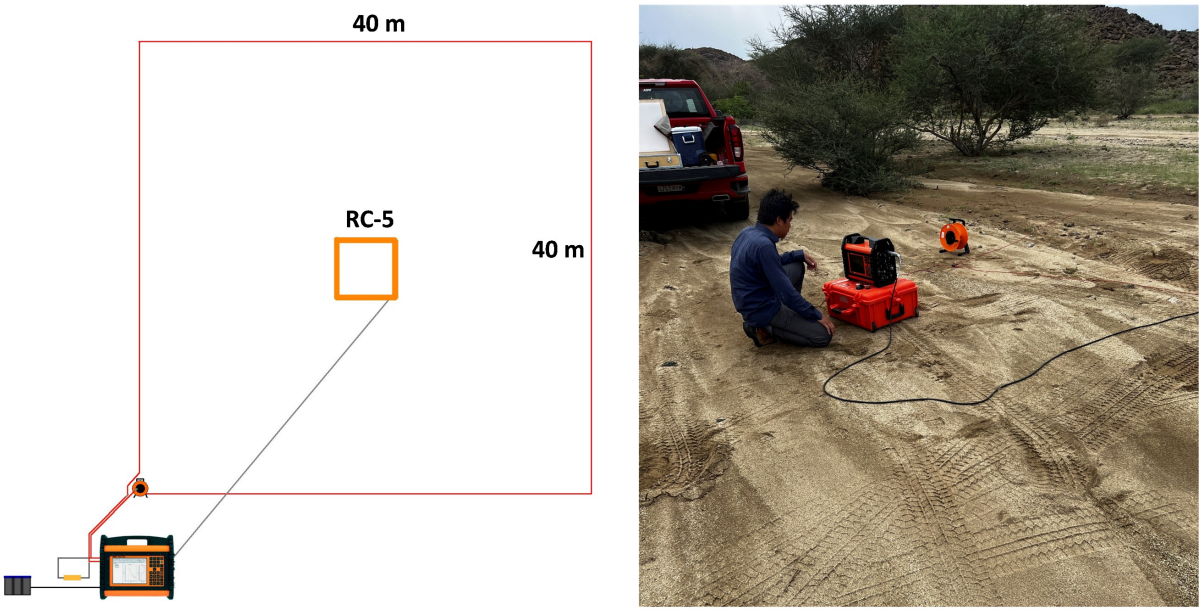

Figure 5.4: Scheme layout using a central loop TEM configuration, with a 40 X 40 m^2 transmitter and an RC-5 receiver loop (left), and a picture of the TEM installation on the field (right).

Chapter 6

Data Processing and Analysis

This chapter deals with the field data processing and analysis. First, all the steps applied to MT data in order to estimate the transfer functions are explained. A detailed explanation of the used robust processing scheme is given. Regarding the TEM data, all the procedures applied before the subsequent 1D inversion are described in this chapter. Finally, the dimensionality analysis and static shift effect of the MT data is discussed.

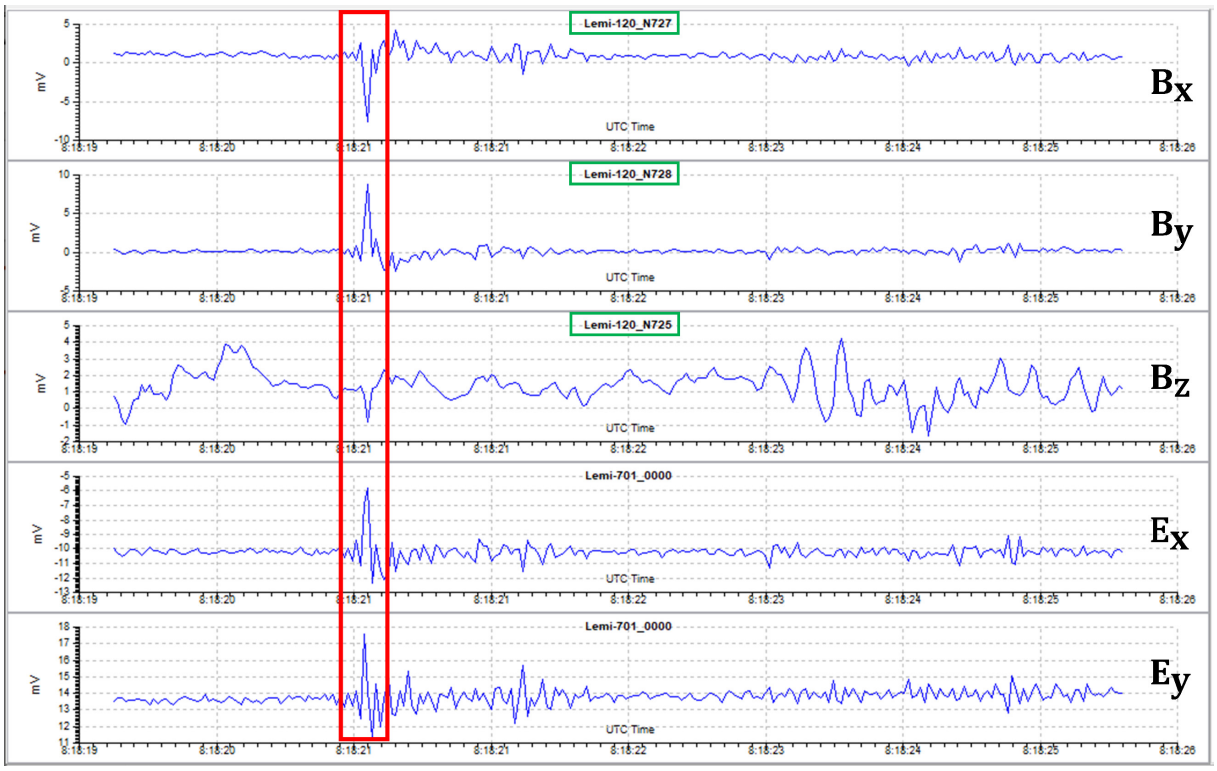

Figure 6.1: Example of unfiltered time series recorded at MT09 highlighting the correlation between B_y and E_x components and the anti-correlation between B_x and E_y. The sensor model and the serial number of each induction coil, which is related to the calibration factors, are also visible.

6.1 MT Data Processing

To estimate the MT transfer functions, including impedances and tippers, the measured MT data were processed using a robust statistical technique developed by Smirnov (2003). This technique employs a robust regression proposed by Siegel (1982), which

utilizes a repeated median algorithm with a high breakdown point of 50%. In addition to the robust regression technique, a notch filter was applied during data processing to eliminate narrow frequency bands of interference, such as the 60 Hz noise from power lines, while leaving the remaining spectrum unchanged. Before data processing, pre-processing steps, including data quality assurance and quality control, were performed. Any potential data loss due to possible field acquisition errors can be prevented. Spectrum and coherency analysis were also conducted in this stage. Figure 6.1 shows the time series of MT data at station MT09 for the sampling frequency of 40 Hz, highlighting the correlation between B_y and E_x components and the anti-correlation between B_x and E_y. The sensor model and the serial number of each induction coil are also visible, which is related to the calibration factors.

In the processing, I distinguished between high frequency (HF) with sampling rates of 4 kHz and 1 kHz, and low frequency (LF) with sampling rates of 40 Hz. The high frequency bands are contaminated by cultural periodic noise, such as 60 Hz powerline noise and its higher harmonics. Figure 6.2 shows the spectra of the observed MT data at station MT01 for the sampling frequency of 4 kHz as an example. Notable spikes indicate the presence of 60 Hz noise and their harmonics generated by power lines, along with Schumann resonances characterized by a base frequency of 7.8 Hz and their harmonics. These significant anthropogenic noise sources are subsequently removed during data processing by applying digital filters (e.g. notch filter). A Fast Fourier Transform (FFT) window length of 65,536 samples was used to handle both sampling frequency rates of 4 kHz and 1 kHz. For the low frequency (LF) range, with sampling rates of 40 Hz which fall below power line noise, a cascade decimation processing method was employed using short FFT windows of 16, 32, and 64 samples. The decimation step involves low-pass filtering of the time-series with a recursive filter. After the Fourier transformation, a correction by the instrument calibration factor is done (Ashadi et al., 2024; Smirnov, 2003; Wight & Bostick, 1980).

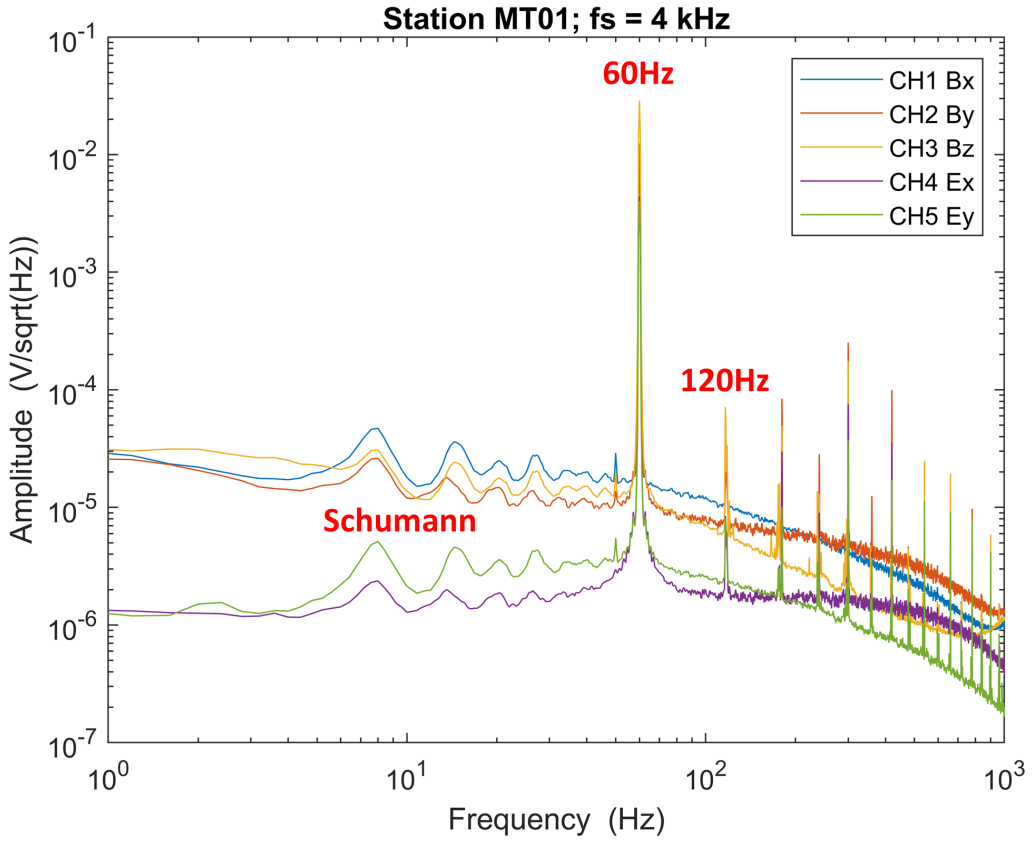

Figure 6.2: Example of spectrum visualization from sounding MT01with sampling frequencies of 4 kHz. The Schumann resonances and the periodic noise of 60 Hz due to the power line can be distinguished.

The processing steps applied to the MT field data are summarized as follows (Ashadi et al., 2024; Smirnov, 2003):

1. Data quality assurance process was done using KMS-820 Acquisition software (kmstechnologies.com) to prevent potential data loss due to possible field acquisition errors. It includes visual inspection of the raw time-series to ensure that all channels were properly recorded.

2. Data quality control is then performed to check the quality of the raw data, conduct spectrum analysis, and examine the coherency in order to evaluate the relationship between orthogonal and parallel fields.

3. Impedance tensor estimations were carried out using KMSProMT program (kmstechnologies.com), employing the robust statistical technique introduced by Smirnov (2003). In practice, the impedance estimation steps can be summarized as follows:
    1) The recorded time series are subdivided into sets of segments

2) An autoregressive (AR) model is used to eliminate and remove obvious outliers and fill short gaps in the time domain before the main processing steps
3) Multiplying each segment with a Hanning window function in order to reduce the bias of spectral estimation
4) Decimation step involving low-pass filtering of the time-series with a recursive filter is applied
5) Fourier transformation is carried out into the segments.
6) A coherence threshold is used to remove highly noisy segments
7) Calculation of auto- and cross-spectral densities
8) Estimation of the MT transfer functions and their errors.

4. The data sampled at low (40 Hz), and high (1 kHz and 4 kHz) frequencies were processed separately with distinct parameter settings.

5. Finally, the multiple impedance tensor results are further processed using KMSProTF to apply robust averaging, plotting, and extraction of the final transfer function data. At this stage, all available partial estimates for a particular site are averaged together (including different frequency bands and possibly from different instruments) to produce the final estimation. Averaging is performed with a robust M-estimator and following bootstrap confidence limits. In this thesis, all MT transfer functions are estimated to have 7 frequencies per decade with a smoothing factor of 2.

6.1.1 Robust MT Processing Theory

As mentioned previously, the MT data field was processed using KMSProMT software, a new advanced robust MT processing algorithm after Smirnov (2003). This technique utilizes a robust scheme proposed by Siegel (1982), which its calculations are based on a repeated median algorithm with a high breakdown point of 50%. This implies that nearly half of the data could be outliers, yet the solution will still produce a reasonable result, demonstrating its effectiveness in handling datasets with a significant amount of noise. Smirnov (2003) has successfully tested this on both noise-free and highly noisy MT field data. The results demonstrate enhanced stability and reduce average misfit across all data components, regardless of the noise levels present in the field data.

Previously, robust MT processing commonly employed an *M*-estimator (Huber, 2011), which has lower breakdown points approaching 30% (Hampel et al., 1986). However, *M*-estimators are much less sensitive to outliers than standard Least-Square estimators

(Chave, 2012, 2017; Chave & Thomson, 2004). It is well known that the breakdown point of the Least Squares estimation is zero, indicating that even a small amount of noise can strongly influence the final estimate. First, a brief explanation of Siegel's estimator is given. Then, how the transfer functions were estimated is explained.

Siegel's Repeated Median Estimator

Siegel's repeated median estimator is a robust statistical method particularly useful for regression in scenarios with a high level of outliers, which can be described as follows. First, a simple linear regression model can be written as

$$y_i = \Theta_1 + \Theta_2 x_i + e_i, \quad i = 1, \dots, M, \tag{6.1}$$

where y_i represents the predicted value for the ith observation of a p-dimensional vector x_i, while e_i denotes the prediction error for that observation. The symbol Θ signifies the p-dimensional vector of unknown regression parameters that need to be estimated. Siegel's repeated median estimator for a set of n-observations denoted as $(x_i, y_i), \dots, (x_{in}, y_{in})$, is defined as follows. The jth component of Θ, referred to as $T^{(j)}$, is:

$$T_n^{(j)} = \underset{i_1}{\text{med}} \left\{ \dots \left\{ \underset{i_{p-1}}{\text{med}} \left\{ \underset{i_p}{\text{med}} \left\{ \Theta^{(j)}(i_1, \dots, i_p) \right\} \right\} \right\} \dots \right\} \tag{6.2}$$

where the median is taken over all indices $i_m = 1, \dots, n$.

For each point (x_i, y_i), the median Θ_{2i} is defined as the median of the $n-1$ slopes of the lines connecting this point to every other point in the set. The repeated median slope estimate Θ_2^* is then determined as the median of the multiset (Θ_{2i}):

$$\Theta_2^* = \underset{i_1}{\text{med}} \underset{j \neq i}{\text{med}} \frac{y_i - y_j}{x_i - x_j} \tag{6.3}$$

To ensure the robustness of outliers, the intercept Θ_1 can be estimated either separately from Θ_2, as

$$\Theta_1^* = \underset{i}{\text{med}} \underset{j \neq i}{\text{med}} \frac{y_i x_j - y_j x_i}{x_j - x_i} \tag{6.4}$$

or hierarchically, as

$$\Theta_1^* = \underset{i}{\text{med}} \{ y_i - \Theta_1^* x_i \} \tag{6.5}$$

In the bivariate linear regression model used to solve the impedance linear system, we have the equation:

$$y_1 = \Theta_1 x_{1i} + \Theta_2 x_{2i} + e_i \tag{6.6}$$

where $p = 2$. The repeated median estimate is computed in a similar way. When the unknown parameter is represented as a complex vector, the equation is split into two independent equations for the real and imaginary parts, which are then solved separately. The components of the vector parameter Θ are estimated individually; for instance, for Θ_1, we have:

$$\Theta_1^* = \underset{i}{\text{med}}\ \underset{j \neq i}{\text{med}} \frac{y_i x_{2j} - y_j x_{2i}}{x_{1i} x_{2j} - x_{1j} x_{2i}} \tag{6.7}$$

Specifically, for each ith observation, the median of combinations with all j observations are first calculated. And then the overall median of these $n - 1$ medians form the final estimation.

Spectral Transformation

We begin by transforming the raw time series data in the time domain into the spectra in the frequency domain. Time-series for the horizontal electromagnetic components are represented as e_x, e_y, h_x, h_y and their corresponding Fourier transforms denoted as E_x, E_y, H_x, H_y, respectively. The linear relations to be evaluated are

$$\begin{pmatrix} \boldsymbol{E}_x \\ \boldsymbol{E}_y \end{pmatrix} = \begin{bmatrix} \boldsymbol{Z}_{xx} & \boldsymbol{Z}_{xy} \\ \boldsymbol{Z}_{yx} & \boldsymbol{Z}_{yy} \end{bmatrix} \begin{pmatrix} \boldsymbol{H}_x \\ \boldsymbol{H}_y \end{pmatrix} \tag{6.7}$$

where $\begin{bmatrix} \boldsymbol{Z}_{xx} & \boldsymbol{Z}_{xy} \\ \boldsymbol{Z}_{yx} & \boldsymbol{Z}_{yy} \end{bmatrix}$ represents the impedance tensor ($\boldsymbol{Z}$).

The original time series is subdivided into sets of segments to perform the spectral analysis. The decimation process involves low-pass filtering of the time series using a recursive filter, followed by a factor decimation of 2. Depending on the number of available data points, the degree of overlapping can vary from 0 to 50 percent.

Using $i = 0, 1, \ldots, N - 1$ as the time index within a segment, we removed the long period trends and means by applying a first difference filter. This process, in the case of e_x, generate new series $\bar{e}_x[i] = e_x[i] - e_x[i-1]$. To minimize the bias in spectral estimation, each segment is also tapered using a Hanning window, yielding

$$\tilde{e}_x[i] = \bar{e}_x[i] h[i];\ h[i] = \frac{1}{2}\left(1 - cos\frac{2\pi i}{N-1}\right) \tag{6.8}$$

A Fourier transform of $\tilde{e}_x[i]$ is then performed, yielding the Fourier coefficients $E_x[j]$, where $j = 1, 2, \ldots, \frac{N}{2}$ represents the frequency index. The Fourier transforms X, Y, and Z denote any of the field components, are combined into non-smoothed auto and cross-spectral values:

$$S_{XY}^n[j] = \frac{1}{N} X^*[j] Y^*[j] \tag{6.9}$$

where X^* and Y^* are the complex conjugate of X and Y, respectively.

Subsequently, coherence sorting is employed to eliminate segments with a high level of noise from further processing. Coherence values range from 0 to 1, with an ideal coherence equal to one. Accordingly, a coherence threshold (*e.g.* 0.8) is established, and thus, all events that do not meet this threshold are discarded. Criteria are the two partial coherences that refer to the orthogonal electric and magnetic components:

$$Co^2_{E_xH_y \cdot H_x} = \frac{\left|S_{E_xH_y \cdot H_x}\right|^2}{S_{E_xE_x \cdot H_x} S_{H_yH_y \cdot H_x}} \tag{6.10}$$

$$Co^2_{E_yH_x \cdot H_y} = \frac{\left|S_{E_yH_x \cdot H_y}\right|^2}{S_{E_yE_y.H_y} S_{H_xH_x.H_y}} \tag{6.11}$$

where $S_{XY \cdot Z} = S_{XY} - \frac{S_{ZY} S_{XZ}}{S_{ZZ}}$. Figure 6.3 plots the coherence values for station MT08 with 1 kHz sampling rate as an example.

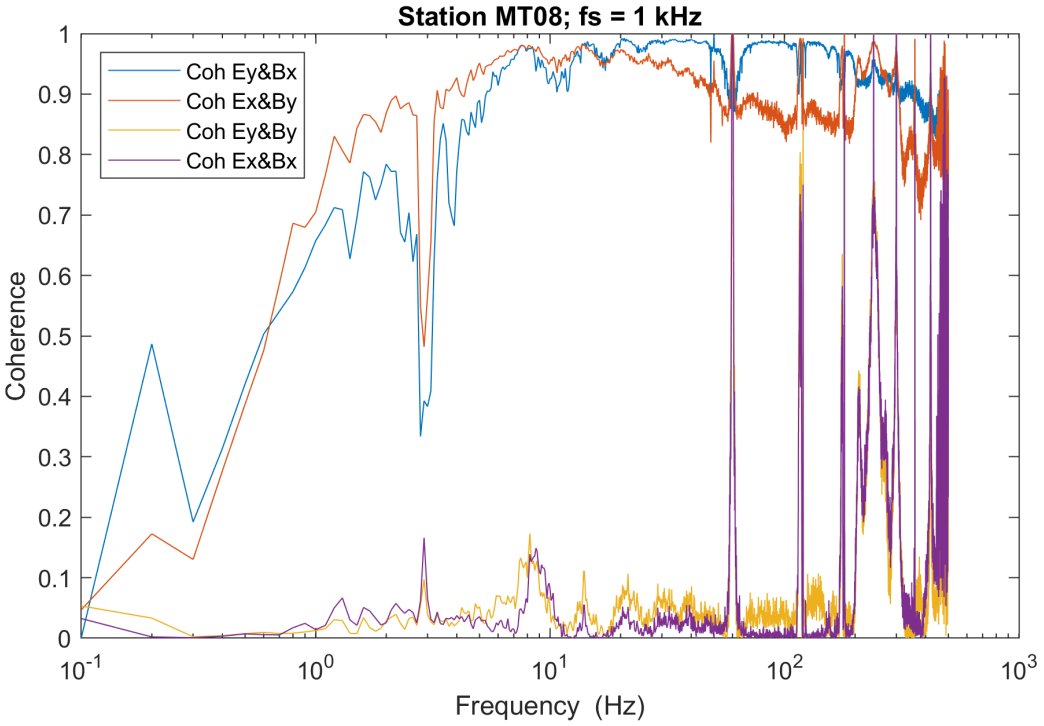

Figure 6.3: Coherence values for MT08 with 1 kHz sampling rate to evaluate the relationship between orthogonal and parallel E and B-field components.

As a result of this spectral transformation step, we now have *M non-smoothed* auto- and cross-spectral values from a selected set of segments for each frequency, which can be denoted as $S^n_{E_xH_xi}$, $S^n_{E_xH_yi}$, $S^n_{E_yH_xi}$, $S^n_{E_yH_yi}$, $S^n_{H_xH_yi}$, $S^n_{E_xE_xi}$, $S^n_{E_yE_yi}$, $S^n_{H_xH_xi}$, and $S^n_{H_yH_yi}$, with $i = 0, 1, \ldots, M$.

Estimation of Transfer Functions

To adapt Siegel's concept of robust estimator to the MT problem, the original system of equations 6.7 is rewritten in terms of auto- and cross-spectral densities:

$$\begin{aligned} S_{E_xH_x} &= \boldsymbol{Z}_{xx}S_{H_xH_x} + \boldsymbol{Z}_{xy}S_{H_yH_x} \\ S_{E_xH_y} &= \boldsymbol{Z}_{xx}S_{H_xH_y} + \boldsymbol{Z}_{xy}S_{H_yH_y} \end{aligned} \tag{6.12}$$

$$\begin{aligned} S_{E_yH_x} &= \boldsymbol{Z}_{yx}S_{H_xH_x} + \boldsymbol{Z}_{yy}S_{H_yH_x} \\ S_{E_yH_y} &= \boldsymbol{Z}_{yx}S_{H_xH_y} + \boldsymbol{Z}_{yy}S_{H_yH_y} \end{aligned} \tag{6.13}$$

where S_{XY} denotes smoothed spectral densities. For example, in the case of Z_{xy}, the impedance tensor can be estimated as follows:

$$Z_{xy} = \frac{S_{E_xH_y}S_{H_xH_x} - S_{E_xH_x}S_{H_xH_y}}{S_{H_xH_x}S_{H_yH_y} - S_{H_xH_y}S_{H_yH_x}} \tag{6.14}$$

The repeated median estimator can be derived considering the estimates of the impedance tensor components from the two systems, equations 6.12 and 6.13, which are unequivocally defined by the two independent realizations of spectral values.

The Siegel estimator for the spectral densities of the real part of the Z_{xy} component is expressed by the following equation:

$$Re\left[Z_{xy}\right]_S = \underset{i}{\text{med}}\ \underset{j\neq i}{\text{med}}\ Re\left[\frac{S_{E_xH_y\,ij}S_{H_xH_x\,ij} - S_{E_xH_x\,ij}S_{H_xH_y\,ij}}{S_{H_xH_x\,ij}S_{H_yH_y\,ij} - S_{H_xH_y\,ij}S_{H_yH_x\,ij}}\right] \tag{6.15}$$

where the indices $i,j = 1,\ldots,M$. The imaginary part is separately estimated in an analogous manner. And the first median operator of equation 6.15 is given by

$$Re\left[Z_{xy}\right]_i^M = \underset{j\neq i}{\text{med}}\ Re\left[\frac{S_{E_xH_y\,ij}S_{H_xH_x\,ij} - S_{E_xH_x\,ij}S_{H_xH_y\,ij}}{S_{H_xH_x\,ij}S_{H_yH_y\,ij} - S_{H_xH_y\,ij}S_{H_yH_x\,ij}}\right] \tag{6.16}$$

where the median is taken over all $M - 1$ values of j.

As an option, unrealistic partial estimates $\left[Z_{xy}\right]_i^M$ can be excluded by using the phase of the off-diagonal impedance elements as criteria, since these phases should lie within the limits. For 1D and 2D structures and in the free-noise, the phases of the Z_{xy} component should be in the first quadrant, *i.e.* $0° < arg\left(Z_{xy}\right) < 90°$, while the phases of Z_{yx} in the third quadrant, *i.e.* $180° < arg\left(Z_{xy}\right) < 270°$ (Weidelt & Kaikkonen, 1994). If the estimate Z_{xy} (or Z_{yx}) is excluded, then the respective estimate Z_{xx} (or Z_{yy}) is also excluded. There are instances where the phase may appear in a different quadrant, particularly when the original time series data is significantly affected by noise (Chouteau & Tournerie, 2000), due to 3D conductive bodies (Ichihara & Mogi,

2009; Piña-Varas & Dentith, 2018; Thiel et al., 2009), electrical anisotropy (Heise & Pous, 2003) or galvanic distortion (Lilley & Weaver, 2010).

This robust MT data processing method has been evaluated using both 'noise-free' and 'noisy' MT data. The results for the 'noise-free' site demonstrate good agreement between both the least squares (LS) and robust techniques, with consistent alignment across the entire period range. The advantages of this algorithm become particularly evident when processing data from a 'noisy' site, which was contaminated by significant noise levels. Coherence sorting greatly enhanced data quality, and a subsequent robust procedure effectively eliminated most of the residual noise, ultimately resulting in a realistic estimate of the impedance tensor (Smirnov, 2003).

6.1.2 MT Transfer Functions

Results of the robust processing scheme as impedance tensor elements are shown in Figure 6.4 to illustrate the data quality. Apparent resistivity and phase curves of the off-diagonal impedance tensor elements are displayed. The individual transfer functions of each MT station are shown in Appendix C. The MT transfer functions are observed smoothly and consistently. The apparent resistivity values range between 25 Ωm and 2000 Ωm. It is evident that both apparent resistivity and phase curves exhibit scattering, which may be attributed to near surface inhomogeneities, target anomalies, or topographic effects. These phenomena, known as galvanic distortions, are generally considered to have a weak impact on the MT phase. However, significant scattering is observed in the phase data, which, although uncertain, is possibly related to large-scale geological structures with strong conductivity contrasts or topographic influences (Jiracek, 1990).

To facilitate a quick analysis of the spatial pattern in the observed MT data, color-coded maps of the apparent resistivity and the phase for the XY components of the impedance tensors are presented in Figures 6.5 and 6.6, respectively. In Figure 6.5, the apparent resistivity maps reveal a conductive anomaly expected to be visible at shallow depth (at 0.004 s). This anomaly appears to enlarge at intermediate depths (from 0.25 s to 2 s) before diminishing in size at greater depths (at 16 s). Figure 6.6 presents the phase maps, which indicate the general subsurface structure is more resistive at shallow depths (at 0.004 s), except in areas where conductive anomaly is indicated in Figure 6.5. At intermediate depths (at 0.25 s to 2 s), the subsurface becomes less resistive, while at deeper depths (at 16 s), the resistivity increases again. This resistivity pattern aligns with the expectation of varying geological structures and conductivity contrasts at different depths.

The geomagnetic transfer function (tipper) responses for 14 of the 50 MT sites are displayed as induction arrows in Figure 6.7. The Parkinson convention (Parkinson,

1959) is used in this study to represent the induction arrows, which point towards more conductive zones. At short periods of 0.088 and 0.353 s, the induction arrows show a substantial alignment with the fault direction indicated in Figure 5.1, as they are orthogonal to it. The vectors for these short periods indicate a possible NW-SE-oriented conductive region, aligning with the geological structure and fault direction. As the period increases (T $\geq$ 2), the direction of most induction vectors shifts towards the southwest.

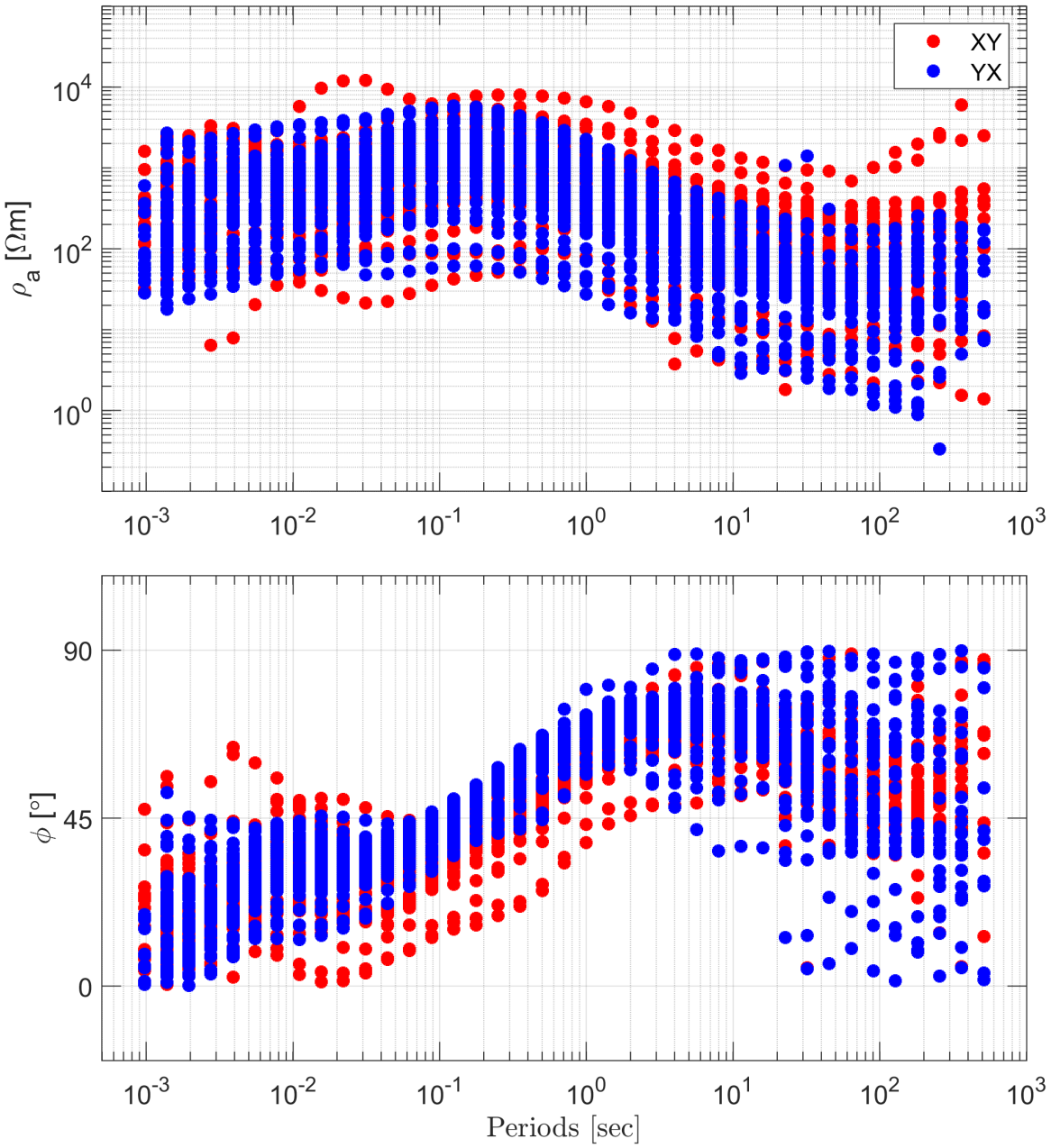

Figure 6.4: Cloud plot showing apparent resistivity (top) and phase (bottom) for all MT sites. The phase values have been adjusted to the [0°, 90°] quadrant. Red dots represent XY elements, and blue dots represent YX elements.

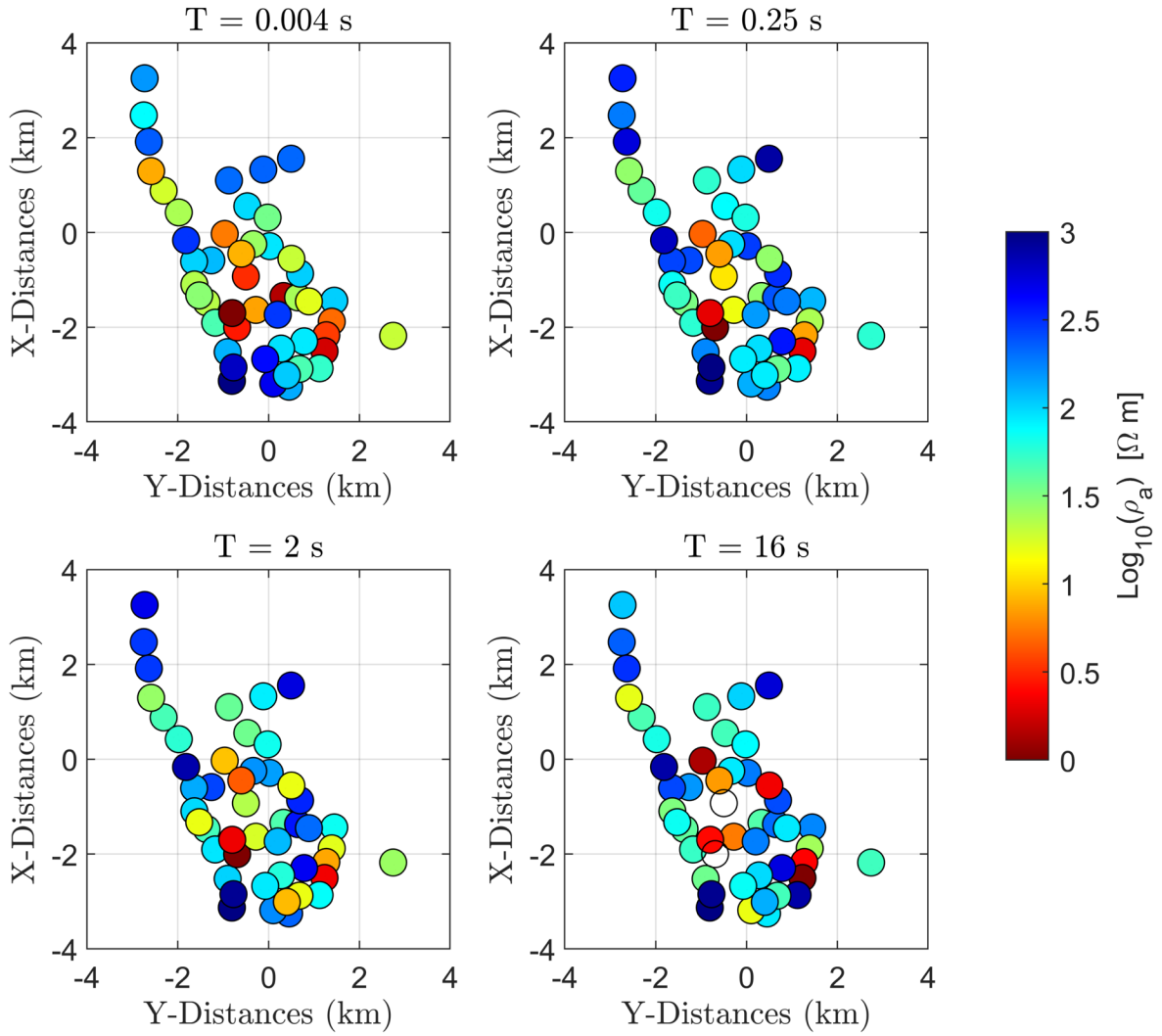

Figure 6.5: Spatial distribution of apparent resistivities for the XY components at four different periods: 0.004 s, 0.25 s, 2 s, and 16 s. White circles indicate locations where data is unavailable.

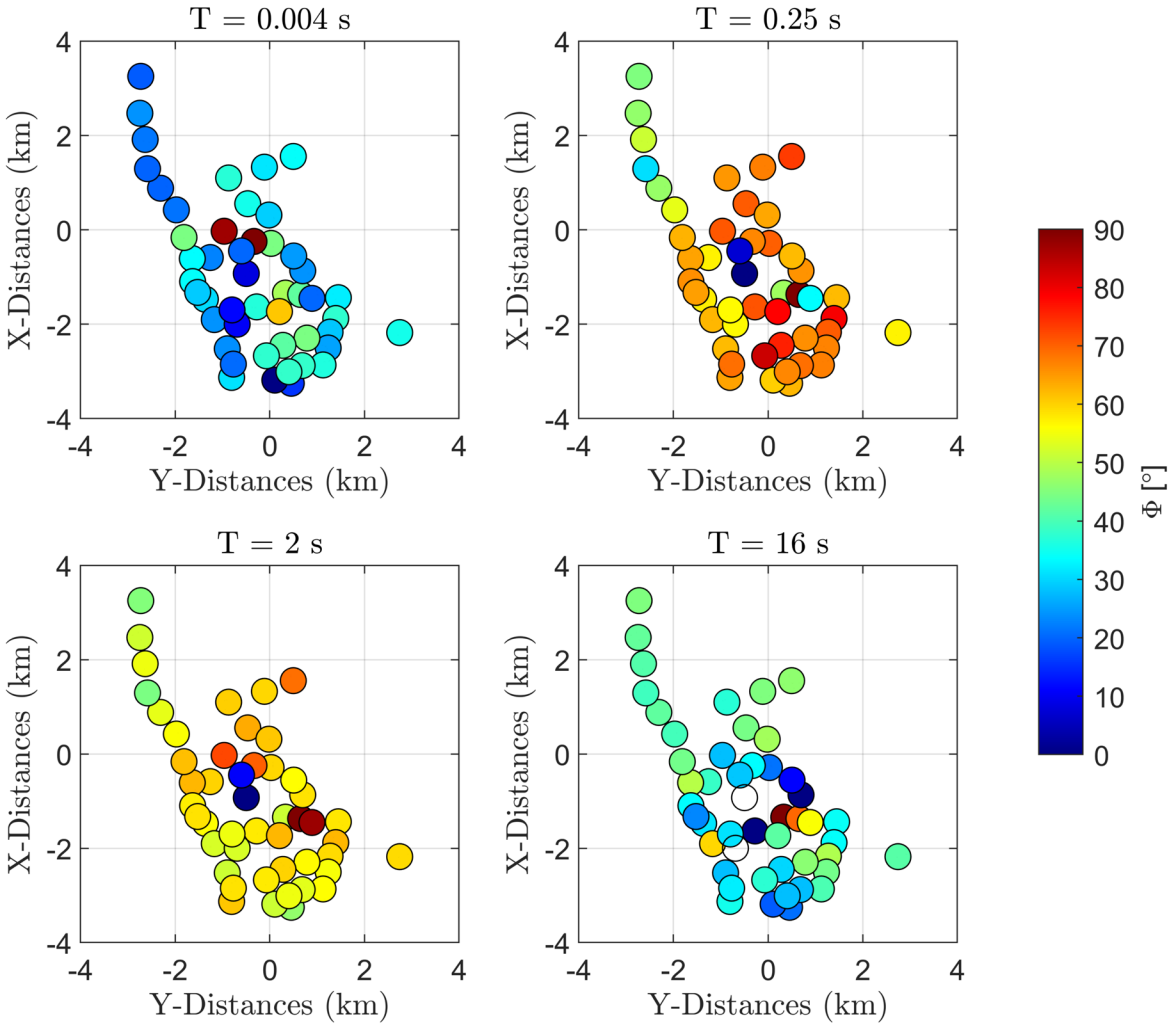

Figure 6.6: Spatial distribution of phases for the YX components at four different periods: 0.004 s, 0.25 s, 2 s, and 16 s. White circles indicate locations where data is unavailable.

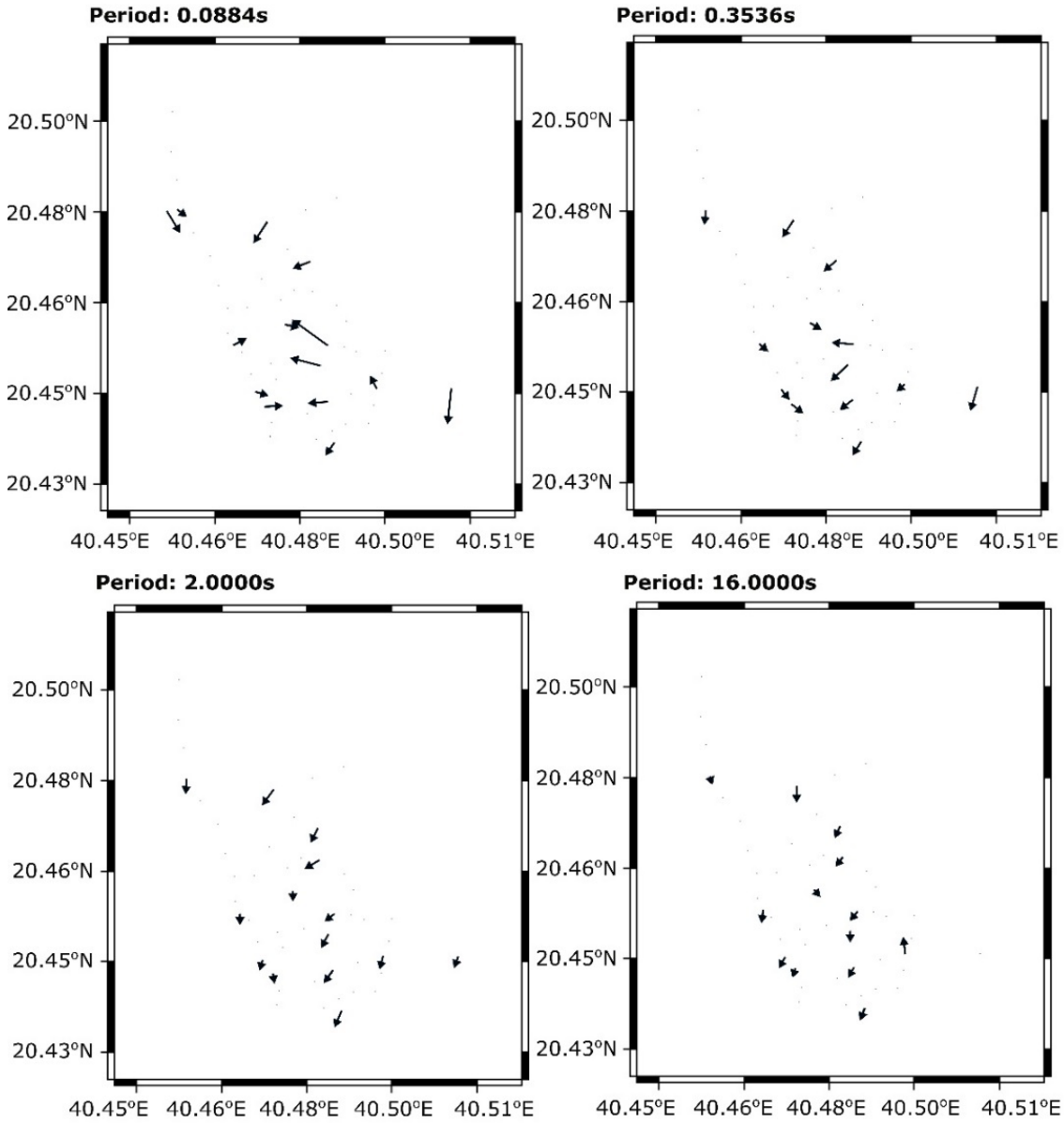

Figure 6.7: Tipper responses represented by arrows at four different periods: 0.0884 s, 0.3536 s, 2 s, and 16 s for the 14 MT sites. At longer periods, the tippers consistently point towards the source of conductive anomalies, following the Parkinson convention.

6.2 TEM Data Processing

Each sounding of the exported raw TEM data consists of 32 sweeps, categorized into three distinct parts: 15 sweeps for the low-moment (LM) part with a low current (~ 1 A), 14 sweeps for the high-moment (HM) part with a high current (~ 7 A), and the final 3 sweeps (no current) which are recorded as noise. These three parts are designated as different channels in the sweep header. The entire dataset is then adjusted using a field shift factor and time delay to ensure consistency. To produce a single transient of each TEM sounding, a robust stacking scheme was applied, utilizing Gaussian error

statistics to estimate data error (e.g., Blanco-Arrué et al., 2021). The transmitter ramp function, which influences early time data, required careful consideration; hence, the LM ramp time of 3E-6 s was selected. After processing, data points suitable for further inversion process were meticulously chosen. As an illustrative example, Figure 6.8 displays the raw, stacked, and selected data points for TEM stations 26 and 27, which corresponds to the location of MT26 and MT27. This numbering allows for a direct comparison between MT and TEM despite the smaller number of TEM soundings. The data points selection for remaining TEM soundings can be shown in Appendix D. Data points below the noise level were discarded, and saturated sections at early times were also excluded from the selected data.

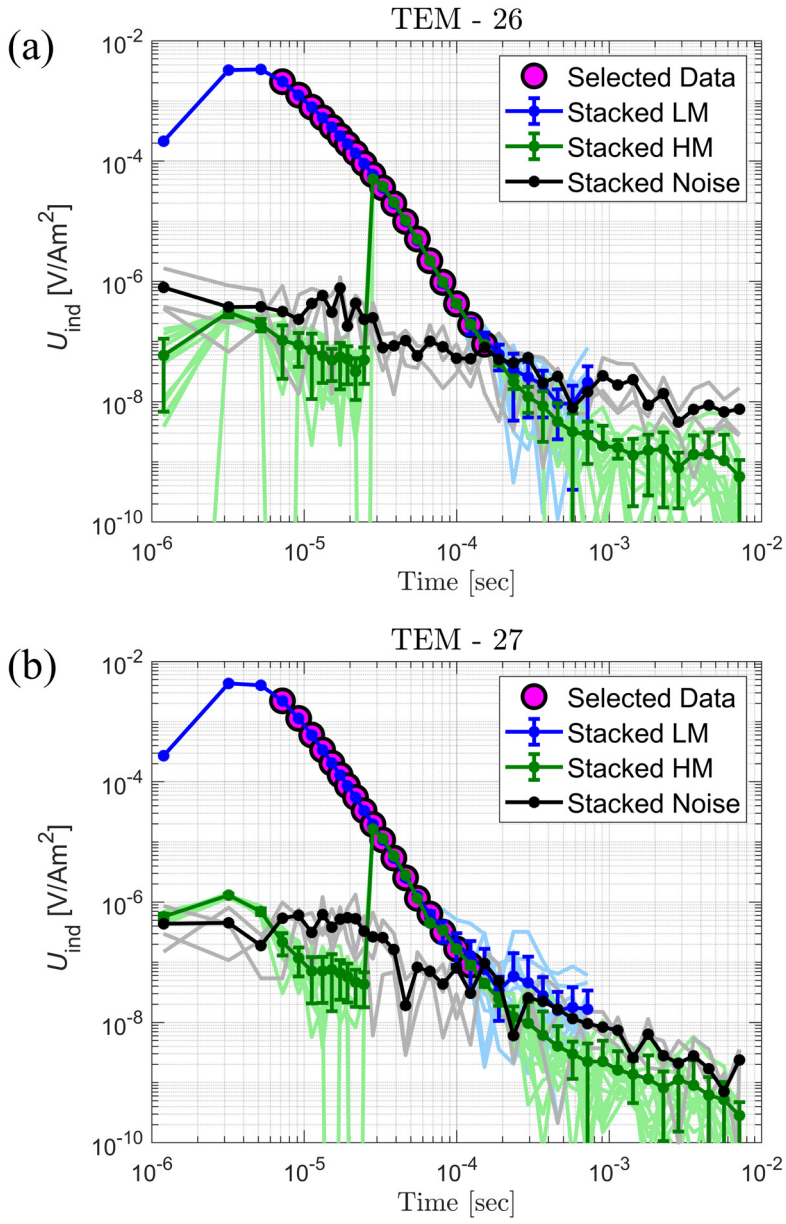

Figure 6.8: Stacked and selected data points of (a) TEM – 26 and (b) TEM – 27 soundings. The magenta circles represent the selected transient data used for further inversion. The stacked data for the low-moment (LM), high-moment (HM), and noise level are shown in blue, green, and black lines, respectively.

6.3 MT Data Analysis

Information of dimensionality and regional strike are fundamental steps in preliminary analysis in any dimension of MT data modeling. In this study, the MT phase tensor with its skew angle is analyzed to indicate the effects of 1D, 2D, or 3D conductivity structure at each site. Phase tensor analysis of the MT impedance is beneficial for dimensionality studies, as galvanic distortion effects are discarded (Bibby et al., 2005; Caldwell et al., 2004).

6.3.1 Dimensionality Analysis

To investigate the effects of a regional conductivity structure (1-D, 2-D, or 3-D) at each site, the MT phase tensor with its associated skew were analyzed. The MT phase tensor is derived from the observed impedance tensor ($\boldsymbol{Z}$) and provides a unique mathematical solution that, unlike invariants, is not influenced by galvanic distortion (Bibby et al., 2005; Caldwell et al., 2004). The distortion-free approach allows the accurate characterization of strike and dimensionality, which can be quantified by the skew angle (β) and the ellipticities of the phase tensor. When the skew angle (β) approaches zero, the subsurface conductivity structure is indicative of either 1-D or 2-D configurations, depending on the tensor's ellipticity. Specifically, a circular (symmetric) phase tensor represents a 1-D structure, while an elliptical (non-symmetric) shape points to a 2-D structure. In the case of a 2-D structure, the principal axis of the ellipse aligns either perpendicular or parallel to the regional strike direction. Conversely, when the phase tensor is elliptical, and the skew angle is significantly large, it suggests a 3-D regional conductivity distribution (Bibby et al., 2005; Caldwell et al., 2004; Chave & Jones, 2012).

Figure 6.9 presents the MT phase tensor ellipses, color-coded according to their skew angles, across all stations for four different periods. At a period of 0.044 s, the skew angles of the phase tensor approach zero, manifesting in two distinct ellipticities: circular and elliptical. The circular shape indicates a 1-D subsurface conductivity structure, while the elliptical shape suggests a 2-D structure. As the period extends to 0.7 and 4 s, most of the phase tensors are represented by ellipses with relatively uniform skew angles. This consistency in skew angles points to a predominant change in the geoelectric structure to a 2-D configuration. At a longer period of 16 s, most skew angles exceed $\pm\ 4^0$, indicating a predominant 3-D structure. This shift in skew angles and tensor shapes across periods highlights the complexity and variability of the subsurface conductivity, transitioning from simpler 1-D and 2-D structures at shorter periods to more intricate 3-D structures at longer periods.

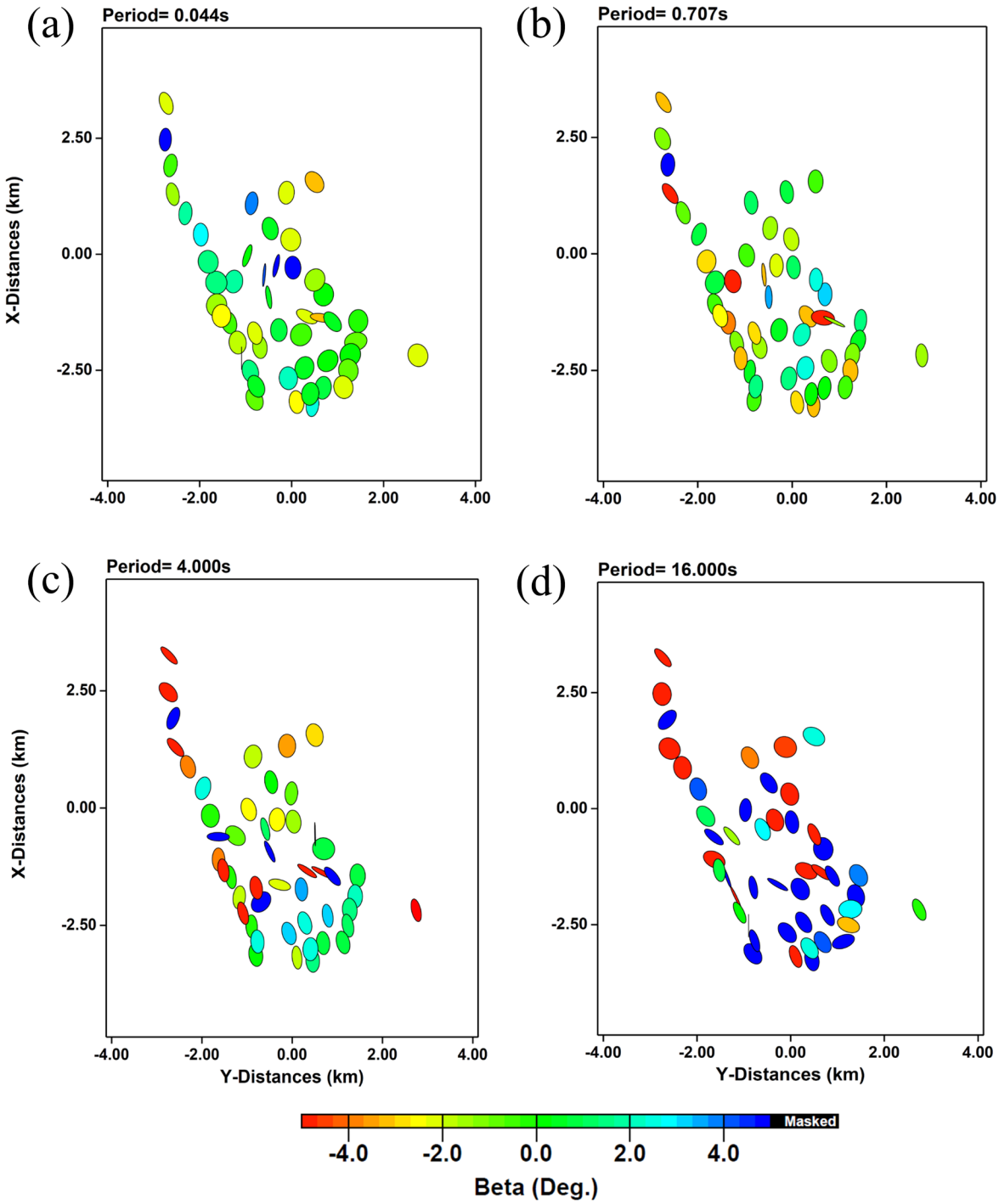

Figure 6.9: MT phase tensor ellipses for four different periods: (a) 0.044 s, (b) 0.707 s, (c) 4 s, and (d) 16 s. The color scale represents the skew angle (β).

6.3.2 Static Shift Corrections

The static shift effects can obscure the actual subsurface conductivity structure, complicating the accurate interpretation of MT data. The static shift effect manifests as a parallel shift in the apparent resistivity curves of an MT sounding, characterized

by a scale factor. This shift is frequency-independent, meaning it does not affect the phase curve of the impedance tensor, but it alters the magnitude of the electric field components, leading to incorrect resistivity estimates. This property highlights the need for careful correction of static shifts to ensure the accurate representation of the subsurface conductivity structure (Árnason et al., 2010; Jiracek, 1990; Jones, 1988; Sternberg et al., 1988).

There are several approaches available for correcting the static shift in MT data. Sternberg et al. (1988) and Pellerin and Hohmann (1990) for example, proposed the use of TEM soundings to address static shift effects. TEM data are relatively unaffected by galvanic distortions, making them a useful tool for this purpose. The approach involves using 1D TEM data to iteratively adjust the invariant of the MT data towards the TEM response. This is based on the assumption that the TEM response accurately reflects the actual 1D conductivity of the subsurface (Árnason et al., 2010).

The method of using TEM data for SSC works by aligning the apparent resistivity curves from MT data with those derived from TEM surveys. Since TEM measurements are less susceptible to near-surface inhomogeneities, they provide a reliable reference. This iterative adjustment continues until the MT data invariant matches the TEM response, ensuring the static shift is mitigated effectively. However, the effectiveness of this method can vary depending on the geological context. Cumming & Mackie (2010) pointed out that TEM might be ineffective for correcting MT static shift in areas where the surface is predominantly covered by thick and resistive rocks. Such conditions can impede the TEM's ability to provide an accurate shallow subsurface resistivity profile, resulting in suboptimal corrections. In the Al-Lith area, the surface is mainly covered by sand and sabkhah deposits, which generally do not exhibit high resistivities.

To correct the static shift at the corresponding MT site, the TEM data were utilized through 1-D joint inversion using ZondMT software (zond-geo.com). This approach was also employed to support the correction of the nearest MT site, provided it was placed on the same geological formation. Figure 6.10 shows the static shift correction for station MT05, where the responses from 1-D TEM and MT joint inversion are plotted. The corrected apparent resistivity for the XY component was shifted by a factor of 0.112, and the YX component by a factor of 0.295. These static shift factors, all being less than 1, indicate that the static shift effects in the survey area were not severe. After applying the SSC to the MT transfer functions, the subsequent inversion is performed without incorporating topography, assuming a flat surface field area. It is important to note that the optimal results in this study, which were used as preferred models, were obtained by incorporating topography in the starting model without applying any static shift corrections to the MT data. This approach and its implications will be discussed in detail in Section 8.2.

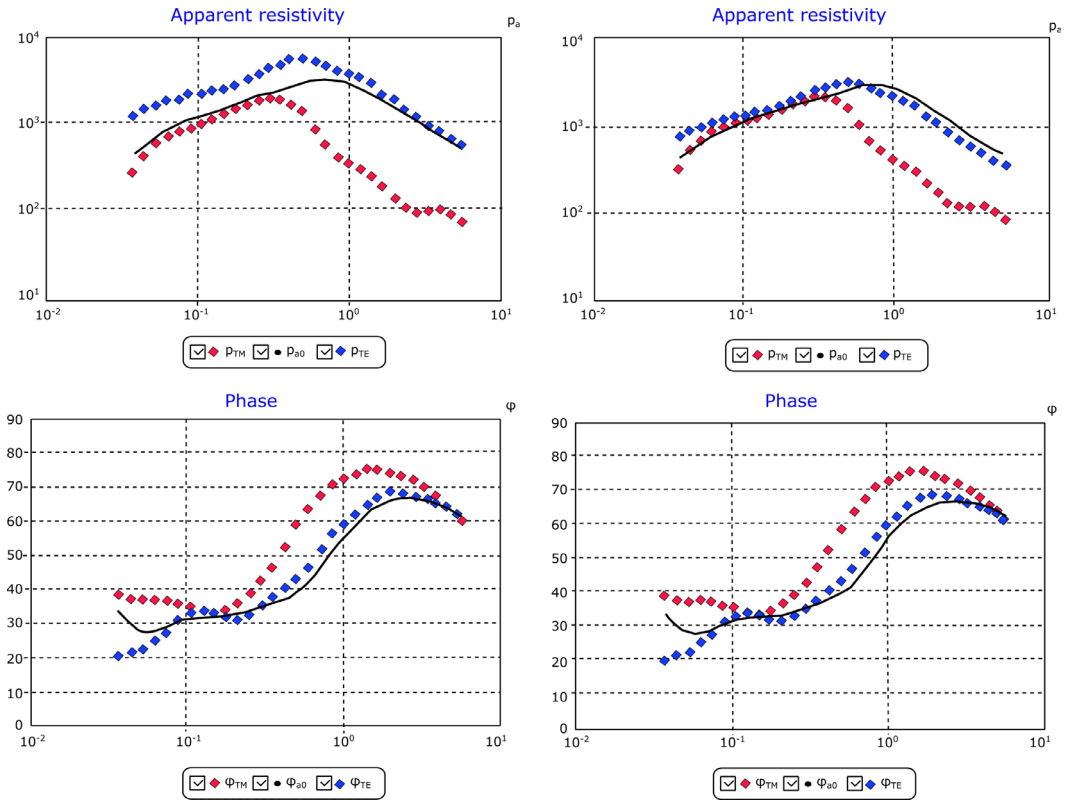

Figure 6.10: Example of static shift correction for station MT05. The apparent resistivity and phase curves for the XY (red) and YX (blue) elements of MT data are shown before static shift correction (left panel) and after applying the static shift correction (right panel). The black solid line represents the response from the 1-D joint inversion.

Chapter 7

3D Synthetic Modeling and Inversion Studies

This chapter discusses the 3D Magnetotellurics (MT) synthetic modeling studies with the help of ModEM algorithm (Kelbert et al., 2014). There are several reasons that make synthetic modeling studies an important tool in the MT method. Synthetic modeling helps assess how sensitive the MT method is to specific features in the subsurface of the study area; by testing different scenarios, we can identify which features are detectable with MT and at what depth, as well as which areas of the model are less resolved or ambiguous. In areas with complex geological structures (e.g., mountainous regions like the Al-Lith area), MT data interpretation can be challenging due to distortions and anisotropy. Synthetic modeling helps account for these complexities by simulating realistic scenarios, leading to more accurate subsurface resistivity interpretations. Furthermore, synthetic modeling is not only valuable for deriving insights into the interpretation of MT inversion data, but it also serves as a powerful tool for optimizing regional survey design (Kirkby & Doublier, 2022). In addition, forward modeling can support the development of MT inversion techniques and algorithms. Testing new inversion approaches on synthetic data from forward models allows geophysicists to improve MT methods (Candansayar & Tezkan, 2008).

In summary, synthetic modeling is a fundamental tool in MT studies. It provides the framework for interpreting field data, refining geological models, and enhancing our understanding of the Earth's subsurface. It allows geophysicists to iteratively develop models that fit observed data, optimize survey parameters, and validate geological hypotheses, ultimately leading to more accurate and reliable results in MT studies (Erdoğan & Candansayar, 2017). In these regards, modeling studies were conducted to explore the detectability of geothermal anomalies using MT technique in the Al-Lith study area. Given the area's mountainous terrain, the influence of topography was also examined. Additionally, the effects of input parameters for the 3D MT inversion using ModEM software were assessed through the analysis of synthetic data.

7.1 The Finite Difference Algorithm

MT Forward modeling aims to solve Maxwell's equations in order to simulate electric and magnetic field distribution in the subsurface based on a given conductivity distribution across various periods or frequencies. Over the past four decades, various methods have been developed for this purpose. In 1-D models, analytic solutions exist for calculating impedances at layer boundaries, using techniques like the Wait recursion formula (Wait, 1954). Analytic solutions have also been found for certain 2-D and 3-D models (Porstendorfer, 1975; Weaver, 1999), typically used to validate numerical solutions.

The most common methods for solving Maxwell's equations are differential equation methods, which discretize the entire earth model into rectangular cells (2D) or cubes (3D) with assigned constant conductivity values. Maxwell's equations are solved for each cell or cube. While these methods offer flexibility in model construction, they require significant computational resources due to fine discretization, leading to large systems of linear equations (Meqbel, 2009). Solutions to the second-order partial differential equations are obtained using either Finite Differences (FD) or Finite Element (FE) methods, with FE offering more design flexibility due to non-rectangular shapes. However, ModEM utilizes the FD approach for accurate 3D forward modeling of complex subsurface conductivity structures (Siripunvaraporn et al., 2002; Kelbert et al., 2014).

Solving the electromagnetic induction problem in 3D is more complex due to the Earth's conductivity varying in three spatial directions $\sigma(x, y, z)$. Furthermore, the 3D induction theory allows for arbitrary geometry, which significantly influences the solution, especially in large earth models where horizontal and uniform field assumptions are no longer valid (Weaver, 1999). However, for simplicity, it's assumed that only conductivity varies in three directions while keeping the source field horizontal and uniform. In frequency domain (assuming a time dependence of $e^{i\omega t}$), the solution of Maxwell's equations in 3D can be formulated in terms of the electric fields[1] as:

$$\nabla \times \nabla \times \boldsymbol{E} + i\omega\mu\sigma\boldsymbol{E} = 0 \tag{7.1}$$

or can also be obtained in terms of magnetic fields from:

$$\nabla \times \rho\nabla \times \boldsymbol{H} + i\omega\mu\sigma\boldsymbol{H} = 0 \tag{7.2}$$

To solve equation 7.1 numerically in three dimensions, the ModEM algorithm utilizes a finite difference (FD) approximation on a staggered grid with dimensions

[1] If displacement currents are neglectable.

$N_x \times N_y \times N_z$, as depicted in Figure 7.1 (Siripunvaraporn et al., 2002; Smith, 1996; Yee, 1966). Here, N_x, N_y, and N_z denote the discretization along the x, y, and z axes, respectively. In the staggered grid formulation, the components of the discretized electric field vector are defined at the edges of the cube while the magnetic field components are defined on the faces of the cube (Figure 7.1). In this case, a solution for $\boldsymbol{E}$ is derived from equation 7.1, followed by obtaining the secondary magnetic field derived from $\boldsymbol{E}$ using Faraday's law (equation 2.3). The staggered grid, known as the Yee-Grid, was introduced by Yee (1966) to solve boundary value problems of Maxwell's equations. This type of numerical grid was later utilized by Siripunvaraporn et al. (2005) and Egbert (2006) for 3D Magnetotellurics (MT).

After grid discretization, the application of FD to equation 7.1 results in a system of equations for a given period or frequency,

$$\boldsymbol{Se} = \boldsymbol{b} \tag{7.3}$$

where $\boldsymbol{e}$ represents the unknown internal electric fields, and $\boldsymbol{b}$ contains terms related to boundary electric fields. The coefficient matrix $\boldsymbol{S}$ is large, sparse, symmetric, and complex, requiring significantly more computational time. For 3-D problems, $\boldsymbol{S}$ becomes very large and challenging to solve directly (Streich, 2009). Therefore, it is often necessitating iterative methods like the bi-conjugate gradient (BiCG) technique (Smith, 1996), the quasi-minimum residual (QMR) method (Siripunvaraporn et al., 2002), and the minimum residual (MRM) method (Mackie et al., 1994). A divergence correction (see Mackie et al., 1994; Smith, 1996) is sometimes applied in these solvers, especially for long period responses, leading to the derivation of surface impedance responses after determining the interior electric fields (Siripunvaraporn, 2012).

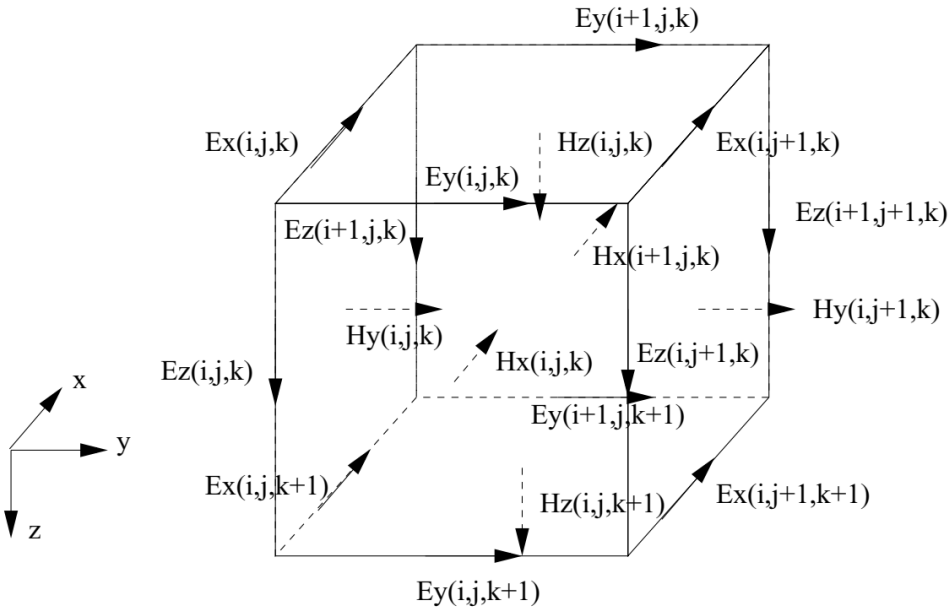

Figure 7.1: The numerical grid used in the finite difference method for the 3-D MT forward problem. The primary electric field components are defined along the edges of the cube and the secondary magnetic field components are defined on the cell faces. Figure taken from Siripunvaraporn et al. (2002).

7.2 Influence of Topography

The influence of topography on Magnetotelluric (MT) data has long been discussed in literature. Early studies highlighted significant distortions in MT transfer functions, leading to misinterpretations of resistivity models (e.g., Berdichevsky & Dmitriev, 1976; Ku et al., 1973). Subsequent research focused on methods to correct or minimize the influence of topography in MT data (e.g., Groom & Bahr, 1992). As discussed in section 2.3, topographic distortions can have both galvanic and inductive effects, which can alter electromagnetic (EM) fields and distort MT transfer functions (Jiracek, 1990; Vozoff, 1991). Topographic distortions can manifest as galvanic effects, due to charge accumulation on slopes, and inductive effects, which alter current density based on terrain features. Inductive effects are most pronounced at short periods, distorting amplitude and phase, while galvanic distortions dominate at long periods, resulting in static shifts (Käufl et al., 2018). This complexity makes it challenging to separate topographic effects from subsurface responses.

2-D numerical modeling indicates that surface topography affects the TM mode more significantly than the TE mode, where effects quickly diminish if topographic features are small relative to subsurface skin depth (Baba & Seama, 2002; Wannamaker et al., 1986). In 3-D scenarios, both galvanic and inductive effects occur in any polarization (Nam et al., 2008), complicating the response further. For accurate MT interpretation,

topographic effects can be integrated into interpretation processes through either incorporation into an earth model during inversion or correcting distortions prior to inversion (Schwalenberg & Edwards, 2004). Inductive effects, particularly at shorter periods, are challenging to mitigate and may exceed a typical uncertainty equivalent to a 5 percent impedance error floor, commonly used in MT inversions. Including topography in the initial model improves inversion outcomes and reduces misinterpretation risks (Käufl et al., 2018). In summary, galvanic distortions due to topography can be significant and need to be accounted for. Inversions that do not account for topography may introduce artifacts in resistivity models (e.g., Mörbe, 2020), misrepresenting subsurface features as being influenced by elevation-induced effects.

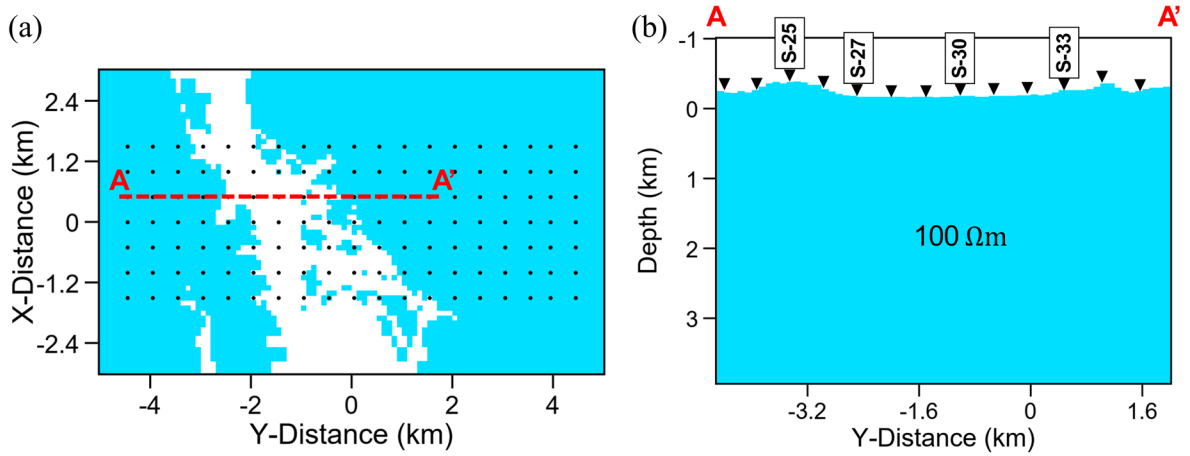

Figure 7.2: A resistivity model with 100 Ωm homogeneous half-space used to test the effect of topography in the study area. (a) and (b) presenting a plan view and a cross-section of the 3D model, respectively. The black cones indicate the distribution of the MT stations. The white color zones in (a) indicate the valley with lower elevation.

The study area is located in steep mountainous terrain, featuring an altitude difference of approximately 600 m, as discussed in Chapter 5. Consequently, a topographic effect on the MT field data was anticipated. In this regard, a forward-modeling investigation has been conducted to validate this effect. The forward calculation utilized a synthetic model composed of a 100 Ωm homogeneous half-space, incorporating topographic data from the Al-Lith area (refer to Figure 7.2). A total of 133 MT stations were positioned along seven distinct east-west profiles, with a separation of 500 m between each station. The 3D finite difference grid employed for model discretization covers an expanse of 82 km in the north-south (x) direction, 85 km in the east-west (y) direction, and reaches a depth of 455 km (z). The model mesh consists of 109 x 114 x 150 nodes in the x, y, and z directions, respectively. In the central region of the mesh, the cells are 100 m on each side. The first 100 vertical layers of the mesh maintain a uniform thickness of 10

m, with subsequent layers increasing by a factor of 1.2. The four components of the impedance tensors were calculated for 42 periods, ranging from 0.001 to 1000 seconds.

Figure 7.3 illustrates the MT responses from forward calculations represented as apparent resistivity (ρ_a) and phase (ϕ) for stations S-25, S-27, S-30, and S-33, which were selected to represent various locations as shown in Figure 7.2. In a flat area, the apparent resistivity should accurately reflect the true subsurface resistivity, which is 100 Ωm in this instance, while the phase should ideally be 45° for a homogeneous half-space model. However, topographic distortions significantly impact the transfer function response at the S-25 station, where the inductive topographic effects are most pronounced due to its positioning at the top of the hill (see Fig. 7.2). These inductive topographic effects also influence S-27 and S-33, though to a lesser extent, particularly noticeable at shorter periods up to 0.1 s. In contrast, at longer periods, galvanic distortions prevail, resulting in static shifts, affecting only the apparent resistivities. This clearly demonstrates that topography can affect both galvanic and inductive distortions. The least distorted responses are observed at the S-30 station, where the influence of the topography is minimal. This is attributed to S-30's location within the valley, an area that is relatively flat and situated at a considerable distance from the hills.

To illustrate the importance of incorporating topography during inversion, the forward calculated data was then inverted using a homogeneous half-space of 50 Ωm under two different scenarios: one that included topography and another that assumed a flat surface without topography. A 5% Gaussian noise was added to the synthetic dataset and prior to the inversion process an error floor was set to 5% of the mean of the complex off-diagonal impedances $|\boldsymbol{Z}_{xy} * \boldsymbol{Z}_{yx}|^{1/2}$ for the impedance tensor elements. Figure 7.4 presents the inversion results; the model accounting for topography successfully retrieved the original 100 Ωm background resistivity with RMS of 1, whereas the model that excluded topography displayed a considerably higher RMS and exhibited artifacts as expected. Notably, these artifacts are clearly visible in the shallow subsurface up to ≈ 400 m, matching the fact that the strongest inductive effects of topography appear at low to medium periods. This forward calculation and inversion test underscore that even in regions like the Al-Lith area, which possess only moderate topography, the inclusion of topography in the model is essential to avoid possible misinterpretation risks.

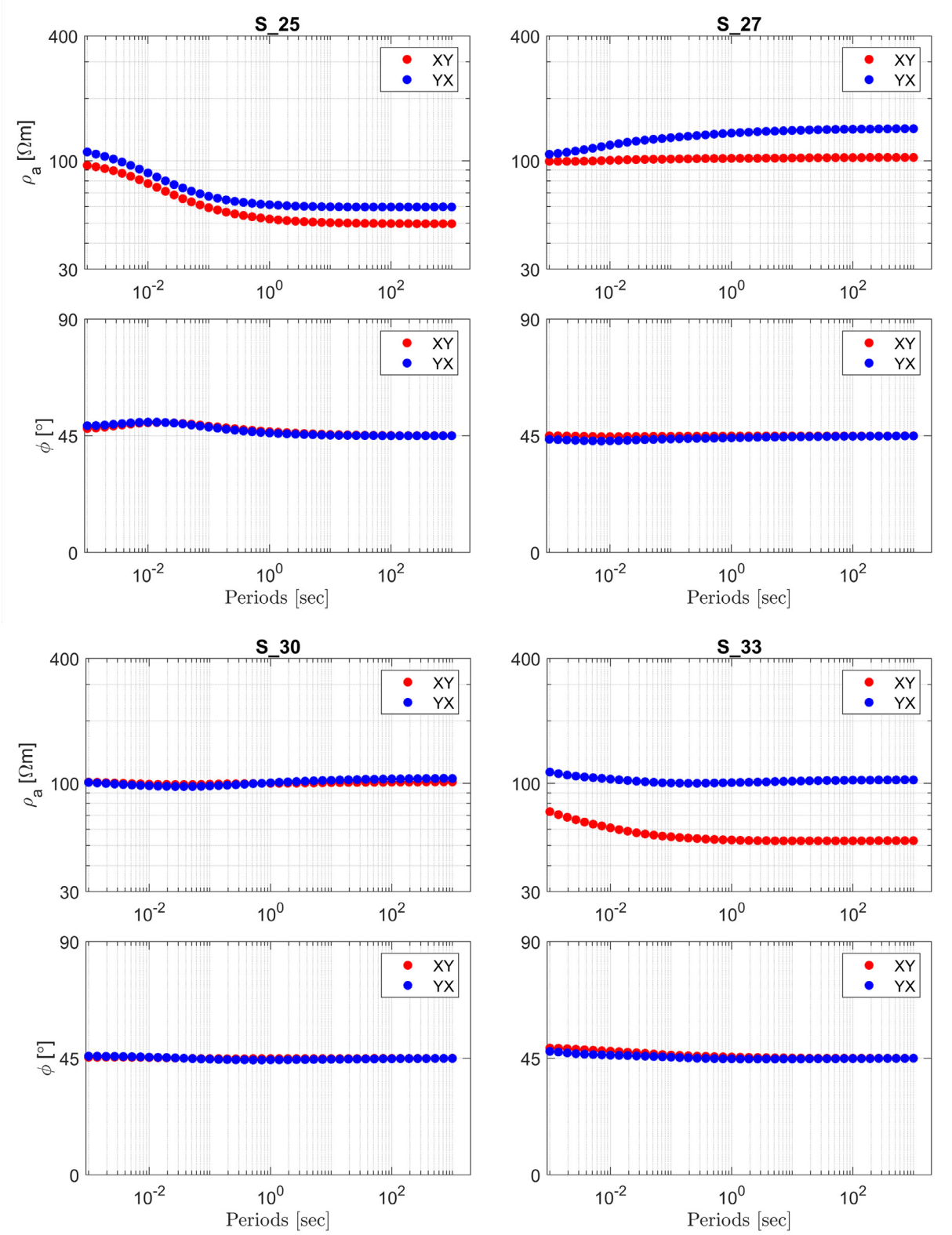

Figure 7.3: Transfer functions represented as apparent resistivity ρ_a and phase ϕ obtained after forward calculation at four stations: S-25, S-27, S-30, and S-33. The phase values have been adjusted to the [0°, 90°] quadrant. Red dots represent XY elements, and blue dots represent YX elements.

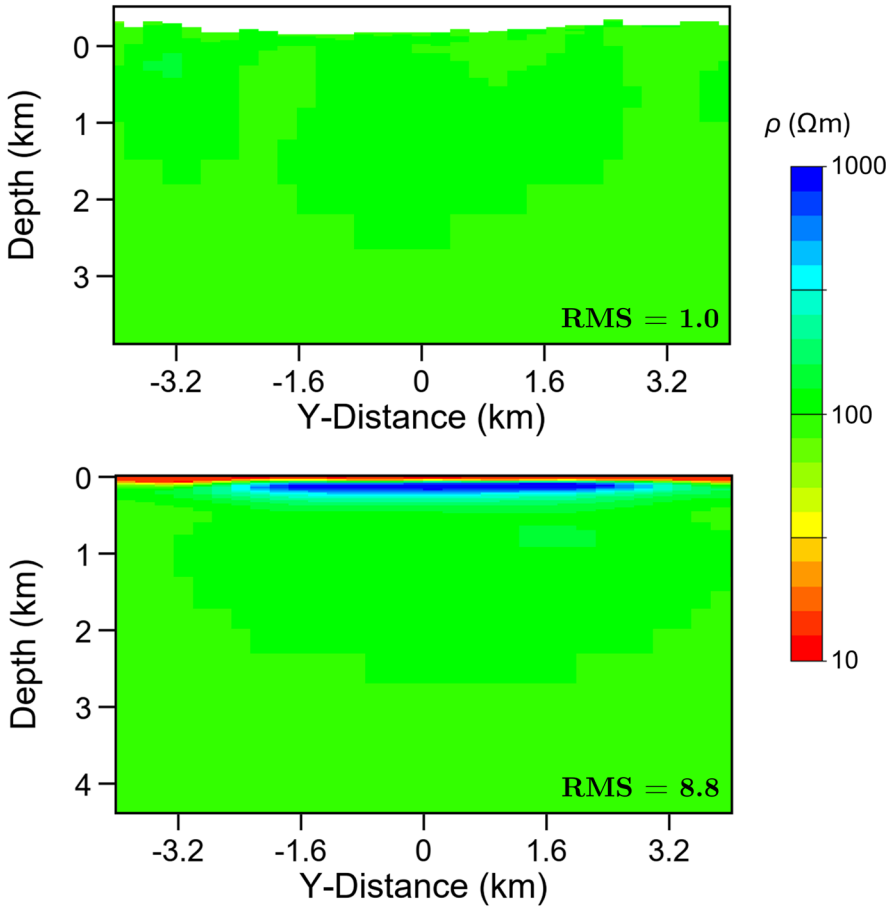

Figure 7.4: Inversion results, derived from the forward-calculated data within the study area, demonstrating an inversion model with and without topography. The inversion model that incorporates topography (top panel) achieved an RMS of 1, significantly outperforming the model that excluded topography (bottom panel). Additionally, it is noteworthy that inversion artifacts were observed in the model without topography.

7.3 Conceptual Model of Geothermal Systems

As described in Chapter 4, regardless of the type of geothermal resources, a general geothermal system conceptually involves the presence of a heat source, a permeable reservoir, a recharge mechanism, and an impermeable rock known as a clay cap (Berktold, 1983; Cumming, 2009; Muñoz, 2014). In a simple hydrothermal context, the geothermal system can be conceptualized with the model of Figure 7.5a (Pellerin et al., 1996), characterized by the following features: the shallow part of the geothermal system is built by a resistive surface layer, represented as zone 1 in Figure 7.5a. Underneath is a highly conductive clay cap (Figure 7.5a, zone 2), which is located above the more resistive reservoir (Figure 7.5a, zone 3). The presence of a clay cap typically results in a low resistivity signature, which is indicative of geothermal systems. However, in certain high-temperature geothermal systems—particularly those

associated with volcanic activity—a clay cap may be absent due to their unique geological conditions (Muñoz, 2014; Patro, 2017). In the case of clay cap absence, the conceptual model can be illustrated in Figure 7.5b.

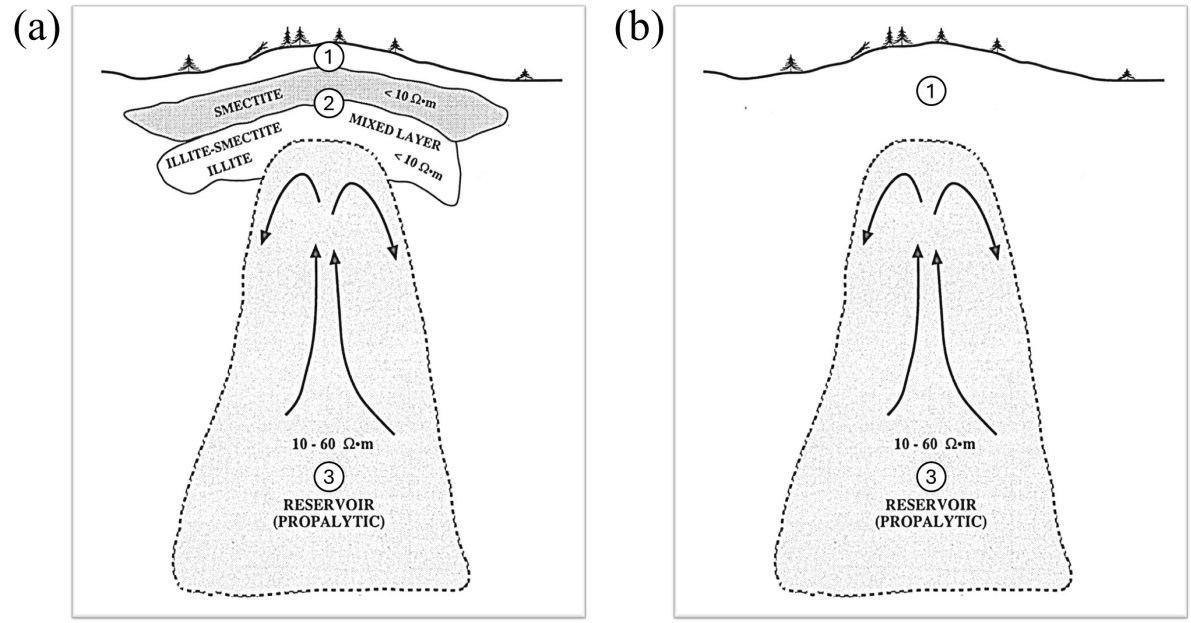

Figure 7.5: Sketch of the generalized conceptual model of a geothermal system in the case of (a) the presence and (b) the absence of a highly conductive clay cap. Zone 1 represents a resistive shallow layer, 2 is a conductive clay cap, and 3 is a reservoir. Figure modified from Pellerin et al. (1996).

7.3.1. 3D Forward Modeling Scenarios

To analyze two different forward modeling scenarios given the uncertainty of a clay cap's presence, two 3D resistivity models, Model A and Model B, have been developed. Model A, depicted in Figure 7.6, includes a 5 Ωm clay cap positioned over a 25 Ωm reservoir, which is situated within a 500 Ωm half-space resistivity background. The dimensions of the clay cap are 3.2 x 4.6 x 0.5 km, while the reservoir measures 2.5 x 2.5 x 4.1 km. On the other hand, Model B, illustrated in Figure 7.7, consists of two distinct protrusions (25 Ωm) above a 15 Ωm geothermal reservoir, also within a 500 Ωm subsurface resistivity background. These protrusions act like pathways for geothermal fluids to migrate, either to the surface or to the near subsurface, which may result in active geothermal surface manifestations such as hot springs. The protrusions measure 1 x 0.8 x 2 km, while the dimensions of the reservoir are 3 x 4.2 x 5 km in the model.

Model A consists of 91 MT stations, which are distributed along seven different E-W profiles, with a separation of 0.5 km and 1 km between each station, as shown in Figure

7.6. In Model B, due to the larger size of the anomaly, there are 77 MT stations spaced 0.8 km and 1 km apart, also arranged along seven different E-W profiles, as illustrated in Figure 7.7. The 3D finite difference grid used for model discretization contains 79 x 109 x 80 nodes for Model A and 49 x 78 x 86 nodes for Model B, corresponding to the x, y, and z directions, respectively. The grid for both models is centered at the midpoint of the study area, located at a latitude of 20.469 °N and a longitude of 40.482 °E. Topography has also been incorporated into both models. Afterward, a 3D MT forward modeling approach was applied to the two described models. The four components of the impedance tensor, along with the two VTF components (Tipper data), were calculated for 24 periods ranging from 0.001 s to 500 s for both models. A 5% Gaussian noise was added to the synthetic dataset.

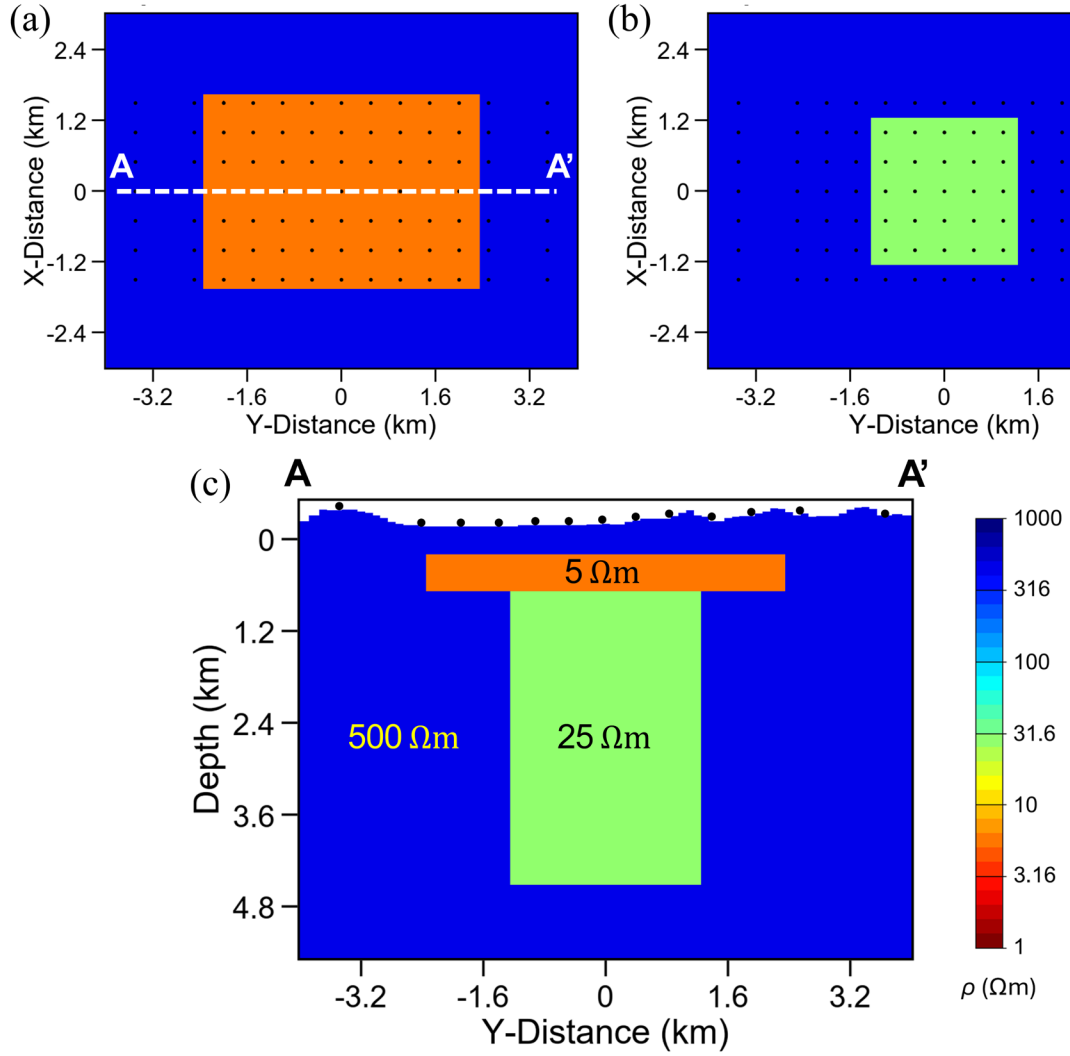

Figure 7.6: Model A representing a 3D model used to conceptualize the geothermal system with the presence of a highly conductive clay cap. MT site locations are marked with black dots. (a) plan view of the clay cap, (b) plan view of the geothermal reservoir, and (c) vertical cross-section of the profile A-A'. Topography is included in the model.

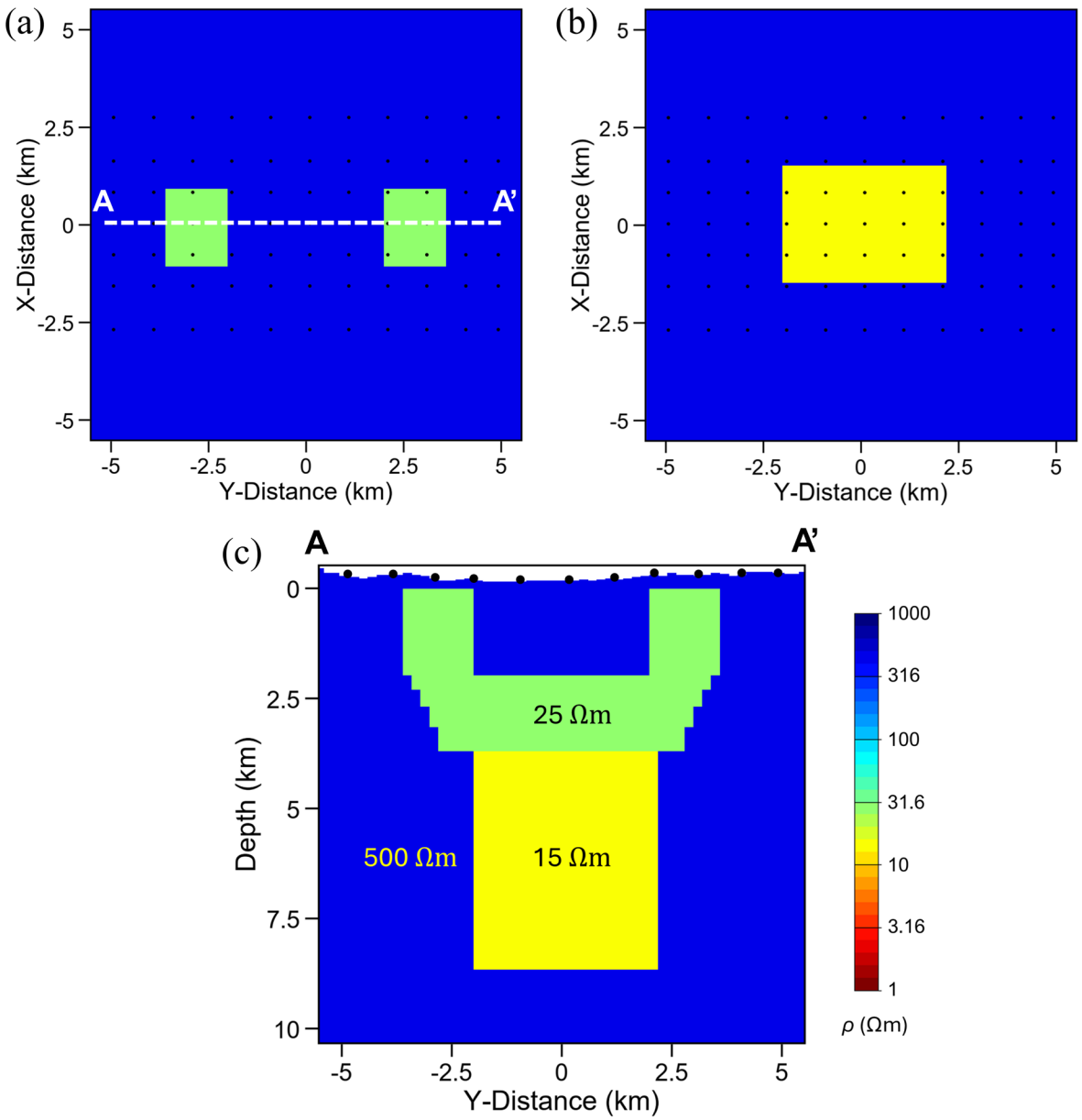

Figure 7.7: Model B represents a 3D model conceptualizing the geothermal system with the absence of a highly conductive clay cap. MT site locations are marked with black dots. (a) plan view of the individual protrusions above the reservoir, (b) plan view of the geothermal reservoir, and (c) vertical cross-section of the profile A-A'. Topography is included in the model.

7.3.2. 3D Inversion of Synthetic Dataset

The calculated synthetic data of both models was then used to perform 3D MT inversion in order to see its capability. Prior to the inversion process, data errors were set to 5% of the mean of the complex off-diagonal impedances $|\boldsymbol{Z}_{xy} * \boldsymbol{Z}_{yx}|^{1/2}$ for the impedance tensor elements and a constant value of 0.05 for the tipper data. A homogeneous half-space of 100 Ωm was utilized as a starting model for the inversion

for both models. The result of the Model A's 3D inversion can be seen in Figures 7.8 and 7.9 as resistivity depth slices and a vertical cross section, respectively. While Figures 7.10 and 7.11 are Model B's inversion results. Both inversion models achieved an overall RMS of 1, indicating that both models fit the data within the level of data error.

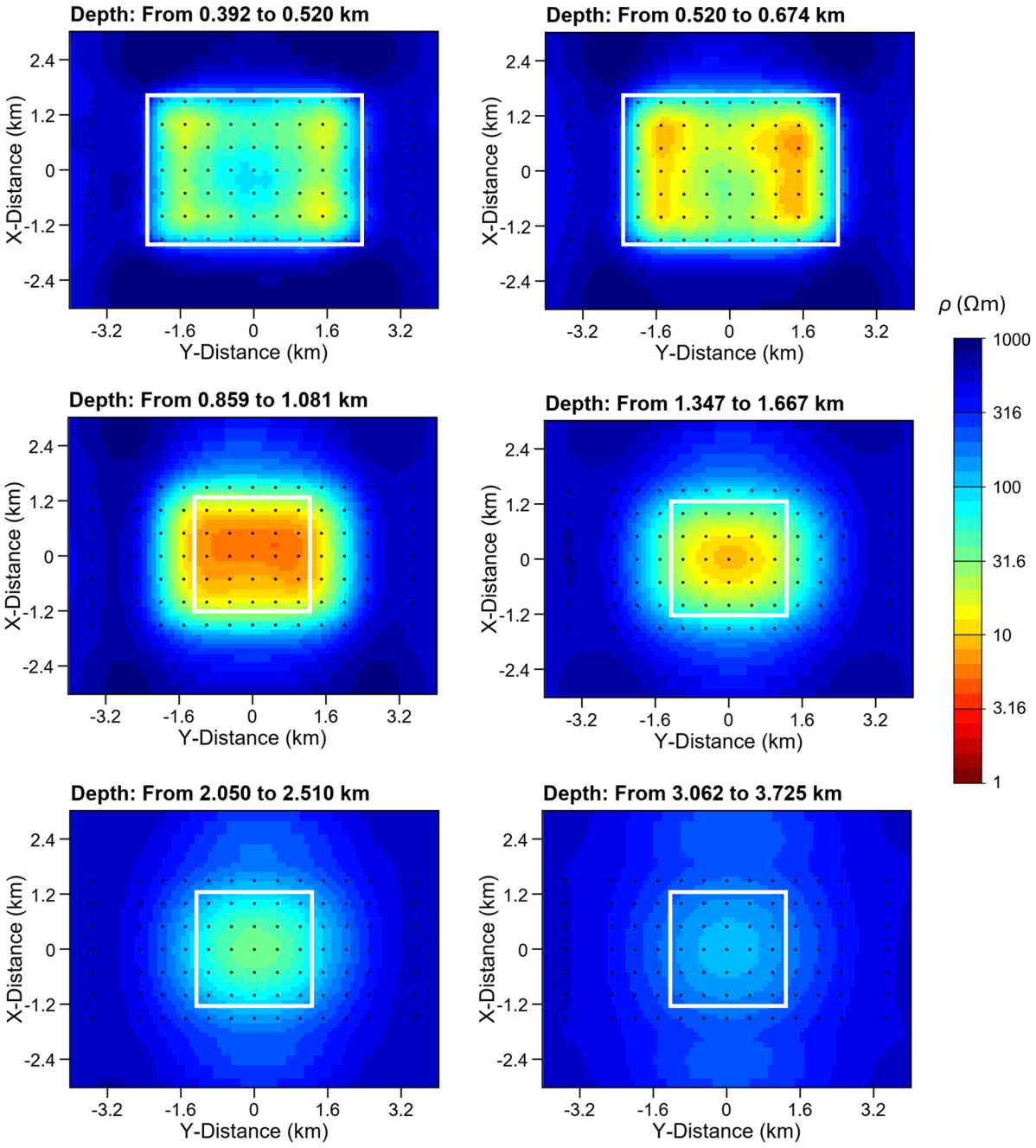

Figure 7.8: 3D inversion results of Model A displayed as resistivity depth slices, with projected surface MT site locations marked by black dots. White lines indicate the actual position of the clay cap and reservoir.

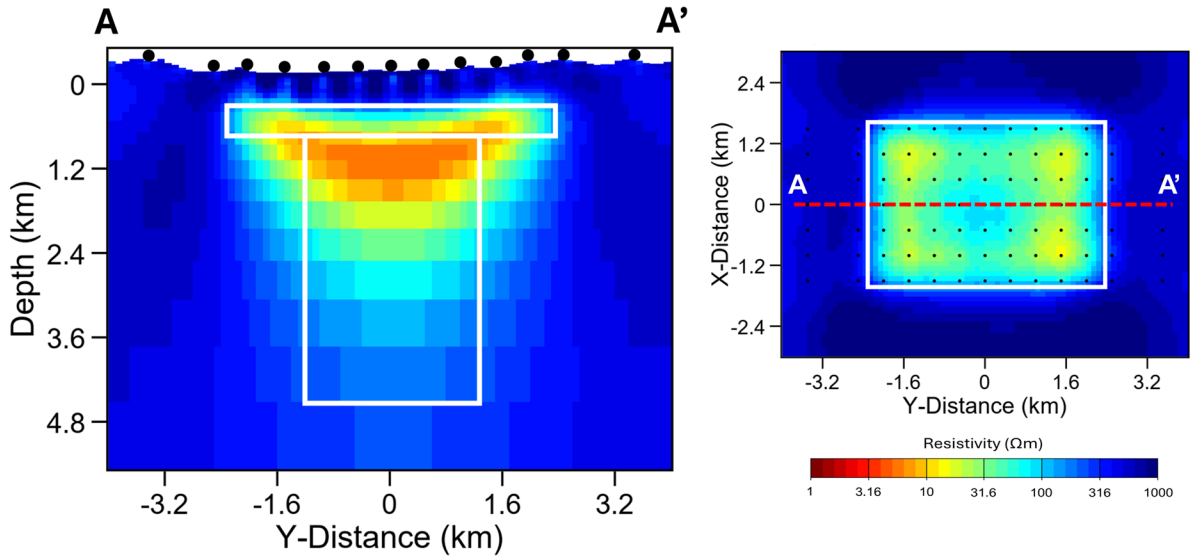

Figure 7.9: Cross section AA' extracted from the inversion results of Model A (left panel). The red dashed line shows the projection of section AA' onto the plan view (right panel). The positions of the MT stations are marked with black dots, while the white lines indicate the actual positions of both the clay cap and the reservoir.

In the case of the clay cap's presence in a geothermal system, the 3D MT inversion proves to be highly effective in accurately identifying the clay cap structure. However, it is important to note that the delineation of the geothermal reservoir, particularly in its lower section, remains inadequately defined, as illustrated in Figures 7.8 and 7.9. Furthermore, the impact of the conductive clay cap can still be observed in certain areas of the upper section of the reservoir, indicating that the clay cap does influence the overall conductivity of the reservoir's geometry. Despite these challenges, the MT method successfully maps the conductive clay cap and delineates the transition to the geothermal reservoir, providing valuable insights for geothermal exploration.

In another scenario where a conductive clay cap is absent, the 3D MT inversion demonstrates significantly enhanced coverage of both the geothermal reservoir and its associated protrusions, as depicted in Figures 7.10 and 7.11. The 3D MT inversion technique effectively reveals the intricate structural details of both protrusions in Model B. In addition, the MT method more effectively delineates the structure of the geothermal reservoir in Model B (without a clay cap) compared to Model A (with a clay cap). This modeling study demonstrates the capability of the MT method to characterize geothermal anomalies. Furthermore, its proficiency in accurately imaging the clay cap and the protrusion above the reservoir is critical for identifying inflow and outflow areas, ultimately aiding in the selection of optimal drilling sites.

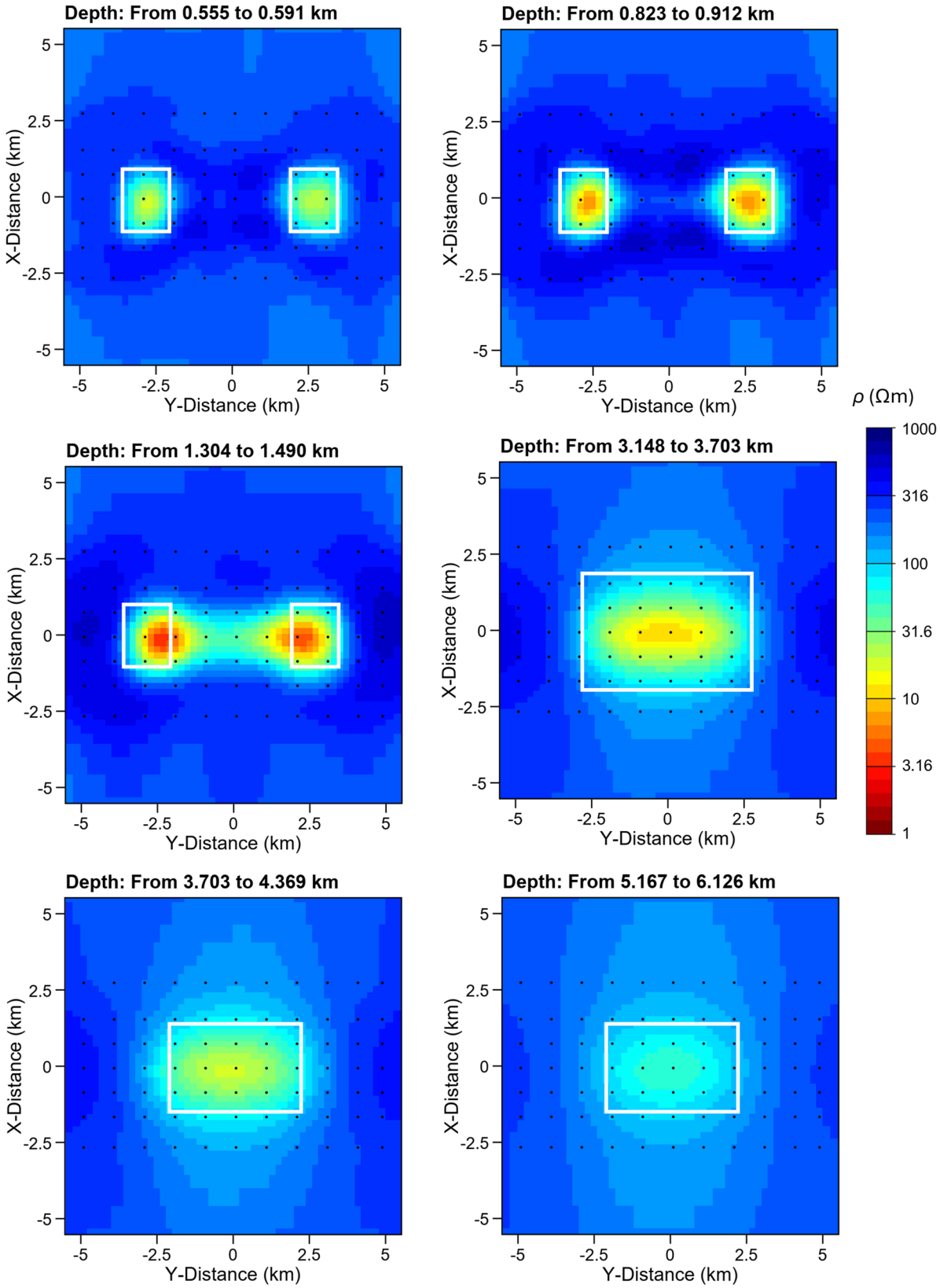

Figure 7.10: 3D inversion results of Model B displayed as resistivity depth slices, with projected surface MT site locations marked by black dots. White lines indicate the actual position of the conductive anomaly.

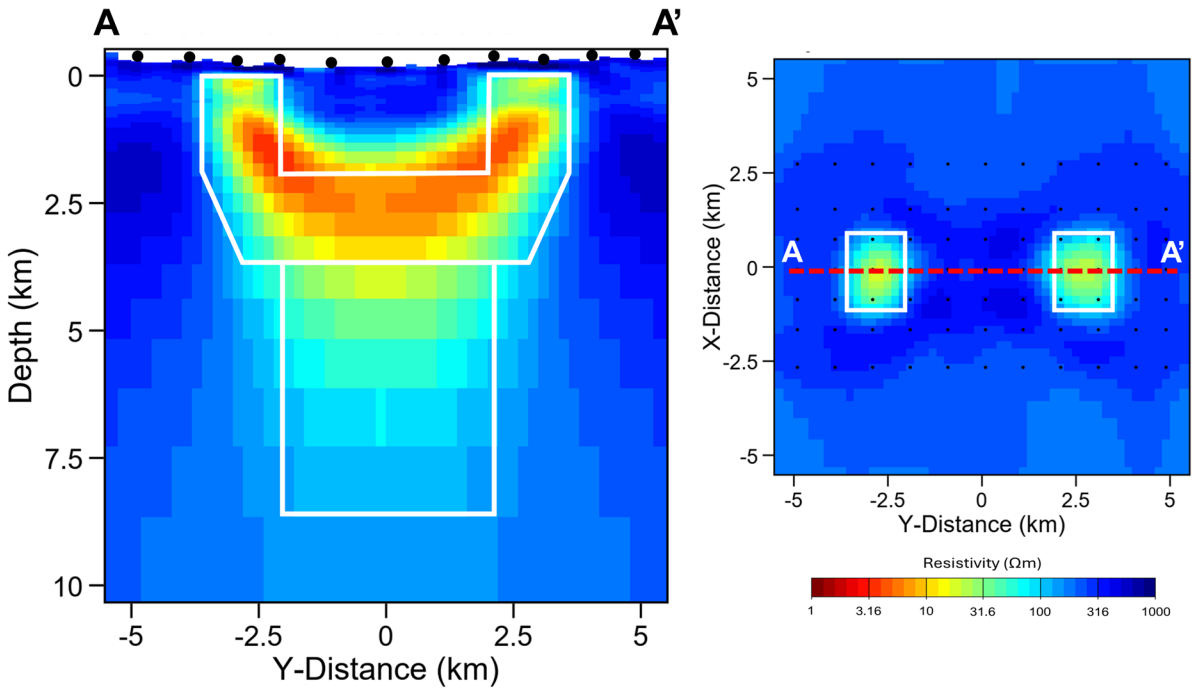

Figure 7.11: Cross section AA' extracted from the inversion results of Model B (left panel). The red dashed line shows the projection of section AA' onto the plan view (right panel). The locations of MT stations are marked with black dots. The white lines indicate the actual position of the conductive anomaly.

7.4 Input Parameters of the 3D MT inversion

As previously discussed, a common issue faced with Electromagnetic (EM) geophysical data inversion is that it is a strongly ill-posed problem, resulting in non-linear and non-uniqueness solutions. Due to the limitations of the data and the presence of noise, numerous models can fit the data within a specified tolerance threshold. Therefore, this section explores the impact of the input parameters used in the 3D inversion software ModEM. In this context, several inversion trials were conducted, employing various initial resistivity models, different values for the model covariance (α), and diverse error settings. The discussion will focus on how these chosen parameters influence the inversion models. In light of recent discoveries regarding the geothermal systems in Al-Lith, western Saudi Arabia, Model B from section 7.3— which represents the conceptual geothermal system model without a highly conductive clay cap— will be employed in subsequent synthetic studies. The 3D synthetic model consists of two distinct protrusions (25 Ωm) above a 15 Ωm geothermal reservoir, embedded in a 500 Ωm half-space (Figure 7.6). Topography was incorporated into the model, and a total of 77 MT stations were deployed. Afterwards, the calculated data was used to perform 3D inversion trials with different input parameters.

7.4.1 Initial Resistivity Model

Selecting an appropriate prior or initial resistivity model is crucial in the 3D inversion scheme, as it serves as the initial point for optimization and establishes the penalty function (Meqbel et al., 2014). A good initial model provides a reasonable starting point that prevents drastic changes in resistivity during iterations, which can destabilize the inversion. Starting from an initial model close to the true resistivity distribution reduces the number of iterations required for the inversion to converge, thereby lowering computational demands (Zhdanov, 2015). For this reason, four distinct initial resistivity models were tested: 1, 10, 100, and 1000 Ωm.

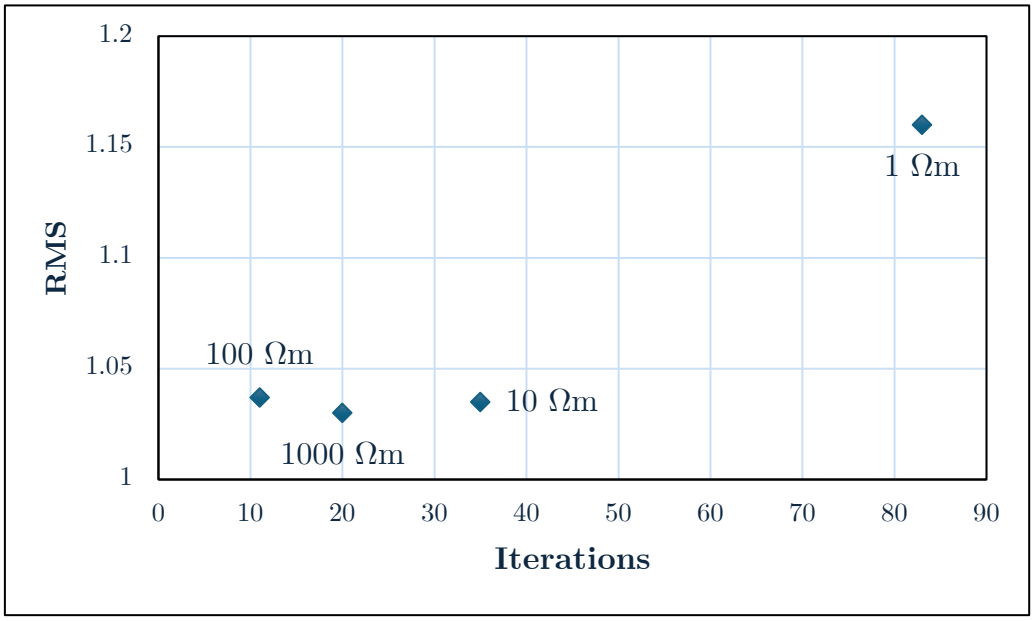

Figure 7.12: Overall RMS values and the total number of NLCG iterations required for 3D inversion tests of four different initial models.

The analysis of the inversion tests revealed that each inversion test required a different number of NLCG iterations as shown in Figure 7.12. The actual position of the conductive anomaly is represented with white lines. Among the four different inversion tests conducted, the initial resistivity model of 100 Ωm achieved the fastest iterations and also yielded the optimal overall RMS. In contrast, the 1 Ωm starting model suffered the longest iteration process and highest overall RMS. While the differences in RMS values among the four initial models were not significant, the distinctions between the inverse models were quite pronounced, as seen in Figure 7.13. A comparison of the inversion subsurface models reveals that the 100 Ωm initial resistivity model produced the most reasonable and reliable results. This suggests that the most efficient iterations and the smallest overall RMS values are obtained when the initial model resistivities

are close to the regional average resistivity. Therefore, different starting models should be tested and examined on the MT field dataset to obtain the most reliable result.

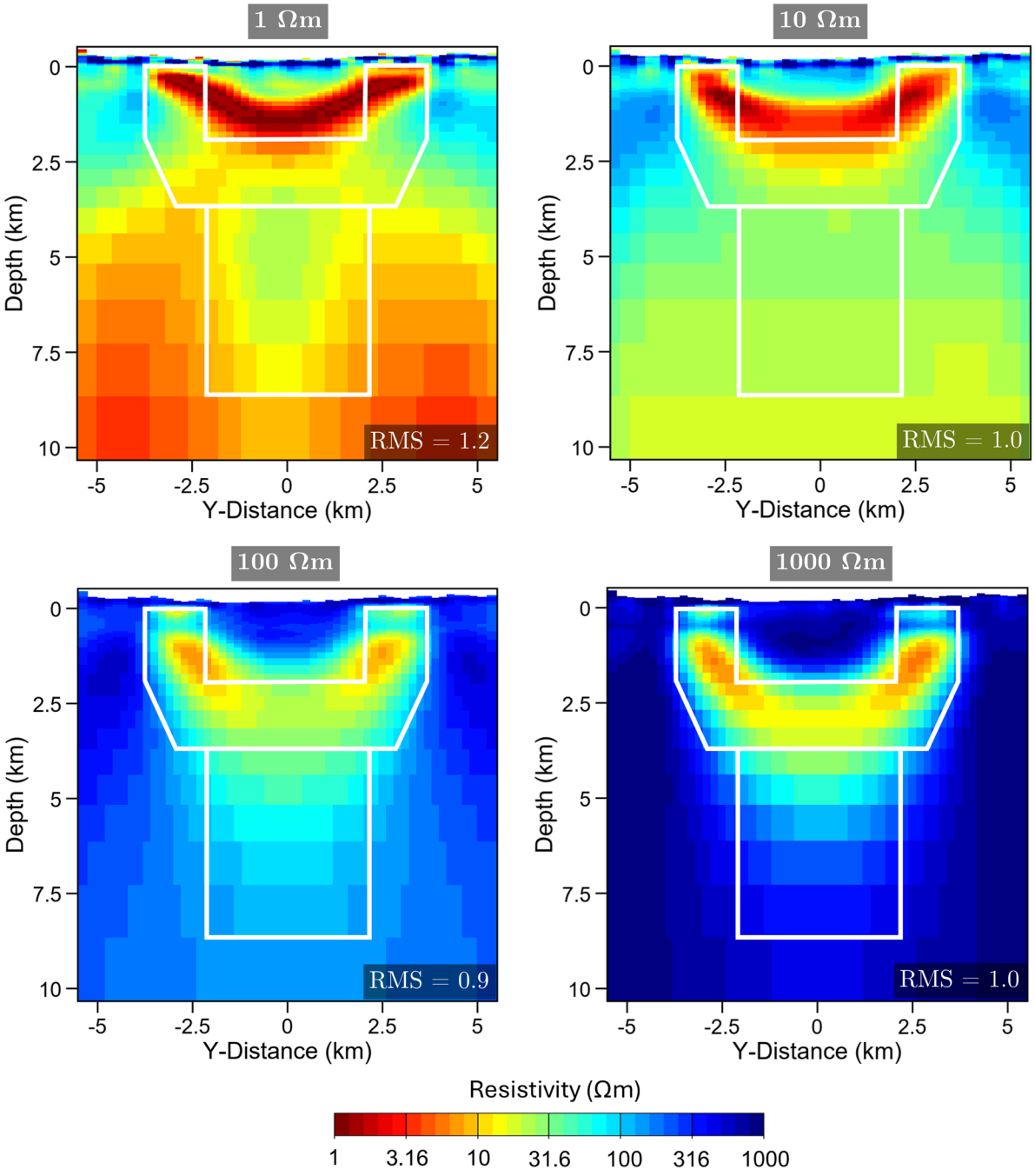

Figure 7.13: Vertical cross-sections of the 3D inversion test with four different starting models. The white lines indicate the actual positions of the conductive anomaly.

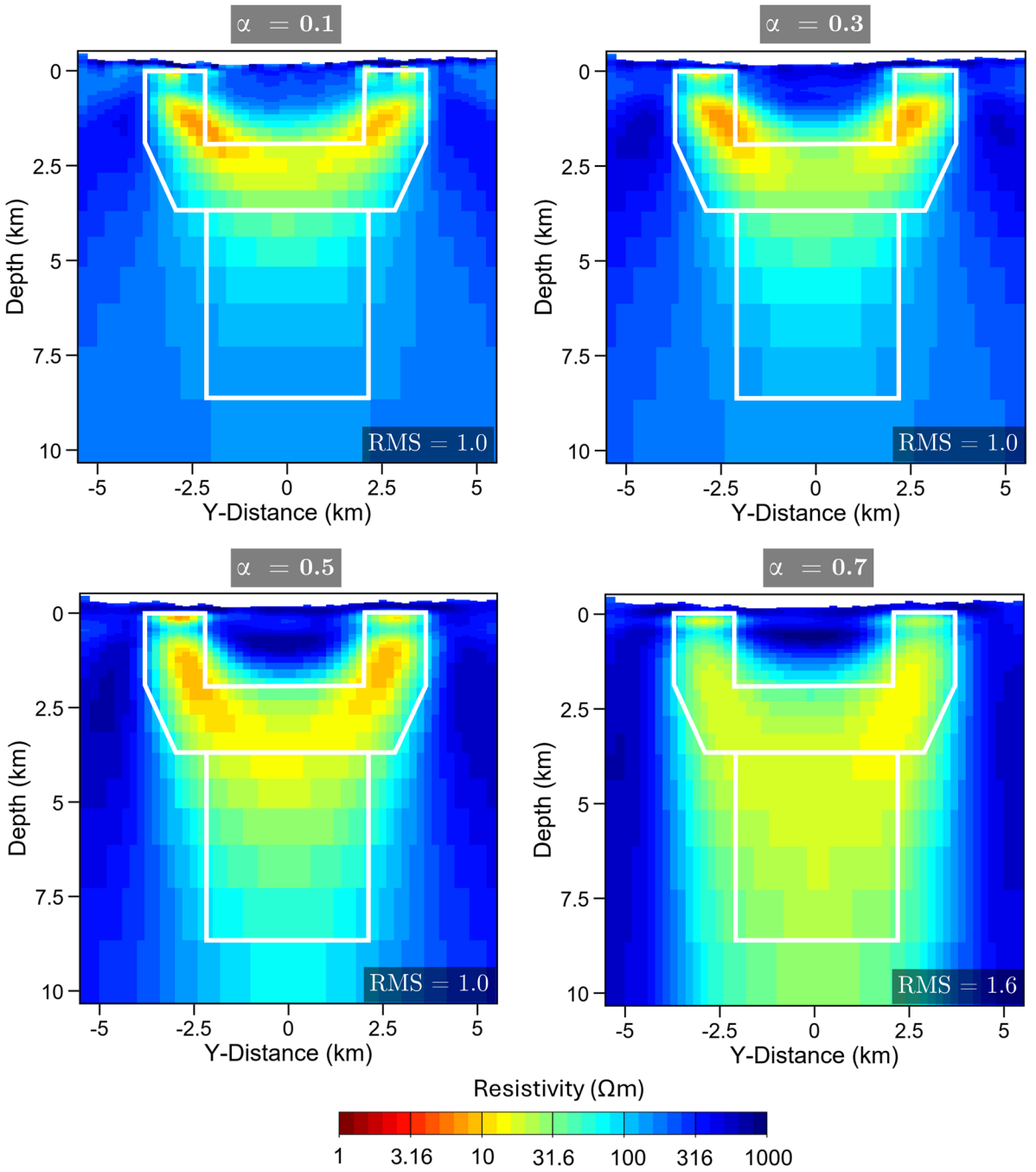

Figure 7.14: 3D inversion models presented as vertical cross-sections for the four different smoothing parameters. The actual position of the conductive anomaly structure is represented with the white lines.

7.4.2 Model Covariance Parameter (α)

In ModEM 3D MT Inversion, the model covariance parameter plays a crucial role in the regularization process. It determines the degree of model smoothness and can be defined independently in three different directions: x, y, and z. The spatial smoother implemented is a recursive auto-regressive covariance operator with a quasi-Gaussian

smoothing kernel (Kelbert et al., 2014). ModEM simplifies the specification of the model covariance by using directional smoothing weights and trade-off parameters, rather than requiring direct input of the covariance matrix. This parameter ranges from 0 to 1 (Tietze, 2012), with higher values leading to stronger smoothing in the corresponding direction. A more detailed explanation of the covariance matrix and its parameters will be provided in Section 8.1. To assess the impact of the smoothing parameter, trials were conducted on Model B using α values of 0.1, 0.3, 0.5, and 0.7.

The inversion results from all four trials are displayed in Figure 7.14 as vertical cross-sections. The differences between the inverse models, influenced by the chosen smoothing parameter, are notorious. Specifically, the inversion model with a smoothing parameter of $\alpha = 0.1$ reveals primarily local conductive bodies near the MT stations, as evidenced by the two protruding structures. In contrast, the model with $\alpha = 0.3$ achieves sufficient smoothness to connect the parameters of the cells, thereby encompassing the entire structure. With a smoothing parameter of $\alpha = 0.5$, the conductive bodies appear larger and deeper due to the increased smoothing value. Meanwhile, the inversion model with $\alpha = 0.7$ reveals a much larger dimension, especially on the reservoir conductive structure. In terms of RMS values, the inversion models for $\alpha = 0.1$, 0.3, and 0.5 achieved an optimal value of 1, whereas the model for $\alpha = 0.7$ yielded a higher RMS of 1.6. It is essential to find a balance between data misfit and model smoothness; thus, $\alpha = 0.3$ was selected as it demonstrated an acceptable RMS along with reasonable model smoothness.

7.4.3 Data Error Settings

In the following part, the influence of different error settings on the 3D inversions is studied, as the data error settings also represent a crucial input parameter that must be systematically assessed to identify the most appropriate configuration for the given dataset. To achieve this, data errors were determined relative to the mean of the off-diagonal elements $|\boldsymbol{Z}_{xy} * \boldsymbol{Z}_{yx}|^{1/2}$ for the impedance tensor components and constant values for the VTF or tipper elements (Meqbel, 2009; Patro & Egbert, 2011; Tietze, 2012). Accordingly, trials were conducted on Model B with different data errors, ranging from 1% to 20% of $|\boldsymbol{Z}_{xy} * \boldsymbol{Z}_{yx}|^{1/2}$ for impedance tensor components and from 0.01 to 0.2 for tipper data. The 3D inversion was performed using the off-diagonal elements and tipper data. Identical inversion input parameters were maintained across all inversion runs, including a smoothing parameter of 0.3 and a starting model of 100 Ωm.

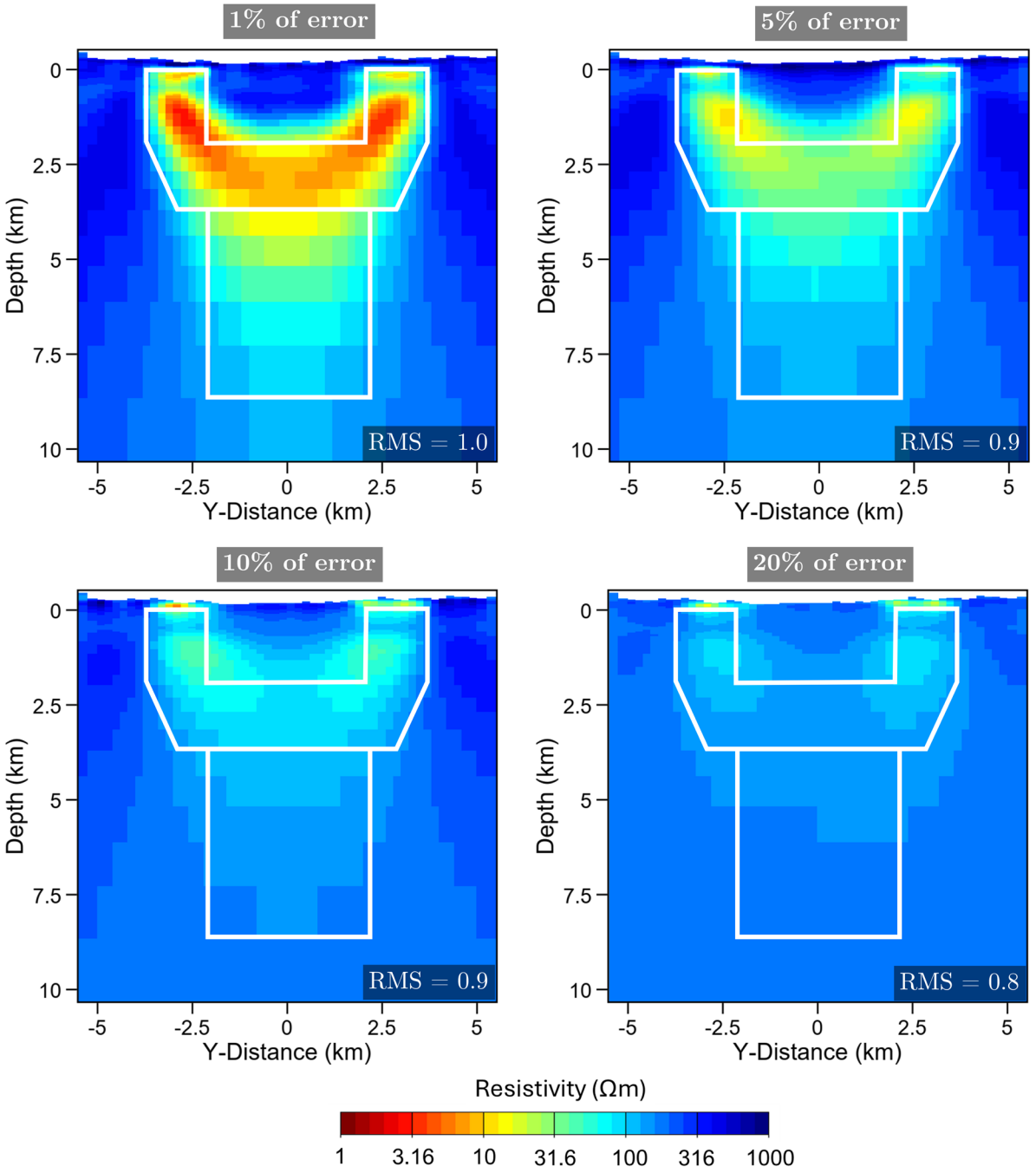

Figure 7.15: Inversion results utilizing different error settings presented as vertical cross-sections. The actual position of the conductive anomaly structure is indicated by the white lines.

Figure 7.15 displays the influence of the error level on the resolution of the anomaly and the RMS values throughout the inversion model. The actual position of the conductive anomaly is indicated by distinct white lines for clarity. It is clear that the structure is better retrieved when data errors are set to 1%. However, this setting produces significantly lower resistivities than the actual values, particularly in the upper structure of the anomaly. On the other hand, both the location and resistivity values of the reservoir (lower part) and its associated protrusions anomaly (upper part) can

be reasonably detected with data errors of 5% in impedance. With the increasing error level, the error-weighted sensitivity gets smaller, and the resistivity value and shape of the anomaly are less well retrieved. At an error level of 20%, the ability to accurately resolve either the location or resistivity value of the anomaly is severely compromised, with neither aspect being effectively captured in the model.

7.5 Influence of Different Data Components

In this sub-chapter, a comprehensive investigation of various inversion scenarios based on different data components was carried out to assess their reliability and data misfit. The initial focus was on performing 3D inversion using different elements of the impedance tensor. Specifically, inversions that utilized only the off-diagonal elements against those that employed the full impedance tensor (which includes both off-diagonal and diagonal elements) were examined and compared. Following this, the effect of integrating tipper data into the 3D inversion process was investigated. This inclusion allowed us to compare the results of inversions that utilized both datasets against those that relied solely on the impedance tensor, providing insights into the advantages and limitations of each approach in capturing the complexities of the subsurface.

7.5.1 Full Impedance Tensor and Off-Diagonal Tensor Elements

3D MT inversion can be performed by inverting only the off-diagonal elements of the impedance tensor, $\boldsymbol{Z_{xy}}$ and $\boldsymbol{Z_{yx}}$, which couple orthogonal electric and magnetic field components. Alternatively, the inversion can include the full impedance tensor comprising the diagonal elements $\boldsymbol{Z_{xx}}$ and $\boldsymbol{Z_{yy}}$, which are parallel electric and magnetic fields. Various studies have examined the reliability and effectiveness of each tensor data element. For instance, Siripunvaraporn et al. (2005) emphasized the significance of incorporating the diagonal impedance elements $\boldsymbol{Z_{xx}}$ and $\boldsymbol{Z_{yy}}$ in the 3D inversion process. These elements are strongly influenced by structures off the profile, making their inclusion vital for producing a more accurate model near the data transect, especially when significant off-profile structures are present. In contrast, Newman et al. (2008) observed that the diagonal elements ($\boldsymbol{Z_{xx}}$ and $\boldsymbol{Z_{yy}}$) exhibit significantly lower magnitudes and, consequently, lower signal-to-noise ratios in comparison to the off-diagonal elements ($\boldsymbol{Z_{xy}}$ and $\boldsymbol{Z_{yx}}$). This discrepancy tends to degrade the performance of the inversion process. However, it is important to highlight that neither of the studies considered topographic terrain, as is not the case in the Al-Lith area. Therefore, both scenarios will be evaluated and explored in this study.

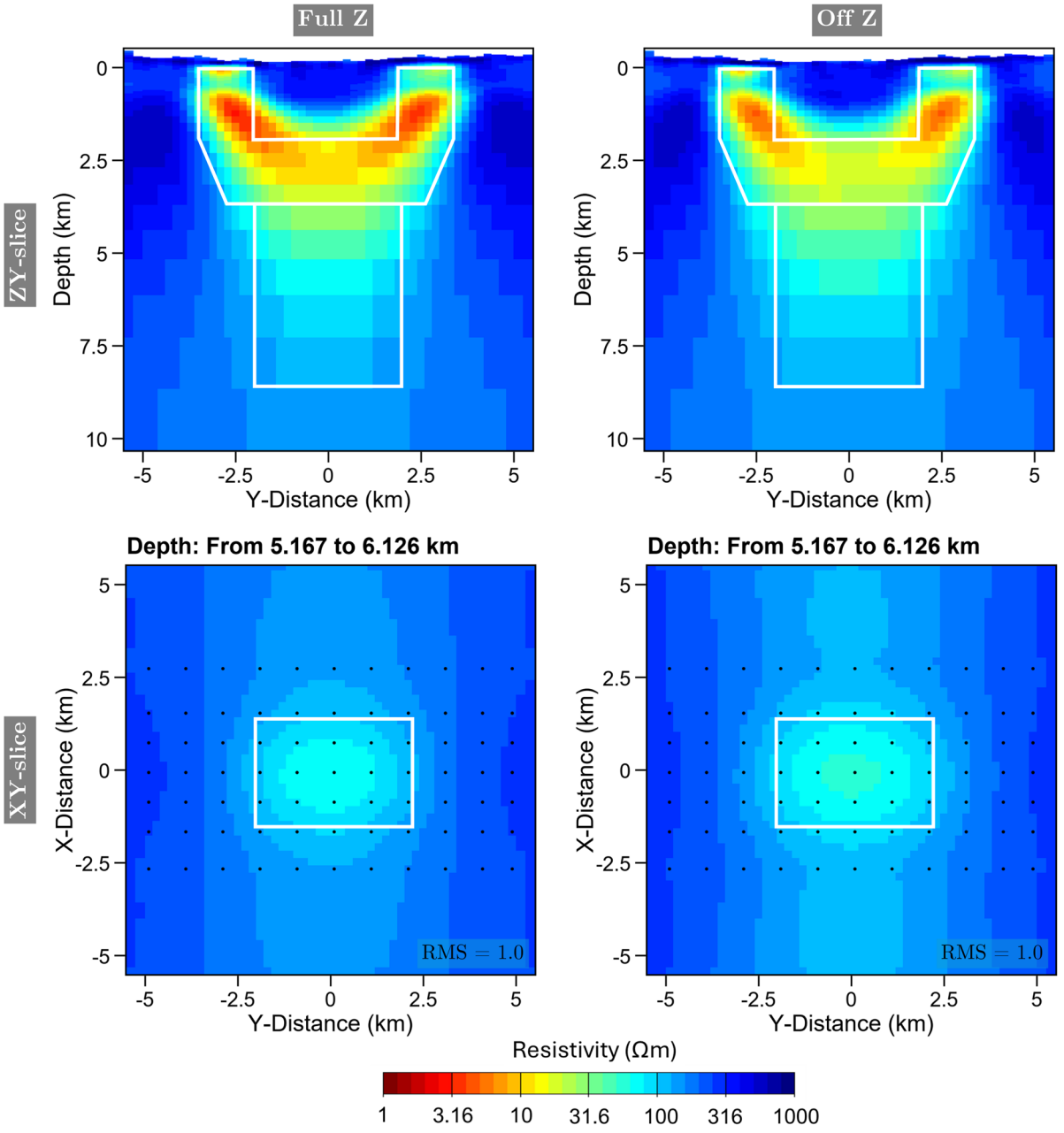

Figure 7.16: Inversion results presented as vertical cross-sections (ZY-slice) and horizontal views (XY-slice) utilizing different data tensor elements. The actual position of the conductive anomaly structure is marked with white lines.

Figure 7.16 shows the inversion results of both full impedance tensors (Full Z) and off-diagonal tensor elements (Off Z) applied to the calculated data of Model B. The starting model and the inversion parameters used remained the same across both tests, ensuring a level of consistency in the approach. Notably, both scenarios achieved an optimal RMS value of 1 and yielded satisfactory results. The anomaly structure was successfully retrieved in both inversion tests; however, there is a slight variation in the coverage. The upper part of the anomaly is better resolved when the full impedance tensor is selected compared to the off-diagonal elements model. But, for the lower part of the

anomaly (reservoir), the inversion model utilizing off-diagonal elements demonstrates better coverage (i.e., reaching a similar size to the actual dimension), whereas the full impedance tensor model primarily images the center of the anomaly. In the specific case of the Al-Lith area, both the full impedance tensor and the off-diagonal tensor elements are applicable for inversion, each with its own advantages and disadvantages in some parts. Further testing of both scenarios on actual MT field data is necessary.

7.5.2 Inclusion of Tipper Data

In addition to the impedance tensor, valuable insights into lateral variations in subsurface conductivity structure can be obtained from the tipper data. The tipper, also known as the vertical magnetic transfer function (VTF), exhibits a high sensitivity to lateral conductivity contrasts (e.g., boundaries of conductive and resistive regions). It is particularly useful for identifying 3D structures and detecting anomalies that might not be evident from the impedance tensor alone (Berdichevsky & Dmitriev, 2008). While the impedance tensor addresses horizontal field interactions, the tipper includes vertical field responses, making it complementary for 3D inversion. Since tipper data are primarily influenced by magnetic fields, they are less susceptible to the galvanic effects that can significantly distort impedance tensor measurements, allowing for a more reliable assessment of subsurface conductivity structures[2].

Several studies have compared the two approaches and demonstrated that incorporating tipper data alongside the impedance tensor enhances the reliability of the subsurface model. Berdichevsky et al. (2003) explored tipper data through analytical and modeling approaches and concluded that incorporating these additional induction transfer functions can substantially enhance the reliability of geoelectrical models. Siripunvaraporn & Egbert (2009) proposed that a joint inversion of tipper and impedance tensor data can effectively constrain subsurface structures, as demonstrated in both synthetic and real data examples. Additionally, inclusion of tipper data improved the sensitivity at depth and obtained the lateral constraints (Čuma et al., 2017). In straightforward cases where structures are already well resolved by impedance data, the contribution of tipper data to the inverse solution may be minimal. However, in more complex scenarios, incorporating tipper data leads to significant adjustments in the inverse solution. Since the joint inversion model accommodates both datasets, it is likely to yield more reliable results. Moreover, this approach effectively combines the high spatial resolution of the full impedance tensor with the superior depth sensitivity of the tipper (Čuma et al., 2017; Pace et al., 2022).

[2] When galvanic distortions are present.

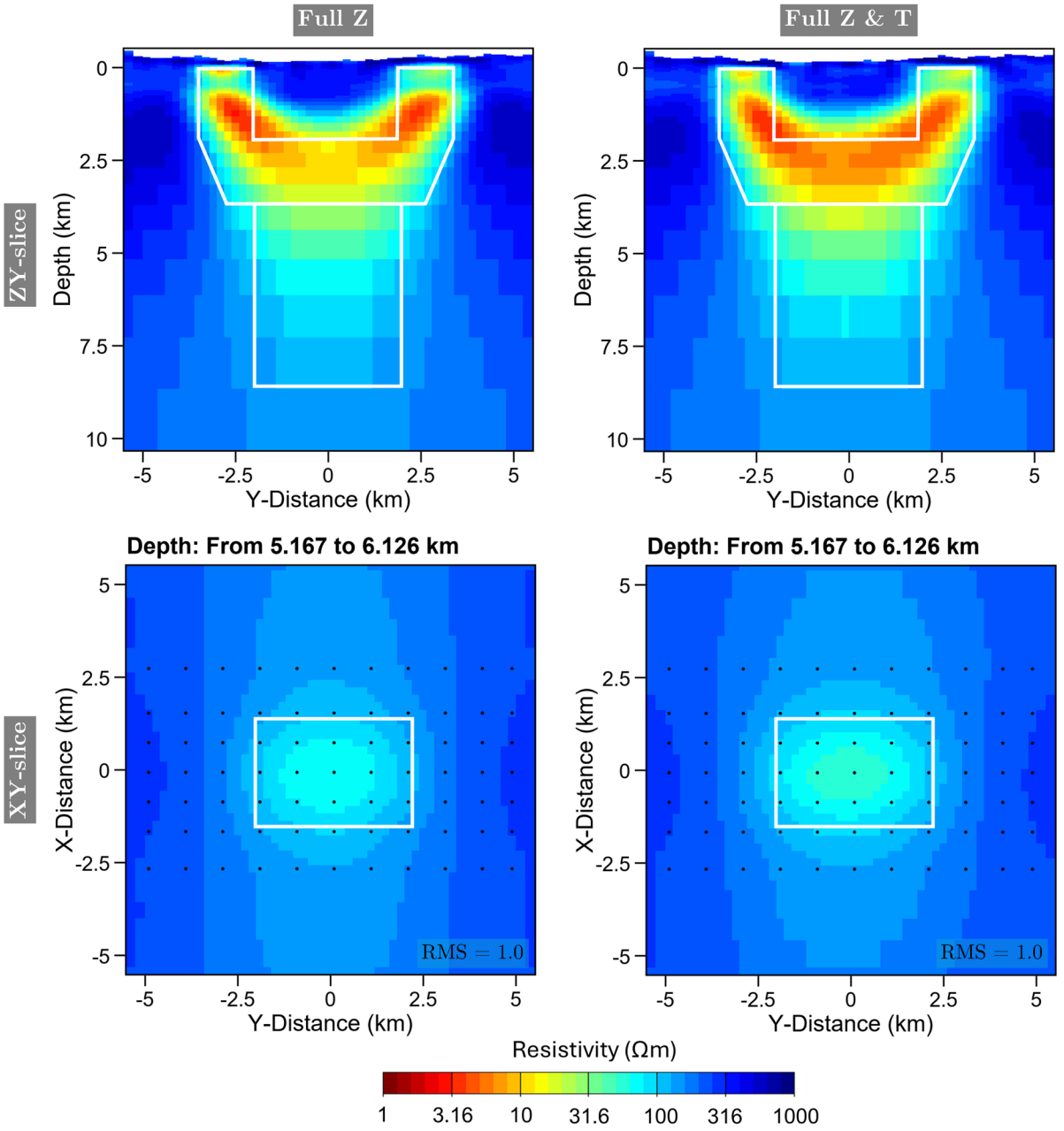

Figure 7.17: Inversion results of two scenarios: with and without tipper (VTF) data, presented as vertical cross-sections (ZY-slice) and horizontal views (XY-slice). The actual position of the conductive anomaly structure is marked with white lines.

The inversion of full impedance tensors, both with and without the inclusion of tipper data, was carried out on the synthetic Model B. The comparison of the results of both scenarios is displayed in Figure 7.17. Notably, both scenarios achieve an impressive overall RMS value of 1, suggesting that even without tipper data, it is capable of effectively delineating the underlying anomaly structure. However, a closer examination of the results indicates that incorporating tipper data leads to notable enhancements, particularly regarding the dimension size of the anomaly. Specifically, the model that included tipper data offers a more accurate representation of the protrusions,

demonstrating superior coverage and detail. Furthermore, for the deeper part of the anomaly—identified as a reservoir—the resistivity values derived from the model with tipper data were closer to the actual value, suggesting that this additional data contributes to a more reliable inversion outcome. Therefore, it is recommended to incorporate tipper data alongside the impedance tensor, as it enhances the reliability of the subsurface model. Nonetheless, the extent of improvement may vary depending on the complexity of the actual model.

7.6 Summary of 3D Synthetic Modeling Studies

The 3D synthetic modeling studies conducted provided valuable insights into the application of the Magnetotellurics (MT) method in geothermal exploration, as well as various parameters that can influence or potentially hinder the effectiveness of the 3D MT inversion process. To fully assess the capabilities of 3D MT inversion for geothermal exploration, two scenarios were analyzed: one with a highly conductive clay cap and the other without. Prior to this, the effects of topographic variations within the study area were also analyzed. The findings of this chapter can be summarized as follows:

- The topography of the Al-Lith area caused significant inductive and galvanic distortions on the MT transfer function data. Therefore, incorporating topography into the initial model is crucial to mitigate the risks of misinterpretation.

- In geothermal systems with a conductive clay cap, the MT method effectively maps the conductive clay cap and delineates the transition to the geothermal reservoir. This provides valuable insights for geothermal exploration. Conversely, in systems without a clay cap, 3D MT inversion demonstrates considerably enhanced coverage of the geothermal reservoir and its associated protrusions, which act as pathways for geothermal fluids to migrate, either to the surface or the near subsurface.

- Selecting an appropriate prior or initial resistivity model is vital for the 3D MT inversion. A well-chosen initial model serves as a solid starting point that avoids dramatic resistivity variations during iterations, which could destabilize the inversion. The most efficient iterations and the lowest overall RMS values are achieved when the initial model is close to the regional average resistivity.

- All input parameters for the 3D MT inversion must be systematically tested to identify the most suitable ones for the specific data set, particularly the smoothing

parameter and data errors, as they have a significant influence on the inversion output.

- 3D MT inversion can be performed by inverting only the off-diagonal elements of the impedance tensor or by including the full impedance tensor, which consists of both the diagonal and off-diagonal elements. Each approach has its own advantages and disadvantages, and further testing on actual MT field data is necessary to determine the best scenario.

- Finally, it is recommended to incorporate tipper data alongside the impedance tensor, as this enhances the reliability of the subsurface model. However, the extent of improvement may vary depending on the complexity of the actual geological model.

Chapter 8

3D Inversion of MT Field Data

As demonstrated in Chapter 6, the dimensionality analysis of the MT phase tensor and its skew calculations reveals the complexity and variability of the subsurface conductivity in the study area, transitioning from simpler 1D and 2D structures at shorter periods to more intricate 3D structures at longer periods, particularly at longer periods of ≥16 s. In response to these findings, 3D MT data inversion was carried out using the well-established 3D modular EM inversion algorithm ModEM (Egbert & Kelbert, 2012; Kelbert et al., 2014).

Inversion serves as a mathematical tool designed to transform observed or collected data into a more meaningful model structure. Due to the non-uniqueness of inversion, it is possible for the same dataset, accompanied by identical error bars, to produce multiple models that adequately fit the data (Siripunvaraporn, 2012). To address this challenge, extensive 3D MT inversion tests were conducted. These tests varied several parameters, including the type of data inverted, smoothing factors, static-shift corrections, topography incorporation, and initial resistivity model adjustments. This systematic test aimed to evaluate the robustness and reliability of the resulting 3D models.

The 1D resistivity model derived from TEM shallow data was also integrated into the starting model to optimize the 3D MT inversion process. Following the inversion, sensitivity studies were conducted to determine the depth of investigation and to assess the detected structures' reliability. The most reasonable inversion model, validated through these tests, was then used for further interpretation and correlated with the geological data from the study area. This chapter begins with a theoretical overview of the inversion algorithm used, providing context for the methodology and ensuring a clear understanding of its application to the study.

8.1 ModEM Inversion Scheme

ModEM is a widely used software package that includes both forward and inversion schemes for EM geophysical data. The inversion scheme implemented is based on the non-linear conjugate gradient (NLCG) method (e.g., Rodi & Mackie, 2001), which has

been described in chapter 3. In order to recover an Earth conductivity model, ModEM considers regularized inversion through gradient-based minimization of a penalty functional of the form:

$$\boldsymbol{\Phi}(\boldsymbol{m},\boldsymbol{d}) = \big(\boldsymbol{d}-\boldsymbol{F}(\boldsymbol{m})\big)^T \boldsymbol{C}_d^{-1}\big(\boldsymbol{d}-(\boldsymbol{F}(\boldsymbol{m})\big) + \lambda(\boldsymbol{m}-\boldsymbol{m}_0)^T \boldsymbol{C}_m^{-1}(\boldsymbol{m}-\boldsymbol{m}_0) \tag{8.1}$$

where $\boldsymbol{d}$ is the observed data, $\boldsymbol{F}(\boldsymbol{m})$ describes the forward problem, $\boldsymbol{C}_d$ is the covariance matrix of data errors, $\boldsymbol{m}_0$ is a set of prior or first guess model parameters, λ is the so-called trade-off parameter, and $\boldsymbol{C}_m$ is the model covariance or regularization term which describes the model smoothness. This model regularization $\boldsymbol{C}_m$ removes excessively rough solutions and/or those that significantly deviate from the prior model by imposing an additional constraint on the data fit. The trade-off parameter λ controls the balance between data fit and model smoothness. Initially, the inversion process is primarily driven by model smoothness; as it progresses, the focus shifts to minimizing data misfit while gradually reducing the smoothness constraint by decreasing λ . The NLCG inversion scheme iteratively solves for the subsurface model by searching for the steepest gradient of the penalty function (equation 8.1) at each iteration.

In the ModEM algorithm, the data covariance C_d is represented as a diagonal matrix containing the inverse of the squared data errors for each data point:

$$C_d = diag\left(\frac{1}{{e_i}^2}\right) \tag{8.2}$$

The model covariance matrix C_m is constructed as a sequence of 1D smoothing and scaling operators:

$$C_m = c_x c_y c_z c_z^T c_y^T c_x^T \tag{8.3}$$

The 1D smoothing operators are block-diagonal and have the form (e.g. for the x-direction):

$$c_x = \begin{pmatrix} c_{11}^x & & & \\ & c_{21}^x & & \\ & & \ddots & \\ & & & c_{N_yN_z}^x \end{pmatrix} \tag{8.4}$$

with one block corresponding to each x-yz cell pair of the model mesh with Ny and Nz cells in y- and z-directions, respectively. Each block c_{jk}^x is constructed by an autoregression scheme:

$$c_{jk}^x = \begin{pmatrix} 1 & & & \\ \alpha_x & 1 & & \\ \alpha_x^2 & \alpha_x & 1 & \\ \vdots & & & \ddots \\ \alpha_x^{N_{x-1}} & & \dots & 1 \end{pmatrix} \tag{8.5}$$

The parameter α_x governs the level of model smoothness in x-direction, and similarly, smoothing is set up for y- and z-directions, where the parameter ranges from 0 to 1 (Tietze, 2012). To evaluate the quality of the inversion result, the normalized root means square misfit (RMS) is calculated using equation 3.7 ($RMS = \chi$), with N is the number of responses at all MT sites and all periods.

The ModEM modules are organized in three layers, illustrated in Figure 8.1. The basic layer on the left focuses on the discretization and numerical solution for the forward problem, while the right-side features generic routines for various EM inverse problems. The central interface layer conceals the implementation details, ensuring modularity and usability. Each layer contains modules that, like the inversion algorithms, remain independent of data types and discretization. The ModEM package is coarsely parallelized to enhance efficiency by distributing forward modeling and sensitivity calculations across multiple processors, reducing memory use and run times. Maximum efficiency is achieved by distributing the modeling task over $2 \times Np$ processors, with Np is the number of periods used. The parallelization development of ModEM3DMT is detailed in Meqbel (2009), and a description of the implementation of MT transfer functions and phase tensor can be found in Tietze (2012).

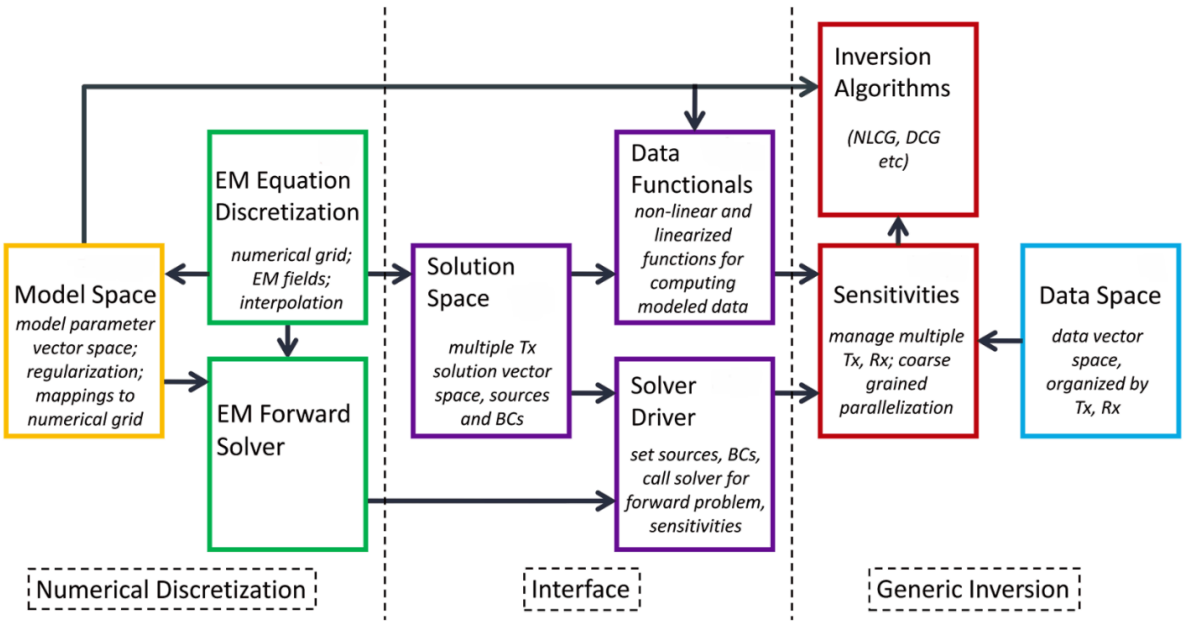

Figure 8.1: Schematic overview of the ModEM system. Boxes represent modules organized in three layers, with dependencies defined by arrows. Figure modified from Egbert & Kelbert (2012).

8.2 Inclusion of SSC and Implementation of Topography

The study area, located in a mountainous region, exhibits moderate to extreme topographic variations, as shown in Figure 5.2. As described in Section 7.2, topographic distortions can significantly impact MT data, manifesting both galvanic and inductive effects, leading to erroneous interpretations of subsurface resistivity structures. The so-called galvanic distortions, induced by topography or near-surface heterogeneities, are known as static shift effects (Jiracek, 1990; Sternberg et al., 1988). According to some researchers (e.g. Árnason, 2015; Árnason et al., 2010; Ledo et al., 2002), static shift effects must be corrected from the data before the inversion process, with transient electromagnetic (TEM) soundings commonly used for this purpose (Pellerin & Hohmann, 1990; Sternberg et al., 1988). However, Watts et al. (2013) highlighted the limitations of correcting MT static shifts using TEM data in the area with significant topographic variations, as it can produce misleading results. They emphasized that, with modern broad-band MT instrumentation, comprehensive modeling of the topography is more likely to yield an accurate image of the subsurface.

Static shift corrections (SSC) and the incorporation of topography in inversion cannot be implemented simultaneously, as correcting static shifts using TEM data while also incorporating topography would lead to double counting the shifts due to topography (Árnason, 2015). Therefore, in this section, two different inversions were examined: the first, with SSC and assuming a flat surface—referred to as the "SSC – Flat" model. The second model includes topography without applying any static shift corrections—termed the "No SSC – Topography" model. The high-resolution digital topographic data was extracted from the Shuttle Radar Topography Mission (SRTM), featuring a spatial resolution of approximately 30 meters. This high-resolution topographic data ensures that the inversion process accurately accounts for the terrain variations. It is important to note that both 3D inversion approaches utilize the full impedance tensor and tipper data.

Figure 8.2 presents the models generated by the two different approaches shown as vertical cross-sections (ZY-slice) and horizontal views (XY-slice). The most notable distinction between the two models occurs in shallow structures, extending to approximately 3 km in depth. In contrast, for deeper structures, both models exhibit a high degree of similarity. This indicates that the SSC effectively resolved the galvanic effects of topography which dominate at long periods, but not the inductive effects which are more pronounced at shorter periods. A detailed discussion on the influence of topography can be found in Section 7.2. Regarding the overall RMS values, the Topography – no SSC model achieved a lower value of 2.09, compared to 2.31 for the

SSC – Flat model. Consequently, the model incorporating topography without static shift corrections was chosen for further interpretation and analysis. This approach is also justified by the capabilities of the ModEM 3D inversion code, which compensates for minor galvanic distortions by introducing a sufficiently fine parameterization in the uppermost part of the starting model (Meqbel et al., 2014; Tietze & Ritter, 2013).

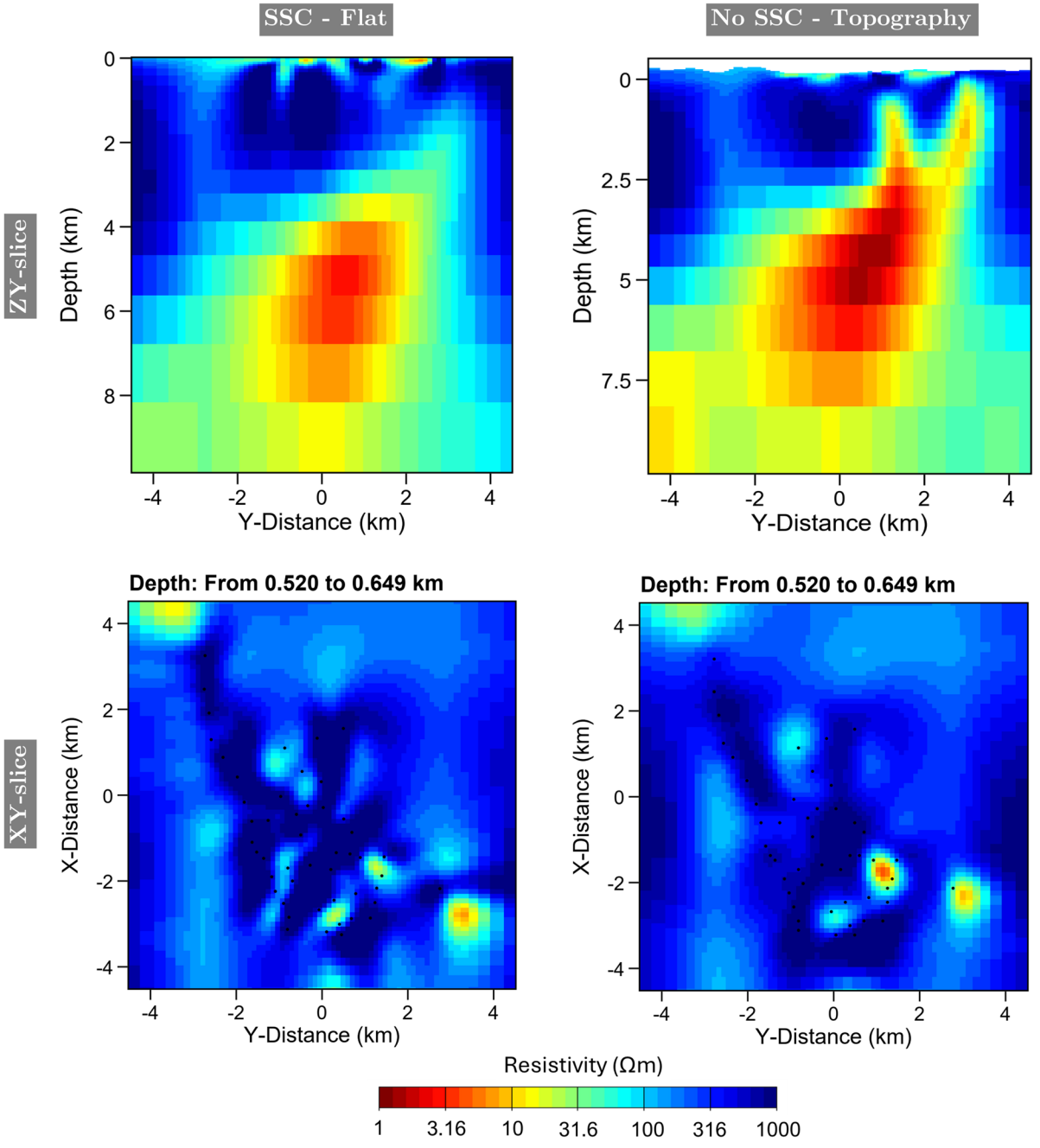

Figure 8.2: The results of both the SSC – Flat and No SSC – Topography inversion models illustrated as vertical cross-sections (ZY-slice) and horizontal views (XY-slice). The models achieved final RMS values of 2.31 for SSC – Flat model and 2.09 for No SSC – Topography model. The most significant difference between the two models is observed in shallow structures, extending to approximately 3 km in depth.

8.3 Selection of Inversion Parameters

ModEM is highly customizable, enabling users to adjust a variety of parameters to optimize inversion results. Therefore, in this study, an extensive series of 3D inversion tests were conducted to systematically assess the robustness of the results and select the most suitable model for further interpretation. Tested parameters included the initial resistivity models, the discretization of cell sizes, the smoothness, and data error settings. These parameters were selected based on the latest literature findings and adapted to our particular dataset and site conditions.

8.3.1 Initial Resistivity Models

As explained in Subsection 7.4.1, selecting an appropriate initial resistivity model has an important role in the 3D inversion scheme. To identify the most suitable starting model for further interpretation, inversion runs are conducted on the MT field data using various starting models. In this study, inversion tests were performed with four distinct homogeneous resistivity values of 10, 100, 250, and 500 Ωm. Four components ($\boldsymbol{Z}_{xx}$, $\boldsymbol{Z}_{xy}$, $\boldsymbol{Z}_{yx}$, and $\boldsymbol{Z}_{yy}$) of impedance tensor and the tipper data were used in the inversion runs. At this stage, the topography was incorporated into the initial models due to the result with topography being better than the one applying static shift correction and without topography.

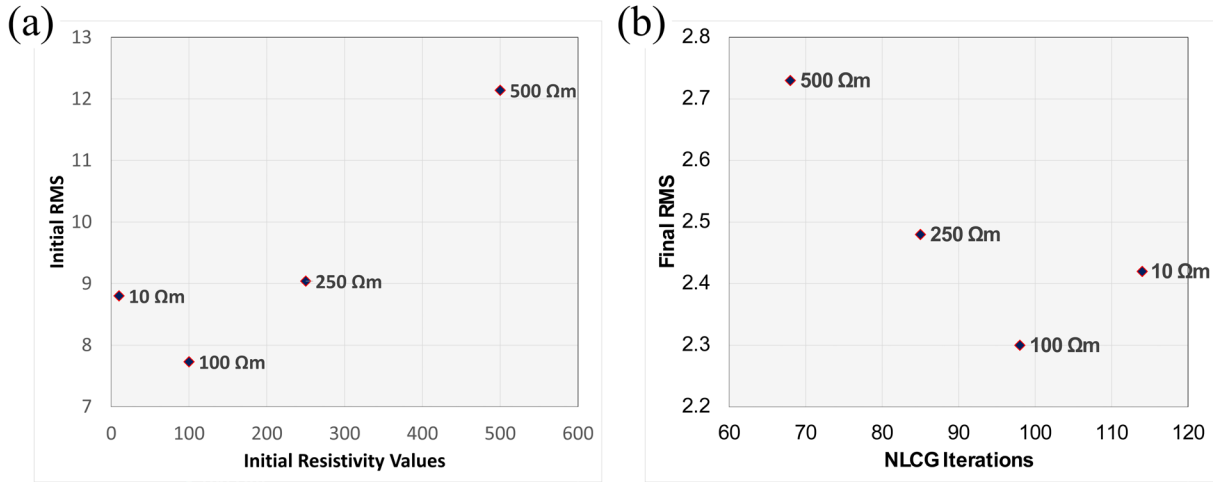

Figure 8.3: Graphic showing (a) initial RMS and (b) final overall RMS values from the 3D inversion trial with four different starting models. The total number of NLCG iterations required for each inversion trial is also plotted.

Figure 8.3 shows the initial and final overall RMS values resulting from four distinct 3D inversion tests, indicating that the starting resistivity model of 100 Ωm achieved the lowest RMS misfit, both initially and upon completion. In order to compare the effects of different initial models, Figure 8.4 presents the resistivity slices at a depth of

~ 6 km from the four inversion trials. The inversion model based on the 100 Ωm initial resistivity value exhibits the most significant contrast between the conductive anomaly and the surrounding host geology. Therefore, due to this pronounced contrast and the lowest RMS value, a resistivity of 100 Ωm was selected as the starting model for subsequent analyses and interpretation.

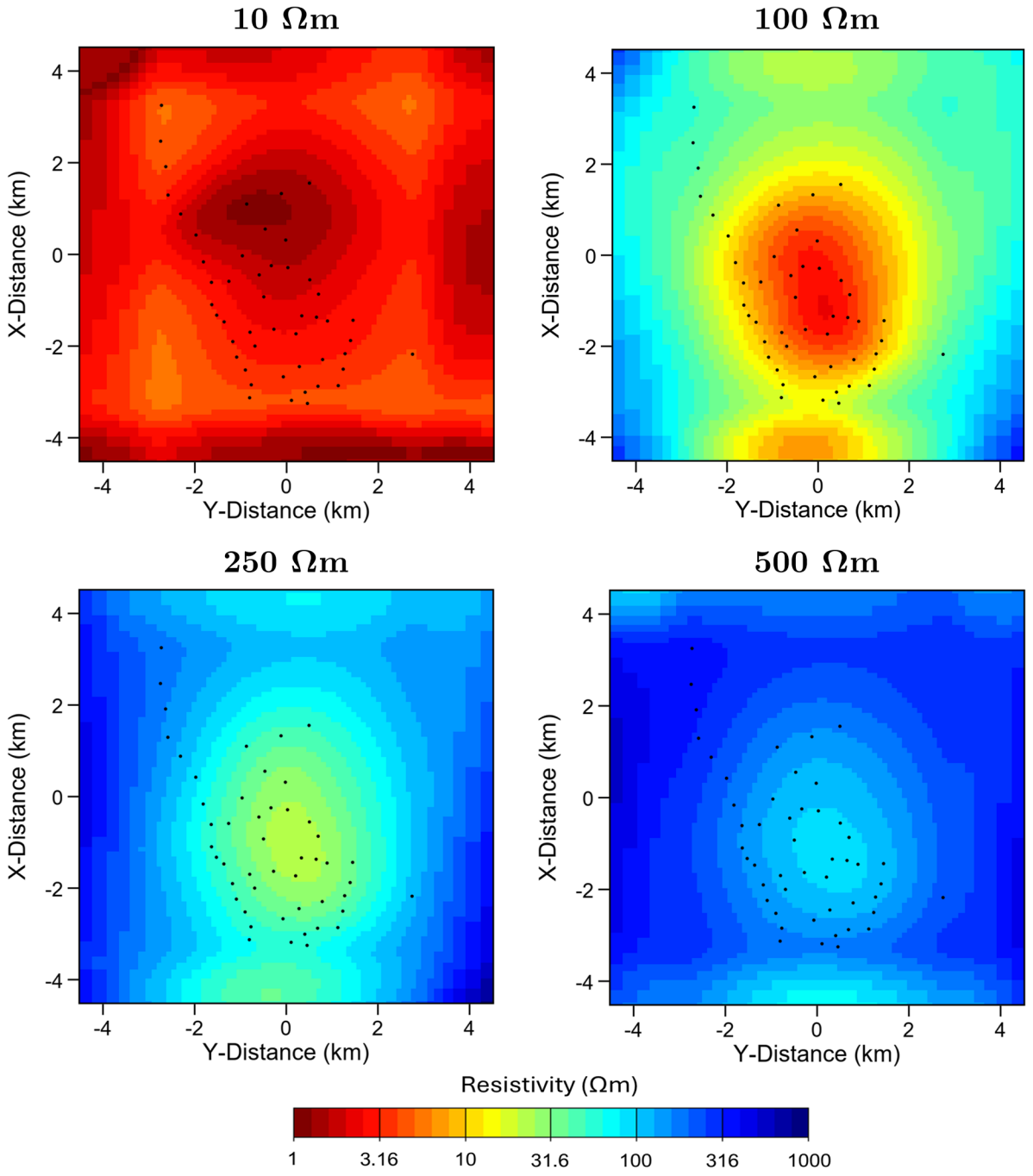

Figure 8.4: Results of the 3D inversion test with four different starting models presented as horizontal resistivity slices at depths of ~ 6 km. The locations of the MT sites are displayed as black dots.

8.3.2 Grid Discretization

It's recommended to run a couple of inversions with different grid resolutions to assess the impact on results, since improper grid discretization can generate errors in the results (Siripunvaraporn, 2012). Please note that the grid must extend sufficiently far beyond the area of interest to avoid boundary effects on the computed EM fields. At the same time, avoid excessively fine grids that increase memory and runtime requirements without significantly improving resolution. When designing the grid, consider skin depth, MT stations separation, and target anomaly structure. Some guidelines for designing a satisfactory grid can be found in Simpson and Bahr (2005). For this purpose, three different vertical (z) grid configurations were tested: (1) 60 layers or nodes, extending to a maximum depth of 153 km; (2) 62 layers with a maximum depth of 265 km; and (3) 65 layers with a maximum depth of 381 km. The dimensions in the other directions were kept constant with 35 km in the N-S (x) direction and 34 km in the E-W (y) direction.

The mesh uses a 3D finite difference grid comprising 98 nodes in the x direction, 88 nodes in the y direction, and three distinct nodes in the z direction. The mesh is centered on the midpoint of the study area, located at a latitude of 20.4685°N and a longitude of 40.4821°E. The horizontal cell dimension is 109 m x 109 m. To accumulate the boundary effects, 17 padding cells are added in each horizontal direction, with their size increasing by a factor of 1.2. The first 20 vertical layers of the mesh have a uniform thickness of 25 m each. Beyond these, the thickness of subsequent layers increases by a factor of 1.2 until the total number of vertical layers is reached.

The results of three different inversion runs are illustrated in Figure 8.5, showcasing horizontal resistivity slices along with their corresponding overall RMS values. The differences among the models tested are minimal, primarily noticeable in the size of the detected anomalies. The fundamental structure of these anomalies shows a remarkable similarity across all models. Among the models tested, the one utilizing 60 vertical layers resulted in a slightly smaller diameter of the anomaly. In contrast, the inversion models employing 62 and 65 vertical layers yielded anomalies of comparable sizes. The analysis of the RMS values highlights that the 60-layer model achieved the highest RMS value, exceeding 2.8, indicating a lower fit to the data. Both the 62- and 65-layer models, however, demonstrated more comparable RMS values, maintaining a range of 2.2. Ultimately, the model with 62 vertical layers was selected for further analysis, as it provided a balanced combination of reasonable results and a favourable RMS value, coupled with faster iteration times compared to the model with 65 layers.

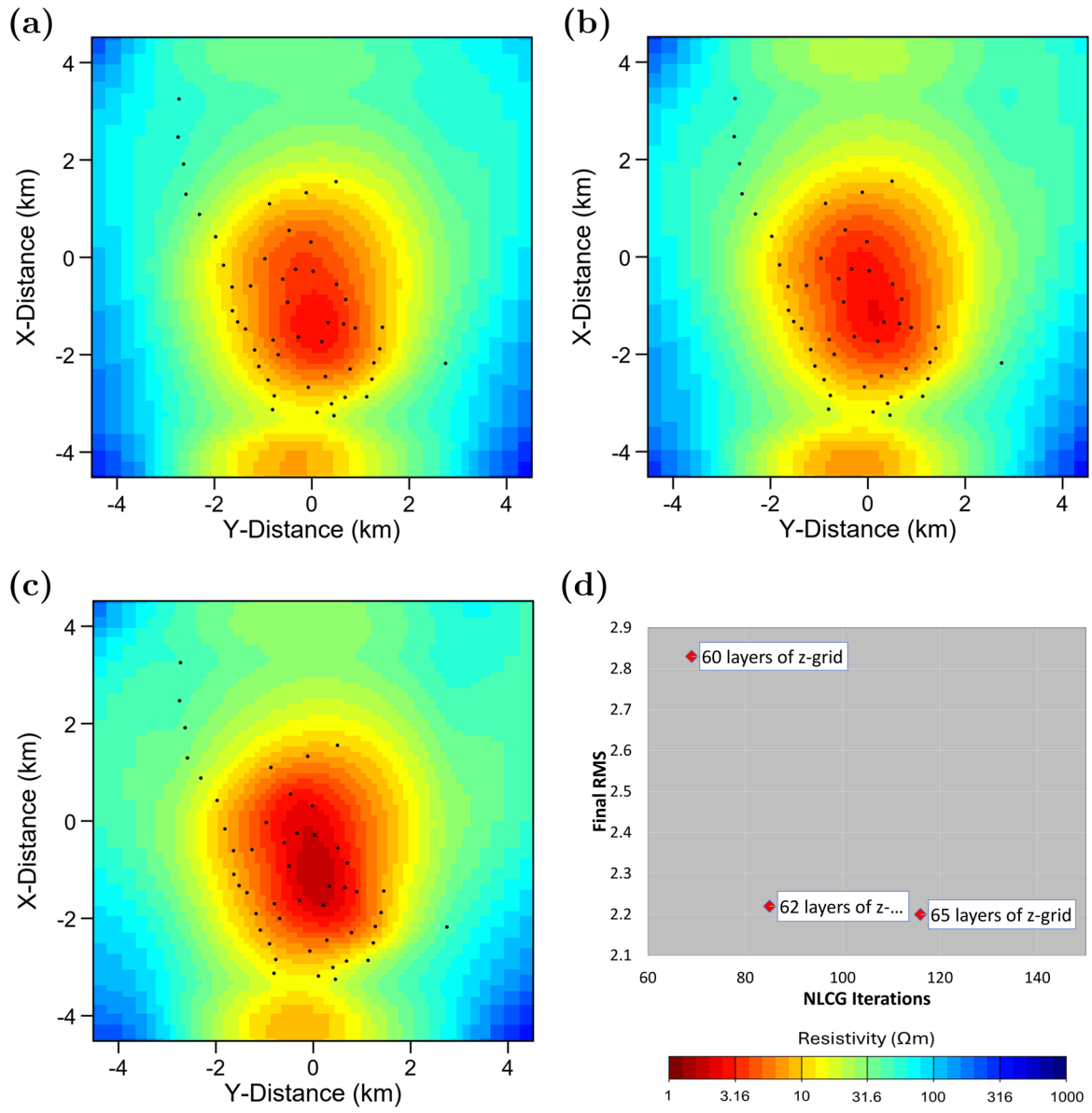

Figure 8.5: Horizontal resistivity slices at depths of ~ 6 km extracted from the 3D inversion trials with (a) 60 layers, (b) 62 layers, and (c) 65 layers of vertical z-grid discretizations. (d) The final RMS values of the 3D inversion trials corresponding to the total number of NLCG iterations required.

8.3.3 Smoothing Parameter (α)

As outlined in Subsection 7.4.2, it's important to test various smoothing parameters (α) to achieve an optimal balance between data misfit and model smoothness. Trials were conducted on the MT field data using three different α values of 0.1, 0.3, and 0.5. The smoothing parameter 0.7 was excluded, as it did not yield a satisfactory RMS value during the synthetic modeling studies discussed in Chapter 7. The inversion results from all three trials are presented in Figure 8.6 as horizontal slices at ~ 2 km depth. The differences among the inverse models, influenced by the chosen smoothing

parameter, are significant. Specifically, the inversion model with a smoothing parameter of $\alpha = 0.1$ reveals a larger area of the conductive anomaly, yet it achieved the smallest overall RMS value. However, it required more than 180 iterations, which makes it impractical. In contrast, the model utilizing $\alpha = 0.3$ yielded a more focused representation of the conductive anomaly with a reasonable RMS value. This concentrated appearance of the conductive anomaly suggests the individual protrusions occurring at shallower depths. On the other hand, the model with $\alpha = 0.5$ is deemed unreliable, as the resistive structure dominates nearly the entire layer, and its RMS is also higher. For these reasons, $\alpha = 0.3$ is selected, as it demonstrates an acceptable RMS alongside reasonable model smoothness and iteration time.

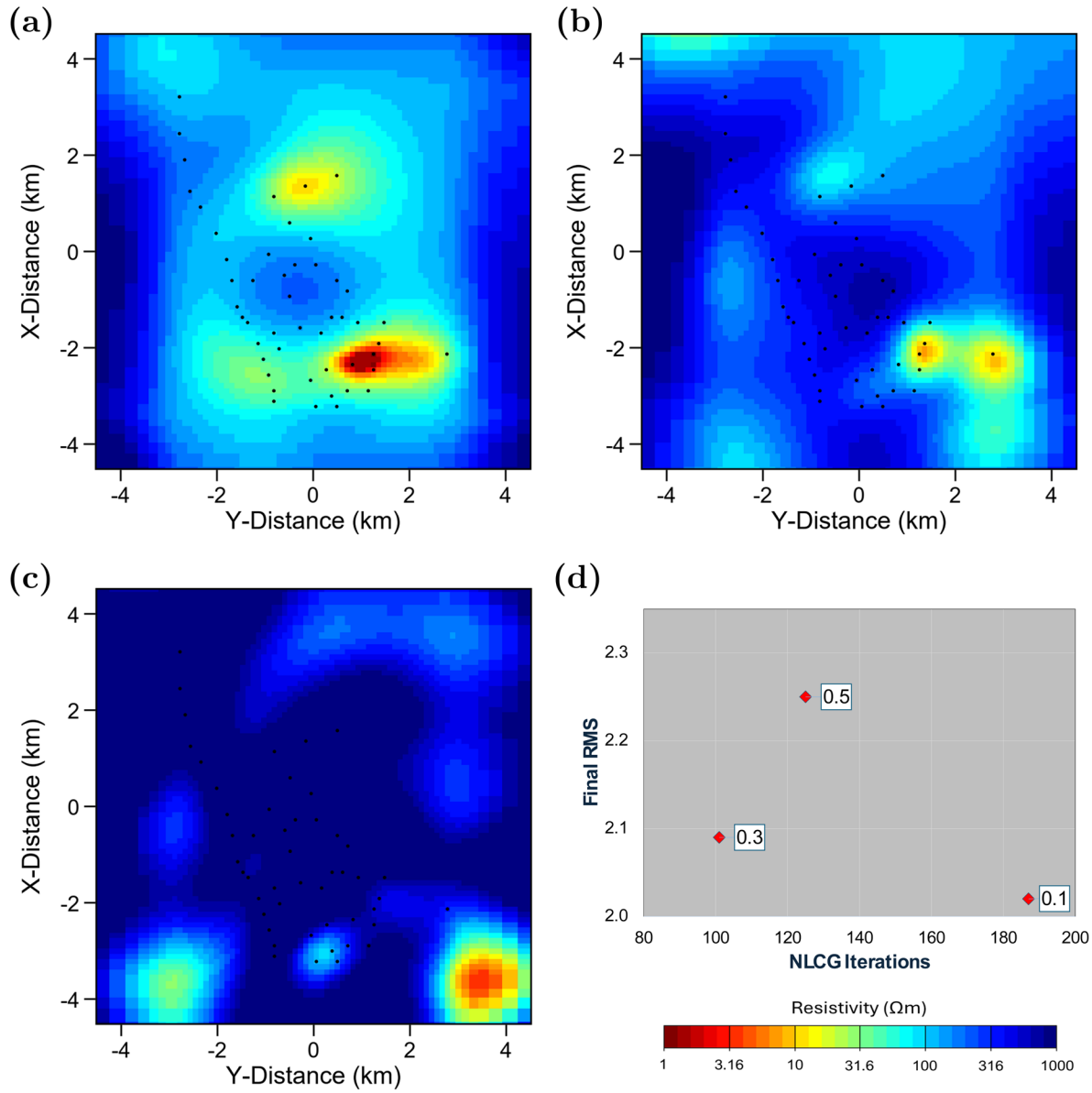

Figure 8.6: 3D inversion models displayed as horizontal resistivity slices at depths of ~ 2 km for various smoothing parameters: (a) $\alpha = 0.1$, (b) $\alpha = 0.3$, and (c) $\alpha = 0.5$. (d) The final RMS values of the 3D inversion trials correspond to the total number of NLCG iterations required.

8.3.4 Error Floor Settings

As demonstrated in the modeling investigation outlined in Subsection 7.4.3, data error settings are an essential input inversion parameter that should be systematically tested to identify the most appropriate option for the given dataset. In this thesis, error floors were determined relative to the mean of the off-diagonal elements $|\boldsymbol{Z}_{xy} * \boldsymbol{Z}_{yx}|^{1/2}$ for the impedance tensor components and constant values for the VTF or tipper elements (Meqbel, 2009; Patro & Egbert, 2011; Tietze, 2012). Three different error floor settings are tested by inverting the off-diagonal elements of the impedance tensor: 1%, 5%, and 10%. The larger error settings are excluded because their ability to accurately resolve the anomaly is severely compromised, as demonstrated in the synthetic studies (Chapter 7). Since the MT field data contains its original error, the associated error was established as the greater value between the original error and the error floor.

Figure 8.7 displays the influence of the error level on the anomaly's imaging, presented as vertical cross-sections. Accompanying this figure, Table 8.1 summarizes the overall RMS values along with the total number of NLCG iterations required for each scenario. Upon analyzing three distinct error floors, it becomes evident that the inversion models exhibit only minor differences. These variations are primarily observed in the resolution of the shallower protrusions (less than 2.5 km) and the deeper conductive structures (greater than 7 km). Despite these slight discrepancies, the overall structural characteristics of the anomalies remain consistent across the different error levels. The RMS values show only modest fluctuations yet correspond to varying iteration times required for convergence. Notably, all three error floors are viable options for 3D inversion. However, the 5% error floor is the most advantageous choice, delivering the lowest RMS values and the shortest iteration times. This makes it the preferred option for achieving optimal results in the inversion process.

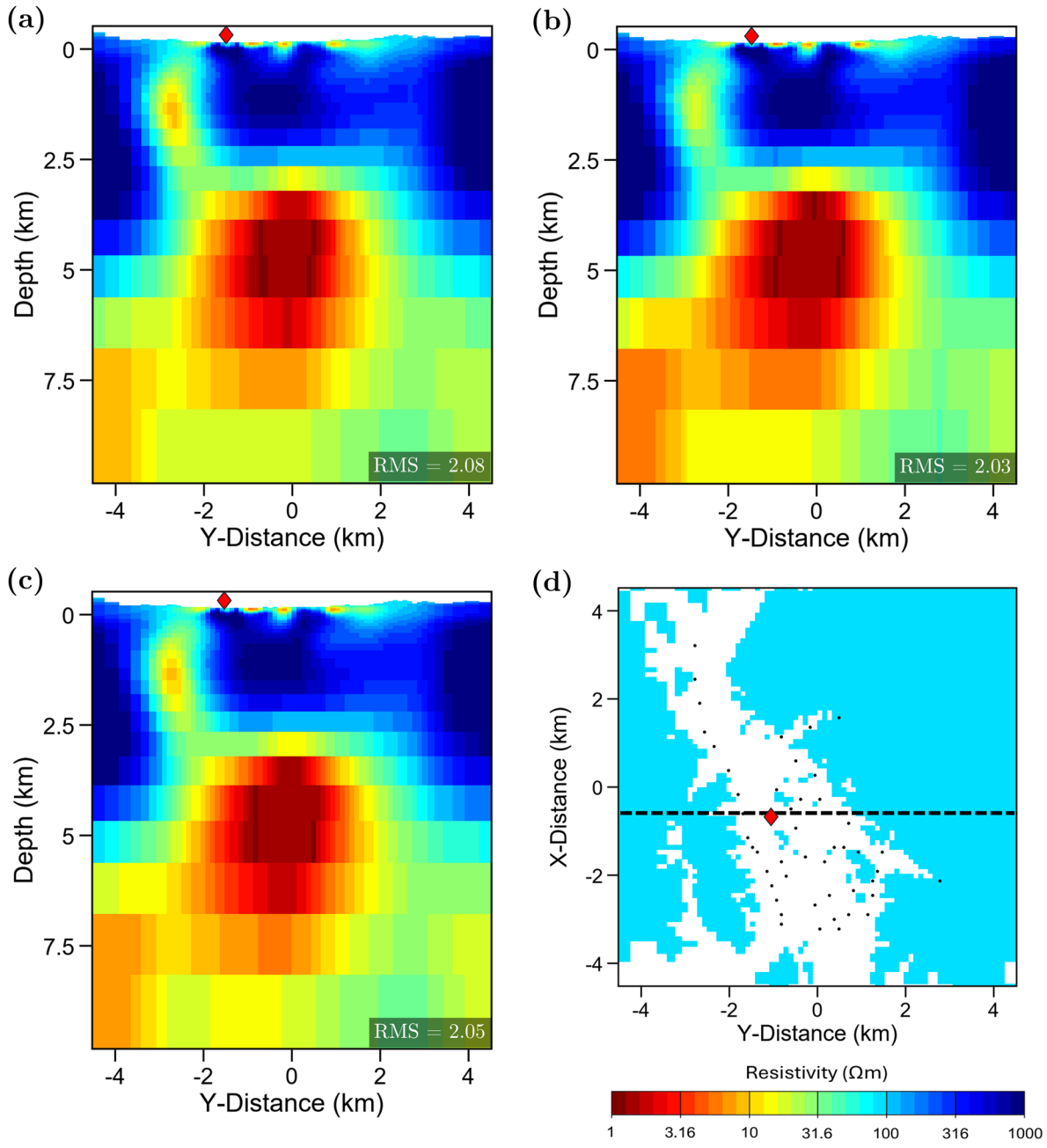

Figure 8.7: Vertical cross-sections extracted from the 3D inversion trials with (a) 1%, (b) 5%, and (c) 10% of error floor settings. (d) The projection of the profile sections onto the plan view. The locations of the MT stations are indicated by black dots, while the red diamond marks the position of the Ain Al-Harrah hot spring.

Table 8.1: Initial and final RMS values of the inversion trials with different error floor settings.

Error Floor	Initial RMS	Final RMS	NLCG Iterations
1%	10.61	2.08	117
5%	10.51	2.03	108
10%	10.53	2.05	131

8.4 Inversion with Different Data Components

This section investigates various inversion scenarios using different tensor elements from the MT field data. The initial focus is on performing 3D inversion by integrating tipper data alongside the impedance tensor. Subsequently, 3D inversions employing different impedance tensor elements are explored. Specifically, inversions that utilized only the off-diagonal elements against those that employed the full impedance tensor (which includes both off-diagonal and diagonal elements) are examined and compared. To ensure consistency throughout the inversion tests, the starting model is set at 100 Ωm, and the inversion parameters remain identical across inversion runs. These parameters include a smoothing parameter of 0.3, an initial damping parameter (λ) of 1, and a 5% error floor.

8.4.1 Inclusion of Tipper Data

It is recommended to incorporate tipper data alongside the impedance tensor, as it enhances the reliability of the subsurface model, as discussed and demonstrated in Section 7.5. However, the extent of improvement may vary depending on the complexity of the actual geological model. In some cases where structures are already well resolved by impedance data, the contribution of tipper data to the inverse solution may be minimal. In this thesis, two scenarios—one with and one without the inclusion of tipper data—are examined using MT field data. The inversion process was carried out on full impedance tensors, with results analyzed for both cases.

The comparative analysis of the two inversion scenarios is depicted in Figure 8.8, showcasing horizontal depth slices. Notably, the inversion model that included tipper data achieved a slightly improved RMS error of 2.09, in contrast to 2.10 for the model without it. While this difference may appear minor, it indicates a trend where the incorporation of tipper data contributes positively to model quality. Particularly at a depth of $\sim$ 1 km, the individual geological features appear more distinctly defined in the model that utilized tipper data, suggesting that its inclusion indeed enhances the granularity of the output model. Nevertheless, it's important to highlight that this improvement was not overwhelmingly substantial, primarily due to the limited availability of tipper data in this study. As a routine procedure, the tipper data used for inversion underwent visual inspection to identify and exclude clearly erroneous responses. After assessing the data quality, 13 out of 14 MT sites that included tipper data were deemed suitable for further detailed analysis, ensuring the robustness of the results obtained. Although the improvement was minimal, the inversion model incorporating tipper data is favored for subsequent analysis and interpretation.

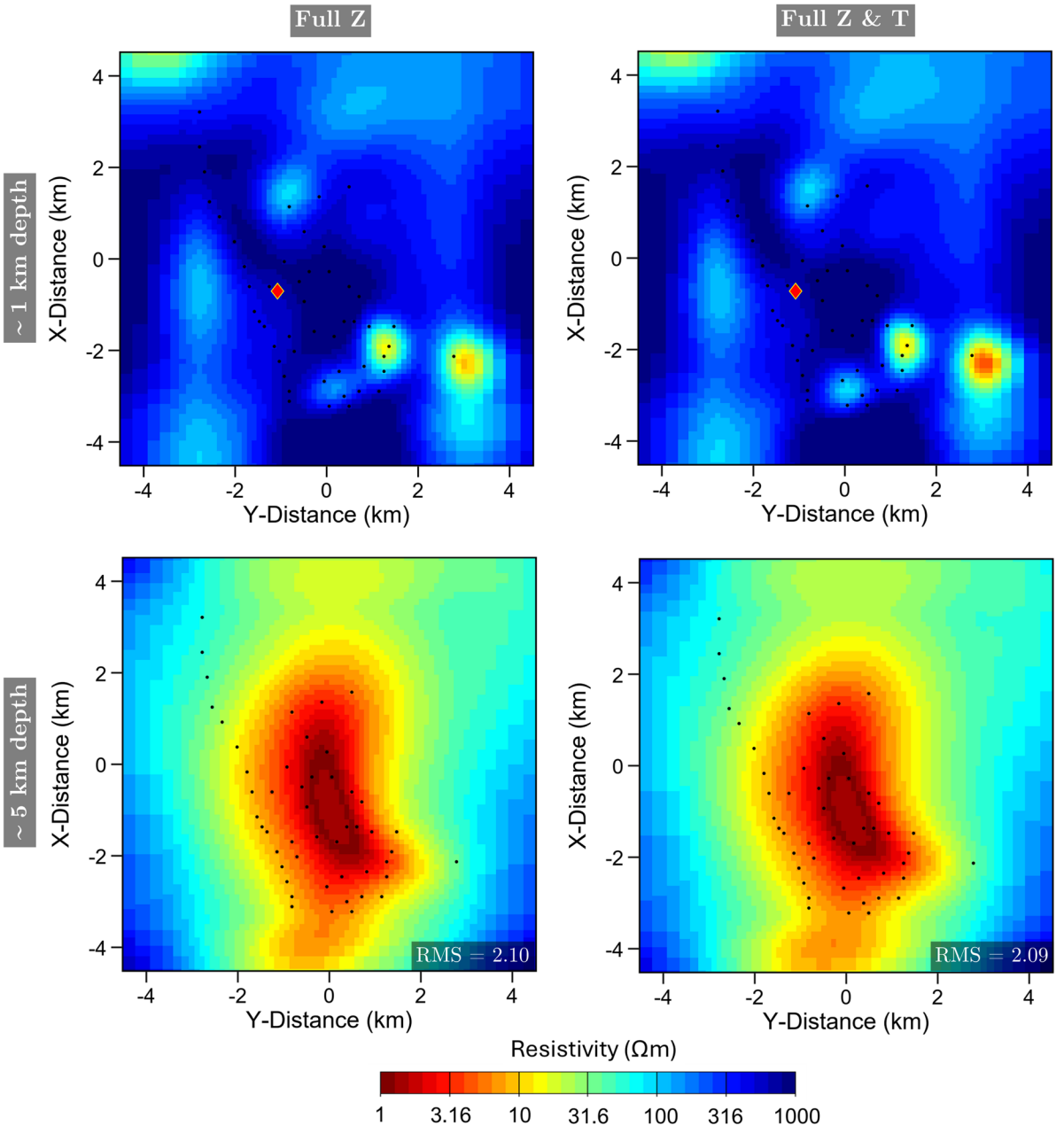

Figure 8.8: The results of two inversion scenarios—one excluding (Full Z) and the other including tipper data (Full Z & T), presented as horizontal resistivity slices at depths of ~ 1 and ~ 6 km. The locations of the MT sites are displayed as black dots.

8.4.2 Off-Diagonal Element and Full Impedance Tensors

As discussed in the 3D Synthetic Modeling Studies (Section 7.5), both the off-diagonal tensor elements and the full impedance tensor are applicable for 3D inversion as both achieved an optimal RMS value and yielded satisfactory results. However, it is important to recognize that each approach presents its own set of advantages and disadvantages. Consequently, further testing on actual MT field data is essential to fully

assess their performance. Figure 8.9 shows horizontal depth slices derived from the inversion results, with both approaches—using the full impedance tensors and the off-diagonal tensor elements—being compared. Tipper data was included in both approaches. To maintain consistency throughout the study, the starting model and inversion parameters were identical across both inversion runs.

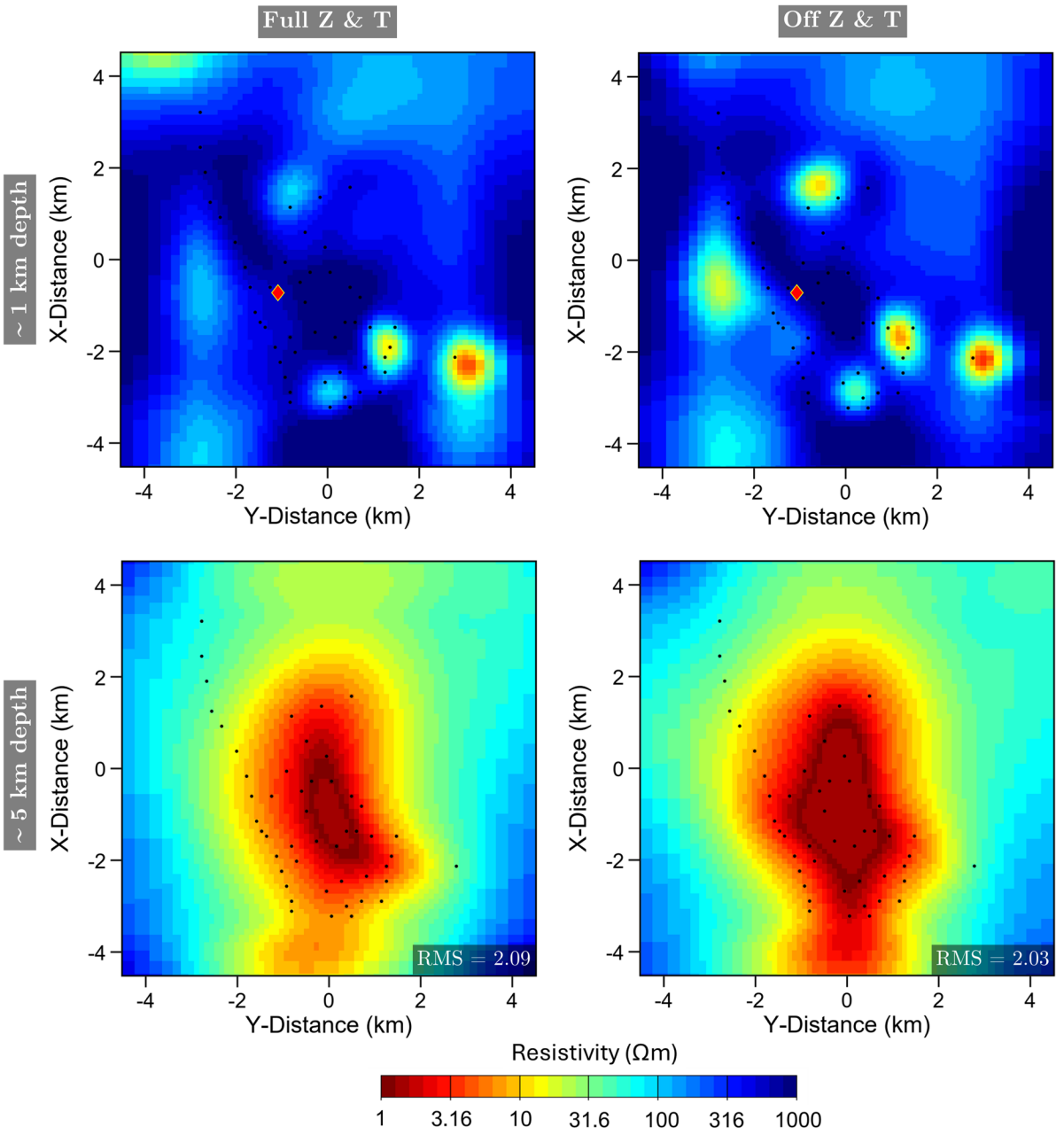

Figure 8.9: The results of two inversion scenarios—one incorporating the full impedance tensor along with tipper data (Full Z & T), and the other utilizing the off-diagonal elements with tipper data (Off Z & T), presented as horizontal resistivity slices at depths of ~ 1 and ~ 5 km. The locations of the MT sites are displayed as black dots.

Notably, the inversion model utilizing off-diagonal elements (Off-Z & T) achieved a better overall RMS of 2.03, compared to 2.09 for the full impedance tensor model (Full

Z & T). At a depth of ~ 1 km, the individual conductive anomalies revealed by the Off Z & T model are notably more distinct and well-defined when compared to those identified by the Full Z & T model. Additionally, at a depth of ~ 5 km, the off-diagonal (Off Z & T) model presents a single dominant conductive anomaly with a larger diameter than that observed in the full impedance tensor (Full Z & T) results. For these reasons, the inversion of the off-diagonal tensor elements is preferred for the MT field data measured in this study, resulting in a more clearly defined model with a lower RMS, which enhances the overall reliability of the findings.

8.5 Inversion with TEM Data As A Priori Information

An additional inversion process was conducted by integrating the TEM model as a priori information. TEM data can be utilized not only to correct static shifts in the MT data but also to enhance the optimization of the 3D MT inversion (e.g. Ruiz-Aguilar et al., 2020). In this section, strategies for incorporating information derived from TEM data are discussed. Prior to that, a description of the 1D inversion of TEM data is provided.

8.5.1 1D Inversion of TEM Data

The processed TEM data were then inverted using the EMUPLUS code developed by the University of Cologne (Scholl, 2005) to generate a suitable resistivity model. Two different 1D inversion techniques were employed: the smoothness-constraint Occam inversion scheme (Constable et al., 1987) and the Levenberg-Marquardt technique (Menke, 2018; Scholl, 2005). The Occam inversion method calculates a multi-layered resistivity model using a first order (R1) smoothness constraint, aiming to produce models with minimal contrasts between adjacent layers by imposing a slight vertical resistivity gradient. This smoothness constraint helps in creating a continuous resistivity profile that is less sensitive to abrupt changes, which might not be justified by the data resolution. In contrast, the Marquardt technique is designed to obtain a simpler earth model characterized by a limited number of layers with distinct layer interfaces, making it useful for interpreting data in terms of discrete geological layers and interfaces. A homogeneous initial resistivity model of 100 Ωm with 30 logarithmically spaced layers was used for the Occam inversion. The resulting model from the Occam inversion model served as a reference and starting model for the Levenberg-Marquardt algorithm, as the latter's results are highly dependent on the initial model input. In addition to generating resistivity models, the uncertainties of the models were derived using equivalent models. These equivalent models provide additional insights into the resolution of the resistivity and thickness of each layer

(Menke, 2018; Yogeshwar et al., 2020). To assess the quality of the inversion, the data misfit was estimated according to Equation 3.7.

Figure 8.10 presents exemplary TEM inversion models and their corresponding data fits for stations TEM26 and TEM27. Similar results were obtained at the rest of the TEM soundings, as seen in Appendix E. The 1D inversion models reveal three main layers: (1) a conductive layer in the first few meters depth, characterized by low resistivity, indicating high water content likely due to infiltrated rainwater from a recent precipitation event, as the TEM survey was conducted during the winter season; (2) a resistive layer extending to a depth of approximately 120 m, probably composed of hard rock or other geologically resistant materials, with high resistivity suggesting dry or les porous formations; and (3) a layer below 120 m depth exhibiting decreasing resistivity, likely associated with sediments saturated with groundwater, indicating the transition to more porous and water-bearing formations at greater depths. Other TEM soundings in the survey area exhibited a similar three-layer structure, with slight variations in resistivity values and depth, attributed to local geological differences and the heterogeneous nature of subsurface materials.

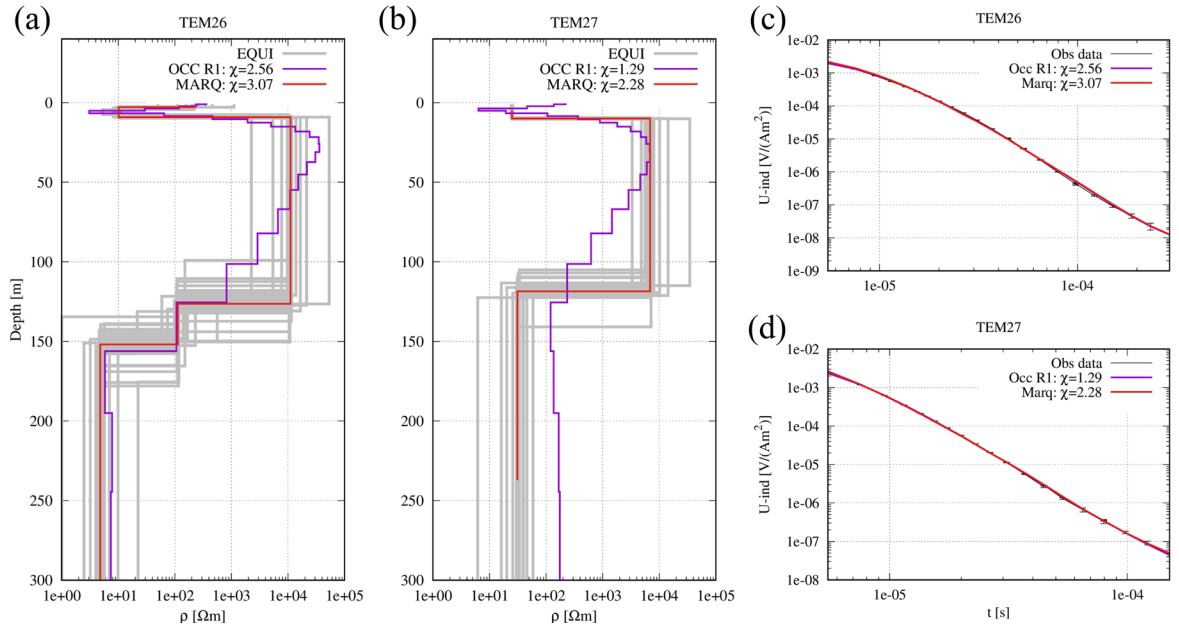

Figure 8.10: 1D inversion results obtained from stations (a) TEM26 and (b) TEM27 with different algorithms: Levenberg-Marquardt (red lines), Occam with a first-order smoothness constraint (magenta lines), and the equivalent model (grey lines). Induced voltage decay over time for observed and calculated TEM data for each inversion approach at stations (c) TEM26 and (d) TEM27.

8.5.2 3D Inversion with A Priori Information from TEM

The resistivity model derived from the Occam inversion of the TEM data was incorporated into the initial model used as a starting point for 3D MT inversion. Figure

8.11 shows the resistivity slices at four different depths, demonstrating how the 1D TEM model was integrated into the initial model for the 3D MT inversion. The model parameters were not fixed, and the TEM information was only used as *a priori*. Due to data quality considerations, 10 out of 13 TEM soundings were incorporated into the starting model. The 3D model, which leveraged a priori information from TEM results, achieved a lower overall RMS of 1.96 after 113 iterations. In comparison, the unconstrained inversion model recorded a slightly higher RMS of 2.03 after 125 iterations. Thus, in terms of RMS, the model that incorporated a priori information from the TEM data resulted in better RMS and allowed for faster convergence.

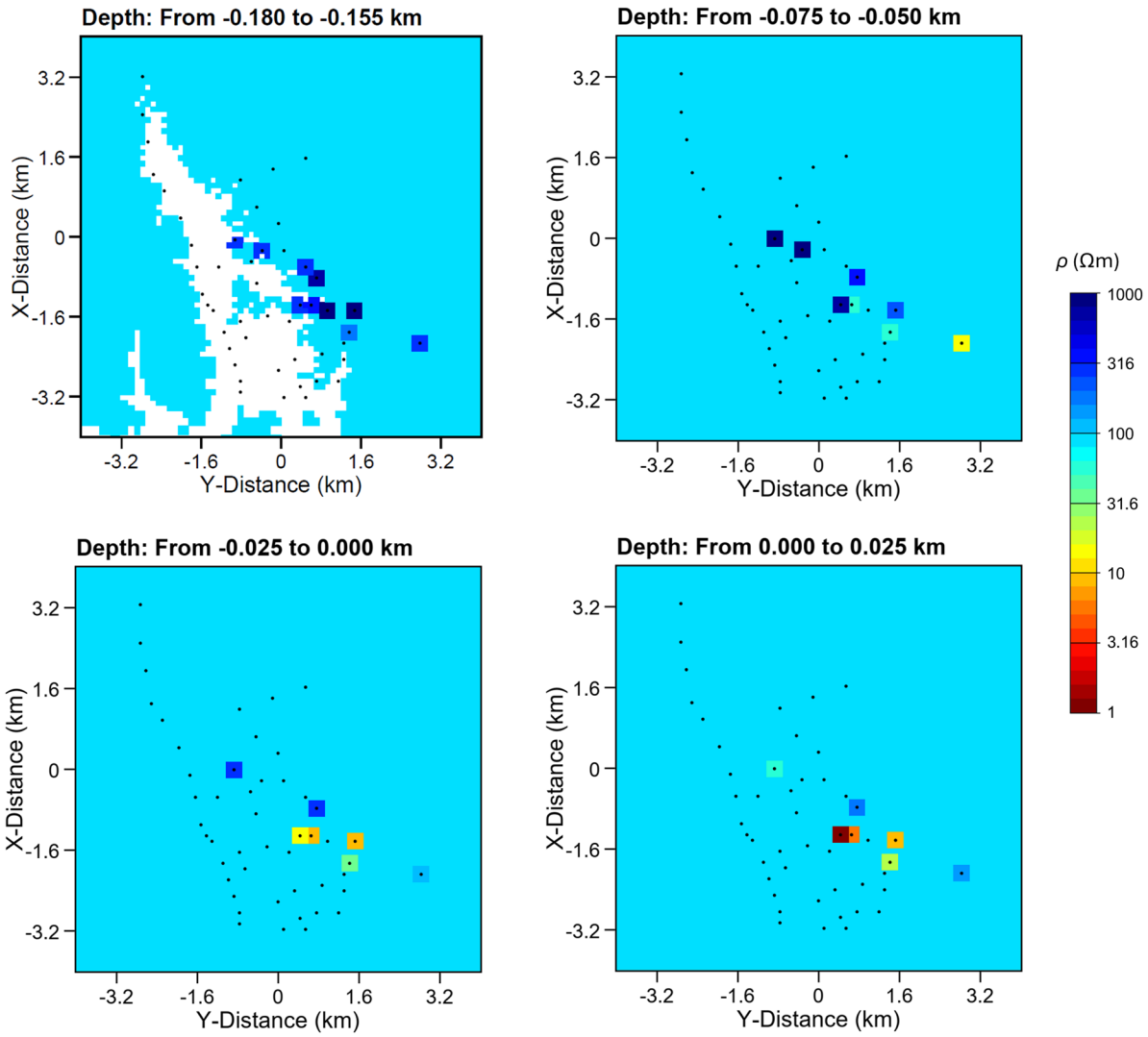

Figure 8.11: Illustration of how the information obtained from the 1D TEM model was incorporated into the starting model used for the 3D MT inversion. The color-coded squares indicate resistivity variations extracted from the 1D TEM model at four different depths. The black dots represent the locations of the MT sites.

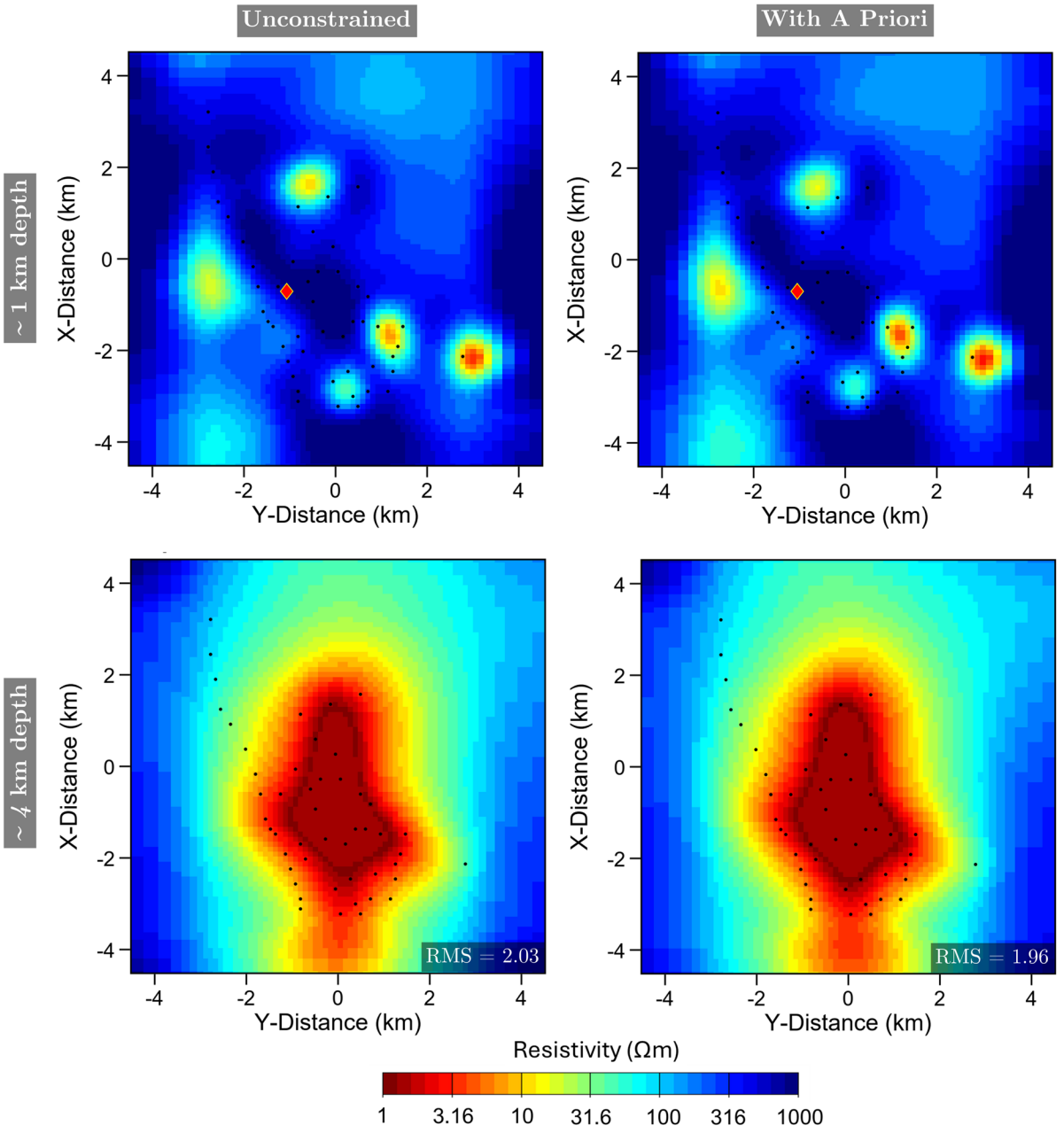

Figure 8.12: Horizontal view of the 3D MT models resulting from the unconstrained inversion and the inversion with a priori information at two different depths (~ 1 km and ~ 4 km). The locations of the MT sites are displayed as black dots, while the red diamond marks the position of the Ain Al-Harrah hot spring.

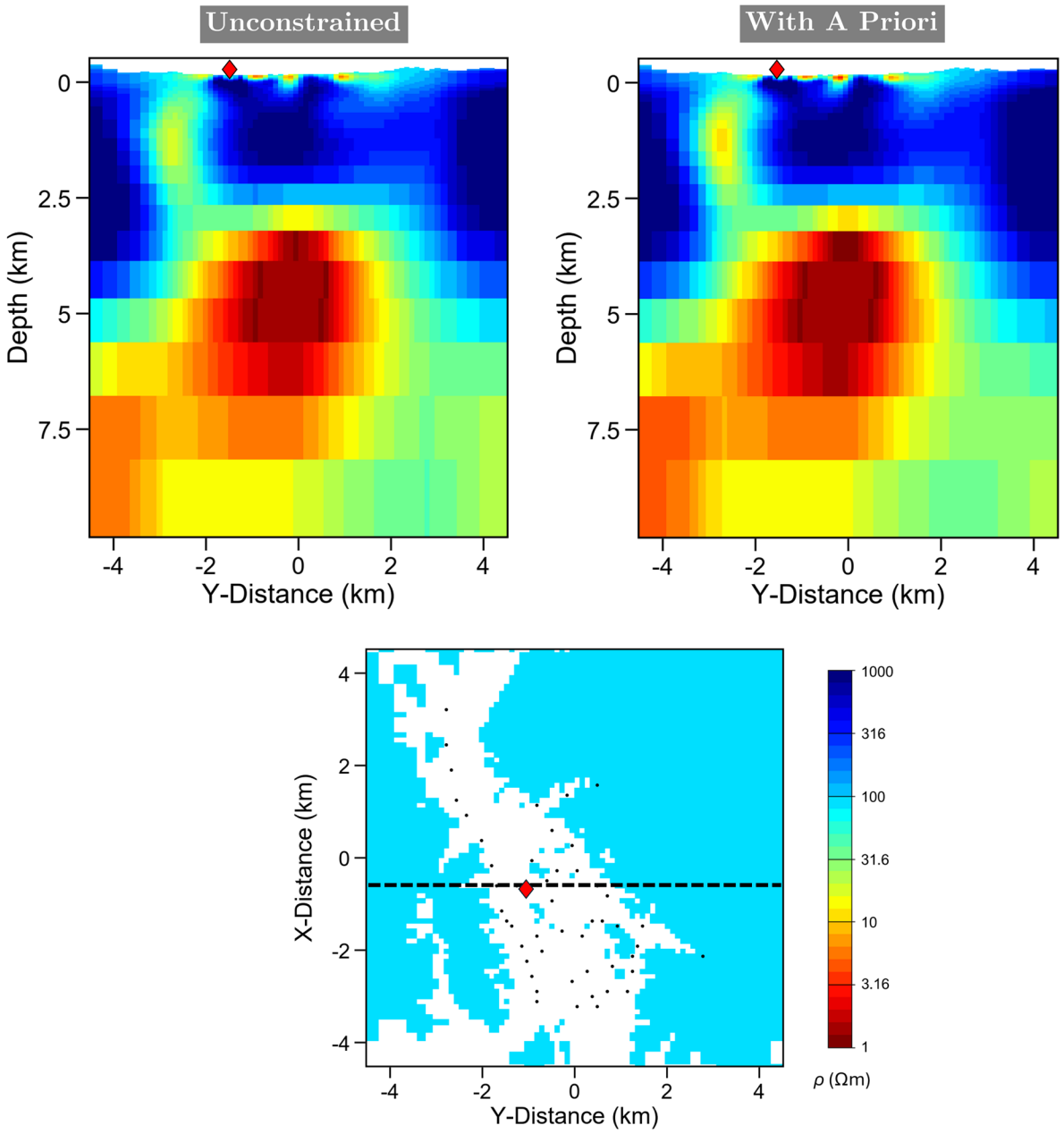

Figure 8.13: Vertical cross-sections extracted from the 3D models resulted from the unconstrained inversion and the inversion with priori information. The projection of the profile sections onto the plan view is shown in the lowest panel.

Figure 8.12 displays the results of both the unconstrained inverse model and the inversion with a priori information, presented as horizontal slices at shallow (~ 1 km) and medium (~ 4 km) depths. As expected, each inverse model reveals slightly different resistivity distribution, given that 3D MT inversion is categorized as an ill-posed problem. At shallow depths of ~ 1 km, the individual pathways identified in the inversion with a priori information are more clearly defined. Furthermore, at a depth of ~ 4 km, the inversion model that includes priori information reveals a main conductive anomaly with a slightly larger diameter than that observed in the unconstrained model. The results from both the unconstrained inversion and the

inversion with priori information are further illustrated as cross sections in Figure 8.13. The principal difference between the two models lies in the distinctiveness of individual protrusion; the model utilizing priori information presents this feature in a more defined manner than the unconstrained model. This protrusion is particularly interesting because it likely serves as a pathway for geothermal fluids as it ascends toward the surface. This upward movement has the potential to create active geothermal hot springs, as indicated by the red diamond in the figure. Overall, the incorporation of TEM data as a priori information appears to enhance the 3D inversion results.

Figure 8.14 provides data fitting to evaluate how well the model's predicted responses match the observed data at stations MT33 and MT35, which were selected due to their significant differences. The data fit for all MT stations can be found in Appendix F. Overall, the inversion with priori information exhibits better data fitting at both soundings. The inclusion of priori information from the TEM model enhances the resolution and accuracy of the resistivity pathways, especially at shallower depths, where near-surface heterogeneities play a crucial role. This improvement is evident in the clearer definition of conductive and resistive structures in the inversion results. Thereby, it is selected as a preferred model, and it will be used for subsequent interpretations.

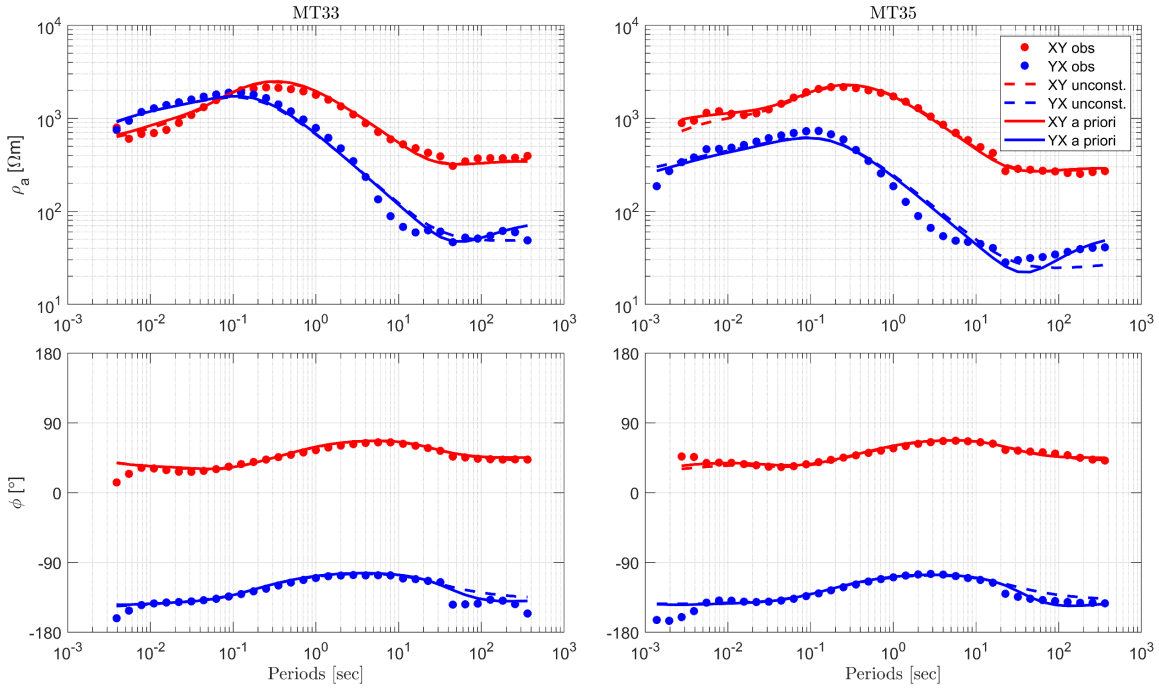

Figure 8.14: Data fit comparison of observed versus predicted MT transfer functions from the unconstrained inversion (dashed curve) and the inversion with a priori information from TEM data (solid curve) at stations MT33 and MT35. The individual dots represent the observed XY (red) and YX (blue) components of the MT tensor.

8.6 Model Assessment

To test the robustness of the generated model, a model assessment known as squeeze test was performed to determine the maximum depths at which the inverse model remains sensitive to the data (Allen & Tromp, 2005). This was achieved by replacing the inverse model parameters with fixed resistivity values below specific depths and then calculating the forward response. The RMS value between the original inverse model and the response from the fixed resistivities model was assessed to evaluate the influence of such constraints. For the squeeze test, the parameters of the preferred inverse model were fixed to a background resistivity value of 100 Ωm at depths of 9.8 km, 5.6 km and 2.7 km. These specific depths were selected based on the variations in the features observed in the inverse model. The squeeze test helps to validate the depth of investigation of the inversion model and ensures that the features detected at these depths are not artifacts of the inversion process. This method provides a way to verify the reliability of the inverse model, particularly in complex geological settings where depth-related sensitivity can significantly impact the interpretation of subsurface resistivity structures.

Figure 8.15 shows some selected profiles extracted from the unconstrained model and from the models with fixed resistivities at various depths. The change in RMS for the 15 selected sites across different models is depicted in Figure 8.16 as a bar diagram. Based on these results, for the shallow depth of 2.7 km and the medium depth of 5.6 km, the RMS values significantly diverge from those obtained from the unconstrained model at all MT stations. The absolute RMS differences from the unconstrained inversion reach up to 1.1 on average for the shallow depth and more than 10.0 for the medium depth, indicating that deeper structures are sensitive to the observed data. At a deeper depth of 9.8 km, certain stations (MT04, MT10, MT20, MT24, MT31, and MT35) display significant RMS differences greater than 0.5, suggesting that deeper structures are necessary to fit the data from these soundings. However, some other MT stations (MT01, MT14, MT19, MT37, and MT41) exhibit RMS differences approaching the data misfit levels obtained with the unconstrained model, indicating that these sites are not sensitive to the deeper structures. The longer period data from these sites were primarily removed due to noise. Consequently, structures deeper than 10 km will not be interpreted in this study, as the data do not reliably constrain them.

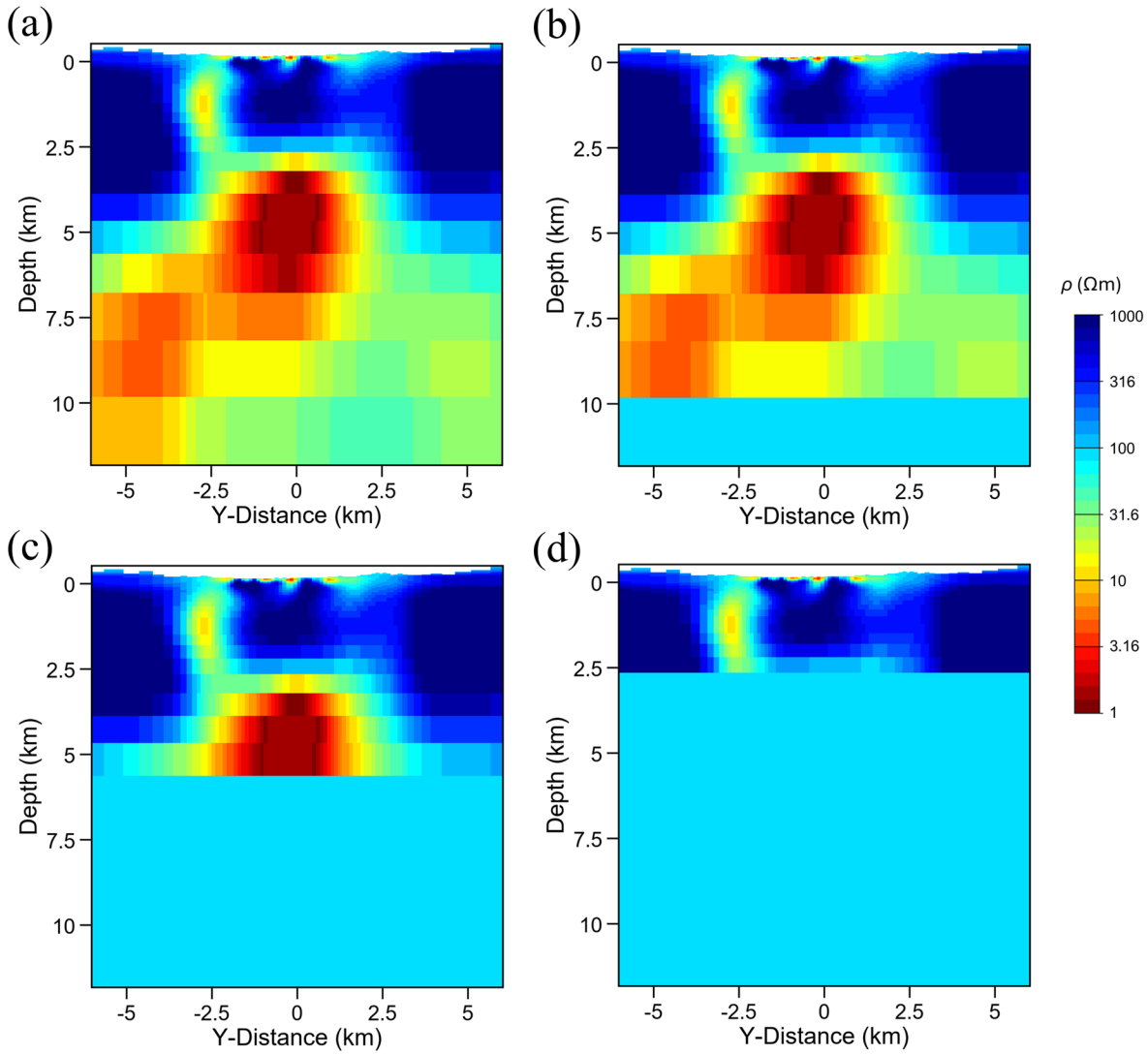

Figure 8.15: Selected vertical slices extracted from four different models: (a) unconstrained inverse model, (b) inverse model with fixed resistivity at below 9.8 km, (c) inverse model with fixed resistivity below 5.6 km, and (d) inverse model with fixed resistivity below 2.7 km.

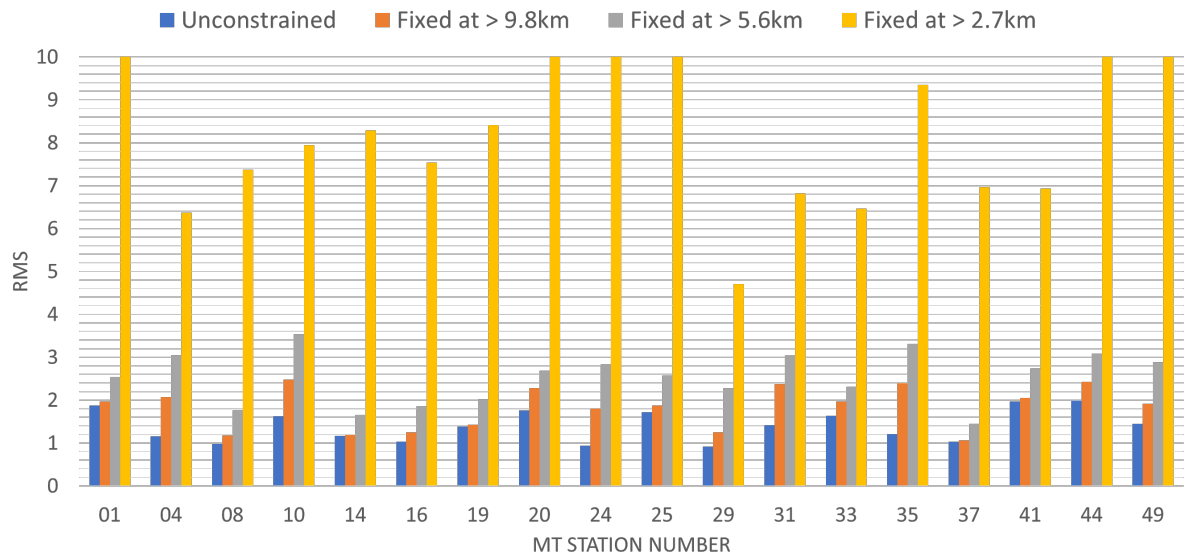

Figure 8.16: Comparison of RMS values obtained from the unconstrained inversion and the inversion runs with fixed resistivity models.

8.7 Preferred 3D Resistivity Models

As it was previously explained, the 3D inversion model incorporating a priori information from the TEM model produced more reliable results, indicated by a lower RMS value. Therefore, this resultant model has been selected as the preferred 3D inversion model for further analysis. Figure 8.17 presents horizontal slices from the 3D inversion model at various depths, with projected surface MT site locations indicated by black dots. At the shallowest depth (-0.200 to -0.175 km), there is a complex pattern of high and low conductivity zones, with high conductivity areas (warmer colors) interspersed with regions of lower conductivity (cooler colors). The slice from 0.000 to 0.025 km shows a more heterogeneous distribution, featuring several high conductivity zones surrounded by lower conductivity regions. At an intermediate depth (from 1.480 to 1.801 km), the conductivity values form more distinct zones, with a few high conductivity spots suggesting potential geothermal activity or fluid pathways. Deeper, from 2.648 to 3.203 km, two major high conductivity bodies are visible, indicating significant transition subsurface features. At a depth of 4.667 to 5.626 km, a prominent high conductivity zone likely signifies a major geothermal reservoir or a large area of highly conductive materials. The deepest slice, from 9.812 to 11.800 km, shows a more uniform conductivity distribution, with less pronounced high conductivity zones compared to shallower depths, indicating a more stable and homogeneous geological structure at these depths. Overall, the slices reveal a complex and varied subsurface conductivity structure, with significant heterogeneity and several key features indicative of geothermal activity.

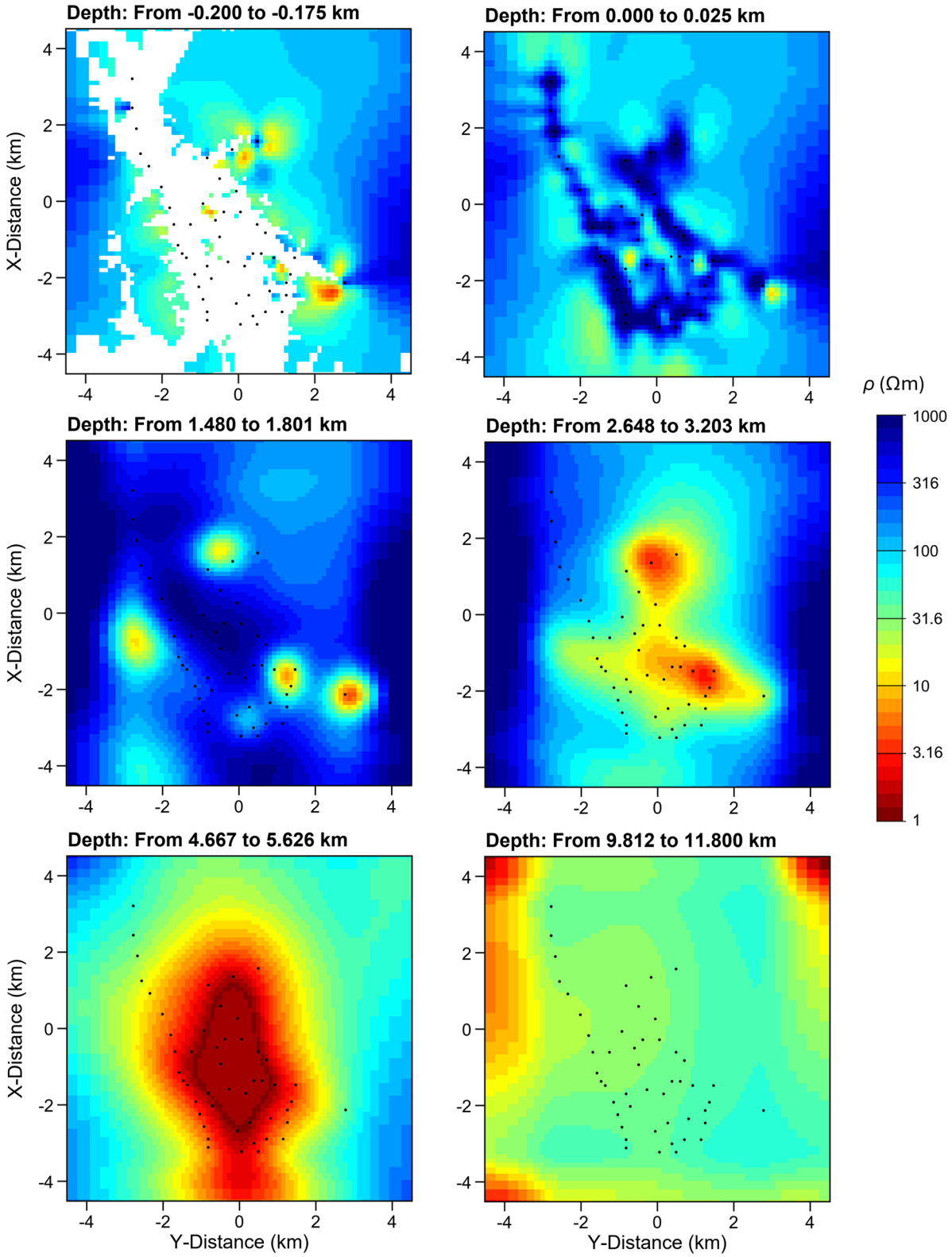

Figure 8.17: Horizontal slices from the preferred 3D resistivity model at six various depths, with projected surface MT site locations indicated by black dots.

Figure 8.18 presents vertical slices from the preferred 3-D inversion model along profiles A-A', B-B,' and C-C', with the yellow star indicating the location of the Ain Al-Harrah hot spring. In profile A-A', a near-surface localized low-resistivity zone (C0), with an

average thickness of less than 300 m, is interpreted as sediments fully saturated with freshwater. In the same profile, several low-resistivity zones (C1, C2, C3) are identified as potential pathways for geothermal fluids. A prominent deep low-resistivity body (C5), extending from ~ 2 km to 8 km depth, indicates a significant geothermal reservoir. Profile B-B' highlights two notable shallow low-resistivity zones (C1 and C4), likely indicating fluid pathways or fractures. The extensive low-resistivity body (C5), also observed here, spans depths of ~ 2.5 km to 8 km, further supporting the presence of a geothermal reservoir beneath the study area. Profile C-C' similarly reveals shallow low-resistivity zones (C2 and C4), interpreted as possible fluid pathways. The deep low-resistivity body (C5), consistent across all profiles, extends from ~ 2.5 km to 8 km depth, confirming the existence of a substantial geothermal feature. The map view in Figure 8.18(d) shows the study area layout, with the yellow star denoting the Ain Al-Harrah hot spring, black dots representing MT site, and red dashed lines outlining the vertical slice locations. In summary, the vertical slices reveal a complex subsurface resistivity structure, characterized by several shallow low-resistivity zones (C1, C2, C3 and C4), identified as potential pathways for geothermal fluids, and a deep low-resistivity (C5), strongly suggesting the presence of a significant geothermal reservoir.

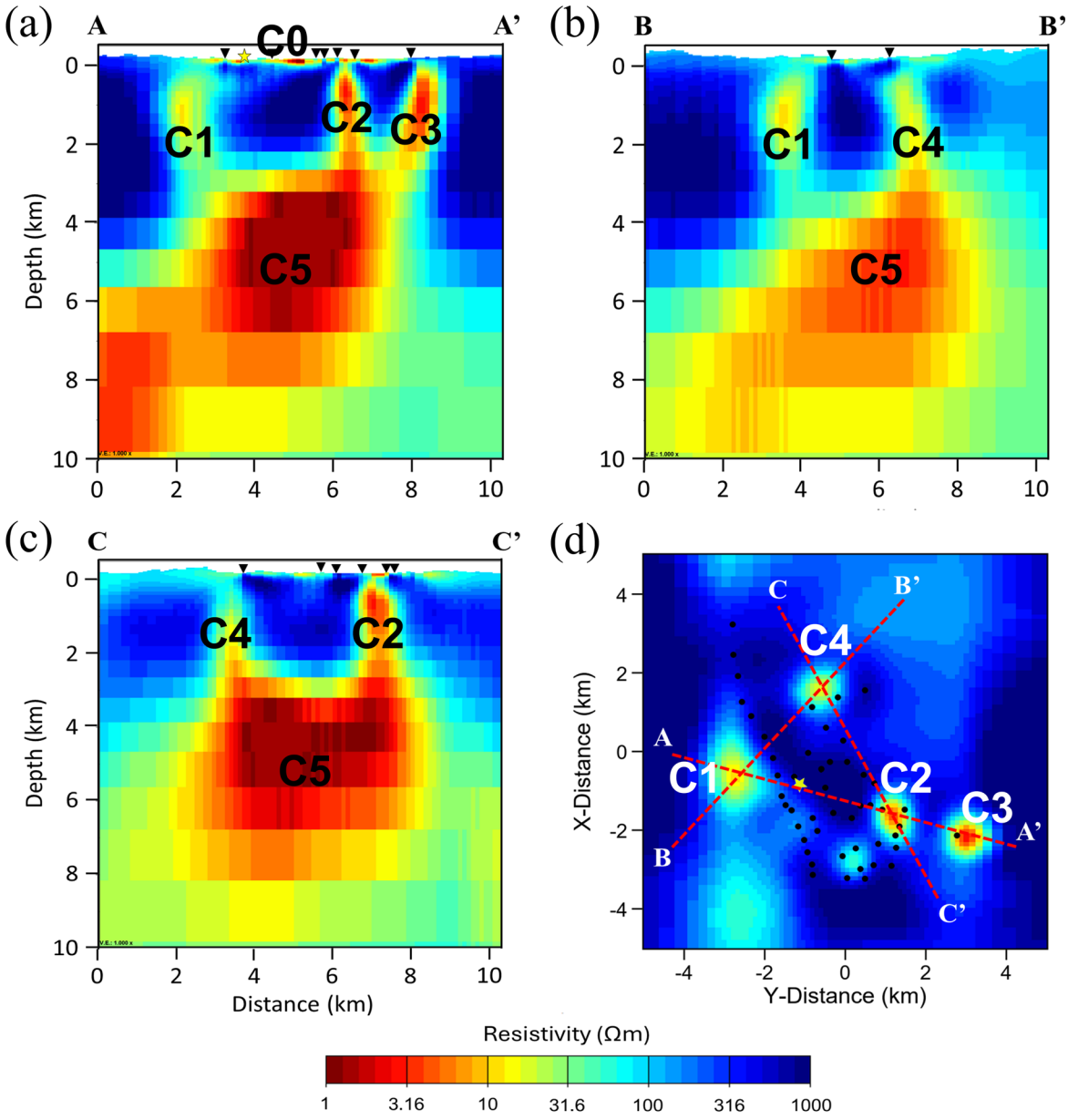

Figure 8.18: Vertical cross-sections extracted from the preferred 3D model along A-A' (a), B-B' (b), and C-C' (c). The red dashed lines show the projection of the three profiles on the top view section (d). The location of Ain Al-Harrah hot spring visualized as a yellow star.

8.8 Interpretation of the 3D Models

Geothermal resources can be categorized based on temperature, reservoir characteristics, and geological control. One fundamental classification is based on their connection to magma activity. Magmatic geothermal systems encompass convectional hydrothermal systems, either hot water or steam-dominated, hot dry rock (HDR) systems, and partial melt systems. These systems are typically found in regions with high geothermal gradients, such as volcanic and tectonically active areas. The heat in

these systems is directly linked to magmatic processes, which makes them highly productive and suitable for power generation. In contrast, non-volcanic geothermal resources are typically associated with hot fluids in sedimentary basins or crystalline formations (Meju, 2002; Moeck, 2014). These systems rely on conductive heat transfer from deeper heat sources and are less directly linked to magmatic activity. Although they generally have lower geothermal gradients, non-volcanic systems can still provide viable geothermal resources, particularly for direct-use applications such as district heating, greenhouse heating, or aquaculture. Among these classifications, hydrothermal systems are the most frequently utilized and economically viable. Their accessibility, relatively high temperatures, and natural permeability make them suitable for electricity generation and direct-use applications.

A typical hydrothermal system transfers heat through groundwater circulation, either in liquid or vapor form via convection. Conceptually, such systems are composed of three key components: a heat source, typically a magma body or deep-seated pluton; a groundwater system that transports and occasionally stores heat in a reservoir located above the heat source; and a clay cap, a conductive layer formed by hydrothermal alteration that traps heat and fluid within the system (Cumming, 2009; Muñoz, 2014). However, in some high-temperature geothermal systems, especially those associated with volcanic activity, the clay cap may be absent due to unique geological conditions, such as rapid fluid flow, high permeability, or specific mineralogical compositions that inhibit clay formation (Muñoz, 2014; Patro, 2017). In the Al-Lith geothermal system, the heat source, convection pattern, and groundwater system are likely to have formed in conjunction, reflecting the interconnected nature of geothermal processes. However, the clay cap, commonly absent in some high-temperature volcanic-associated geothermal fields, appears not clearly delineated in the 3D model results.

In summary, the 3D inversion results, presented in Figures 8.17 and 8.18, reveal four noteworthy features:

1. A near-surface conductive zone with resistivity around $\sim 50\ \Omega$m extends across almost the entire study area up to 300 m depth. This zone likely represents sedimentary deposits with high water content, facilitating efficient heat transfer. These sediments are often crucial in geothermal systems as they can act as both a reservoir and a pathway for the movement of geothermal fluids. The presence of this permeable aquifer suggests a well-developed groundwater system capable of supporting geothermal activity and sustaining the geothermal system's recharge mechanism.

2. A low-resistivity anomaly with values less than 20 Ωm observed at depths greater than 2.5 km likely indicates the presence of a geothermal reservoir. The low resistivity in this context likely indicates the presence of hot, mineralized fluids or molten rock, marking it as the primary source of thermal energy. This feature is critical for geothermal energy extraction, as it represents the main resource base. Identifying its precise location and extent is essential for estimating potential energy output, economic viability, and designing targeted exploration and development strategies.

3. Individual protrusions extending upward from the reservoir are identified as possible pathways for geothermal fluids. These features facilitate fluid migration to the surface or the near subsurface and may be associated with active geothermal surface manifestations, such as hot springs.

4. Zones with high resistivity values exceeding 200 Ωm are associated with hard-rock geological formations. These formations are significant for several reasons: they often act as barriers to fluid migration, helping to contain the geothermal reservoir, and they can affect the overall heat flow and reservoir dynamics. Knowing the location and characteristics of these hard-rock formations is crucial for the design and drilling of geothermal wells, as they influence drilling conditions and the structural stability of the geothermal system.

Chapter 9

Conclusion and Outlook

Electromagnetic (EM) techniques are becoming increasingly important for exploring and characterizing geothermal reservoirs due to their ability to effectively map the subsurface electrical properties and identify key features, such as heat sources, faults, and fluid pathways. Among various EM methods, the Magnetotelluric (MT) technique is the most widely used and potent tool for investigating geothermal resources due to its relatively low cost, high effectiveness, and deep subsurface penetration. In addition to MT, the Transient Electromagnetic (TEM) method is also used in geothermal exploration, albeit less frequently. TEM can be utilized not only to correct static shifts in the MT data but also to enhance the optimization of the 3D MT inversion.

The Al-Lith area in western Saudi Arabia is notable for its geothermal surface manifestations, such as hot springs, and is considered one of the most significant sites for geothermal resources in the country. Its geothermal reserve holds a significant promise for providing clean power energy sustainably over the long term. Although geothermal energy utilization for power generation is not yet economically viable, some direct-use applications of low-grade geothermal resources have already been implemented. To date, only a limited number of geophysical measurements have been conducted in this region, aimed at enhancing the understanding of the geothermal system. This research comprehensively examines the potential of geothermal resources in the Al-Lith area utilizing EM methods, particularly MT and TEM techniques. A total of 50 broadband MT stations were deployed, covering a time range of 0.001 to 512 seconds, in addition to 13 TEM soundings. The average spacing between neighboring MT stations was around 400 m, ensuring adequate spatial resolution for the survey. Due to logistical limitations and the challenging terrain of the study area, the vertical component of the magnetic field was measured at only 14 locations.

The acquired MT data were processed using a well-validated, robust statistical technique to estimate transfer functions for each sounding. Dimensionality analyses using phase tensor and skew calculations revealed a complex subsurface conductivity structure, characterized by predominantly 1D/2D geoelectric behavior at short periods (< 2 sec) and transitioning to a more complex 3D structure a longer period. Prior to the inversion of the MT data, 3D MT synthetic modeling and inversion studies were carried out to assess the detectability of geothermal anomalies, optimize survey

parameters, and evaluate the sensitivity of various inversion inputs. To fully assess the capabilities of 3D MT inversion for geothermal exploration, two scenarios were analyzed: one with a highly conductive clay cap and the other without. In geothermal systems with a conductive clay cap, the MT method effectively maps the conductive clay cap and delineates the transition to the geothermal reservoir. Conversely, in systems without a clay cap, 3D MT inversion significantly enhances the coverage of the geothermal reservoir and its associated protrusions, which serve as pathways for geothermal fluids to migrate toward the surface or near subsurface layers.

Given that the study area is situated in steep mountainous terrain, a thorough examination of the influence of topography was conducted. This topographic effect poses considerable challenges for MT studies in the region, resulting in significant inductive and galvanic distortions in the MT transfer functions. To effectively mitigate these distortions, it is crucial to integrate topography into the initial model, which ultimately helps to minimize the risk of misinterpretation. In such scenarios, applying static shift corrections to the data should be avoided, as this could result in accounting for shifts more than once, potentially leading to erroneous interpretations. Selecting an appropriate initial resistivity model is crucial, as it can greatly influence the accuracy of the 3D inversion results. The most effective iterations and the lowest overall RMS values are typically achieved when the initial model closely aligns with the regional average resistivity. Furthermore, all input parameters for the 3D MT inversion should be systematically tested to determine the most suitable ones for the specific data set, particularly focusing on the smoothing parameter and data errors, as these have a substantial impact on the inversion output.

3D MT inversion can be performed by either inverting solely the off-diagonal elements of the impedance tensor or by including the full impedance tensor, which comprises both diagonal and off-diagonal elements. In this study, the preference is for inverting the off-diagonal tensor elements ($\boldsymbol{Z}_{xy}$ and $\boldsymbol{Z}_{yx}$), leading to a model that is more clearly defined and exhibits a lower RMS, thereby enhancing the overall reliability of the results. This preference may stem from the significantly lower magnitudes of the diagonal elements ($\boldsymbol{Z}_{xx}$ and $\boldsymbol{Z}_{yy}$), which can adversely affect the inversion performance. Additionally, incorporating tipper data alongside the impedance tensor is recommended, as it can improve the reliability of the subsurface model. However, it is important to note that this enhancement was not overwhelmingly substantial, largely due to the limited availability of tipper data in this study.

The TEM data were inverted using the EMUPLUS code to generate a suitable 1D resistivity model. Two different techniques were employed: the smoothness-constraint Occam inversion scheme and the Levenberg-Marquardt technique. The 1D inversion models from TEM data reveal three main layers: (1) a conductive layer in the first few meters depth, characterized by low resistivity, which likely indicates high water content

resulting from recent rainwater infiltration; (2) a resistive layer extending to a depth of approximately 120 m, probably composed of hard rock or other geologically resistant materials, with high resistivity suggesting dry or les porous formations; and (3) a layer below 120 m depth exhibiting decreasing resistivity, likely associated with sediments saturated with groundwater, indicating the transition to more porous and water-bearing formations at greater depths. The resistivity model derived from the TEM data was subsequently incorporated into the initial model as a priori information to optimize the 3D MT inversion process. This integration led to more reliable outcomes. Consequently, the resulting model was chosen as the preferred final 3D inversion model.

The integration of MT and TEM measurements in the Al-Lith area has revealed a 3D electrical resistivity distribution around the main hot spring, confirming the promising geothermal energy potential of the region. The final 3D resistivity model, with an error-weighted RMS of 1.96 after 113 iterations, successfully images key geothermal features in the study area, including the heat source, convection patterns, and groundwater system associated with the Al-Lith geothermal system. However, the clay cap is not imaged in the 3D model, which is common in the high-temperature geothermal systems associated with volcanic activity. The individual protrusions identified in the model indicate pathways for geothermal fluids, either to the surface or to the near subsurface, potentially leading to active surface manifestations (hot springs) of the geothermal activity. The geothermal reservoir, indicated by a conductive zone with resistivity around 10 Ωm, is shallow, located at a depth of approximately 2.5 km to over 8 km depths, and spans a diameter of more than 4 km.

Future research should focus on expanding the MT and TEM surveys to increase spatial coverage and enhance the resolution of the 3D resistivity model. A denser dataset would improve the delineation of fluid pathways, fracture zones, and heat sources, providing a more comprehensive understanding of the geothermal system. Incorporating full tensor MT data, including tipper measurements, would further refine the inversion process and enhance sensitivity to lateral resistivity variations, which are crucial for characterizing the deep geothermal reservoir. Integrating geophysical results with seismic and geochemical data would strengthen interpretations of subsurface structures and fluid dynamics. Seismic tomography could help identify fault networks and permeability variations, while geochemical analysis of thermal waters would provide insights into fluid origins, circulation patterns, and reservoir temperatures. A multi-disciplinary approach would significantly improve the accuracy of geothermal resource assessments and reduce exploration uncertainties.

Exploratory drilling remains a critical next step in validating geophysical interpretations. Drilling would provide direct measurements of temperature, permeability, and reservoir composition, confirming the depth and characteristics of the geothermal resource. Temperature logging and rock core analysis would allow for

further refinement of the resistivity model and help assess the economic feasibility of geothermal energy extraction. Beyond the Ain Al-Harrah study, the methodologies and workflows developed in this research can be applied to other prospective geothermal regions. Integrating MT and TEM methods, combined with advanced inversion techniques, provides a robust framework for future geothermal exploration efforts. As Saudi Arabia transitions toward renewable energy under Vision 2030, further studies should explore additional geothermal sites to support sustainable energy development and diversify the country's energy portfolio.

In conclusion, the results presented in this thesis provide crucial insights into the characterization and complexity of the geothermal system in the Al-Lith region of western Saudi Arabia, confirming its significant potential for sustainable energy development. The derived 3D resistivity model successfully visualizes the key geothermal features, providing a detailed subsurface image that improves our understanding of the geothermal system's structure and dynamics. The findings contribute to Saudi Arabia's Vision 2030 by advancing knowledge on geothermal resources and supporting the transition toward renewable energy. Further investigations, including additional geophysical surveys and drilling programs, are necessary to assess the region's feasibility of geothermal energy extraction fully.

Bibliography

Aboud, E., Qaddah, A., Harbi, H., & Alqahtani, F. (2021). Geothermal Resources Database in Saudi Arabia (GRDiSA): GIS model and geothermal favorability map. *Arabian Journal of Geosciences*, *14*(2), 112. https://doi.org/10.1007/s12517-020-06426-z

Adams, C. A., Auld, A. M. C., Gluyas, J. G., & Hogg, S. (2015). Geothermal energy - The global opportunity. *Proceedings of the Institution of Mechanical Engineers, Part A: Journal of Power and Energy*, *229*(7). https://doi.org/10.1177/0957650915590704

Aldaajani, T., & Furlong, K. P. (2022). The Makkah–Madinah Transform Zone: a relic rift-to-rift continental transform formed during early Arabia–Nubia plate separation. *Geoscience Letters*, *9*(1). https://doi.org/10.1186/s40562-022-00228-9

Aldabesh, A., Soufi, J., Omer, S., & Haredy, A. (2021). Unlocking the residential retrofitting potential in a three-degree world: A holistic approach to passive design in hot climates. *Buildings*, *11*(6). https://doi.org/10.3390/buildings11060228

Al-Dayel, M. (1988). Geothermal resources in Saudi Arabia. *Geothermics*, *17*(2–3), 465–476. https://doi.org/10.1016/0375-6505(88)90076-4

Al-Douri, Y., Waheeb, S. A., & Johan, M. R. (2019). Exploiting of geothermal energy reserve and potential in Saudi Arabia: A case study at Ain Al Harrah. *Energy Reports*, *5*, 632–638. https://doi.org/10.1016/j.egyr.2019.05.005

Ali, A., Al-Sulaiman, F. A., Al-Duais, I. N. A., Irshad, K., Malik, M. Z., Shafiullah, M., Zahir, M. H., Ali, H. M., & Malik, S. A. (2021). Renewable portfolio standard development assessment in the kingdom of saudi arabia from the perspective of policy networks theory. *Processes*, *9*(7). https://doi.org/10.3390/pr9071123

Allen, R. M., & Tromp, J. (2005). Resolution of regional seismic models: Squeezing the Iceland anomaly. *Geophysical Journal International*, *161*(2), 373–386. https://doi.org/10.1111/j.1365-246X.2005.02600.x

Archie, G. E. (1942). The electrical resistivity log as an aid in determining some reservoir characteristics. *Transactions of the AIME*, *146*(01).

Árnason, K. (2015). The static shift problem in MT Soundings. *Proceedings World Geothermal Congress 2015*, *April*.

Árnason, K., Eysteinsson, H., & Hersir, G. P. (2010). Joint 1D inversion of TEM and MT data and 3D inversion of MT data in the Hengill area, SW Iceland. *Geothermics*, *39*(1). https://doi.org/10.1016/j.geothermics.2010.01.002

Ashadi, A. L., Martinez, Y., Kirmizakis, P., Hanstein, T., Xu, X., Khogali, A., Paembonan, A. Y., AlShaibani, A., Al-Karnos, A., Smirnov, M., Strack, K., & Soupios, P. (2022). First High-Power CSEM Field Test in Saudi Arabia. *Minerals*, *12*(10). https://doi.org/10.3390/min12101236

Ashadi, A. L., Tezkan, B., Yogeshwar, P., Hanstein, T., Kirmizakis, P., Khogali, A., Chavanidis, K., & Soupios, P. (2023). Magnetotelluric Case Study from Ain Al-Harrah Hot Spring, Al-Lith, Saudi Arabia. *Arabian Journal for Science and Engineering*. https://doi.org/10.1007/s13369-023-08293-8

Ashadi, A. L., Tezkan, B., Yogeshwar, P., Hanstein, T., Kirmizakis, P., Khogali, A., Chavanidis, K., & Soupios, P. (2024). Magnetotelluric Case Study from Ain Al-Harrah Hot Spring, Al-Lith, Saudi Arabia. *Arabian Journal for Science and Engineering*, *49*(1), 899–912. https://doi.org/10.1007/s13369-023-08293-8

Avdeev, D. B. (2005). Three-dimensional electromagnetic modelling and inversion from theory to application. In *Surveys in Geophysics* (Vol. 26, Issue 6). https://doi.org/10.1007/s10712-005-1836-x

Baba, K., & Seama, N. (2002). A new technique for the incorporation of seafloor topography in electromagnetic modelling. *Geophysical Journal International*, *150*(2). https://doi.org/10.1046/j.1365-246X.2002.01673.x

Benderitter, Y., & Cormy, G. (1990). Possible approach to geothermal research and relative cost estimate. *Small Geothermal Resources. UNITAR/UNDP Centre for Small Energy Resources*, 61–71.

Berdichevsky, M. N., & Dmitriev, V. I. (1976). Distortion Of Magnetic And Electrical Fields By Near-Surface Lateral Inhomogeneities. *Acta Geodaet. Geophys. et Montanist. Acad. Hung.*, *11*, 447–483.

Berdichevsky, M. N., & Dmitriev, V. I. (2008). Models and methods of magnetotellurics. In *Models and Methods of Magnetotellurics*. https://doi.org/10.1007/978-3-540-77814-1

Berdichevsky, M. N., Dmitriev, V. I., Golubtsova, N. S., Mershchikova, N. A., & Pushkarev, P. Y. (2003). Magnetovariational sounding: New possibilities. *Izvestiya, Physics of the Solid Earth*, *39*(9).

Berktold, A. (1983). Electromagnetic studies in geothermal regions. *Geophysical Surveys*, *6*(1–2). https://doi.org/10.1007/BF01454000

Bibby, H. M., Caldwell, T. G., & Brown, C. (2005). Determinable and non-determinable parameters of galvanic distortion in magnetotellurics. *Geophysical Journal International*, *163*(3). https://doi.org/10.1111/j.1365-246X.2005.02779.x

Blanco-Arrué, B. (2024). *Multidimensional inversion of transient electromagnetic data for the exploration of clay pans in the Atacama Desert, Chile* [Universität zu Köln]. https://kups.ub.uni-koeln.de/72721/

Blanco-Arrué, B., Yogeshwar, P., Tezkan, B., & Díaz, D. (2021). Loop source transient electromagnetics in an urban noise environment: A case study in Santiago de Chile. *Geophysics*, *86*(3), B135–B147. https://doi.org/10.1190/geo2020-0322.1

Bodvarsson, G., & Eggers, D. E. (1972). The exergy of thermal water. *Geothermics*, *1*(3). https://doi.org/10.1016/0375-6505(72)90033-8

Bosworth, W., Huchon, P., & McClay, K. (2005). The Red Sea and Gulf of Aden Basins. *Journal of African Earth Sciences*, *43*(1–3). https://doi.org/10.1016/j.jafrearsci.2005.07.020

Cacace, M., Blöcher, G., Watanabe, N., Moeck, I., Börsing, N., Scheck-Wenderoth, M., Kolditz, O., & Huenges, E. (2013). Modelling of fractured carbonate reservoirs: Outline of a novel technique via a case study from the Molasse Basin, southern Bavaria, Germany. *Environmental Earth Sciences*, *70*(8). https://doi.org/10.1007/s12665-013-2402-3

Cagniard, L. (1953). Basic Theory Of The Magneto-Telluric Method Of Geophysical Prospecting. *GEOPHYSICS*, *18*(3). https://doi.org/10.1190/1.1437915

Caldwell, G., Pearson, C., & Zayadi, H. (1986). Resistivity of Rocks in Geothermal Systems: A Laboratory Study. *Proceedings 8th NZ Geothermal Workshop*, *1*.

Caldwell, T. G., Bibby, H. M., & Brown, C. (2004). The magnetotelluric phase tensor. *Geophysical Journal International*, *158*(2). https://doi.org/10.1111/j.1365-246X.2004.02281.x

Candansayar, M. E., & Tezkan, B. (2008). Two-dimensional joint inversion of radiomagnetotelluric and direct current resistivity data. *Geophysical Prospecting*, *56*(5), 737–749. https://doi.org/https://doi.org/10.1111/j.1365-2478.2008.00695.x

Chandrasekharam, D., Lashin, A., & Al Arifi, N. (2014). The potential contribution of geothermal energy to electricity supply in Saudi Arabia. *International Journal of Sustainable Energy*, *35*(9). https://doi.org/10.1080/14786451.2014.950966

Chandrasekharam, D., Lashin, A., Al Arifi, N., Al Bassam, A. A., & Varun, C. (2015). Evolution of geothermal systems around the Red Sea. *Environmental Earth Sciences*, *73*(8). https://doi.org/10.1007/s12665-014-3710-y

Chave, A. D. (2012). Estimation of the magnetotelluric response function. In *The Magnetotelluric Method: Theory and Practice*. https://doi.org/10.1017/CBO9781139020138.007

Chave, A. D. (2017). Estimation of the Magnetotelluric Response Function: The Path from Robust Estimation to a Stable Maximum Likelihood Estimator. *Surveys in Geophysics*, *38*(5). https://doi.org/10.1007/s10712-017-9422-6

Chave, A. D., & Jones, A. G. (2012). The magnetotelluric method: Theory and practice. In *The Magnetotelluric Method: Theory and Practice*. https://doi.org/10.1017/CBO9781139020138

Chave, A. D., & Thomson, D. J. (2004). Bounded influence magnetotelluric response function estimation. *Geophysical Journal International*, *157*(3). https://doi.org/10.1111/j.1365-246X.2004.02203.x

Chave, A. D., & Weidelt, P. (2012). The theoretical basis for electromagnetic induction. In *The Magnetotelluric Method: Theory and Practice*. https://doi.org/10.1017/CBO9781139020138.003

Chouteau, M., & Tournerie, B. (2000). Analysis of magnetotelluric data showing phase rolling out of quadrant (PROQ). *SEG Technical Program Expanded Abstracts*, *19*(1). https://doi.org/10.1190/1.1816062

Christiansen, A. V., Auken, E., & Sørensen, K. (2009). The transient electromagnetic method. In R. Kirsch (Ed.), *Groundwater Geophysics: A Tool for Hydrogeology* (pp. 179–226). Springer Berlin Heidelberg. https://doi.org/10.1007/978-3-540-88405-7_6

Constable, S. C., Parker, R. L., & Constable, C. G. (1987). Occam's inversion; a practical algorithm for generating smooth models from electromagnetic sounding data. *Geophysics*, *52*(3), 289–300. https://doi.org/10.1190/1.1442303

Čuma, M., Gribenko, A., & Zhdanov, M. S. (2017). Inversion of magnetotelluric data using integral equation approach with variable sensitivity domain: Application to EarthScope MT data. *Physics of the Earth and Planetary Interiors*, *270*, 113–127. https://doi.org/10.1016/J.PEPI.2017.06.003

Cumming, W. (2009). Geothermal Resource Conceptual Models Using Surface Exploration Data. *PROCEEDINGS, Thirty-Fourth Workshop on Geothermal Reservoir Engineering*.

Cumming, W. B., & Mackie, R. L. (2010). Resistivity Imaging of Geothermal Resources Using 1D, 2D and 3D MT Inversion and TDEM Static Shift Correction Illustrated by a Glass Mountain Case History. *In Proceedings World Geothermal Congress 2010*.

Demirbas, A., Alidrisi, H., Ahmad, W., & Sheikh, M. H. (2016). Potential of geothermal energy in the Kingdom of Saudi Arabia. In *Energy Sources, Part A: Recovery, Utilization and Environmental Effects* (Vol. 38, Issue 15). https://doi.org/10.1080/15567036.2015.1045999

Dentith, M., & Mudge, S. (2014). Geophysics for the mineral exploration geoscientist. In *AusIMM Bulletin* (Issue 6). https://doi.org/10.1017/cbo9781139024358

DiPippo, R. (2012). Geothermal power plants: Principles, applications, case studies and environmental impact. In *Geothermal Power Plants: Principles, Applications, Case Studies and Environmental Impact*. https://doi.org/10.1016/C2011-0-05384-X

Dwikorianto, T., & Zuhro, A. (2010). Lessons Learned from Kamojang Geothermal Steam Field Management: from the Beginning Until Now. *World Geothermal Congress*.

Egbert, G. D. (2006). *Ef cient Inversion of Multi-frequency and Multi-source Electromagnetic Data: Final Project Report*. https://core.ac.uk/reader/71312950

Egbert, G. D., & Kelbert, A. (2012). Computational recipes for electromagnetic inverse problems. *Geophysical Journal International*, *189*(1). https://doi.org/10.1111/j.1365-246X.2011.05347.x

Elders, W. A., & Moore, J. N. (2016). Geology of geothermal resources. *Geothermal Power Generation: Developments and Innovation*, 7–32. https://doi.org/10.1016/B978-0-08-100337-4.00002-4

Erdoğan, E., & Candansayar, M. E. (2017). The conductivity structure of the Gediz Graben geothermal area extracted from 2D and 3D magnetotelluric inversion: Synthetic and field data applications. *Geothermics*, *65*, 170–179. https://doi.org/10.1016/J.GEOTHERMICS.2016.09.007

Essene, E. J., & Peacor, D. R. (1995). Clay mineral thermometry - A critical perspective. *Clays and Clay Minerals*, *43*(5). https://doi.org/10.1346/CCMN.1995.0430504

Etemoglu, A. B., & Can, M. (2007). Classification of geothermal resources in Turkey by exergy analysis. In *Renewable and Sustainable Energy Reviews* (Vol. 11, Issue 7). https://doi.org/10.1016/j.rser.2006.01.001

Farquharson, C. G., & Oldenburg, D. W. (2004). A comparison of automatic techniques for estimating the regularization parameter in non-linear inverse problems. *Geophysical Journal International*, *156*(3). https://doi.org/10.1111/j.1365-246X.2004.02190.x

Faulds, J., & Coolbaugh, M. F. (2010). Characterizing structural controls of geothermal reservoirs in the Great Basin, USA, and Western Turkey: Developing successful exploration strategies in extended. *Proceedings World Geothermal Congress*, *April*.

Fleck, R. J., Coleman, R. G., Cornwall, H. R., Greenwood, W. R., Hadley, D. G., Schmidt, D. L., Prinz, W. C., & Ratté, J. C. (1976). Geochronology of the Arabian Shield, western Saudi Arabia: K-Ar results. *Bulletin of the Geological Society of America*, *87*(1). https://doi.org/10.1130/0016-7606(1976)87<9:GOTASW>2.0.CO;2

Fletcher, R., & Reeves, C. M. (1964). Function minimization by conjugate gradients. *The Computer Journal*, *7*(2), 149–154. https://doi.org/10.1093/comjnl/7.2.149

Frey, M., Bär, K., Stober, I., Reinecker, J., van der Vaart, J., & Sass, I. (2022). Assessment of deep geothermal research and development in the Upper Rhine Graben. In *Geothermal Energy* (Vol. 10, Issue 1). https://doi.org/10.1186/s40517-022-00226-2

Furqan, T., Kartadjoemena, J., Waren, R., & Yuafrinaldi. (2016). Geothermal Resource Classifications : Can We Talk the Same Language ? *Ametis Institute*, *111*.

Ghoddousi, S., Rezaie, B., & Ghandehariun, S. (2021). Guideline for electricity generation from hot springs (natural energy storage systems): A techno-enviro-economic assessment. *Sustainable Energy Technologies and Assessments*, *47*. https://doi.org/10.1016/j.seta.2021.101407

Goldman, M., & Neubauer, F. M. (1994). Groundwater exploration using integrated geophysical techniques. In *Surveys in Geophysics* (Vol. 15, Issue 3). https://doi.org/10.1007/BF00665814

Groom, R. W., & Bahr, K. (1992). Corrections for near surface effects: Decomposition of the magnetotelluric impedance tensor and scaling corrections for regional resistivities: A tutorial. *Surveys in Geophysics*, *13*(4–5). https://doi.org/10.1007/BF01903483

Haenel, R., Rybach, L., & Stegena, L. (1988). Fundamentals of Geothermics. In *Handbook of Terrestrial Heat-Flow Density Determination*. https://doi.org/10.1007/978-94-009-2847-3_2

Hampel, F. R., Ronchetti, E. M., Rousseeuw, P. J., & Stahel, W. A. (1986). Robust Statistics: The Approach Based on Influence Functions. *The Statistician*, *35*(5). https://doi.org/10.2307/2987975

Hartig, C. M. (2018). Porous media of the Red River Formation, Williston Basin, North Dakota: a possible Sedimentary Enhanced Geothermal System. *International Journal of Earth Sciences*, *107*(1). https://doi.org/10.1007/s00531-016-1398-9

Hassan, O. (2020). Artificial Intelligence, Neom and Saudi Arabia's Economic Diversification from Oil and Gas. *Political Quarterly*, *91*(1). https://doi.org/10.1111/1467-923X.12794

Heise, W., & Pous, J. (2003). Anomalous phases exceeding 90° in magnetotellurics: Anisotropic model studies and a field example. *Geophysical Journal International*, *155*(1). https://doi.org/10.1046/j.1365-246X.2003.02050.x

Herrington, R. (2021). Mining our green future. In *Nature Reviews Materials* (Vol. 6, Issue 6). https://doi.org/10.1038/s41578-021-00325-9

Hersir, G. P., & Árnason, K. (2013). Resistivity of rocks. *Short Course VIII on Exploration for Geothermal Resources*, 000.

Hill, G. J. (2020). On the Use of Electromagnetics for Earth Imaging of the Polar Regions. In *Surveys in Geophysics* (Vol. 41, Issue 1). https://doi.org/10.1007/s10712-019-09570-8

Hochstein, M. P. (1990). Classification and assessment of geothermal resources. In *Small geothermal resources: A guide to development and utilization*.

Hoteit, H., He, X., Yan, B., & Vahrenkamp, V. (2023). Uncertainty quantification and optimization method applied to time-continuous geothermal energy extraction. *Geothermics*, *110*. https://doi.org/10.1016/j.geothermics.2023.102675

Huber, P. J. (2011). Robust Statistics. In M. Lovric (Ed.), *International Encyclopedia of Statistical Science* (pp. 1248–1251). Springer Berlin Heidelberg. https://doi.org/10.1007/978-3-642-04898-2_594

Hussein, M. T., Lashin, A., Al Bassam, A., Al Arifi, N., & Al Zahrani, I. (2013). Geothermal power potential at the western coastal part of Saudi Arabia. *Renewable and Sustainable Energy Reviews*, *26*, 668–684. https://doi.org/10.1016/J.RSER.2013.05.073

Ichihara, H., & Mogi, T. (2009). A realistic 3-D resistivity model explaining anomalous large magnetotelluric phases: The L-shaped conductor model. *Geophysical Journal International*, *179*(1). https://doi.org/10.1111/j.1365-246X.2009.04310.x

Jalilinasrabady, S. (2022). Geothermal Resources Classification - A Review. *Transactions - Geothermal Resources Council*, *46*.

Jalilinasrabady, S., & Itoi, R. (2013). Classification of geothermal energy resources in Japan applying exergy concept. *International Journal of Energy Research*, *37*(14). https://doi.org/10.1002/er.3002

Jiracek, G. R. (1990). Near-surface and topographic distortions in electromagnetic induction. *Surveys in Geophysics*, *11*(2–3). https://doi.org/10.1007/BF01901659

Jolie, E., Scott, S., Faulds, J., Chambefort, I., Axelsson, G., Gutiérrez-Negrín, L. C., Regenspurg, S., Ziegler, M., Ayling, B., Richter, A., & Zemedkun, M. T. (2021). Geological controls on geothermal resources for power generation. *Nature Reviews Earth & Environment*, *2*(5), 324–339. https://doi.org/10.1038/s43017-021-00154-y

Jones, A. G. (1988). Static shift of magnetotelluric data and its removal in a sedimentary basin environment. *GEOPHYSICS*, *53*(7). https://doi.org/10.1190/1.1442533

Jones, F. W., & Price, A. T. (1970). The Perturbations of Alternating Geomagnetic Fields by Conductivity Anomalies. *Geophysical Journal of the Royal Astronomical Society*, *20*(3). https://doi.org/10.1111/j.1365-246X.1970.tb06073.x

Käufl, J. S., Grayver, A. V., & Kuvshinov, A. V. (2018). Topographic distortions of magnetotelluric transfer functions: A high-resolution 3-D modelling study using real elevation data. *Geophysical Journal International*, *215*(3). https://doi.org/10.1093/gji/ggy375

Kelbert, A., Meqbel, N., Egbert, G. D., & Tandon, K. (2014). ModEM: A modular system for inversion of electromagnetic geophysical data. *Computers and Geosciences*, *66*. https://doi.org/10.1016/j.cageo.2014.01.010

Khiyami, M., Serour, E., Shehata, M., & Bahklia, A. (2012). Thermo-aerobic bacteria from geothermal springs in Saudi Arabia. *AFRICAN JOURNAL OF BIOTECHNOLOGY*, *11*(17). https://doi.org/10.5897/ajb11.3339

Kirkby, A., & Doublier, M. P. (2022). Synthetic magnetotelluric modelling of a regional fault network–implications for survey design and interpretation. *Exploration Geophysics*. https://doi.org/10.1080/08123985.2022.2144212

Ku, C. C., Hsieh, M. S., & Lim, S. H. (1973). The Topographic Effect in Electromagnetic Fields. *Canadian Journal of Earth Sciences*, *10*(5). https://doi.org/10.1139/e73-065

Lashin, A., & Al Arifi, N. (2014). Geothermal energy potential of southwestern of Saudi Arabia "exploration and possible power generation": A case study at Al Khouba area – Jizan. *Renewable and Sustainable Energy Reviews*, *30*, 771–789. https://doi.org/10.1016/J.RSER.2013.10.037

Lashin, A., Al Arifi, N., Chandrasekharam, D., Al Bassam, A., Rehman, S., & Pipan, M. (2015). Geothermal energy resources of Saudi Arabia: country update. *Proceedings World Geothermal Congress*.

Lashin, A., Al-Arifi, N., & Al Bassam, A. (2012). Assessment Of Geothermal Resources At The Al-Lith Area, Kingdom Of Saudi Arabia. *New Zealand Geothermal Workshop*.

Lashin, A., Alarifi, N., Al Bassam, A., Bassam, A., Arifi, A., & Faifi, A. (2020). A review of the Geothermal Resources of Saudi Arabia: 2015-2020. *Proceedings World Geothermal Congress*. https://www.researchgate.net/publication/337910641

Lashin, A., Chandrasekharam, D., Al Arifi, N., Al Bassam, A., & Varun, C. (2014). Geothermal energy resources of wadi Al-Lith, Saudi Arabia. *Journal of African Earth Sciences*, *97*, 357–367. https://doi.org/10.1016/J.JAFREARSCI.2014.05.016

Lashin, A., Pipan, M., Al Arifi, N., Al Bassam, A., Mocnik, A., & Forte, E. (2015). Geophysical Exploration of the Western Saudi Arabian Geothermal Province: First Results from the Al-Lith Area. *Proceedings World Geothermal Congress*, 19–25.

Ledo, J., Gabàs, A., & Marcuello, A. (2002). Static shift levelling using geomagnetic transfer functions. *Earth, Planets and Space*, *54*(5). https://doi.org/10.1186/BF03353040

Lee, K. C. (2001). Classification of geothermal resources by exergy. *Geothermics*, *30*(4). https://doi.org/10.1016/S0375-6505(00)00056-0

Levenberg, K. (1944). A method for the solution of certain nonlinear problems in least squares. *Quarterly of Applied Mathematics*, *2*(2), 164–168. http://www.jstor.org/stable/43633451

Lilley, F. E. M., & Weaver, J. T. (2010). Phases greater than 90° in MT data: Analysis using dimensionality tools. *Journal of Applied Geophysics*, *70*(1). https://doi.org/10.1016/j.jappgeo.2009.08.007

Lines, L. R., & Treitel, S. (1984). A review of least-squares inversion and its application to geophysical problems. *Geophysical Prospecting*, *32*(2). https://doi.org/10.1111/j.1365-2478.1984.tb00726.x

Llera, F. J., Sato, M., Nakatsuka, K., & Yokoyama, H. (1990). Temperature dependence of the electrical resistivity of water- saturated rocks. *Geophysics*, *55*(5). https://doi.org/10.1190/1.1442869

Lund, J. W., & Toth, A. N. (2021). Direct utilization of geothermal energy 2020 worldwide review. *Geothermics*, *90*. https://doi.org/10.1016/j.geothermics.2020.101915

Mackie, R. L., Rodi, W., & Donald Watts, M. (2001). 3-D magnetotelluric inversion for resource exploration. *SEG Technical Program Expanded Abstracts*, *20*(1). https://doi.org/10.1190/1.1816392

Mackie, R. L., Smith, J. T., & Madden, T. R. (1994). Three-dimensional electromagnetic modeling using finite difference equations: The magnetotelluric example. *Radio Science*, *29*(4). https://doi.org/10.1029/94RS00326

Marquardt, D. W. (1963). An Algorithm for Least-Squares Estimation of Nonlinear Parameters. *Journal of the Society for Industrial and Applied Mathematics*, *11*(2). https://doi.org/10.1137/0111030

McKenna, J. R., & Blackwell, D. D. (2004). Numerical modeling of transient Basin and Range extensional geothermal systems. *Geothermics*, *33*(4). https://doi.org/10.1016/j.geothermics.2003.10.001

Meju, M. A. (1994). Geophysical Data Analysis: Understanding Inverse Problem Theory and Practice. In *Geophysical data analysis: understanding inverse problem theory and practice*.

Melouah, O., Ebong, E. D., Abdelrahman, K., & Eldosouky, A. M. (2023). Lithospheric structural dynamics and geothermal modeling of the Western Arabian Shield. *Scienti/c Reports*, *13*(1). https://doi.org/10.1038/s41598-023-38321-4

Menke, W. (2012). Geophysical Data Analysis: Discrete Inverse Theory. In *Geophysical Data Analysis: Discrete Inverse Theory*. https://doi.org/10.1016/C2011-0-69765-0

Menke, W. (2018). *Geophysical Data Analysis: Discrete Inverse Theory*. Academic press.

Meqbel, N. M. (2009). *The electrical conductivity structure of the Dead Sea Basin derived from 2D and 3D inversion of magnetotelluric data*. http://dx.doi.org/10.17169/refubium-4467

Meqbel, N. M., Egbert, G. D., Wannamaker, P. E., Kelbert, A., & Schultz, A. (2014). Deep electrical resistivity structure of the northwestern U.S. derived from 3-D inversion of USArray magnetotelluric data. *Earth and Planetary Science Letters*, *402*(C). https://doi.org/10.1016/j.epsl.2013.12.026

Miensopust, M. P. (2010). *Multidimensional Magnetotellurics: A 2D Case Study and A 3D Approach to Simultaneously Invert for Resistivity Structure and Distortion Parameters* [PhD Thesis]. National University Ireland.

Moeck, I. S. (2013). Classification of geothermal plays according to geological habitats. In R. Bracke, C. Harvey, & H. Rueter (Eds.), *Geothermal Exploration Best Practices x Geology, Exploration Drilling, Geochemistry, Geophysics* (Vol. 1, pp. 1–10). IGA Service GmbH.

Moeck, I. S. (2014). Catalog of geothermal play types based on geologic controls. In *Renewable and Sustainable Energy Reviews* (Vol. 37). https://doi.org/10.1016/j.rser.2014.05.032

Moeck, I., Schandelmeier, H., & Holl, H. G. (2009). The stress regime in a Rotliegend reservoir of the Northeast German Basin. *International Journal of Earth Sciences*, *98*(7). https://doi.org/10.1007/s00531-008-0316-1

Mohammadzadeh Bina, S., Jalilinasrabady, S., Fujii, H., & Pambudi, N. A. (2018). Classification of geothermal resources in Indonesia by applying exergy concept. *Renewable and Sustainable Energy Reviews*, *93*. https://doi.org/10.1016/j.rser.2018.05.018

Monged, M. H. E., Hussein, M. T., & Khater, A. E. M. (2018). Elemental and radiological aspects of geothermal springs and nearby soil and sediment of Al-Lith area: concentration and risk assessment. *Environmental Earth Sciences*, *77*(12). https://doi.org/10.1007/s12665-018-7602-4

Mörbe, W. (2020). *Deep Controlled Source Electromagnetics for Mineral Exploration: A Multidimensional Validation Study in Time and Frequency Domain* [Universität zu Köln]. https://kups.ub.uni-koeln.de/10696/

Muffler, P., & Cataldi, R. (1978). Methods for regional assessment of geothermal resources. *Geothermics*, *7*(2–4). https://doi.org/10.1016/0375-6505(78)90002-0

Muñoz, G. (2014). Exploring for Geothermal Resources with Electromagnetic Methods. In *Surveys in Geophysics* (Vol. 35, Issue 1). https://doi.org/10.1007/s10712-013-9236-0

Nabighian, M. N. (1979). Quasi-static transient response of a conducting half-space - an approximate representation. *Geophysics*, *44*(10). https://doi.org/10.1190/1.1440931

Nabighian, M. N., & Macnae, J. C. (1991). 6. Time Domain Electromagnetic Prospecting Methods. In *Electromagnetic Methods in Applied Geophysics*. https://doi.org/10.1190/1.9781560802686.ch6

Nam, M. J., Kim, H. J., Song, Y., Lee, T. J., & Suh, J. H. (2008). Three-dimensional topography corrections of magnetotelluric data. *Geophysical Journal International*, *174*(2). https://doi.org/10.1111/j.1365-246X.2008.03817.x

Newman, G. A., & Alumbaugh, D. L. (2000). Three-dimensional magnetotelluric inversion using non-linear conjugate gradients. *Geophysical Journal International*, *140*(2). https://doi.org/10.1046/j.1365-246X.2000.00007.x

Newman, G. A., Gasperikova, E., Hoversten, G. M., & Wannamaker, P. E. (2008). Three-dimensional magnetotelluric characterization of the Coso geothermal field. *Geothermics*, *37*(4), 369–399. https://doi.org/10.1016/J.GEOTHERMICS.2008.02.006

Newman, G. A., Hoversten, G. M., & Alumbaugh, D. L. (2002). Chapter 8 Three-dimensional magnetotelluric modeling and inversion: Application to sub-salt imaging. *Methods in Geochemistry and Geophysics*, *35*(C). https://doi.org/10.1016/S0076-6895(02)80090-7

Ouda, O. K. M., Al-Bassam, A. M., & Lashin, A. A. (2022). Economic and Technical Potential of Geothermal Energy in the Kingdom of Saudi Arabia. In *Advances in Science, Technology and Innovation*. https://doi.org/10.1007/978-3-031-00808-5_90

Pace, F., Martí, A., Queralt, P., Santilano, A., Manzella, A., Ledo, J., & Godio, A. (2022). Three-Dimensional Magnetotelluric Characterization of the Travale Geothermal Field (Italy). *Remote Sensing*, *14*(3). https://doi.org/10.3390/rs14030542

Palacky, G. J. (1988). 3. Resistivity Characteristics of Geologic Targets. In *Electromagnetic Methods in Applied Geophysics*. https://doi.org/10.1190/1.9781560802631.ch3

Pallister, J. S. (1986). *Geologic Map of the Al Lith Quadrangle, Sheet 20D, Kingdom of Saudi Arabia*.

Parkinson, W. D. (1959). Directions of Rapid Geomagnetic Fluctuations. *Geophysical Journal International*, *2*(1), 1–14. https://doi.org/10.1111/j.1365-246X.1959.tb05776.x

Parkinson, W. D. (1962). The Influence of Continents and Oceans on Geomagnetic Variations. *Geophysical Journal of the Royal Astronomical Society*, *6*(4). https://doi.org/10.1111/j.1365-246X.1962.tb02992.x

Patro, P. K. (2017). Magnetotelluric Studies for Hydrocarbon and Geothermal Resources: Examples from the Asian Region. *Surveys in Geophysics*, *38*(5). https://doi.org/10.1007/s10712-017-9439-x

Patro, P. K., & Egbert, G. D. (2011). Application of 3D inversion to magnetotelluric profile data from the Deccan Volcanic Province of Western India. *Physics of the Earth and Planetary Interiors*, *187*(1–2), 33–46. https://doi.org/10.1016/J.PEPI.2011.04.005

Peacock, J. R., Earney, T. E., Mangan, M. T., Schermerhorn, W. D., Glen, J. M., Walters, M., & Hartline, C. (2020). Geophysical characterization of the Northwest Geysers geothermal field, California. *Journal of Volcanology and Geothermal Research*, *399*. https://doi.org/10.1016/j.jvolgeores.2020.106882

Pellerin, L., & Hohmann, G. W. (1990). Transient electromagnetic inversion: a remedy for magnetotelluric static shifts. *Geophysics*, *55*(9). https://doi.org/10.1190/1.1442940

Pellerin, L., Johnston, J. M., & Hohmann, G. W. (1996). A numerical evaluation of electromagnetic methods in geothermal exploration. In *Geophysics* (Vol. 61, Issue 1). https://doi.org/10.1190/1.1443931

Piña-Varas, P., & Dentith, M. (2018). Magnetotelluric data from the Southeastern Capricorn Orogen, Western Australia: an example of widespread out-of-quadrant phase responses associated with strong 3-D resistivity contrasts. *Geophysical Journal International*, *212*(2), 1022–1032. https://doi.org/10.1093/gji/ggx459

Polak, E. (1971). Computational methods in optimization, a unified approach. *Mathematics in Science and Engineering*, *77). Academic Press*. https://doi.org/10.2307/2005111

Polak, E., & Ribiere, G. (1969). Note sur la convergence de méthodes de directions conjuguées. *Revue Française d informatique et de Recherche Opérationnelle. Série Rouge*, *3*(16). https://doi.org/10.1051/m2an/196903r100351

Pope, E. C., Bird, D. K., Arnórsson, S., & Giroud, N. (2016). Hydrogeology of the Krafla geothermal system, northeast Iceland. *Geo{ uids*, *16*(1). https://doi.org/10.1111/gfl.12142

Porstendorfer, G. (1975). *Principles of Magneto-Telluric Prospecting* (Ed. : G. K. D. S. Parasnis, Ed.). Schweizerbart Science Publishers. http://www.schweizerbart.de//publications/detail/isbn/9783443130077/Porstendorfer_Princ_of_Magn_Tell_P

Quist, A. S., & Marshall, W. L. (1968). Electrical conductances of aqueous sodium chloride solutions from 0 to 800° and at pressures to 4000 bars. *Journal of Physical Chemistry*, *72*(2). https://doi.org/10.1021/j100848a050

Raiche, A. P. (1983). Comparison of apparent resistivity functions for transient electromagnetic methods. *Geophysics*, *48*(6), 787–789. https://doi.org/10.1190/1.1441507

Rehman, S., & Shash, A. (2005). Geothermal Resources of Saudi Arabia – Country Update Report DEMANDS AND FUTURE. *Geology*, *April*.

Rodi, W. L., & Mackie, R. L. (2012). The inverse problem. In *The Magnetotelluric Method: Theory and Practice*. https://doi.org/10.1017/CBO9781139020138.010

Rodi, W., & Mackie, R. L. (2001). Nonlinear conjugate gradients algorithm for 2-D magnetotelluric inversion. *Geophysics*, *66*(1). https://doi.org/10.1190/1.1444893

Ruiz-Aguilar, D., Tezkan, B., Arango-Galván, C., & Romo-Jones, J. M. (2020). 3D inversion of MT data from northern Mexico for geothermal exploration using TEM data as constraints. *Journal of Applied Geophysics*, *172*, 103914. https://doi.org/10.1016/J.JAPPGEO.2019.103914

Rybach, L. (2015). Classification of geothermal resources by potential. *Geothermal Energy Science*, *3*(1). https://doi.org/10.5194/gtes-3-13-2015

Sanyal, S. K. (2005). Classification of Geothermal Systems - a Possible Scheme. *Thirtieth Workshop on Geothermal Reservoir Engineering*.

Scholl, C. (2005). *The in{ uence of multidimensional structures on the interpretation of LOTEM data with one-dimensional models and the application to data from Israel* [Universität zu Köln]. https://kups.ub.uni-koeln.de/1597/

Schwalenberg, K., & Edwards, R. N. (2004). The effect of seafloor topography on magnetotelluric fields: An analytical formulation confirmed with numerical results. *Geophysical Journal International*, *159*(2). https://doi.org/10.1111/j.1365-246X.2004.02280.x

Siegel, A. F. (1982). Robust regression using repeated medians. *Biometrika*, *69*(1). https://doi.org/10.1093/biomet/69.1.242

Simpson, F., & Bahr, K. (2005). *Practical Magnetotellurics*. Cambridge University Press. https://doi.org/DOI: 10.1017/CBO9780511614095

Siripunvaraporn, W. (2012). Three-Dimensional Magnetotelluric Inversion: An Introductory Guide for Developers and Users. In *Surveys in Geophysics* (Vol. 33, Issue 1). https://doi.org/10.1007/s10712-011-9122-6

Siripunvaraporn, W., & Egbert, G. (2009). WSINV3DMT: Vertical magnetic field transfer function inversion and parallel implementation. *Physics of the Earth and Planetary Interiors*, *173*(3–4). https://doi.org/10.1016/j.pepi.2009.01.013

Siripunvaraporn, W., Egbert, G., & Lenbury, Y. (2002). Numerical accuracy of magnetotelluric modeling: A comparison of finite difference approximations. *Earth, Planets and Space*, *54*(6). https://doi.org/10.1186/BF03351724

Siripunvaraporn, W., Egbert, G., & Uyeshima, M. (2005). Interpretation of two-dimensional magnetotelluric profile data with three-dimensional inversion: synthetic examples. *Geophysical Journal International*, *160*(3), 804–814. https://doi.org/https://doi.org/10.1111/j.1365-246X.2005.02527.x

Smirnov, M. Y. (2003). Magnetotelluric data processing with a robust statistical procedure having a high breakdown point. *Geophys. J. Int*, *152*, 1–7. https://academic.oup.com/gji/article/152/1/1/701383

Smith, J. T. (1996). Conservative modeling of 3-D electromagnetic fields, Part II: Biconjugate gradient solution and an accelerator. *Geophysics*, *61*(5). https://doi.org/10.1190/1.1444055

Spichak, V., & Manzella, A. (2009). Electromagnetic sounding of geothermal zones. *Journal of Applied Geophysics*, *68*(4). https://doi.org/10.1016/j.jappgeo.2008.05.007

Spies, B. R. (1989). Depth of investigation in electromagnetic sounding methods. *Geophysics*, *54*(7). https://doi.org/10.1190/1.1442716

Spies, B. R., & Frischknecht, F. C. (1991). 5. Electromagnetic Sounding. In *Electromagnetic Methods in Applied Geophysics*. https://doi.org/10.1190/1.9781560802686.ch5

Sternberg, B. K., Washburne, J. C., & Pellerin, L. (1988). Correction for the static shift in magnetotellurics using transient electromagnetic soundings. *GEOPHYSICS*, *53*(11). https://doi.org/10.1190/1.1442426

Stieltjes, L. (1974). *Geothermal reconnaissance in the Kingdom of Saudi Arabia*.

Stimac, J., Goff, F., & Goff, C. J. (2015). Intrusion-Related Geothermal Systems. *The Encyclopedia of Volcanoes*, 799–822. https://doi.org/10.1016/B978-0-12-385938-9.00046-8

Streich, R. (2009). 3D finite-difference frequency-domain modeling of controlled-source electromagnetic data: Direct solution and optimization for high accuracy. *Geophysics*, *74*(5). https://doi.org/10.1190/1.3196241

Suryadarma, Dwikorianto, T., Zuhro, A. A., & Yani, A. (2010). Sustainable development of the Kamojang geothermal field. *Geothermics*, *39*(4). https://doi.org/10.1016/j.geothermics.2010.09.006

Swift, C. M. (1967). A magnetotelluric investigation of an electrical conductivity anomaly in the southwestern United States. In *Massachusetts Avenue Cambridge: Vol. Ph.D.*

Thiel, S. (2008). *Modelling and inversion of magnetotelluric data for 2-D and 3-D lithospheric structure, with application to obducted and subducted terranes* [Thesis (Ph.D.)]. University of Adelaide.

Thiel, S., Heinson, G., Gray, D. R., & Gregory, R. T. (2009). Ophiolite emplacement in NE Oman: Constraints from magnetotelluric sounding. *Geophysical Journal International*, *176*(3). https://doi.org/10.1111/j.1365-246X.2008.04053.x

Tietze, K. (2012). *Investigating the electrical conductivity structure of the San Andreas fault system in the Park/eld-Cholame region, central California, with 3D magnetotelluric inversion* [Freien Universität Berlin]. https://doi.org/http://dx.doi.org/10.17169/refubium-11540

Tietze, K., & Ritter, O. (2013). Three-dimensional magnetotelluric inversion in practice-the electrical conductivity structure of the San Andreas fault in central California. *Geophysical Journal International*, *195*(1). https://doi.org/10.1093/gji/ggt234

Tikhonov, A. (1950). On Determining Electrical Characteristics of the Deep Layers of the Earth's Crust. *Doklady*, *73*(2).

Ucok, H., Ershaghi, I., & Olhoeft, G. R. (1980). Electrical Resistivity Of Geothermal Brines. *JPT, Journal of Petroleum Technology*, *32*(4). https://doi.org/10.2118/7878-PA

Ussher, G., Harvey, C., Johnstone, R., Anderson, E., & Zealand, N. (2000). Understanding the resistivities observed in geothermal systems. *Proceedings World Geothermal Congress*.

Vozoff, K. (1990). Magnetotellurics: Principles and practice. *Proceedings of the Indian Academy of Sciences - Earth and Planetary Sciences*, *99*(4). https://doi.org/10.1007/BF02840313

Vozoff, K. (1991). The Magnetotelluric Method. In *Electromagnetic Methods in Applied Geophysics*. https://doi.org/10.1190/1.9781560802686.ch8

Wait, J. R. (1954). On The Relation Between Telluric Currents and The Earth's Magnetic Field. *Geophysics*, *19*(2). https://doi.org/10.1190/1.1437994

Wang, Y., Xu, T., Cheng, Y., & Feng, G. (2022). Prospects for Power Generation of the Doublet Supercritical Geothermal System in Reykjanes Geothermal Field, Iceland. *Energies*, *15*(22). https://doi.org/10.3390/en15228466

Wannamaker, P. E., Stodt, J. A., & Rijo, L. (1986). Two-dimensional topographic responses in magnetotellurics modeled using finite elements. *Geophysics*, *51*(11), 2131–2144. https://doi.org/10.1190/1.1442065

Ward, S. H., & Hohmann, G. W. (1988). 4. Electromagnetic Theory for Geophysical Applications. In *Electromagnetic Methods in Applied Geophysics*. https://doi.org/10.1190/1.9781560802631.ch4

Watts, M. D., Mackie, R., Scholl, C., & Hallinan, S. (2013). Limitations of MT static shift corrections using time-domain EM data. *Society of Exploration Geophysicists International Exposition and 83rd Annual Meeting, SEG 2013: Expanding Geophysical Frontiers*. https://doi.org/10.1190/segam2013-1078.1

Weaver, J. T. (1999). Numerical modelling in electromagnetic induction. In S. K. and M. K. Roy K. K. and Verma (Ed.), *Deep Electromagnetic Exploration* (pp. 299–363). Springer Berlin Heidelberg. https://doi.org/10.1007/BFb0011918

Weidelt, P., & Kaikkonen, P. (1994). Local 1-D interpretation of magnetotelluric B-polarization impedances. *Geophysical Journal International*, *117*(3). https://doi.org/10.1111/j.1365-246X.1994.tb02466.x

Wiese, H. (1962). Geomagnetische Tiefentellurik Teil II: Die Streichrichtung der untergrundstrukturen des elektrischen Widerstandes, erschlossen aus geomagnetischen Variationen. *Geo/sica Pura e Applicata*, *52*(1). https://doi.org/10.1007/BF01996002

Wight, D. E., & Bostick, F. X. (1980). Cascade Decimation - A Technique for Real Time Estimation Of Power Spectra. *Record - IEEE International Conference on Acoustics, Speech & Signal Processing*, *2*. https://doi.org/10.1109/icassp.1980.1170868

Williams, C. F., Reed, M. J., & Anderson, A. F. (2011). Updating the Classification of Geothermal Resources. *Proceedings, Thirty-Sixth Workshop on Geothermal Reservoir Engineering, Stanford University, Stanford, California, January 31 - February 2, 2011*.

Wright, P. M., Ward, S. H., Ross, H. P., & West, R. C. (1985). State-of-the-art geophysical exploration for geothermal resources. *Geophysics*, *50*(12). https://doi.org/10.1190/1.1441889

Wyering, L. D., Villeneuve, M. C., Wallis, I. C., Siratovich, P. A., Kennedy, B. M., Gravley, D. M., & Cant, J. L. (2014). Mechanical and physical properties of hydrothermally altered rocks, Taupo Volcanic Zone, New Zealand. *Journal of Volcanology and Geothermal Research*, *288*, 76–93. https://doi.org/10.1016/J.JVOLGEORES.2014.10.008

Yee, K. S. (1966). Numerical Solution of Initial Boundary Value Problems Involving Maxwell's Equations in Isotropic Media. In *IEEE Transactions on Antennas and Propagation* (Vol. 14, Issue 3). https://doi.org/10.1109/TAP.1966.1138693

Yogeshwar, P. (2014). *A resistivity-depth model of the central Azraq basin area, Jordan: 2D forward and inverse modeling of time domain electromagnetic data* [Universität zu Köln]. https://kups.ub.uni-koeln.de/5713/

Yogeshwar, P., Küpper, M., Tezkan, B., Rath, V., Kiyan, D., Byrdina, S., Cruz, J., Andrade, C., & Viveiros, F. (2020). Innovative boat-towed transient electromagnetics — Investigation of the Furnas volcanic lake hydrothermal system, Azores. *Geophysics*, *85*(2), E41–E56. https://doi.org/10.1190/geo2019-0292.1

Younger, P. L. (2014). Missing a trick in geothermal exploration. In *Nature Geoscience* (Vol. 7, Issue 7). https://doi.org/10.1038/ngeo2193

Zhang, L., Wang, R., Song, H., Xie, H., Fan, H., Sun, P., & Du, L. (2019). Numerical investigation of techno-economic multiobjective optimization of geothermal water reservoir development: A case study of China. *Water (Switzerland)*, *11*(11). https://doi.org/10.3390/w11112323

Zhdanov, M. S. (2015). Inverse Theory and Applications in Geophysics. In *Inverse Theory and Applications in Geophysics*. https://doi.org/10.1016/C2012-0-03334-0

Appendix

A. 2D MT Inversion Model

The fifteen (15) MT locations from the first stage of the MT survey are shown in Figure A-1. The MT soundings are arranged along a North-South transect within a valley filled with Quaternary fluvial deposits, which are partially flooded with water and intersect the Ain Al-Harrah hot spring. On either side of the valley, steep mountains rise, featuring an altitude difference of approximately 700 meters.

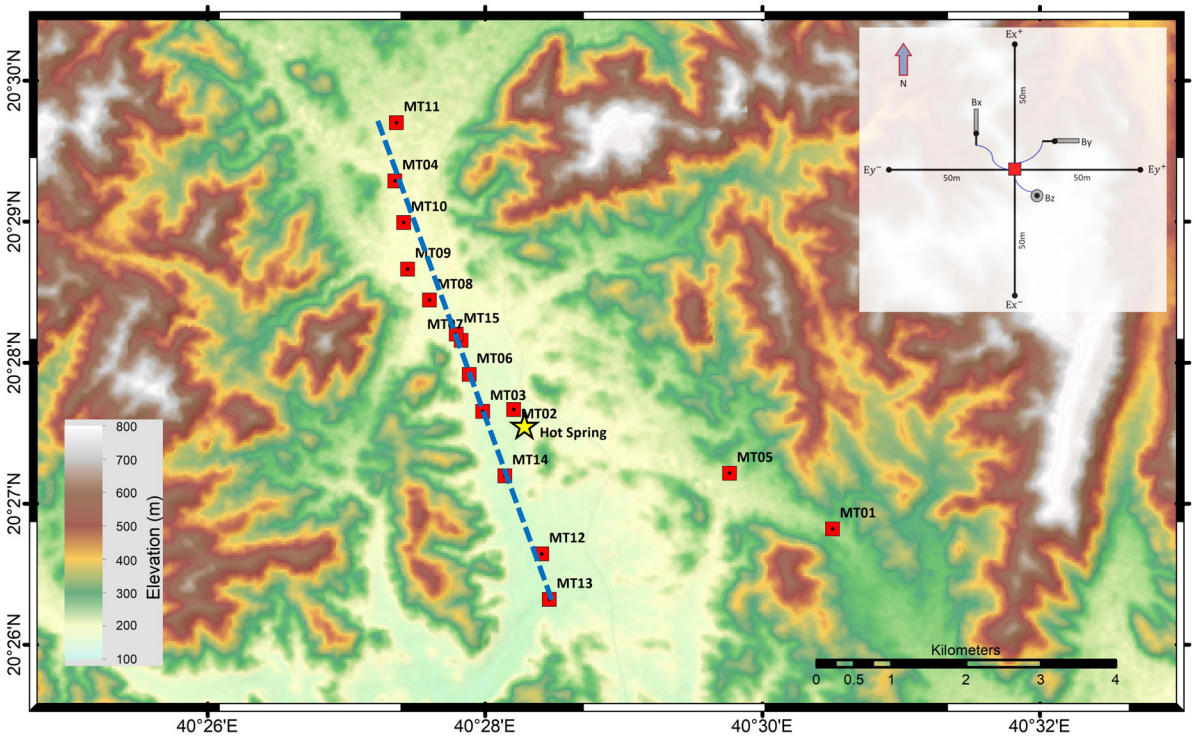

Appendix Figure A-1: A topographic map showing the locations of the 15 MT soundings (indicated by red squares) acquired during the first stage of the MT survey. The yellow star marks the location of Ain Al-Harrah's hot spring. Additionally, the MT layout is displayed in the top right corner of the figure. Figure taken from Ashadi et al. (2024).

Figure A-2 shows the 2D inversion result of the determinant of the impedance tensor of TM- and TE-mode data during the first stage of the MT survey. After 40 iterations, the data achieved an overall error-weighted RMS of 4.0. However, the fit is not optimal within the data error bounds, likely due to the influence of 3D resistivity structure, galvanic effects, and dimensionality challenges. However, the resulting 2D resistivity model is consistent and geologically meaningful, effectively imaging the main geothermal features. It clearly depicts the heat source, the fracture zone and its role in

the convection pattern, and the groundwater system within the Ain Al-Harrah geothermal system (Ashadi et al., 2024).

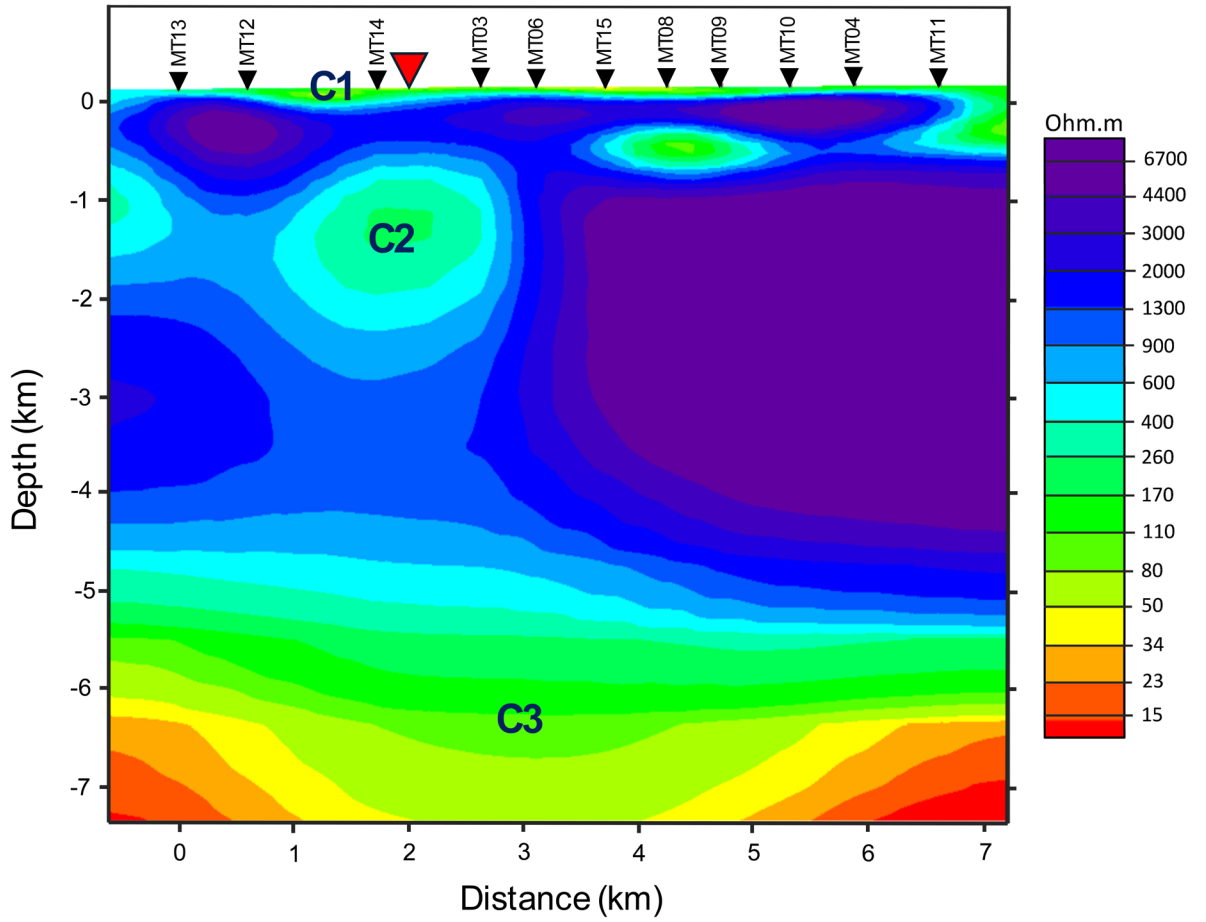

Appendix Figure A-2: The interpreted 2D geoelectrical model along a 7.8 km long profile, generated from the first stage of MT fieldwork. Modified from Ashadi et al. (2024).

The result of the 2D inversion reveals four noteworthy features or units that can be interpreted in the context of the geothermal anomaly (Ashadi et al., 2024):

1. A low resistivity C1 unit (80–200 Ω.m), which represents the uppermost layers of the model, can be interpreted as Quaternary deposits that are saturated or partially saturated with freshwater at the surface.

2. A medium to high resistivity, C2 unit (150–900 Ω.m), appears as a laterally discontinuous resistivity pattern, indicating a fractured or fault zone that serves as a pathway for geothermal fluids to migrate to the near subsurface, potentially leading to active geothermal surface manifestations such as hot springs.

3. A lower resistive C3 unit ($<$ 50 Ω.m), located in the bottom layers of the model, can be interpreted as the heat source situated beneath a depth of 5 km.

4. The high resistivity body (> 1000 Ω.m) is identified in both the northern and southern parts of the basin, associated with the basement structures in the study area.

B. Station Coordinates

In the following Appendix, the stations coordinates are displayed.

Appendix Table B-1: Location of the MT soundings used in this thesis. Whether the vertical induction coil (tipper data) is present and whether the TEM sounding was installed in the corresponding MT station are listed in columns 5 and 6.

Station	**Latitude**	**Longitude**	**Elevation (m)**	**Tipper**	**TEM**
MT01	20.44896	40.50845	197.60	☑	☑
MT02	20.46324	40.47006	165.60	☒	☒
MT03	20.46304	40.46642	171.00	☒	☒
MT04	20.49071	40.45579	184.00	☒	☒
MT05	20.45560	40.49601	204.00	☒	☑
MT06	20.46705	40.46473	170.10	☒	☒
MT07	20.47158	40.46382	166.50	☒	☒
MT08	20.47644	40.45998	170.00	☒	☒
MT09	20.48015	40.45734	177.20	☑	☒
MT10	20.48571	40.45687	175.80	☒	☒
MT11	20.49773	40.45597	183.60	☒	☒
MT12	20.44587	40.47351	161.10	☑	☒
MT13	20.44042	40.47439	146.90	☒	☒
MT14	20.45530	40.46906	161.90	☒	☒
MT15	20.47231	40.46318	164.50	☒	☒
MT16	20.45867	40.46648	177.63	☒	☒
MT17	20.45660	40.46751	158.47	☑	☒
MT18	20.45143	40.47087	159.82	☒	☒
MT19	20.44839	40.47168	158.49	☑	☒
MT20	20.44296	40.47473	160.00	☒	☒
MT21	20.45055	40.47551	162.81	☒	☒
MT22	20.45385	40.47946	165.00	☒	☒
MT23	20.48248	40.48688	208.22	☒	☒
MT24	20.48044	40.48103	193.47	☒	☒
MT25	20.47839	40.47378	181.74	☑	☒
MT26	20.45648	40.48529	184.07	☑	☑
MT27	20.45622	40.48837	181.99	☒	☑
MT28	20.45547	40.49066	184.72	☒	☑
MT29	20.45164	40.49549	175.85	☒	☑

MT30	20.44906	40.49434	182.66	☑	☒
MT31	20.44603	40.49395	173.53	☒	☒
MT32	20.44280	40.49291	168.96	☒	☒
MT33	20.43931	40.48648	174.93	☑	☒
MT34	20.43991	40.48314	163.81	☒	☑
MT35	20.44268	40.48868	169.86	☒	☒
MT36	20.44150	40.48600	168.75	☒	☒
MT37	20.44791	40.48965	184.98	☑	☒
MT38	20.44653	40.48479	171.32	☒	☒
MT39	20.44453	40.48143	159.78	☒	☑
MT40	20.45296	40.48408	180.25	☑	☒
MT41	20.46593	40.48239	185.15	☑	☑
MT42	20.46631	40.47892	179.01	☒	☑
MT43	20.46825	40.47288	170.08	☒	☑
MT44	20.47349	40.47765	179.77	☒	☒
MT45	20.47133	40.48194	189.91	☑	☒
MT46	20.46073	40.48879	186.88	☒	☑
MT47	20.46354	40.48697	182.66	☒	☑
MT48	20.46020	40.47735	169.93	☑	☒
MT49	20.45326	40.47447	163.43	☒	☒
MT50	20.46450	40.47639	185.28	☒	☒

C. MT Transfer Functions

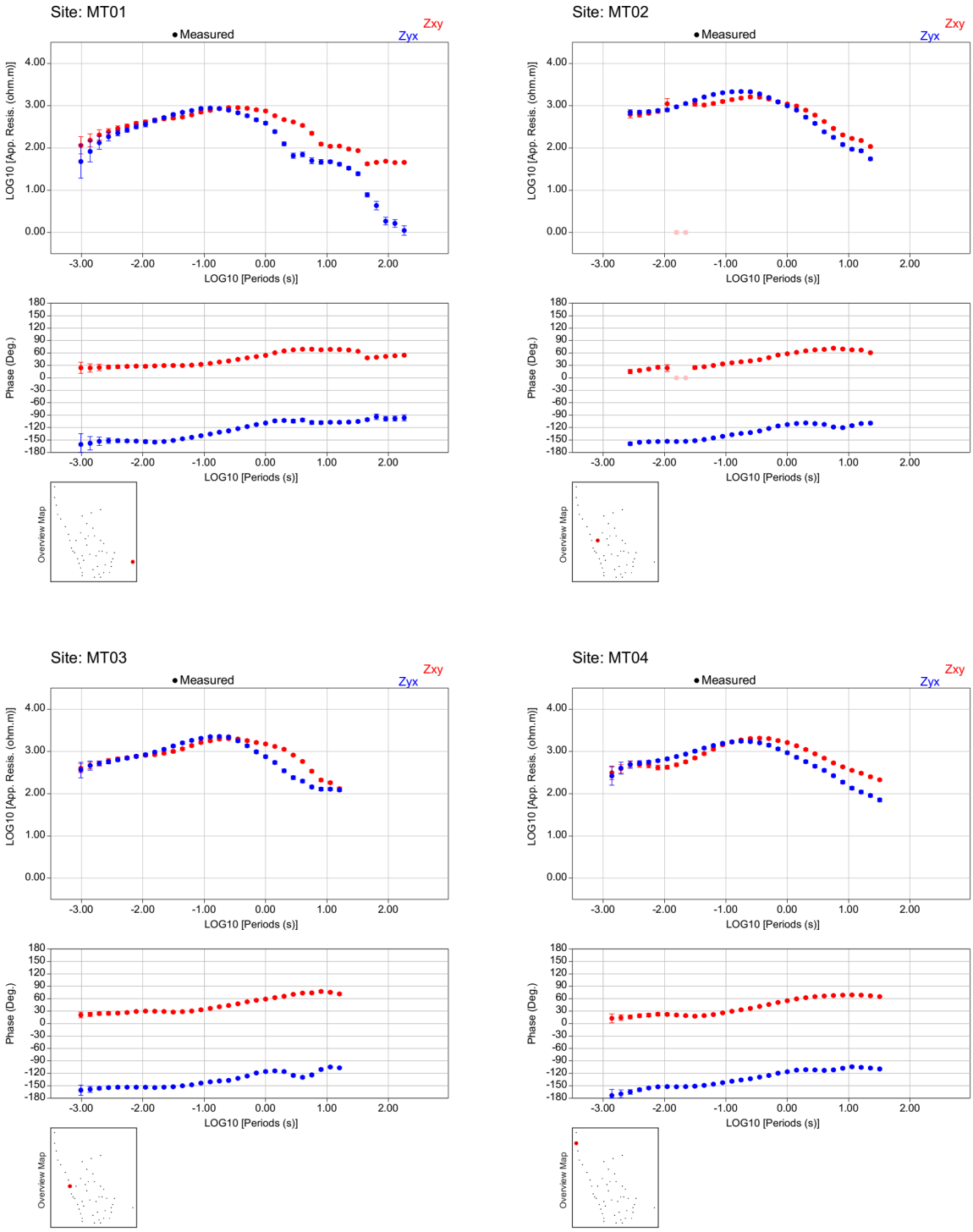

Appendix Figure C-1: MT transfer functions obtained after data processing for stations MT01 to MT04. The red color represents the XY components, while the blue indicates the YX components.

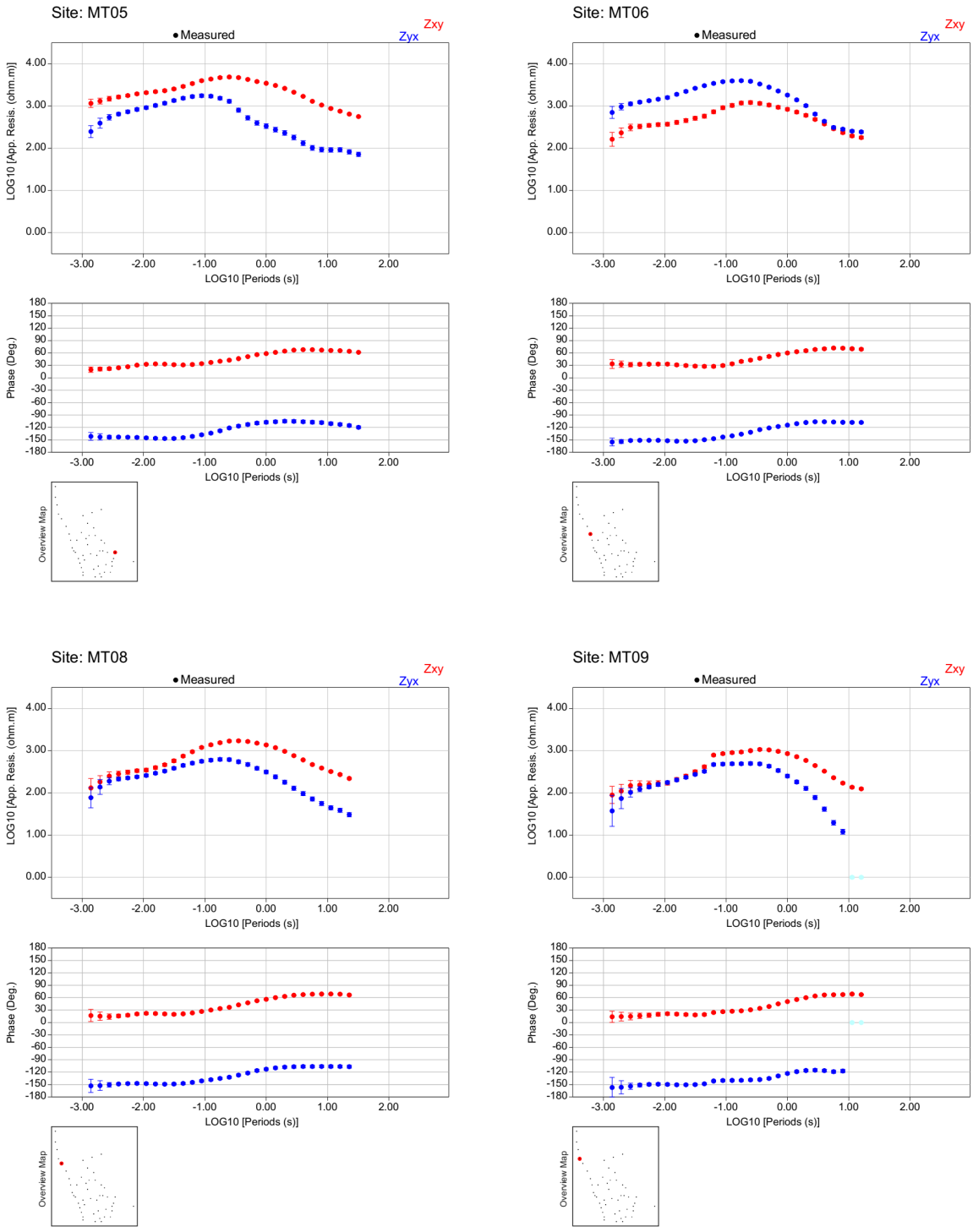

Appendix Figure C-2: MT transfer functions obtained after data processing for stations MT05 to MT09. The red color represents the XY components, while the blue indicates the YX components.

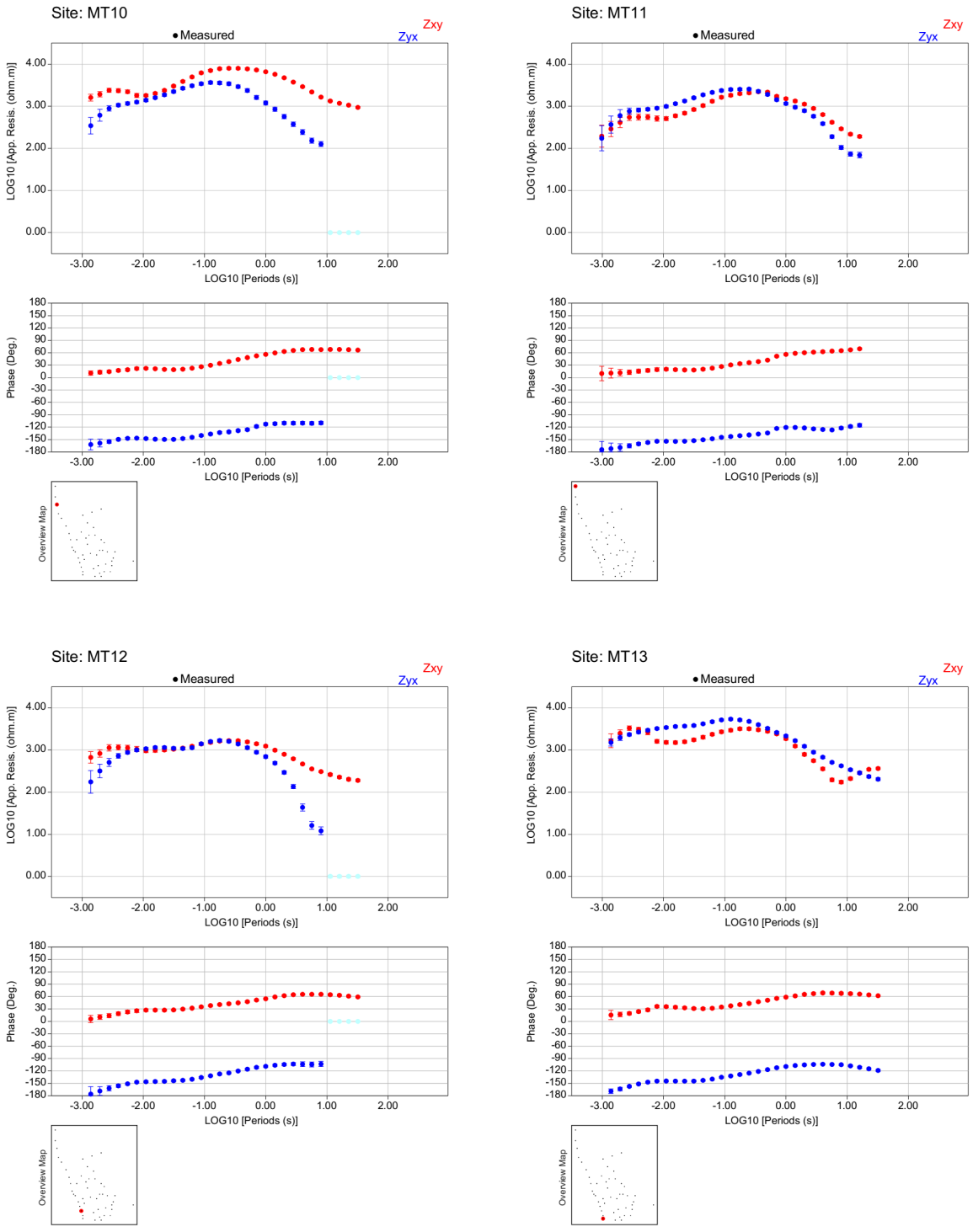

Appendix Figure C-3: MT transfer functions obtained after data processing for stations MT10 to MT13. The red color represents the XY components, while the blue indicates the YX components.

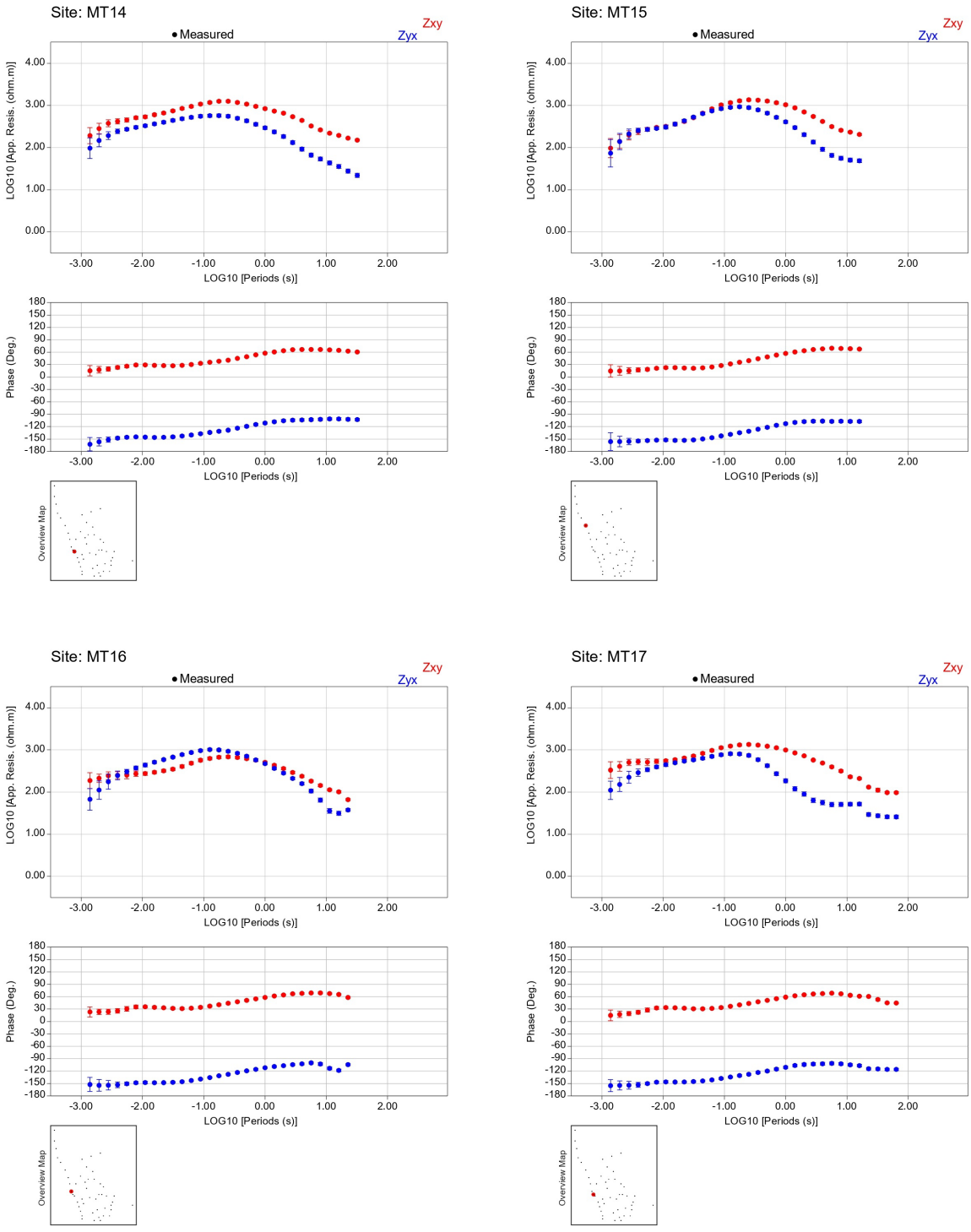

Appendix Figure C-4: MT transfer functions obtained after data processing for stations MT14 to MT17. The red color represents the XY components, while the blue indicates the YX components.

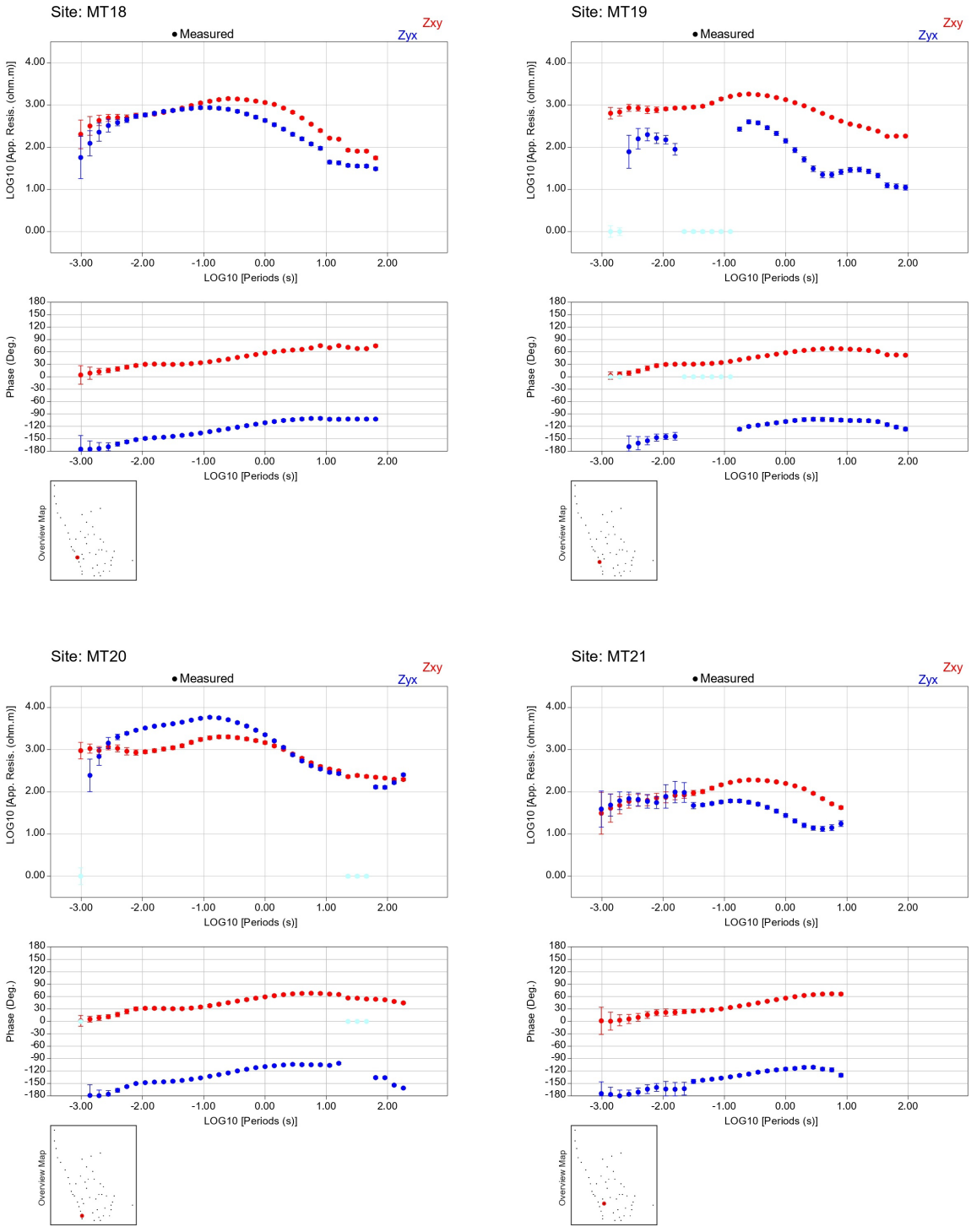

Appendix Figure C-5: MT transfer functions obtained after data processing for stations MT18 to MT21. The red color represents the XY components, while the blue indicates the YX components.

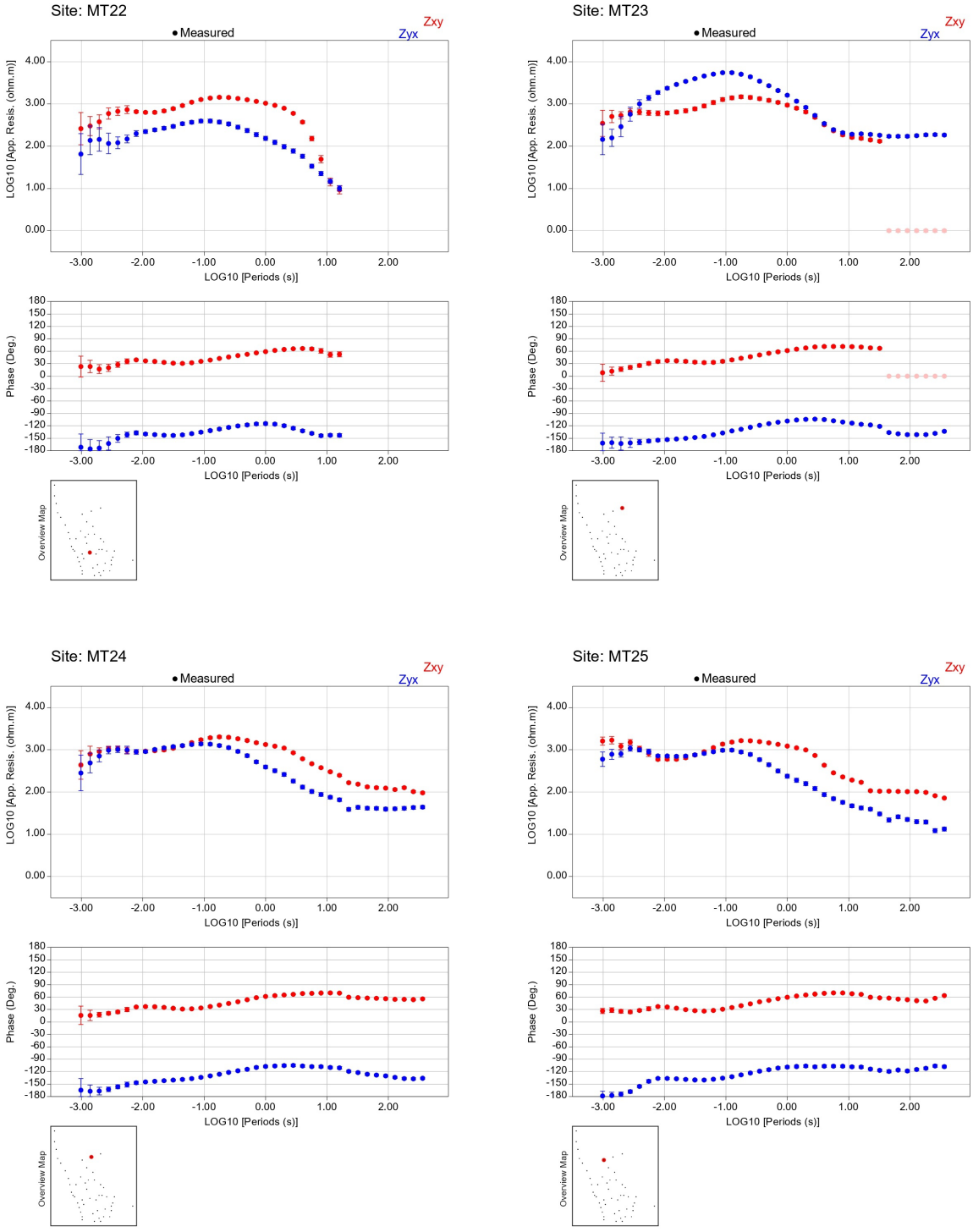

Appendix Figure C-6: MT transfer functions obtained after data processing for stations MT22 to MT25. The red color represents the XY components, while the blue indicates the YX components.

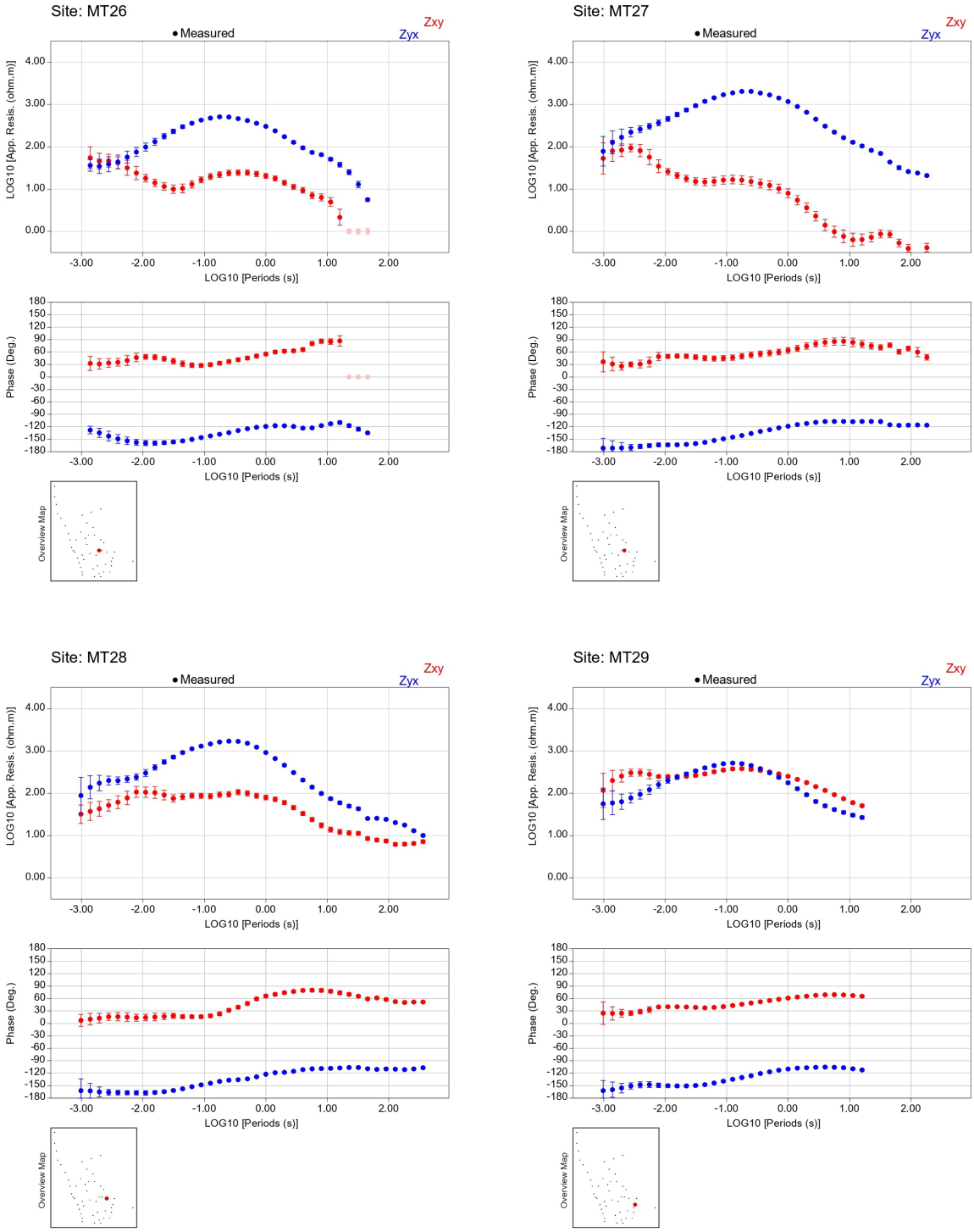

Appendix Figure C-7: MT transfer functions obtained after data processing for stations MT26 to MT29. The red color represents the XY components, while the blue indicates the YX components.

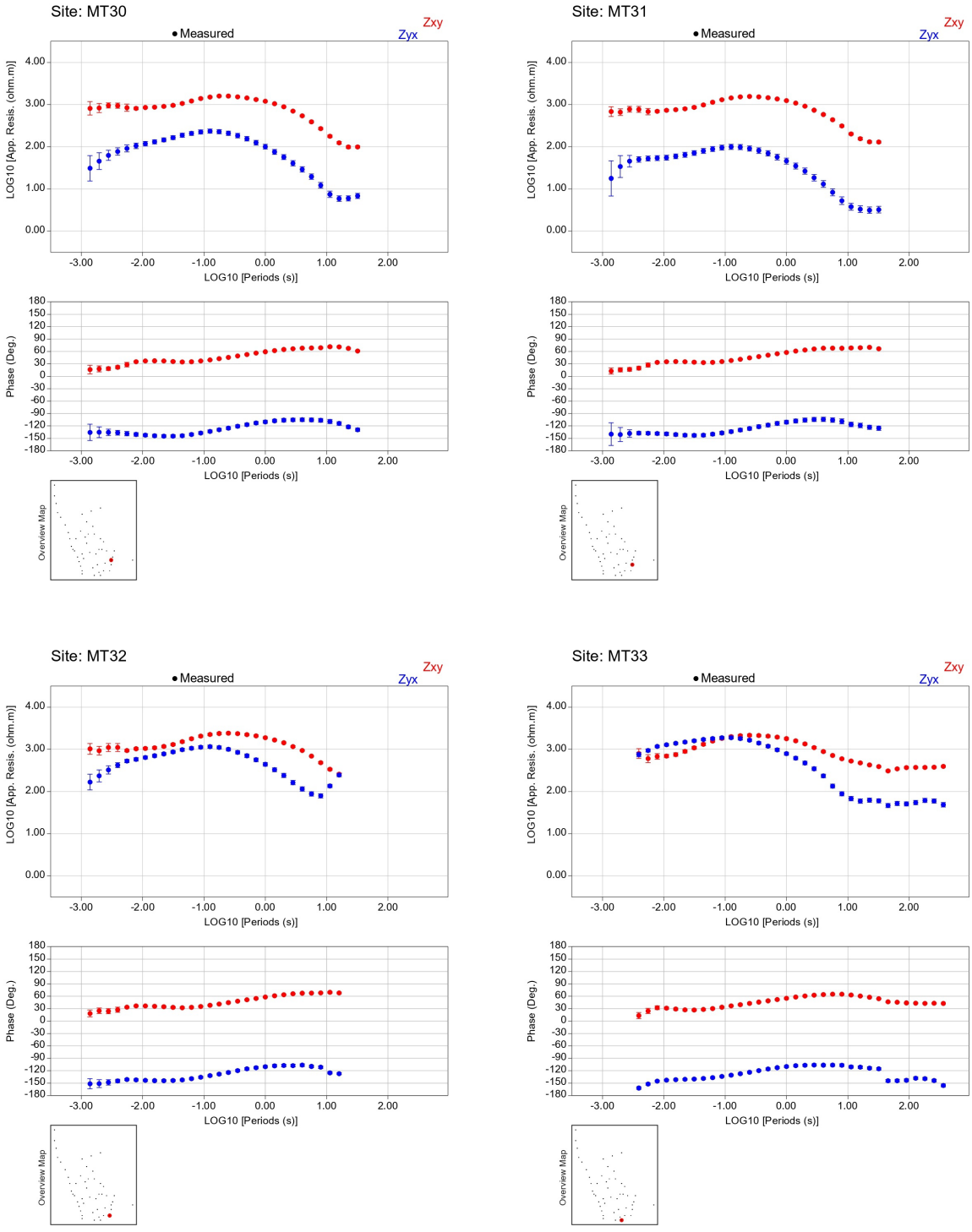

Appendix Figure C-8: MT transfer functions obtained after data processing for stations MT30 to MT33. The red color represents the XY components, while the blue indicates the YX components.

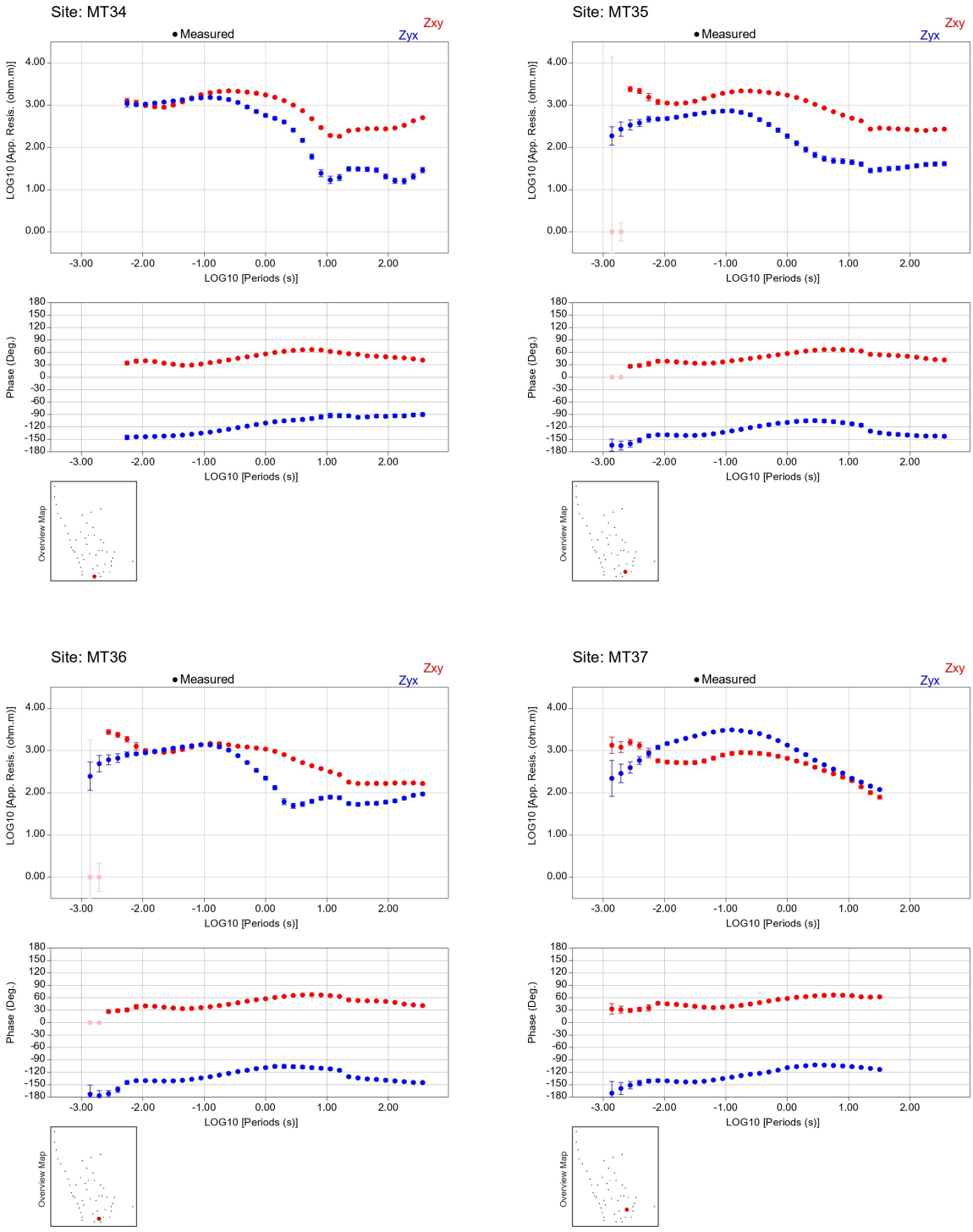

Appendix Figure C-9: MT transfer functions obtained after data processing for stations MT34 to MT37. The red color represents the XY components, while the blue indicates the YX components.

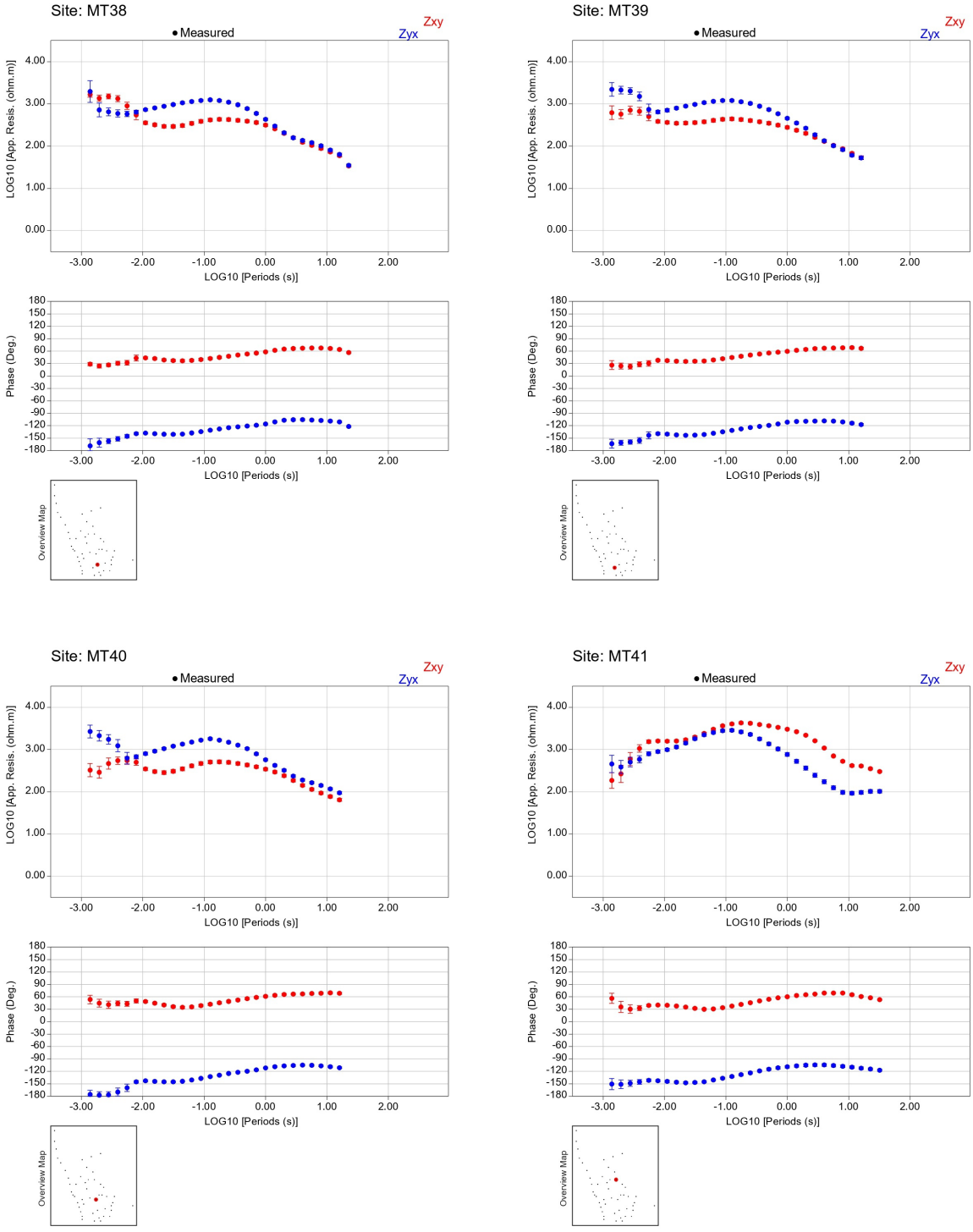

Appendix Figure C-10: MT transfer functions obtained after data processing for stations MT38 to MT41. The red color represents the XY components, while the blue indicates the YX components.

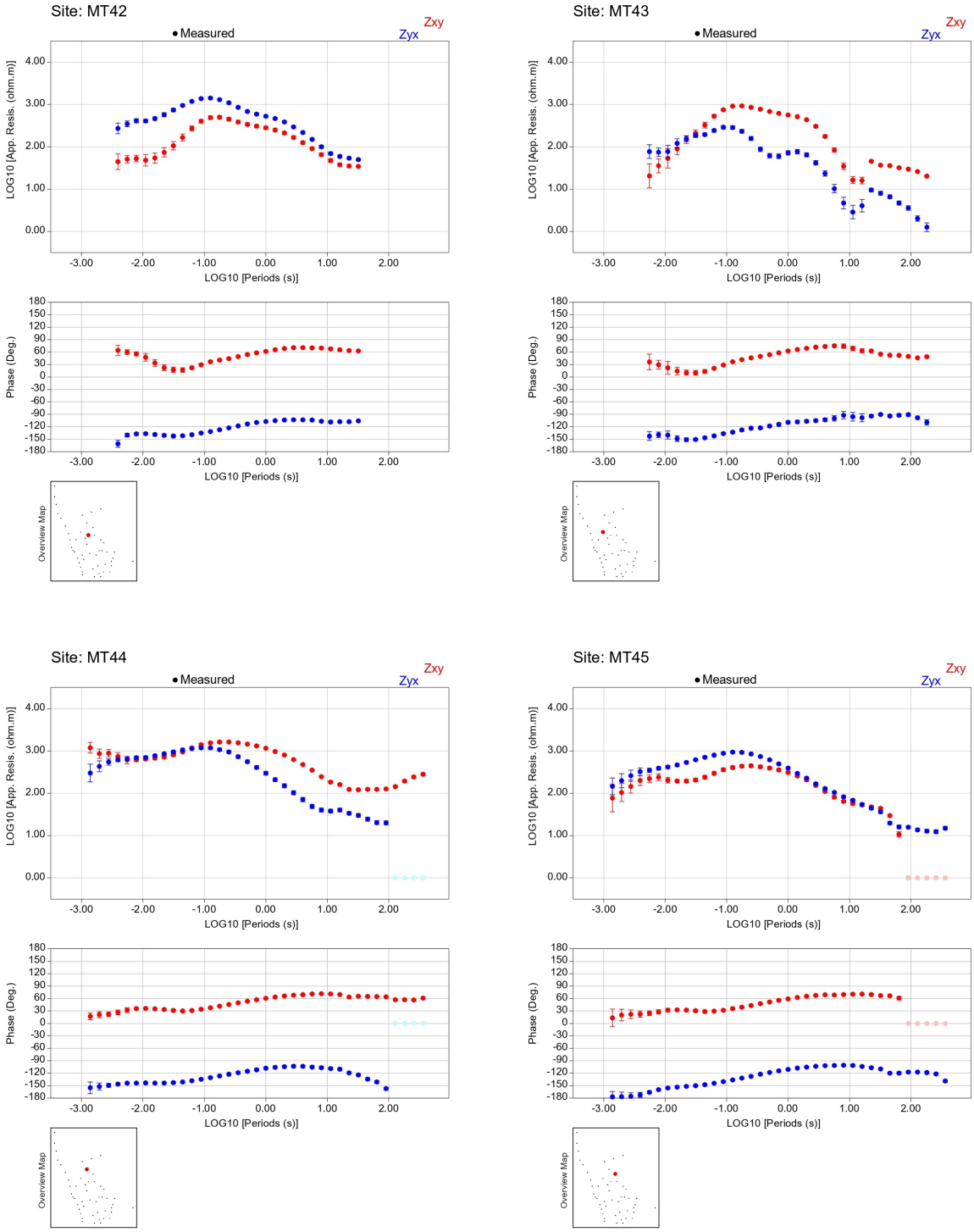

Appendix Figure C-11: MT transfer functions obtained after data processing for stations MT42 to MT45. The red color represents the XY components, while the blue indicates the YX components.

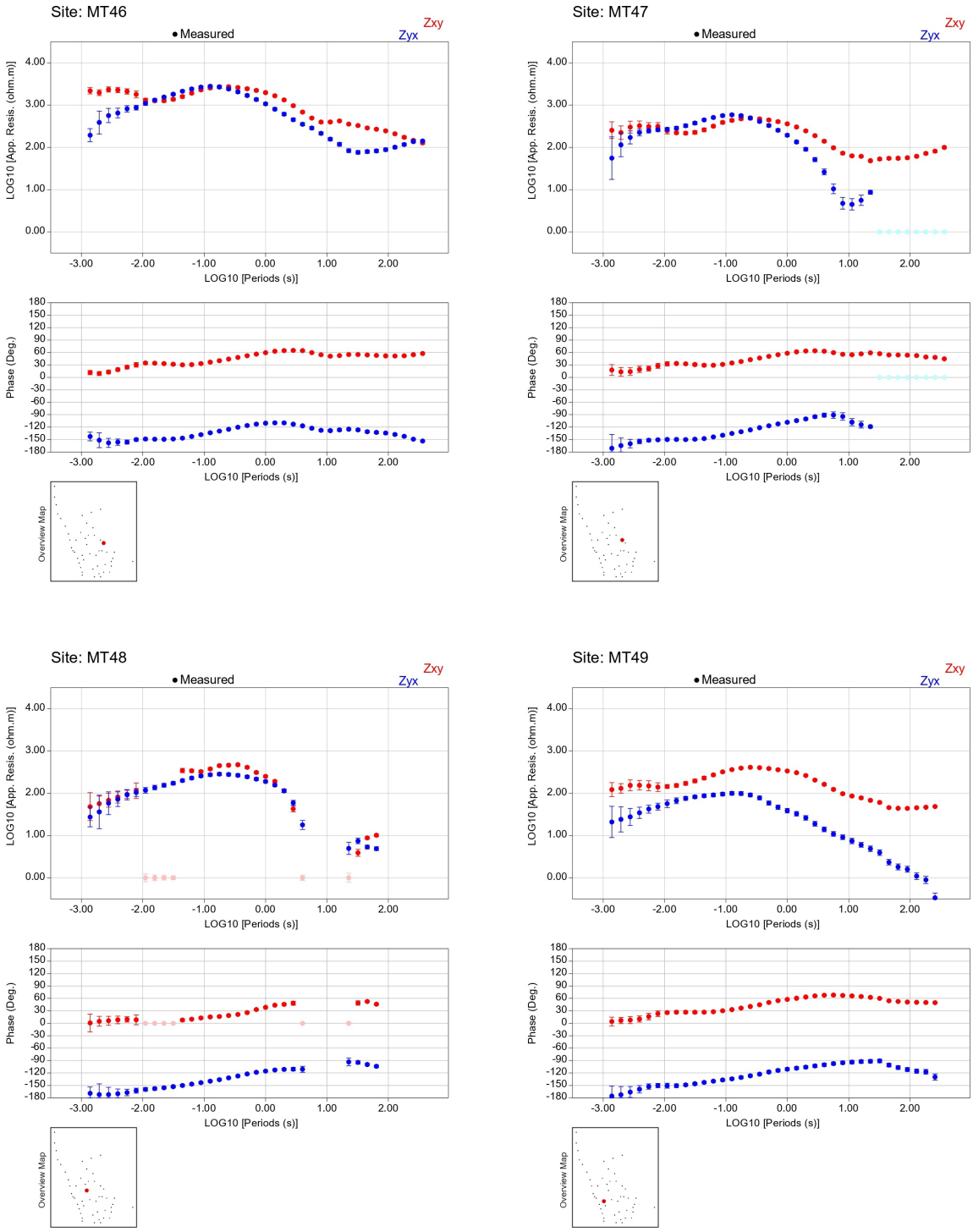

Appendix Figure C-12: MT transfer functions obtained after data processing for stations MT46 to MT49. The red color represents the XY components, while the blue indicates the YX components.

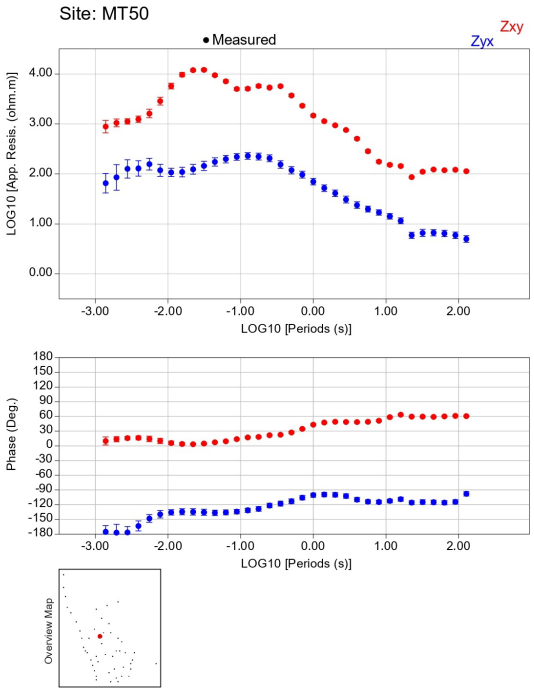

Appendix Figure C-13: MT transfer functions obtained after data processing for station MT50. The red color represents the XY components, while the blue indicates the YX components.

D. TEM Data Selections

Following the processing step, TEM data points suitable for further inversion process were meticulously chosen. The following figures display the raw, stacked, and selected data points for the remaining TEM soundings. Data points below the noise level were eliminated, and saturated sections at early times were also excluded from the selected data.

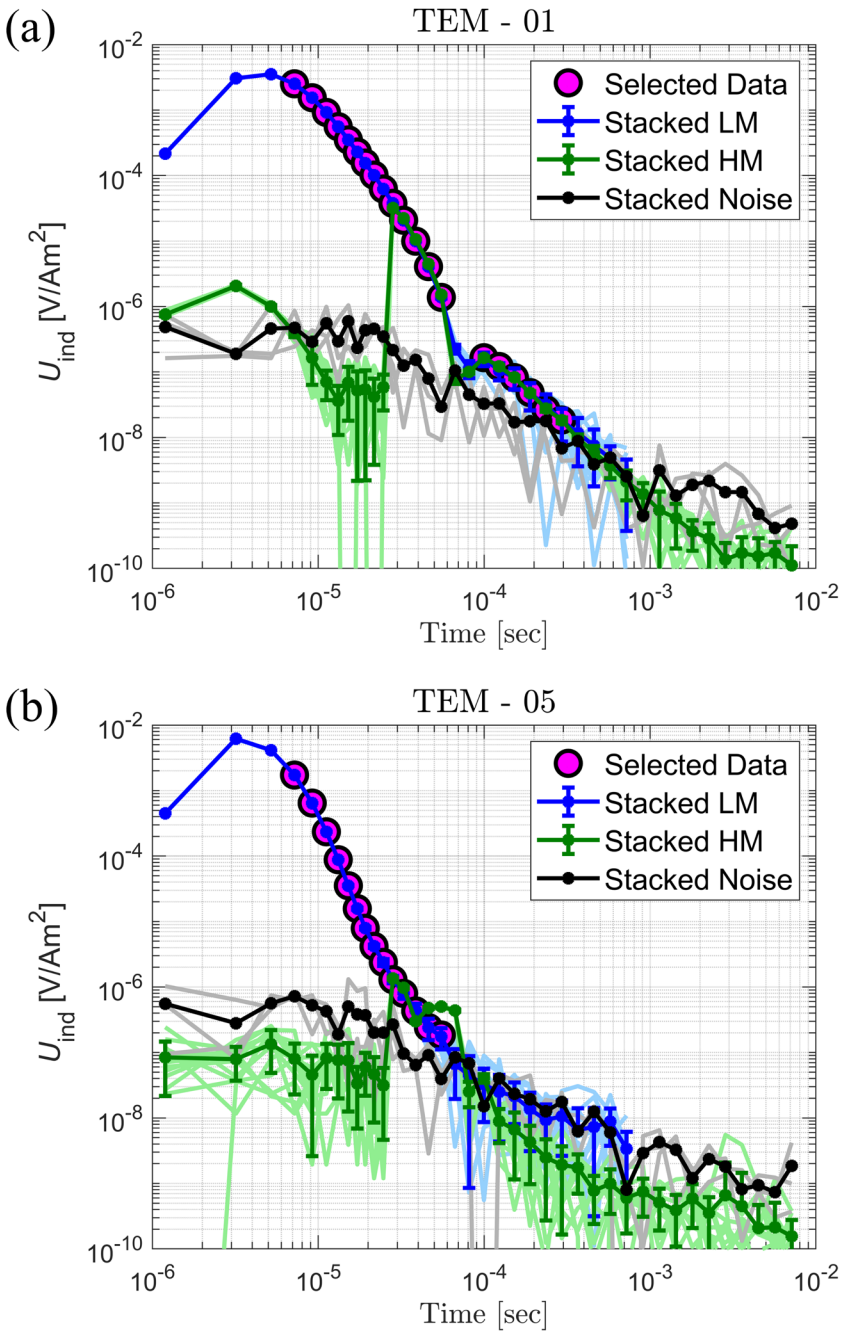

Appendix Figure D-1: Stacked and selected data points of (a) TEM – 01 and (b) TEM – 05 soundings. The magenta circles represent the selected transient data used for further inversion. The stacked data for the low-moment (LM), high-moment (HM), and noise level are shown in blue, green, and black lines, respectively.

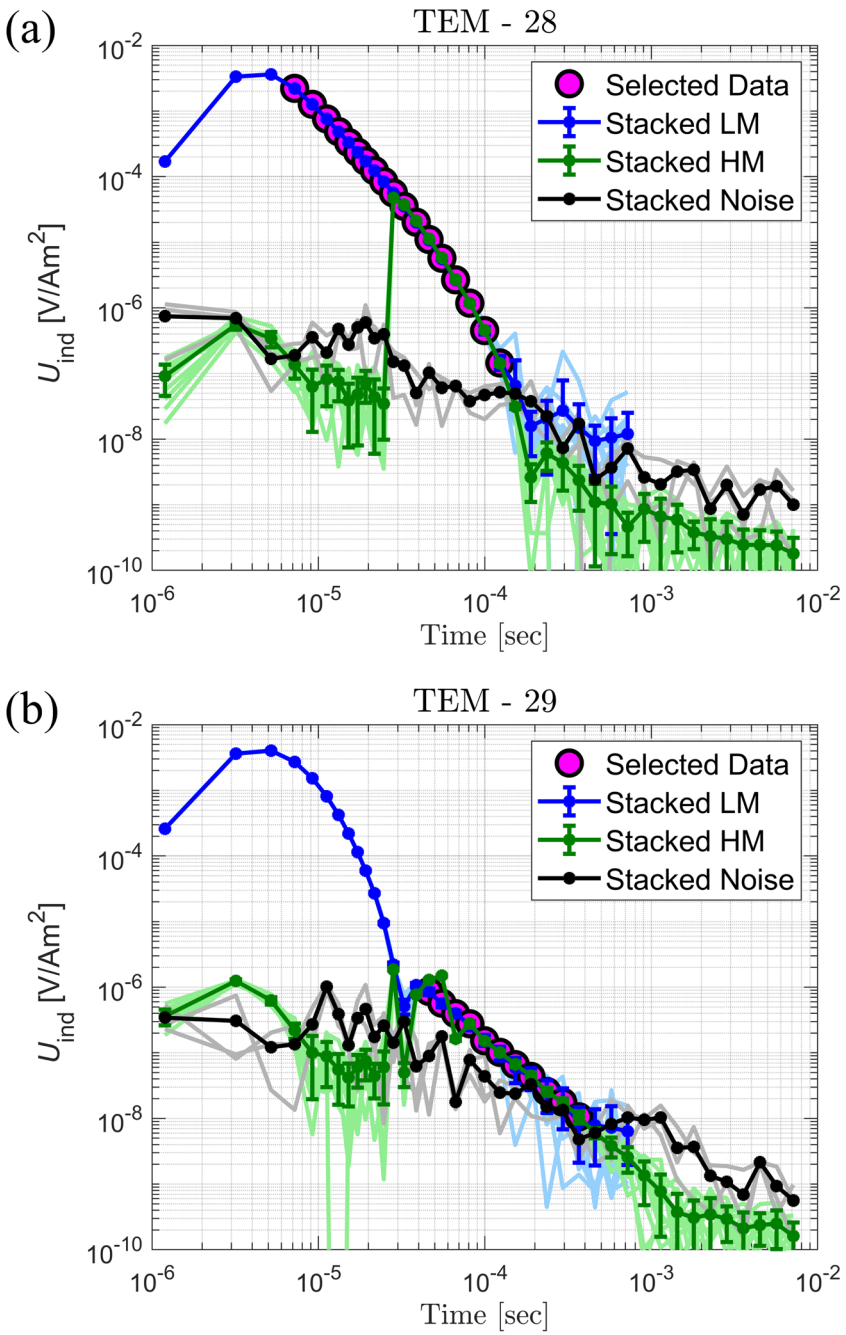

Appendix Figure D-2: Stacked and selected data points of (a) TEM – 28 and (b) TEM – 29 soundings. The magenta circles represent the selected transient data used for further inversion. The stacked data for the low-moment (LM), high-moment (HM), and noise level are shown in blue, green, and black lines, respectively.

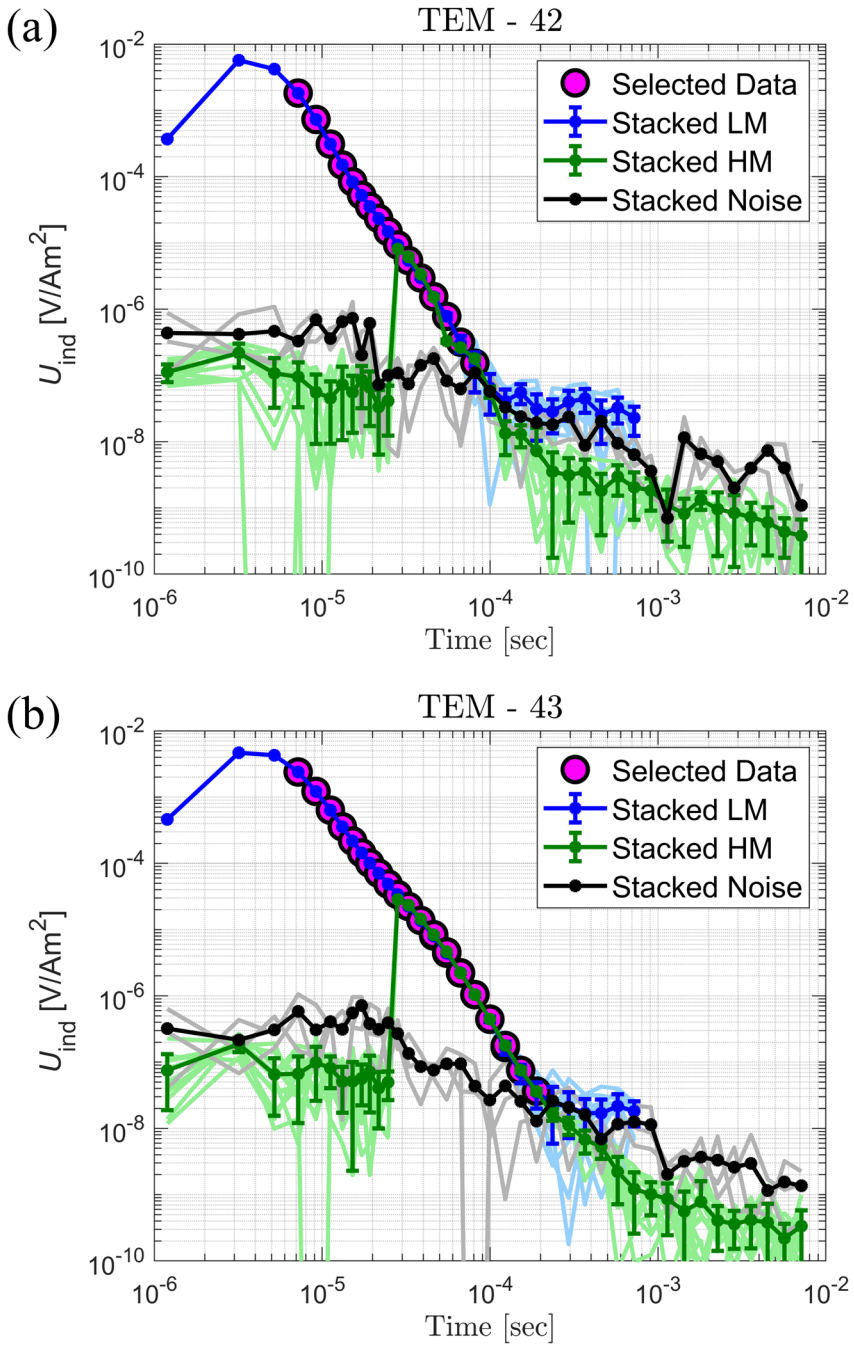

Appendix Figure D-3: Stacked and selected data points of (a) TEM – 42 and (b) TEM – 43 soundings. The magenta circles represent the selected transient data used for further inversion. The stacked data for the low-moment (LM), high-moment (HM), and noise level are shown in blue, green, and black lines, respectively.

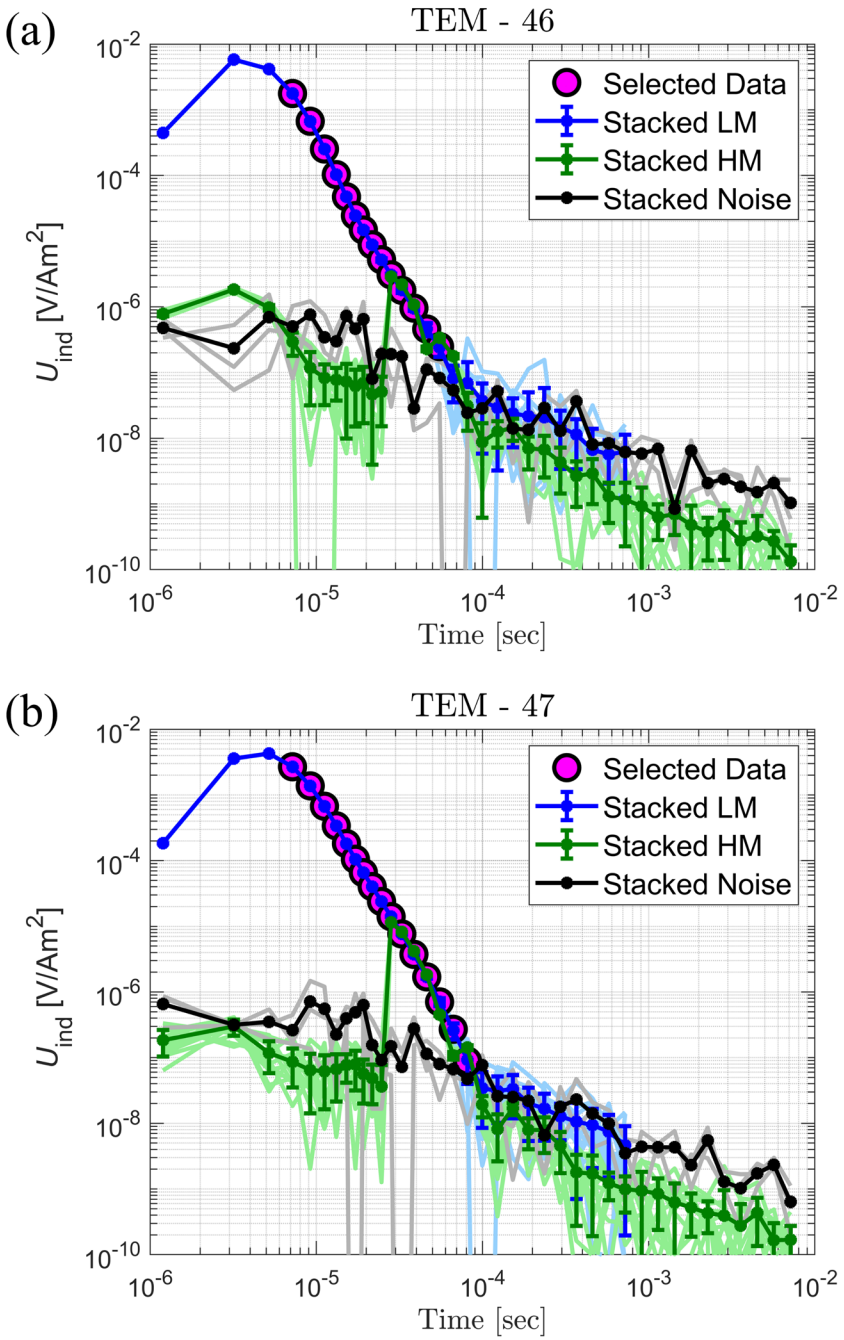

Appendix Figure D-4: Stacked and selected data points of (a) TEM – 46 and (b) TEM – 47 soundings. The magenta circles represent the selected transient data used for further inversion. The stacked data for the low-moment (LM), high-moment (HM), and noise level are shown in blue, green, and black lines, respectively.

E. 1D TEM Inversion Models

The following figures display 1D inversion models and their corresponding data fits for the rest of the TEM soundings.

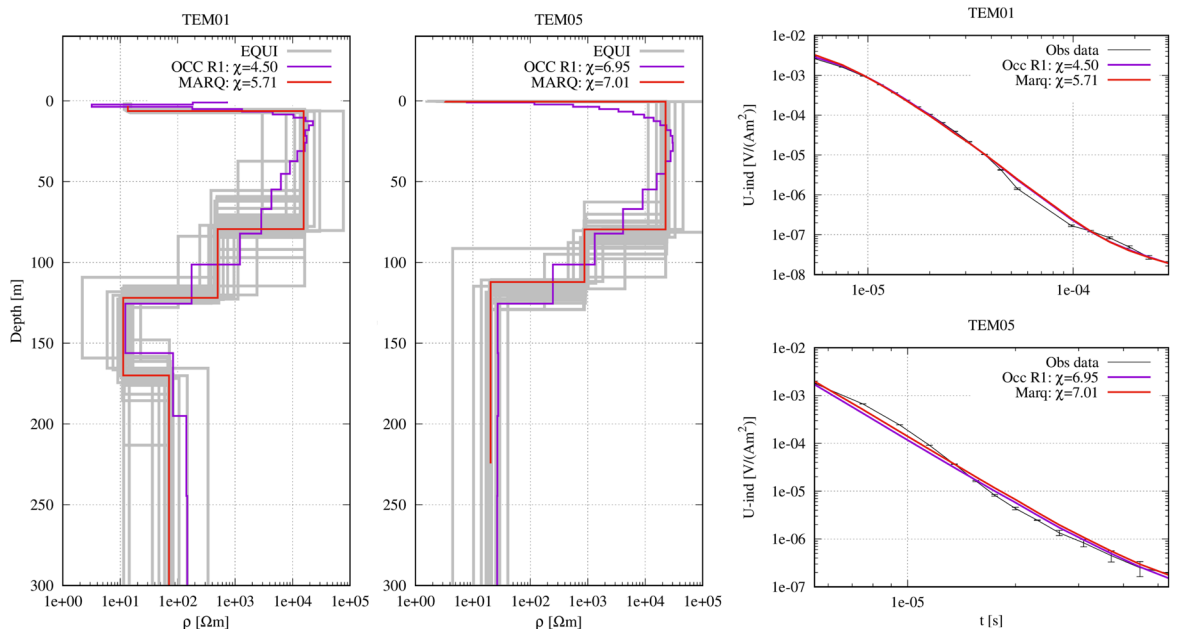

Appendix Figure E-1: 1D inversion results obtained from stations TEM01 and TEM05 with different algorithms: Levenberg-Marquardt (red lines), Occam with a first-order smoothness constraint (magenta lines), and the equivalent model (grey lines) shown in the left panel. The right panel illustrates the induced voltage decay over time, comparing both observed and calculated TEM data for each inversion approach.

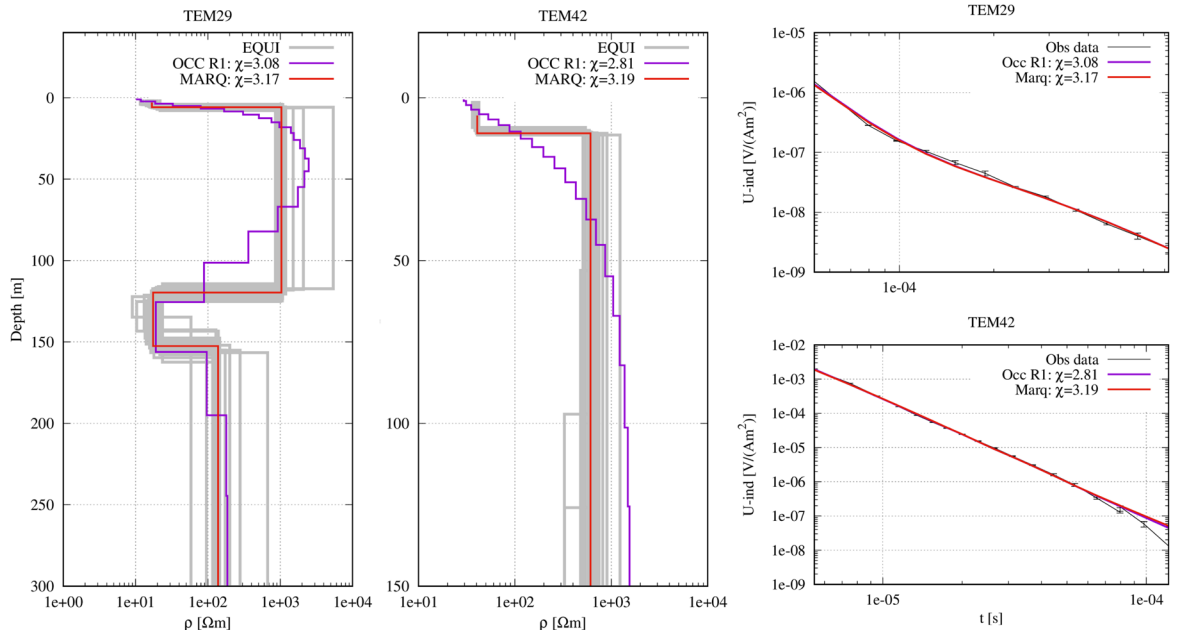

Appendix Figure E-2: 1D inversion results obtained from stations TEM29 and TEM42 with different algorithms: Levenberg-Marquardt (red lines), Occam with a first-order smoothness constraint (magenta lines), and the equivalent model (grey lines) shown in the left panel. The right panel illustrates the

induced voltage decay over time, comparing both observed and calculated TEM data for each inversion approach.

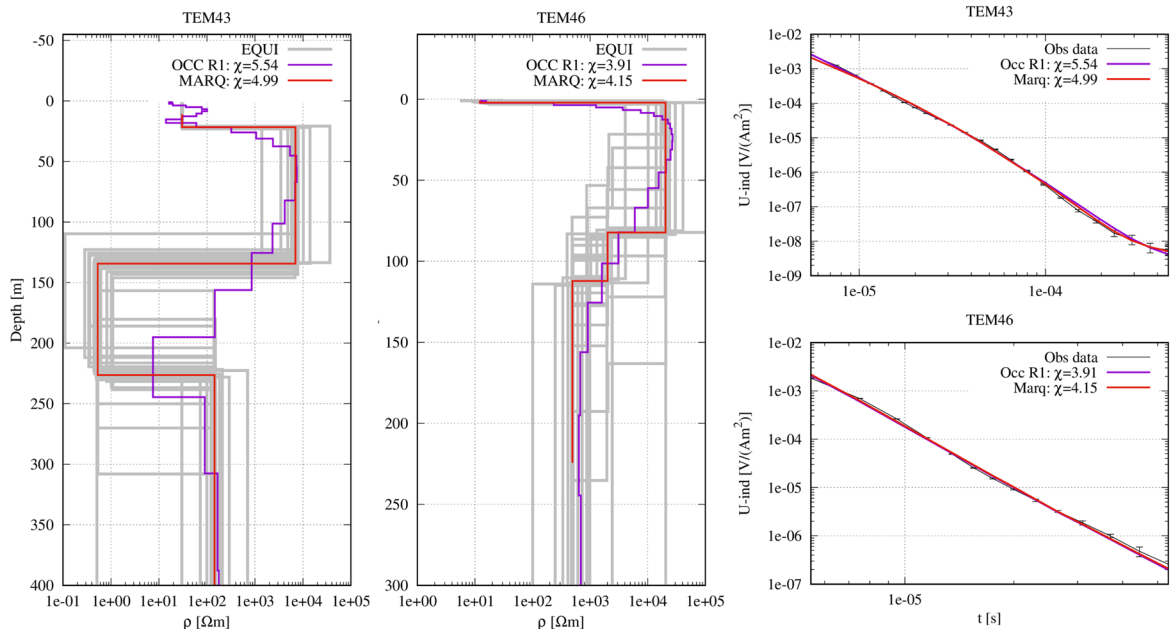

Appendix Figure E-3: 1D inversion results obtained from stations TEM43 and TEM46 with different algorithms: Levenberg-Marquardt (red lines), Occam with a first-order smoothness constraint (magenta lines), and the equivalent model (grey lines) shown in the left panel. The right panel illustrates the induced voltage decay over time, comparing both observed and calculated TEM data for each inversion approach.

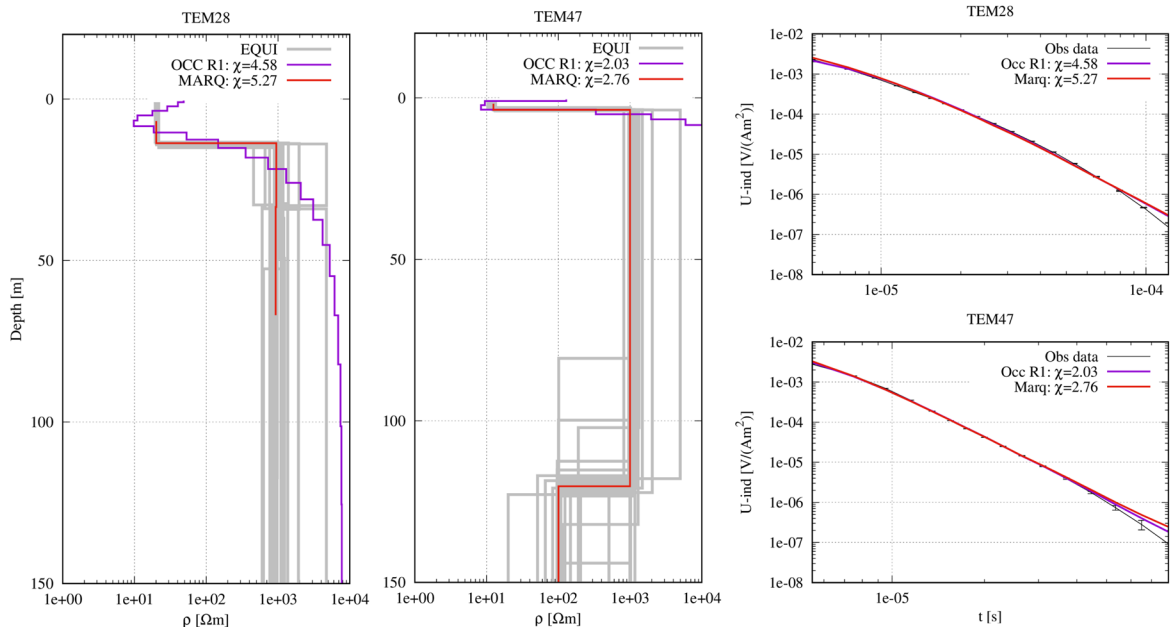

Appendix Figure E-4: 1D inversion results obtained from stations TEM28 and TEM47 with different algorithms: Levenberg-Marquardt (red lines), Occam with a first-order smoothness constraint (magenta lines), and the equivalent model (grey lines) shown in the left panel. The right panel illustrates the induced voltage decay over time, comparing both observed and calculated TEM data for each inversion approach.

F. 3D Inversion Data Fit

This Appendix shows the data fit between calculated and observed data from the preferred 3D MT inversion model, which incorporating the TEM data as a priori information.

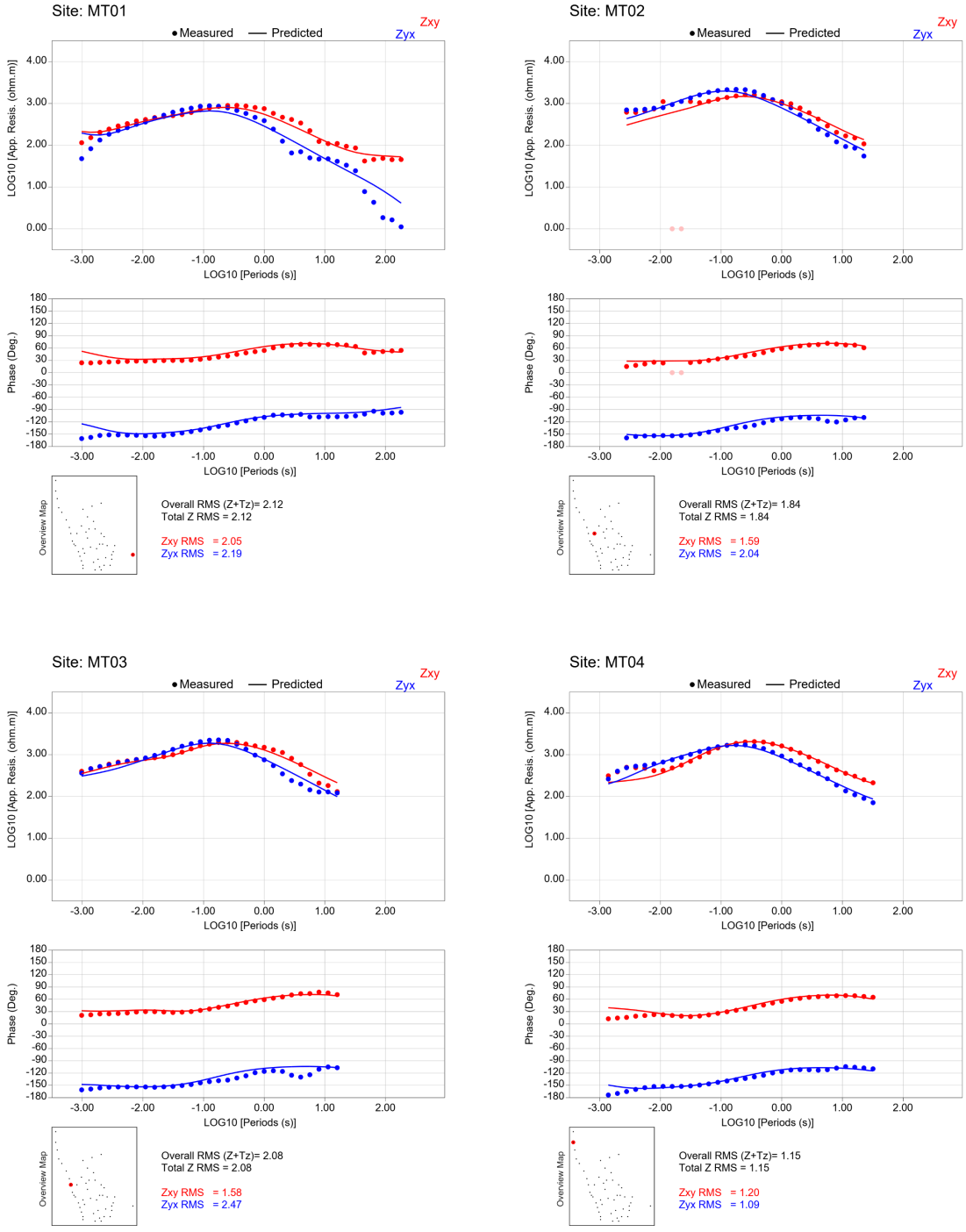

Appendix Figure F-1: Comparison of observed versus predicted MT transfer functions from the preferred model at stations MT01 to MT04. The red color represents the XY components, while the blue indicates the YX components.

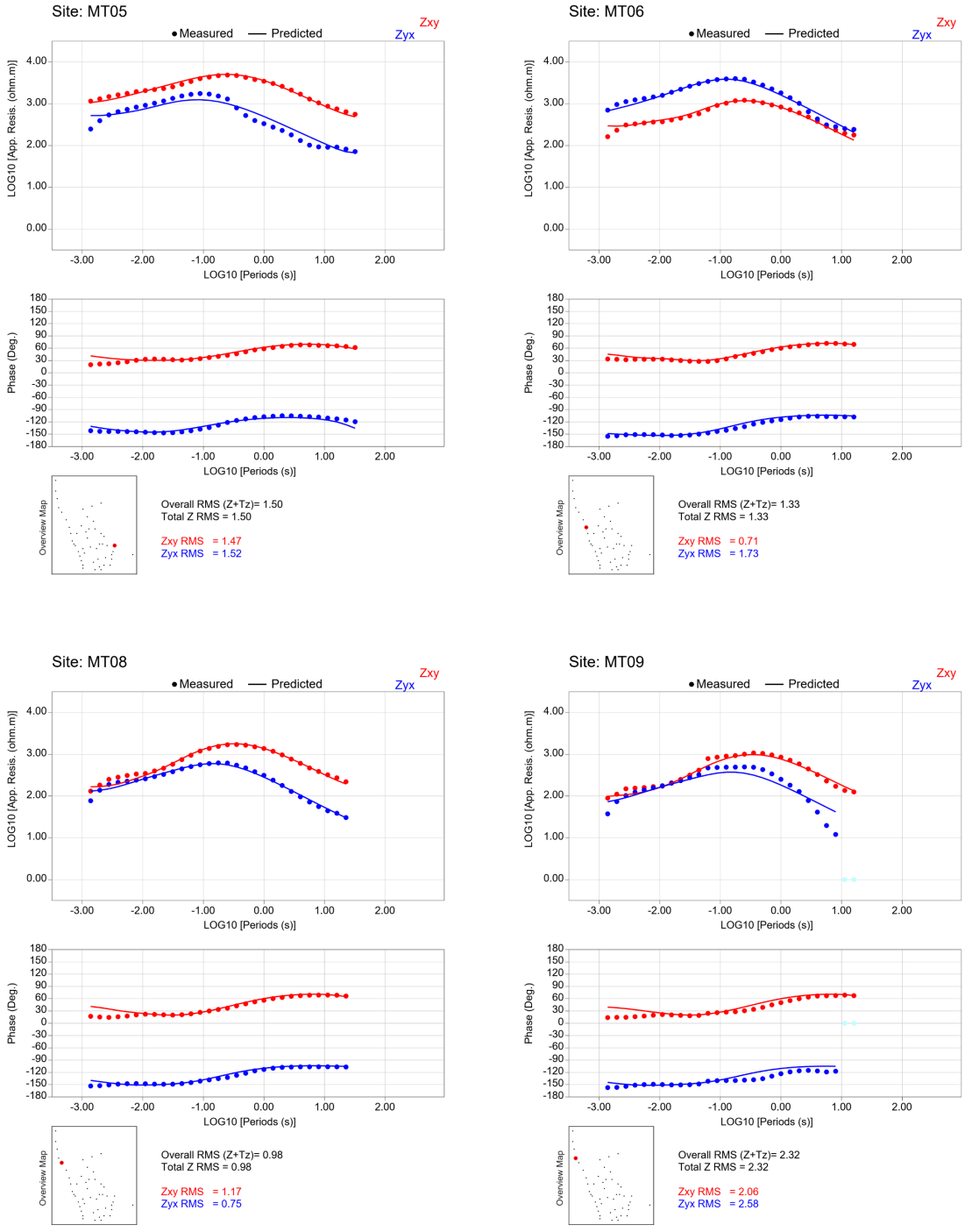

Appendix Figure F-2: Comparison of observed versus predicted MT transfer functions from the preferred model at stations MT05 to MT09. The red color represents the XY components, while the blue indicates the YX components.

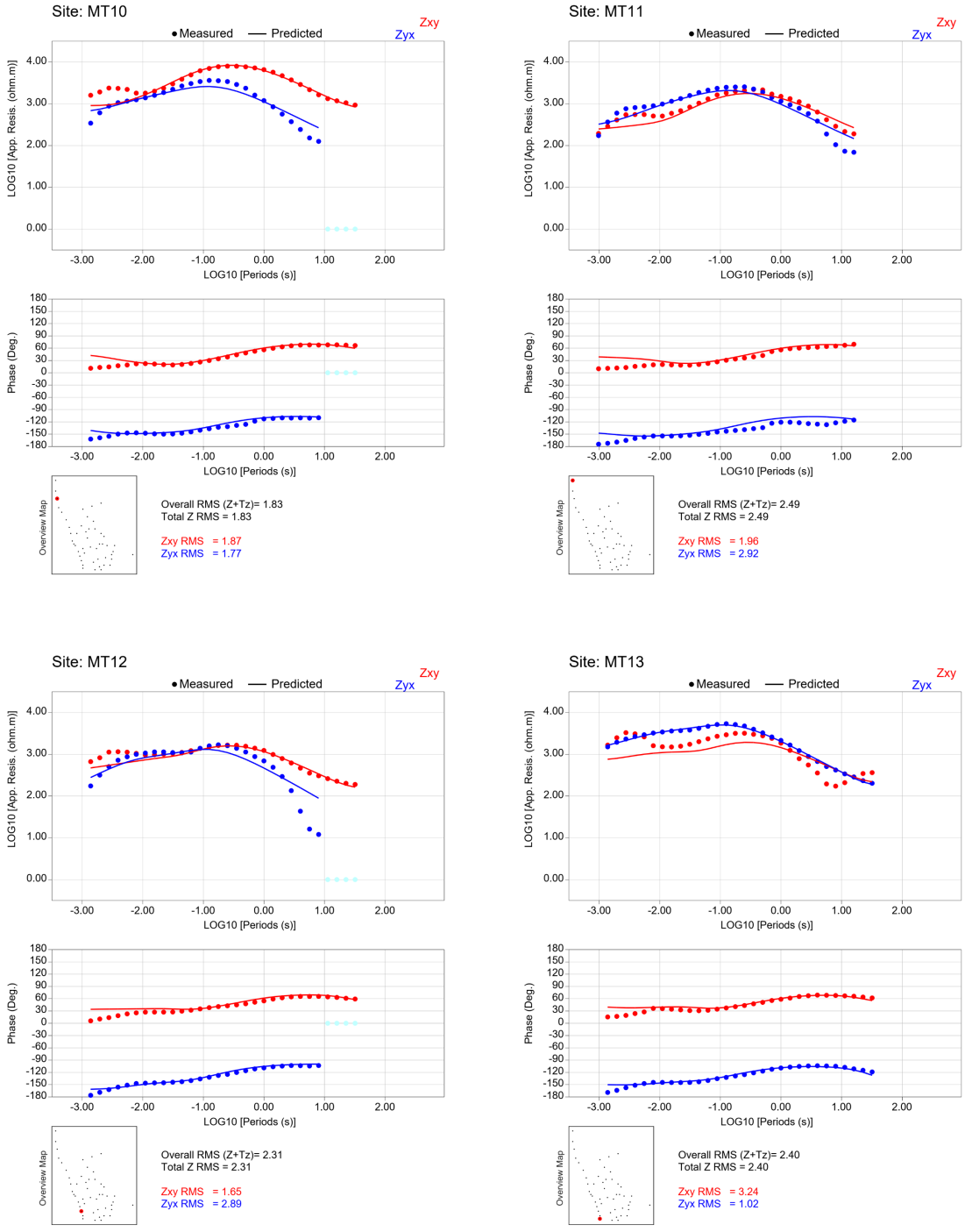

Appendix Figure F-3: Comparison of observed versus predicted MT transfer functions from the preferred model at stations MT10 to MT13. The red color represents the XY components, while the blue indicates the YX components.

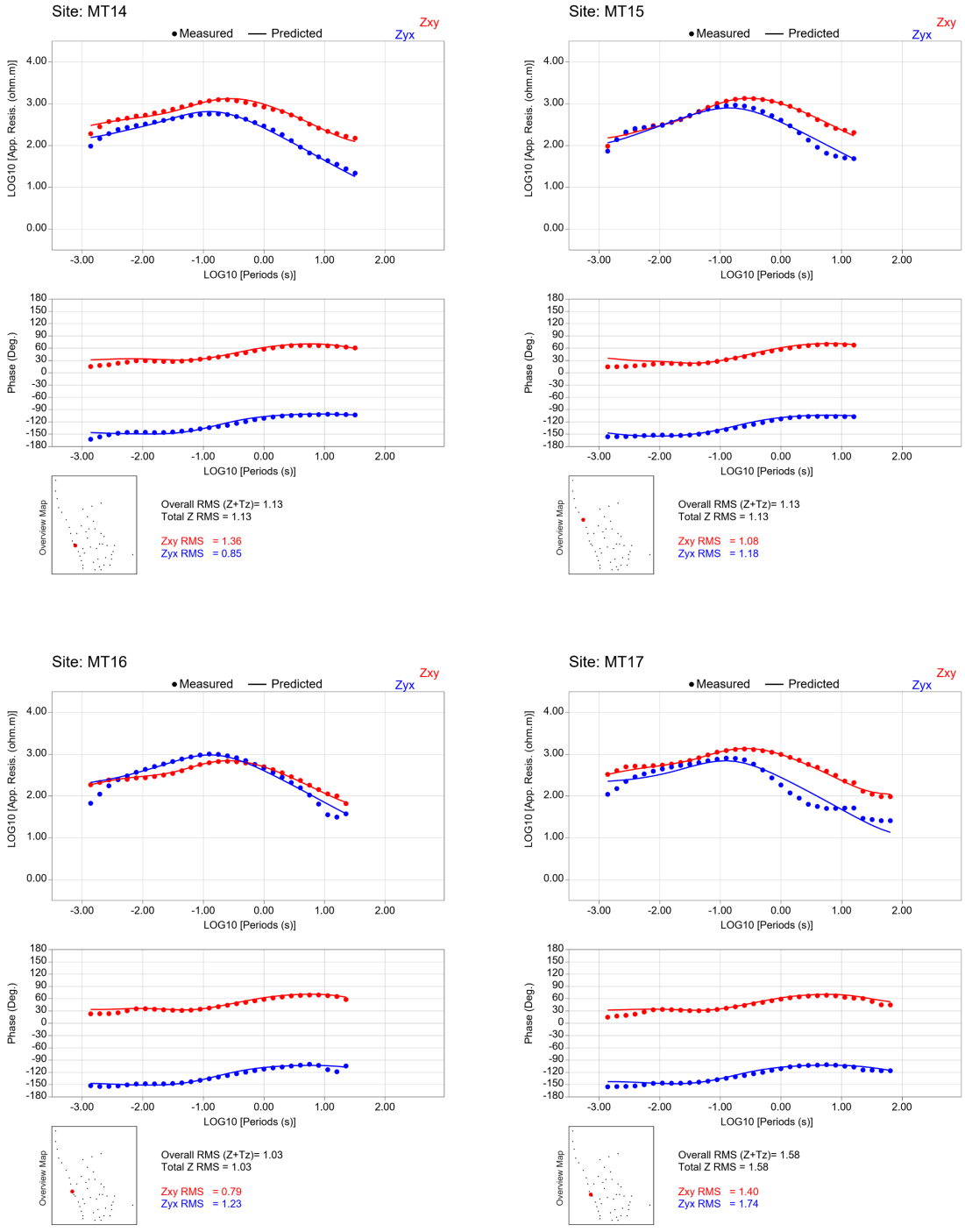

Appendix Figure F-4: Comparison of observed versus predicted MT transfer functions from the preferred model at stations MT14 to MT17. The red color represents the XY components, while the blue indicates the YX components.

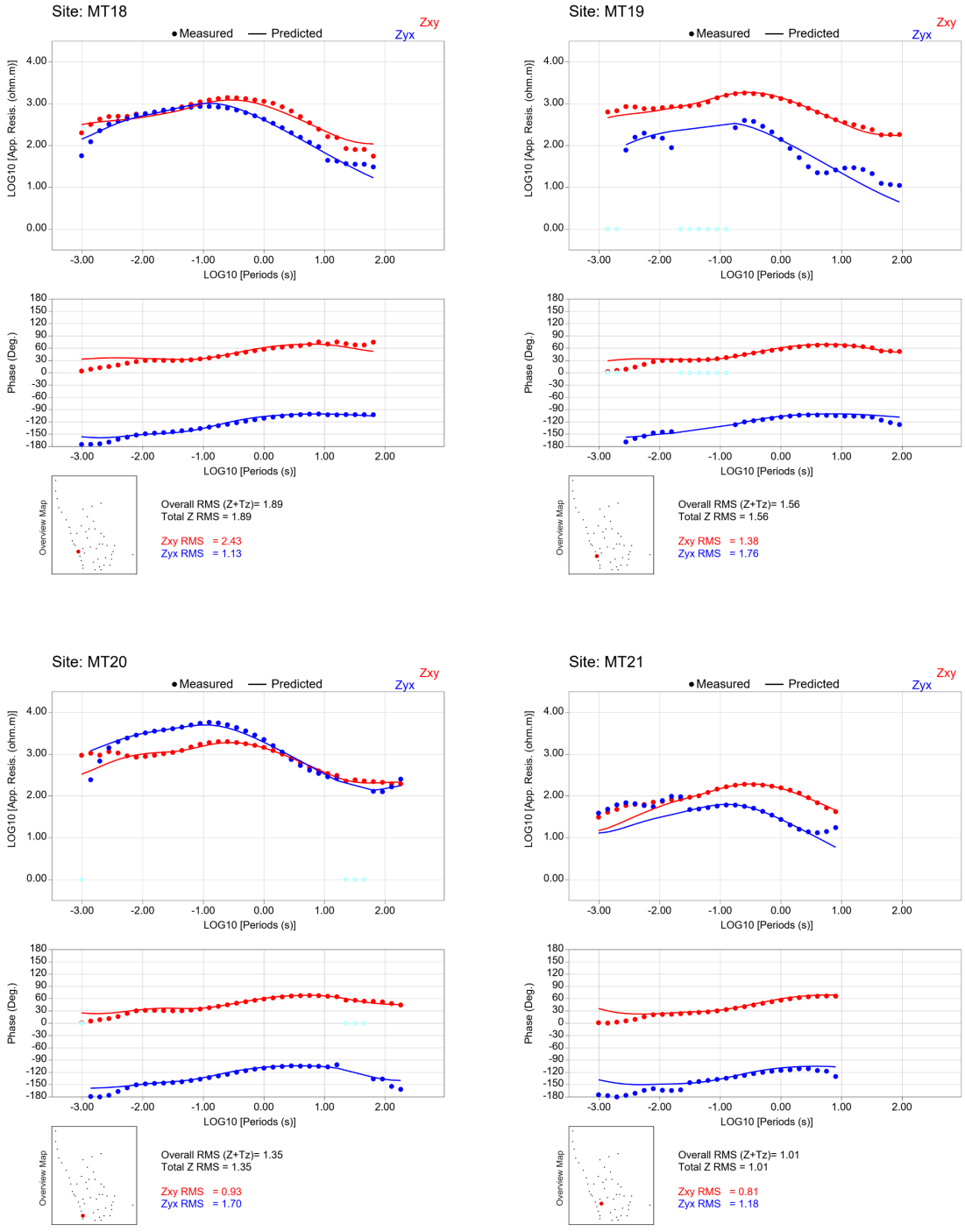

Appendix Figure F-5: Comparison of observed versus predicted MT transfer functions from the preferred model at stations MT18 to MT21. The red color represents the XY components, while the blue indicates the YX components.

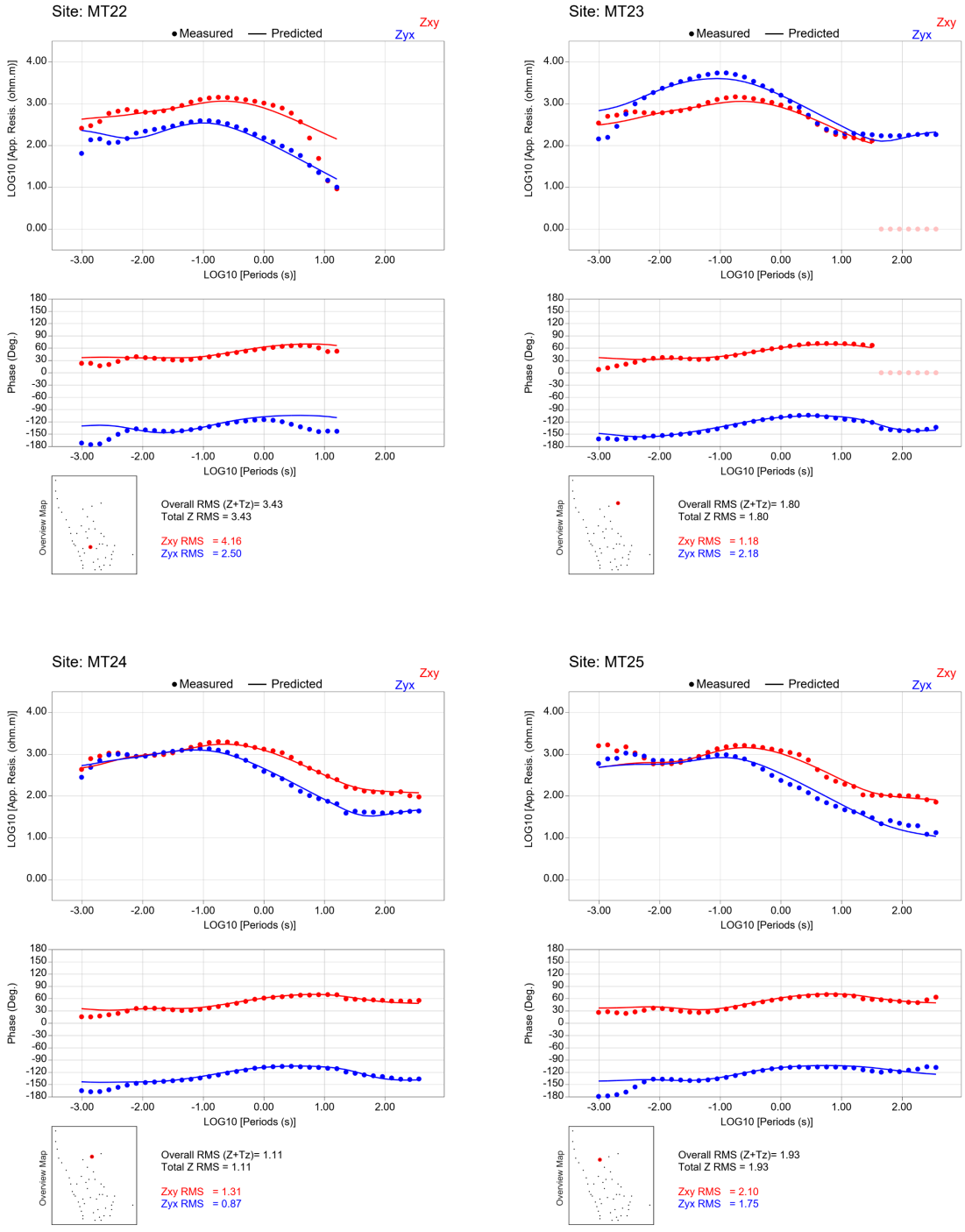

Appendix Figure F-6: Comparison of observed versus predicted MT transfer functions from the preferred model at stations MT22 to MT25. The red color represents the XY components, while the blue indicates the YX components.

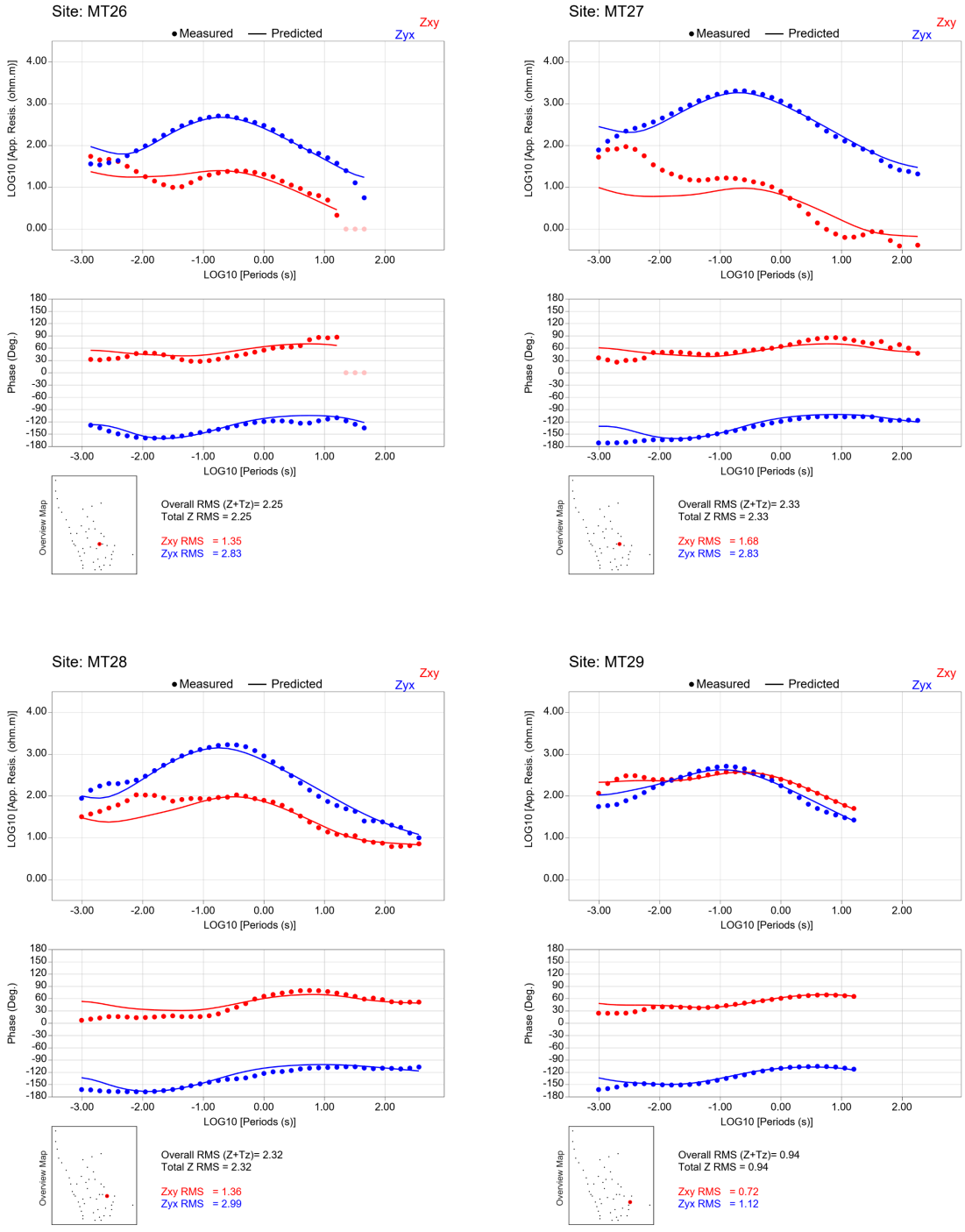

Appendix Figure F-7: Comparison of observed versus predicted MT transfer functions from the preferred model at stations MT26 to MT29. The red color represents the XY components, while the blue indicates the YX components.

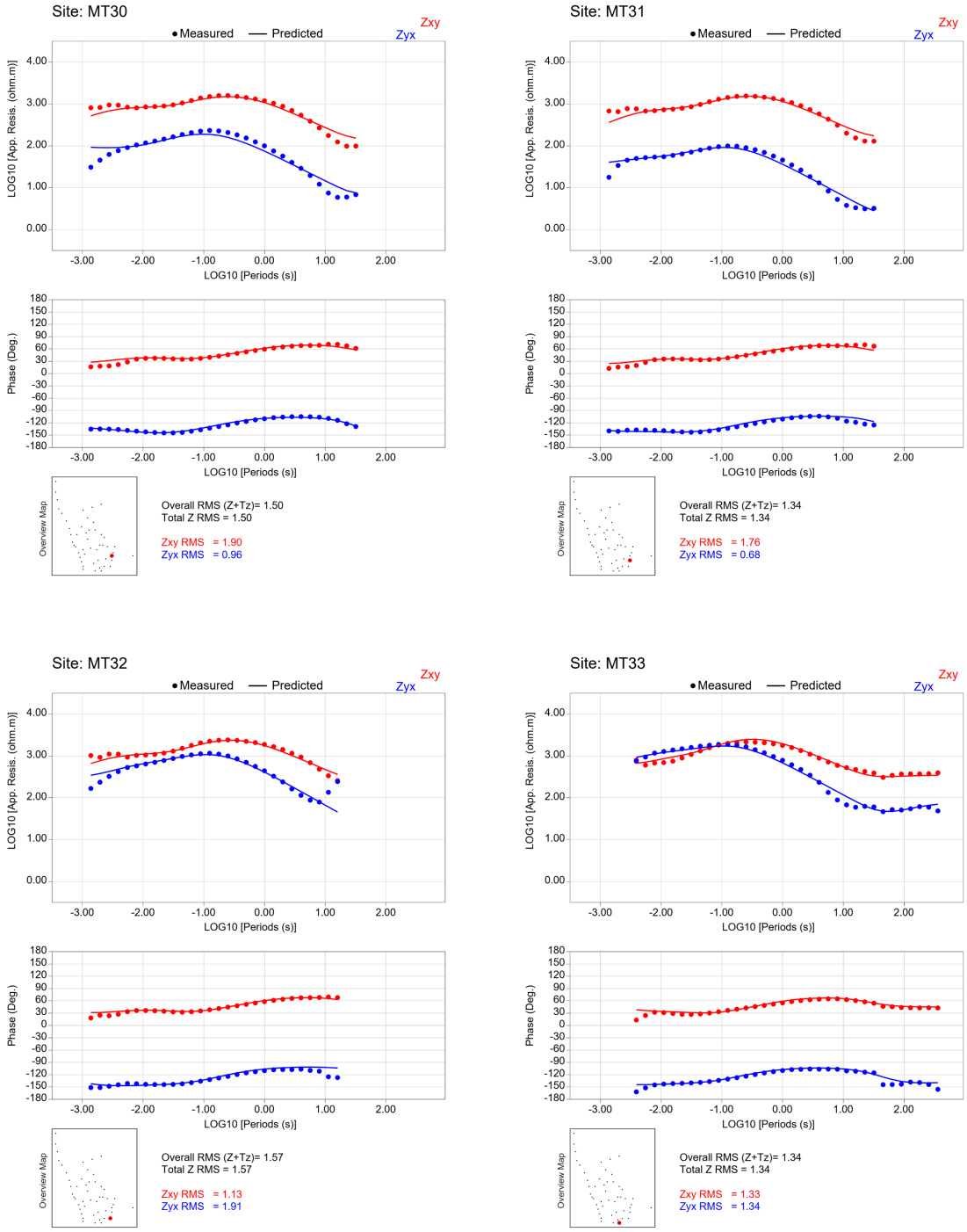

Appendix Figure F-8: Comparison of observed versus predicted MT transfer functions from the preferred model at stations MT30 to MT33. The red color represents the XY components, while the blue indicates the YX components.

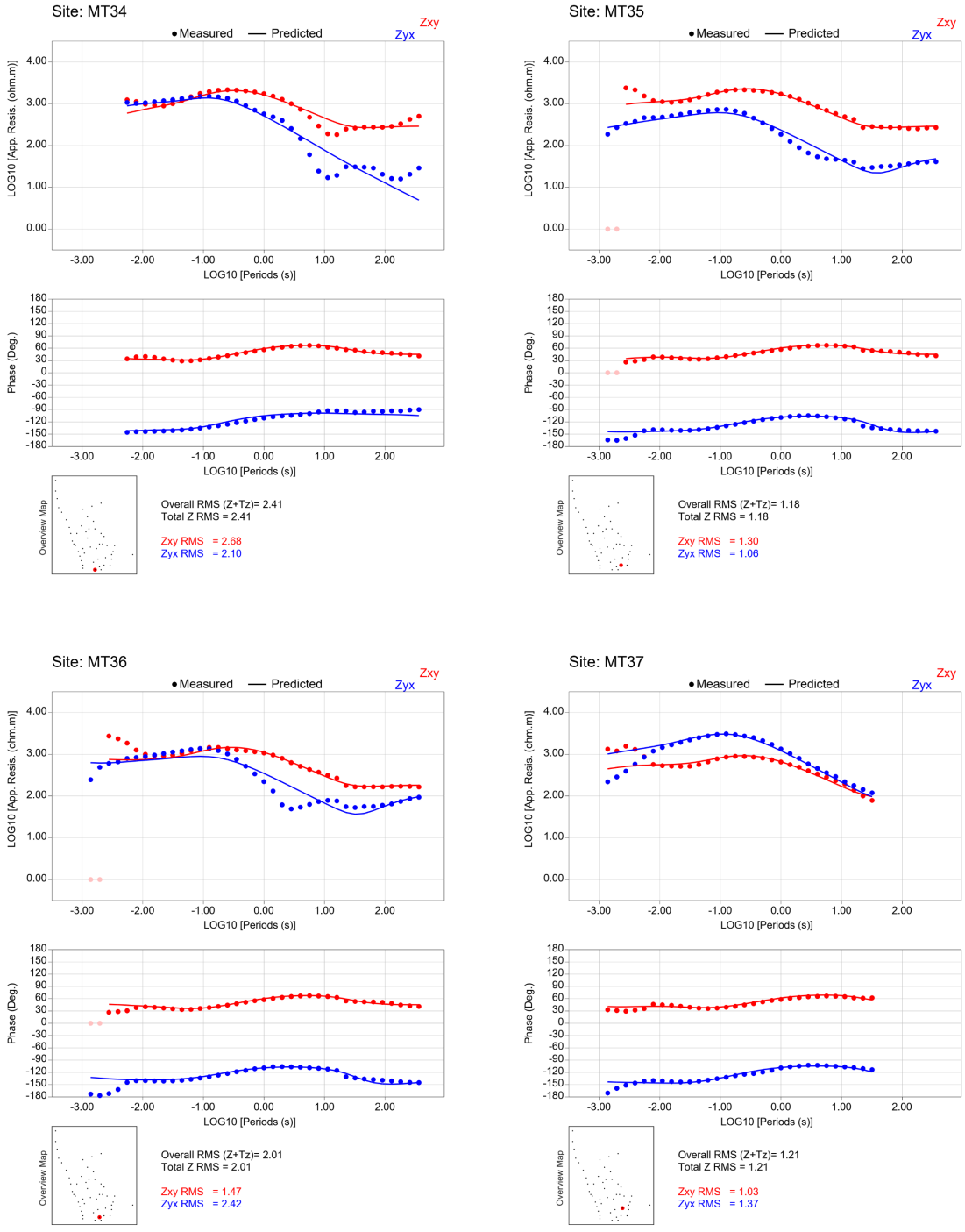

Appendix Figure F-9: Comparison of observed versus predicted MT transfer functions from the preferred model at stations MT34 to MT37. The red color represents the XY components, while the blue indicates the YX components.

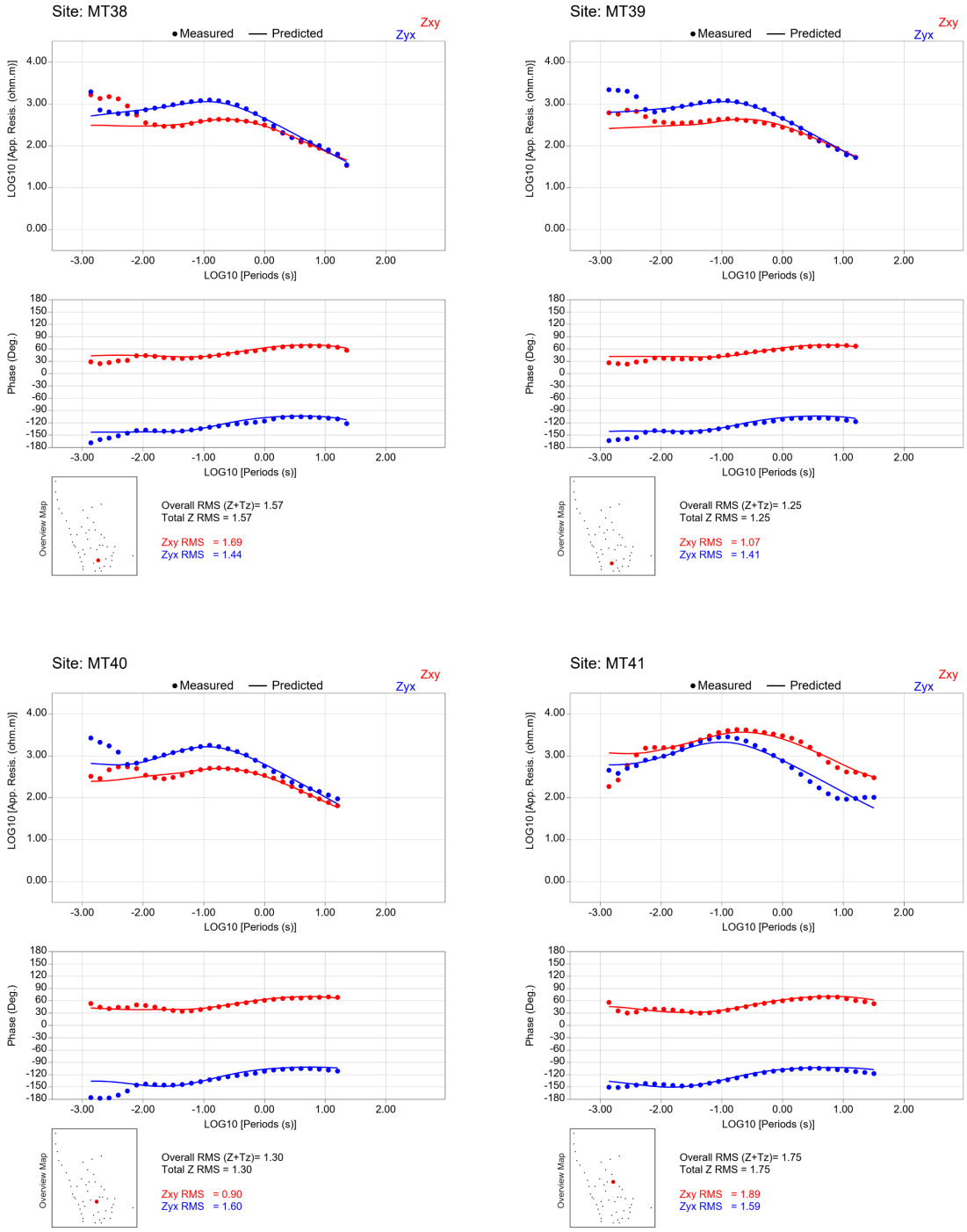

Appendix Figure F-10: Comparison of observed versus predicted MT transfer functions from the preferred model at stations MT38 to MT41. The red color represents the XY components, while the blue indicates the YX components.

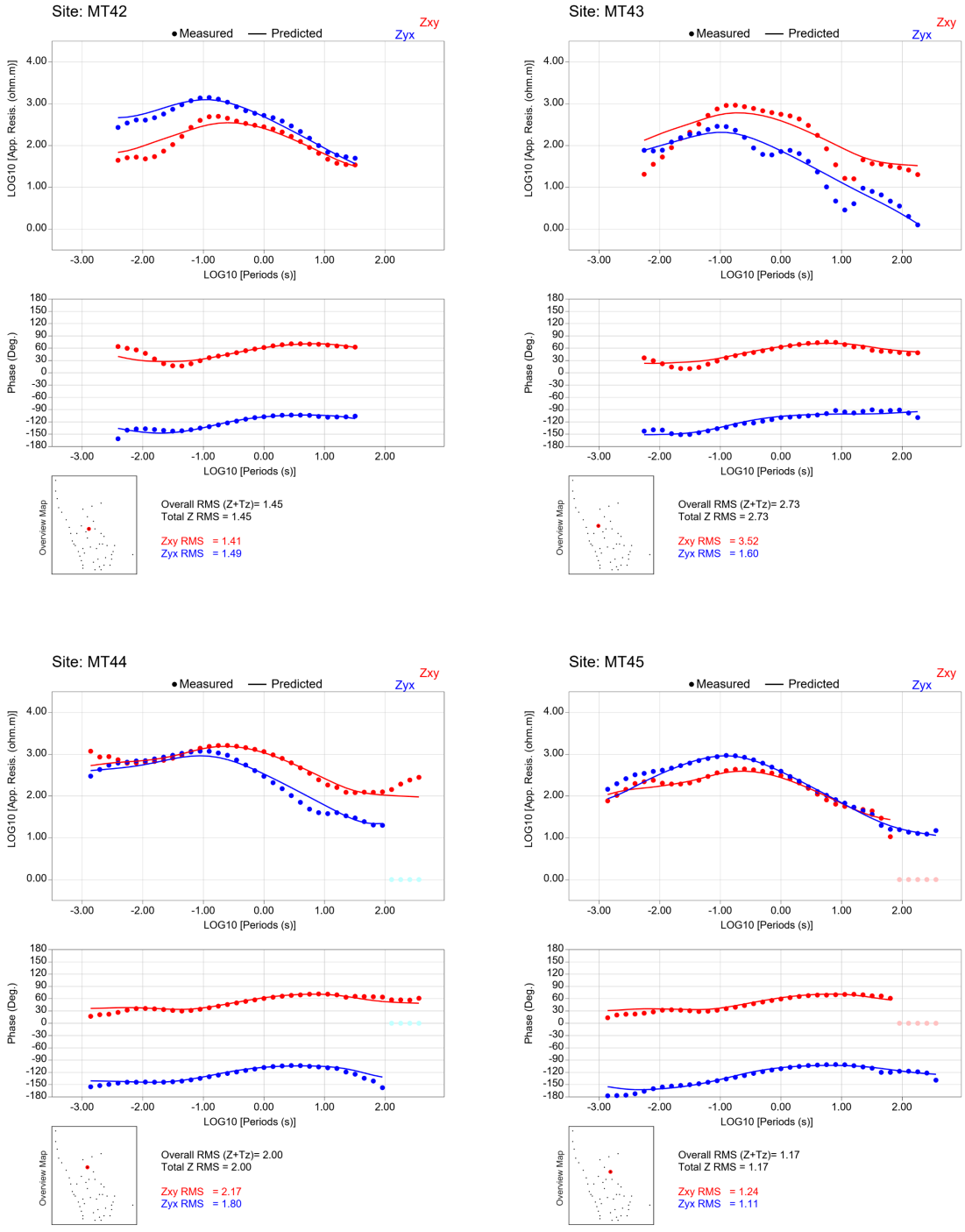

Appendix Figure F-11: Comparison of observed versus predicted MT transfer functions from the preferred model at stations MT42 to MT45. The red color represents the XY components, while the blue indicates the YX components.

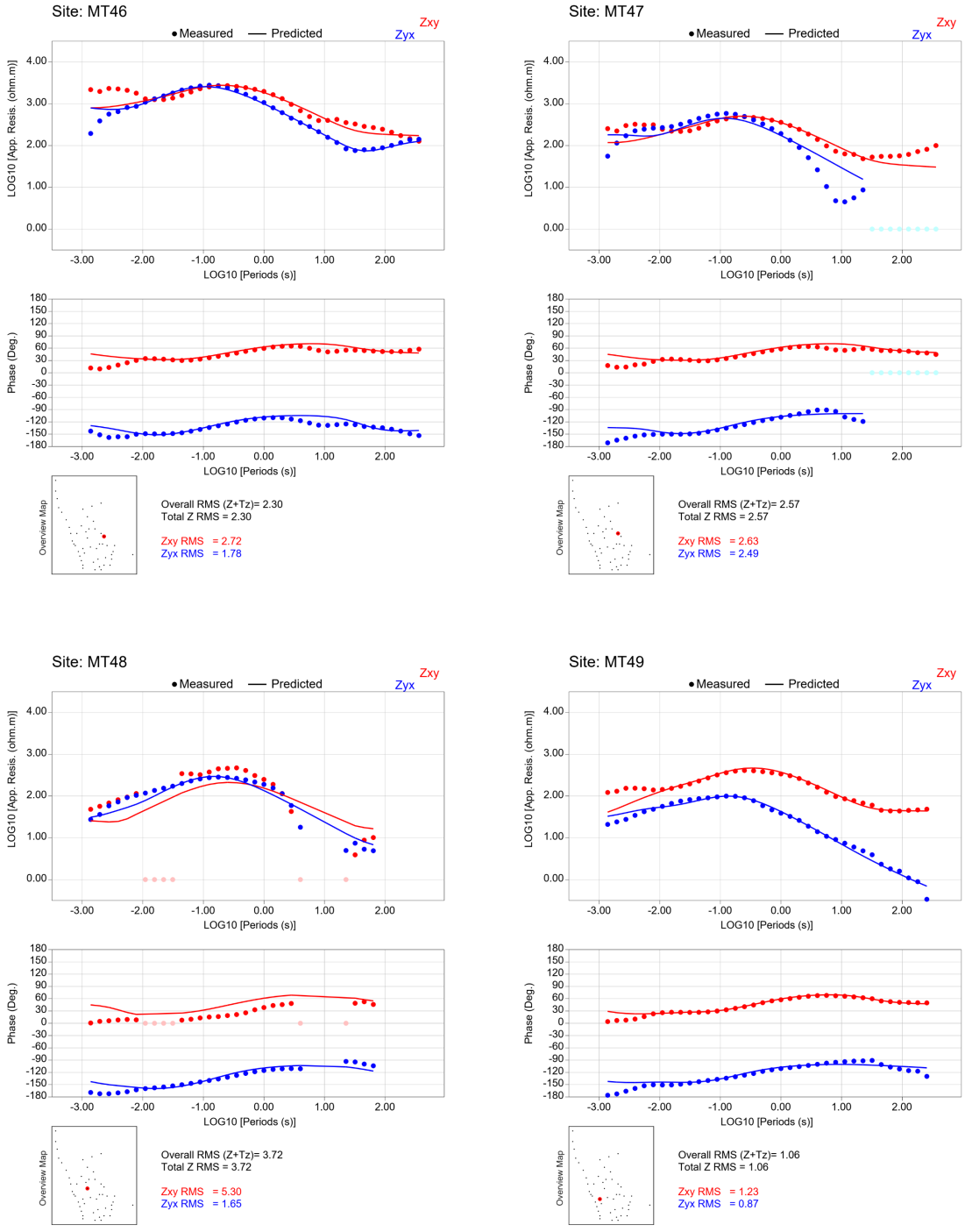

Appendix Figure F-12: Comparison of observed versus predicted MT transfer functions from the preferred model at stations MT46 to MT49. The red color represents the XY components, while the blue indicates the YX components.

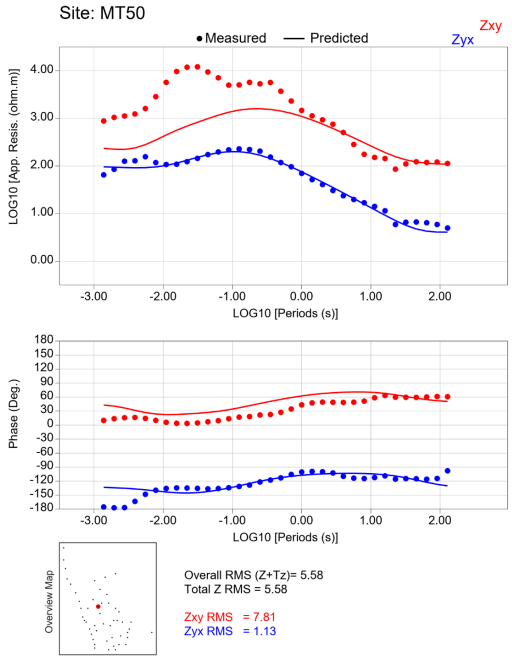

Appendix Figure F-13: Comparison of observed versus predicted MT transfer functions from the preferred model at station MT50. The red color represents the XY components, while the blue indicates the YX components.

Acknowledgments

Completing this PhD thesis has been one of the most challenging and rewarding journeys of my life, and it would not have been possible without the support, guidance, and encouragement of many individuals and institutions. I would like to take this opportunity to express my sincere gratitude to all those who have played a role in helping me reach this milestone.

First and foremost, I am deeply grateful to my supervisors, Prof. Dr. Bülent Tezkan, Prof. Dr. Pantelis Soupios, and Dr. Pritam Yogeswar, whose expertise, patience, and unwavering support have been invaluable throughout this journey. Their insightful feedback, thoughtful guidance, and encouragement have pushed me to sharpen my thinking and elevate my work. I truly appreciate the time and effort they invested in helping me grow both as a researcher and as a professional. I would also like to extend my gratitude to my thesis reviewer, Prof. Dr. Michael Becken, for appraising this thesis.

I also would like to thank Mr. Tilman Hanstein from KMS Technologies for his continued supports and deep discussions during data quality control and processing. Great thanks to Prof. Pantelis Soupios, Dr. Panagiotis Kirmizakis, Dr. Abid Khogali, Dr. Konstantinos Chavanidis and Ahmed Shaibani for their support during the field campaign. Without good teamwork, I don't assure to obtain much field data.

Here, I would like to say thanks to Dr. Panagiotis Kirmizakis, Dr. Pritam Yogeswar, Dr. Wiebke Mörbe, Dr. Fereydoun Sharifi, Mr. Tilman Hanstein, and Dr. Imamal Muttaqien for giving me constructive criticism and reviewing my thesis manuscript.

A heartfelt thank you to my colleagues and friends at the Institute of Geophysics and Meteorology (IGM) of University of Cologne for creating an environment of collaboration, inspiration, and support. The discussions, brainstorming sessions, and shared experiences have made this journey all the more rewarding.

My appreciation also goes to College of Petroleum Engineering & Geosciences (CPG) and Research Center for Renewable Energy and Power System (IRC-REPS) from the King Fahd University of Petroleum and Minerals (KFUPM), Saudi Arabia, for providing the technical and financial support that made this research possible. I am grateful for the resources, opportunities, and trust that enabled me to pursue my academic ambitions.

On a personal note, I am forever indebted to my family — my wife, Dewi Saadah, and my three beautiful daughters, Fusaila, Hunaida and Nusaiba — for their unconditional love, encouragement, and patience. Their belief in me has been a constant source of strength, even during the most challenging times. My family was with me all the time.

Finally, I would like to thank my friends outside academia, who provided balance and perspective when I needed it most. Their humor, kindness, and understanding have been essential in keeping me grounded throughout this journey.

This thesis is the result of collective effort and support, and I am truly grateful to everyone who has been part of this process. Thank you all.

Erklärung

Hiermit versichere ich an Eides statt, dass ich die vorliegende Dissertation selbstständig und ohne die Benutzung anderer als der angegebenen Hilfsmittel und Literatur angefertigt habe. Alle Stellen, die wörtlich oder sinngemäß aus veröffentlichten und nicht veröffentlichten Werken dem Wortlaut oder dem Sinn nach entnommen wurden, sind als solche kenntlich gemacht. Ich versichere an Eides statt, dass diese Dissertation noch keiner anderen Fakultät oder Universität zur Prüfung vorgelegen hat; dass sie - abgesehen von unten angegebenen Teilpublikationen und eingebundenen Artikeln und Manuskripten - noch nicht veröffentlicht worden ist sowie, dass ich eine Veröffentlichung der Dissertation vor Abschluss der Promotion nicht ohne Genehmigung des Promotionsausschusses vornehmen werde. Die Bestimmungen dieser Ordnung sind mir bekannt. Darüber hinaus erkläre ich hiermit, dass ich die Ordnung zur Sicherung guter wissenschaftlicher Praxis und zum Umgang mit wissenschaftlichem Fehlverhalten der Universität zu Köln gelesen und sie bei der Durchführung der Dissertation zugrundeliegenden Arbeiten und der schriftlich verfassten Dissertation beachtet habe und verpflichte mich hiermit, die dort genannten Vorgaben bei allen wissenschaftlichen Tätigkeiten zu beachten und umzusetzen. Ich versichere, dass die eingereichte elektronische Fassung der eingereichten Druckfassung vollständig entspricht.

Teilpublikationen:

- **Ashadi, A. L.**, Tezkan, B., Yogeshwar, P., Hanstein, T., Kirmizakis, P., Khogali, A., Chavanidis, K., & Soupios, P. (2024). *Magnetotelluric Case Study from Ain Al-Harrah Hot Spring, Al-Lith, Saudi Arabia*. Arabian Journal for Science and Engineering, 49(1), 899–912. https://doi.org/10.1007/s13369-023-08293-8

- **Ashadi, A. L.**, Tezkan, B., Yogeshwar, P., Hanstein, T., Kirmizakis, P., Khogali, A., Chavanidis, K., Soupios, P., & Strack, K. (2023). *Exploration of Ain Al-Harrah-Al-Lith geothermal field in Saudi Arabia using EM methods*. GRC Transactions, 47.

February 23, 2025

Abdul Latif Ashadi